Ion Beam Nanopatterning Beyond Conventional Geometries

By

KM Rakhi

Submitted

in fulfillment of the requirements for the degree

of

Doctor of Philosophy

Department of Physics

Indian Institute of Technology Ropar

May 2024

©Indian Institute of Technology Ropar

All rights reserved.

This thesis is affectionately dedicated to

My parents: Mrs. Munesh Baliyan, Mr. Jagpal Singh Baliyan

&

My brother: Rahul Baliyan

Certificate

It is certified that the work contained in this thesis entitled "**Ion Beam Nanopatterning Beyond Conventional Geometries**" by **Ms. KM Rakhi**, a student in the Department of Physics, to Indian Institute of Technology Ropar, for the award of degree of **Doctor of Philosophy** has been carried out under my supervision and this work has not been submitted elsewhere for a degree.

S sarkar

May 2024

Dr. Subhendu Sarkar
Associate Professor
Department of Physics
Indian Institute of Technology Ropar

Declaration

I hereby declare that the work presented in the thesis entitled "**Ion Beam Nanopatterning Beyond Conventional Geometries**" submitted for the degree of **Doctor of Philosophy** in Physics by me to Indian Institute of Technology Ropar has been carried out under the supervision of **Dr. Subhendu Sarkar**. This work is original and has not been submitted in part or full by me elsewhere for a degree.

May 2024

KM Rakhi
PhD Research Scholar
Department of Physics
Indian Institute of Technology Ropar

Acknowledgements

Finally, I am getting the privilege to express my thank to everyone for being a part of my doctoral journey. This achievement has been shaped by the help of many people, I have met along the PhD work.

First and foremost, I want to deeply thank my supervisor, Dr. Subhendu Sarkar, for guiding and supporting me throughout this journey. His advice and help have been really important to me, both in my academic and personal life. I extend special thanks to him for introducing me to the fascinating topic of ion beam irradiation.

I also want to thank the members of my Doctoral Committee, Dr. Mukesh Kumar, Dr. Debangsu Roy, Dr. Partha Sarathi Dutta, and my Chairperson Dr. Asoka Biswas, for their helpful discussions and suggestions. And a big thanks to Mr. Anshu Vaid for their technical and administrative support when I needed it.

I am really grateful for the expertise shared by Mr. Harsimran and Mr. Amit Kaushal in teaching me about SEM, AFM, and XRD techniques. And a big thanks to to Mr. Nand Kishore and his team, as well as the housekeeping staff, for their constant support, especially during the challenging times of the pandemic. They have been a source of comfort and assistance when I needed it most.

I want to express my thanks to Prof. Rodolfo Cuerno from the University Carlos III de Madrid, Spain and Prof. R. Mark Bradley from Colorado State University, USA for their valuable contributions and discussion to my work in understanding the mechanisms of pattern formation, respectively.

Among my fellow students, I owe a lot to Dr. Basanta Kumar Parida and Dr. Shinki Midha for helping me understand the deposition and ion source system. And I am really thankful for the support and friendship of my labmates Dr. Deepa Lohani, Deeksha, Jaspreet, and Pawan. They have made the lab a really great place to work.

I also want to thank the members of the RDRS group, especially Damanpreet Kaur, Raghvendra Posti, and Sanjay Pant, for their friendship and shared experiences. Over the years, our relationships transformed into a tight-knit trio, just like “3 saheli”. This journey has been filled with shared laughter, late-night eating, cooking, singing, comedy, gossip, occasional disagreements, and failed travel plans. Despite these, the experience felt easy and natural, ultimately bringing us to the significant moment of submitting our thesis. The journey would have remained incomplete without Paramjeet, Nitin Joshi, Ajit, Abhay, Faizan Bhai, Abhishek, Nitesh, Badri, Rohit Dahiya, Priya—members of "IIT Ropar family" for their amazing accompany. I will be ever thankful to my dear friends, Doli Pundir, Meenakshi Rajpoot, Upendar, Veg, Rupa, Saloni and Poonam for always caring and loving me unconditionally. My school friend late Driyanka Baliyan is also a blessing to me. I extend my gratitude to Dr. Sikha Saini, and this journey would be incomplete without her guidance.

Most importantly, I want to convey my deep gratitude to my family. I owe a lot to my mummy and papa, who not only gave me life but also supported whatever I wanted to do, even when it was tough for our family. I can not find the right words to thank my brother, Rahul Baliyan. He has been my support, who has always supported me in making my own decisions and pursuing whatever I want in life. I extend my gratitude to my caring and loving sisters and brothers, Ruby and Antima, as well as Shivam, Anuj, Sachin, and Shobit for their constant support and guidance. They have been a patient listener in my times of need. I am also thankful to my Nana Ji (Chandarbhan Pawar) and Nani Ji (Chatarkali Pawar), Dada Ji (Sukhveer Singh Baliyan and Shobharam Baliyan) and Dadi Ji (Shanti Baliyan), Chacha Ji (Ajaypal Singh) and Chachi Ji and Bhabhi (Varsa Baliyan), for their love and blessings showered upon me. I want to express my heartfelt gratitude to my wonderful niece Kornika (Janshu) Baliyan. Your presence in my life brings joy, laughter, and warmth. Lastly, I want to give a big thanks to everyone who has been a part of my life and helped me in any way to achieve this goal. Your support has been incredibly important to me, and I am really grateful for it. Last but not least I extend my gratitude to God for granting me this opportunity.

KM Rakhi
Indian Institute of Technology Ropar, India-140001
May 2024

Life's a constant journey, full of highs and lows

Lay Summary

This thesis explores the evolution of nanopatterns on solid substrates under various unconventional ion beam configurations in contrast to the conventional ones. These configurations include intermittent sputtering sequences to study surface relaxation effects, azimuthally swinging geometry at variable speeds to study surface morphological transitions and azimuthal swinging to study coarsening phenomena and hierarchical surface formation. Additionally, the potential for increased pattern order using these techniques is investigated. Conventional ion beam irradiation methods have been compared with these unconventional approaches. The primary objectives were to understand the mechanisms behind nanopattern formation and to explore methods for improving pattern quality and increasing structural ordering.

The intermittent sputtering method involves irradiating the surface intermittently with Ar^+ ions at oblique incidence, allowing it to relax within intervals of varying durations. Nanoripples dominate the irradiated surfaces, accompanied by hierarchical triangular structures at lower energies. We find that ripple ordering peaks at intermediate sputtering intervals, and the area of triangular structures varies with these intervals. Our findings align with numerical simulations, suggesting that intermittent sputtering holds promise for tailoring ion-beam nanostructured surfaces.

In the next study, we explored the morphological changes on silicon surfaces induced by 500 eV Ar^+ ion sputtering at a 67° incidence angle, using a novel substrate swinging technique. By varying azimuthal angles and rotation speeds, we identified four distinct regimes of nanostructure morphology, including ripples with and without triangular structures, smooth surfaces, and disordered ripple topographies. Notably, ripple wave vector orientations exhibited sudden shifts at certain azimuthal angles. These findings enhance our understanding of surface evolution under unconventional ion sputtering, potentially advancing theoretical models and offering insights into practical applications of surface patterns.

In our follow-up study, we investigated how Si(100) surfaces evolved under 500 eV Ar^+ irradiation at a polar angle of 67°, employing a novel technique of azimuthal sample swinging (20° ($= \Delta\phi$). We found that the swinging sample exhibited prolonged wavelength coarsening, while ripple anticoarsening was observed for the static sample at high fluences. This unconventional geometry directly influenced both linear and nonlinear growth regimes, leading to reduced asymmetries in surface structures. Our findings high-

light the role of near-surface mass redistribution events, sputtered atom re-deposition effects, and differential exposure conditions in the swinging geometry. This study contributes to a better understanding of the spatio-temporal pattern formation benefits of unconventional azimuthal swinging geometry in ion beam sputtering, with potential applications in various fields.

A further work explores the impact of asymmetric azimuthal swinging angles ($\Delta\phi$) on self-organized nanostructures under low-energy Ar^+ ion beam irradiation. This configuration reveals rotated triangular structures and nanoripples. These patterns challenge traditional explanations based on curvature-dependent instability terms. A parameter space for Ar^+ ion bombardment with swinging substrates inducing rotated nanostructures on Si surfaces is identified.

In summary, the experimentally observed results presented in this thesis are very useful. They contribute significantly to the fundamental understanding of pattern formation and ion-solid interaction. Furthermore, they facilitate the investigation of pattern formation under unconventional techniques aimed at enhancing surface ordering and reducing surface defect density.

Keywords: Surface nanopatterning, Low energy ion beam irradiation, Unconventional methods, Power spectral density, 2D slope distribution, Autocorrelation function, Atomic microscopy force

List of abbreviations and symbols

IBI - Ion Beam Irradiation

CVD - Chemical Vapor Deposition

ESD - Effective Surface Diffusion

BH - Bradley Harper

KS - Kuramoto-Sivashinsky

KPZ - Kardar-Parisi-Zhang

AFM - Atomic Force Microscopy

PSD - Power Spectral Density

FWHM - Full Width at Half Maximum

ACF - Auto-Correlation Function

RF - Radio Frequency

DC - Direct Current

EDX - Energy Dispersive X-ray Spectroscopy

FFT - Fast Fourier Transform

SAS - Symmetric Azimuthal Swinging

AAS - Asymmetric Azimuthal Swinging

sccm - Standard Cubic Centimetres per Minute

SRIM - Stopping and Range of Ions in Matter

PSD - Power Spectral Density

RF - Radio Frequency

RMS - Root Mean Square

RPM - Rotation Per Minute

SPM - Scanning Probe Microscopy

SD - Standard Deviation

SEM - Scanning Electron Microscopy

XPS - X-ray Photoelectron Spectroscopy

UV-Vis - Ultraviolet-Visible

UHV - Ultra-High Vacuum

XRD - X-Ray Diffraction

PSPD - Position Sensitive Photodetector

θ - Ion Beam Incidence Angle

α - Local Ion Incidence Angle

θ_c - Critical Ion Incidence Angle (Bradley and Harper Model)

E - Ion Beam Energy

T - Temperature

ν - Negative Surface Tension Coefficient f - Fluence

j - Ion Current Density

ϕ - Azimuthal Angle

K - Thermally Activated Surface Diffusion

λ - Wavelength

ξ- Correlation Length

Contents

1 Introduction 1

1.1 Ion-Solid Interaction 1

1.1.1 Fundamental Aspects of Ion-Solid Interaction 1

1.2 Surface Patterning using Ion Beams 4

1.3 Theoretical Understanding of Ion Beam Patterning 7

1.3.1 Bradley and Harper (BH) model 7

1.3.2 Nonlinear Extension of BH Model 9

1.3.3 Damped Kuramoto-Sivashinsky Equation 10

1.3.4 General Continuum Equation 11

1.4 Applications of Ion Beam Irradiation 12

1.5 Ion Beam Patterning: A brief experimental literature survey 14

1.6 Motivation and Objectives 21

1.7 Thesis Overview 22

2 Materials and Methods 25

2.1 Ultrasonication (Sample Cleaning) 25

2.1.1 Principle 26

2.1.2 Instrumentation 26

2.2 Structuring Techniques 27

2.3 Characterization tools 31

2.3.1 Atomic Force Microscopy 32
2.3.2 Scanning Electron Microscopy (SEM) and Energy Dispersive X-ray Spectroscopy (EDX) 40

3 Towards ordered Si surface nanostructuring: Role of an intermittent ion beam irradiation approach 43

3.1 Introduction 44
3.2 Materials and methods 48
3.3 Results and discussions 53
3.3.1 Surface evolution for continuous sputtering conditions at 900 eV . . 53
3.3.2 Surface evolution for continuous sputtering conditions at 500 eV . . 56
3.3.3 Surface evolution with intermittent sputtering conditions 57
3.3.4 Additional issues 63
3.3.5 Numerical simulations 66
3.4 Conclusions 72

4 Abrupt pattern transitions in argon ion bombarded swinging Si substrates 75

4.1 Introduction 75
4.2 Experimental Techniques 79
4.3 Results and discussions 81
4.3.1 Surface morphology evolution of Si surfaces rotating at 1 RPM . . . 81
4.3.2 Surface morphology of irradiated Si surfaces swinging by different azimuthal angles at a speed of 1 RPM 84
4.3.3 Effect of swing speed on surface morphology of irradiated Si surfaces 91
4.3.4 Effect on local slope distribution 95
4.4 Conclusions 100

5 Prolonged pattern coarsening in ion irradiated swinging Si substrates 103

5.1 Introduction 103

5.2 Materials and Methods 107

5.3 Results and discussions 109

5.3.1 Morphology evolution on static Si surfaces 109

5.3.2 Morphology evolution on azimuthally swinging Si surfaces 112

5.3.3 Spatio-temporal dynamics of statistical topography indicators . . . 115

5.4 Conclusions 128

6 Rotation of hierarchical surface structures under ion bombarded asymmetric swinging geometries 133

6.1 Introduction 133

6.2 Experimental Techniques 137

6.3 Results and discussions 138

6.4 Conclusions 147

7 Summary and Future Outlook 149

7.1 Summary 149

7.2 Future Outlook 153

List of Figures

1.1 Schematic representation of fabrication techniques. 5

2.1 Schematic illustrating the cleaning mechanism during the sonication process. 26

2.2 A simple schematic representation of the Kaufman ion source. 29

2.3 Kaufman ion source facility available in our lab. 31

2.4 The schematic illustrates the sputtering geometry, with (a) representing the conventional setup where the sample remains stationary, and (b) depicting the unconventional setup where the sample can azimuthally rotate, swing, rock (polar angle oscillated), or be non-stationary. 32

2.5 A simple schematic representation of the AFM sample tip geometry. 32

2.6 Schematic of force-distance curve. 33

2.7 Schematic representation of the working of AFM. 34

2.8 Different operating modes of AFM depending on distance between tip and sample. 35

2.9 AFM instrument images in IIT Ropar. 37

2.10 A schematic diagram represents the basic components required for SEM. . 41

3.1 Schematic showing beam-on (sputtering time) and beam-off (relaxation time) steps for irradiation of samples with 500 eV Ar$^+$ ions at 67°. The schematic corresponds to S$_2$ of Table 3.1 as an example. 51

3.2 (a) 3×3 μm^2 AFM micrograph of pristine Si surface. Top right inset: 2D FFT (square root of the 2D PSD) corresponding to the AFM images. (b) Power spectral density of the pristine Si surface. 53

3.3 3×3 μm^2 AFM micrographs of 900 eV Ar$^+$ irradiated Si at 67° for continuous sputtering times t$_N$ of (a) 2 min, (b) 5 min, (c) 10 min, (d) 15 min, and (e) 20 min. Black arrows indicate the ion beam direction. Top right insets: 2D FFT (square root of the 2D PSD) of the corresponding AFM images. 54

3.4 (a) Amplitude, rms roughness, and wavelength (bottom to top) vs sputtering time for continuously sputtered Si surfaces using 900 eV Ar$^+$, for ion fluences from $10{\times}10^{18}$ to $10{\times}10^{19}$ ions cm^{-2}. (b) Log-log plot of 1D PSD versus spatial frequency q (extracted from 1D cuts of AFM images) along the ion beam direction (x-axis). The straight solid line shown as a reference corresponds to power-law behavior as PSD(q) $\sim q^m$, for m as given. All other lines are guides to the eye. 55

3.5 3×3 μm^2 AFM micrographs of 500 eV Ar$^+$ irradiated Si at 67° for continuous sputtering times t$_C$ of (a) 2 min, (b) 5 min, (c) 7 min, (d) 10 min, (e) 15 min, and (f) 20 min. Black arrow indicates the ion beam direction. Top right insets: 2D FFT of corresponding AFM images. The white dashed line in (b) selects a portion of the surface to be compared to a numerically simulated surface in Fig. 3.13. 57

3.6 3×3 μm^2 AFM micrographs of 500 eV Ar$^+$ irradiated Si at 67° for a relaxation time interval (t$_R$) of 5 min and sputtering time intervals t$_S$ (a) 2 min, (b) 5 min, (c) 7 min, (d) 10 min, and (e) 20 min. The total sputtering time (t$_C$) is 20 min and the total ion fluence is 10×10^{19} cm^{-2}. Black arrows indicate the ion beam direction. As noted in Table 3.1, panel (e) for S$_{20}$ is identical to C$_{20}$ from Fig. 3.5 and is reproduced here for the reader's convenience. Top right insets: 2D FFT of corresponding AFM images. Bottom left insets in panels (a) and (e): 1×1 μm^2 AFM micrographs of corresponding AFM images. 58

3.7 3×3 μm^2 AFM micrographs of 500 eV Ar$^+$ irradiated Si at 67° for a relaxation time interval (t$_R$) of 5 min and sputtering time intervals (t$_S$) of 2 min with increasing total time of sputtering for each Si sample from (a) to (j) t$_T$ = (a) 2 min, (b) 4 min, (c) 6 min, (d) 8 min, (e) 10 min, (f) 12 min, (g) 14 min, (h) 16 min, (i) 18 min, and (j) 20 min. Black arrow indicates the direction of incidence of the ion beam. Top right insets: 2D FFT of corresponding AFM images. 59

3.8 3×3 μm^2 AFM micrographs of 500 eV Ar$^+$ irradiated Si at 67° for a sputtering time interval (t$_S$) of 5 min and for relaxation time intervals t$_R$ (a) 0 min, (b) 2 min, (c) 5 min, (d) 7 min, (e) 10 min, and (f) 15 min. The total sputtering time (t$_C$) is 20 min and the total ion fluence is 10×10^{19} cm^{-2}. Black arrows indicate the ion beam direction. As noted in Table 3.1, panel (a) for R$_0$ is identical to C$_{20}$ from Fig. 3.5(f) and to S$_{20}$ from Fig. 3.6(e), and is reproduced here for the reader's convenience. Top right insets: FFT of the corresponding AFM images. Bottom left inset in panel (a): 1×1 μm^2 AFM micrograph of the corresponding AFM image. 60

3.9 Plots showing amplitude, rms roughness, and wavelength dependence with time (bottom to top) for: (a) Continuous sputtering (varying t_C), (b) varying sputtering time interval (t_S), and (c) varying relaxation time interval (t_R). Lines are guides to the eye. 61

3.10 Log-log plot of 1D PSD versus spatial frequency q (as extracted from AFM images) along the projection of the ion beam direction. (a) Continuous sputtering, (b) variable t_S for $\mathrm{t}_R = 5$ min and $\mathrm{t}_C = 20$ min, and (c) variable t_R for $\mathrm{t}_S = 5$ min and $\mathrm{t}_C = 20$ min. Lines are guides to the eye. 62

3.11 AFM images showing typical triangular structures highlighted as black triangles for (a) C_{20}, (b) S_7, and (c) R_7. (d) Typical line profile corresponding to the dashed line on the selected triangular structure shown in panel (b). Black arrow indicates the ion beam direction. 64

3.12 Surface morphologies obtained from numerical simulations of Eq. (3.6) under continuous sputtering conditions for increasing simulation times $t = 2.66$ (a), $t = 9.54$ (b), and $t = 20$ (c). The height scale (in arbitrary units) appears to the right of each image. Insets provide the corresponding FFT functions. Panel (d) shows the time evolution of the rms roughness while panel (e) displays the 1D PSD for times as given in the legend. All lines are guides to the eye and all units are arbitrary. Equation parameters are $\nu_x = -\nu_y = \mathcal{K} = 1$, $\Omega_x = 2$, $\Omega_y = 0$, $\lambda_x^{(1)} = 0.4$, $\lambda_y^{(1)} = 0$, $\mu_x = -0.25$, and $\mu_y = r = 0$ and the lateral system size is $L = 512$. 67

3.13 Comparison between the detail (a) that appears boxed in the AFM top view of the experimental C_5 sample displayed in Fig. 3.5(b) (see that figure for a scale bar) and a portion of a simulated surface morphology (b) obtained from a numerical simulation of Eq. (3.6) under continuous sputtering conditions for simulation time $t = 6.6$. The height scale for panel (b) is in arbitrary units. Equation parameters are as in Fig. 3.12, the lateral system size [approximately twice the side of (b)] is $L = 512$, and the initial condition is a random perturbation of a flat surface, see the text for more details. 68

3.14 Sample surface morphologies obtained from numerical simulations of Eq. (3.6) under intermittent sputtering conditions for increasing sputtering time intervals $\mathrm{t}_S = 2$ (a), $\mathrm{t}_S = 7$ (b), and $\mathrm{t}_S = 10$ (c) for a fixed relaxation time $\mathrm{t}_R = 5$. The height scale (in arbitrary units) appears to the right of each image. Insets provide the corresponding FFT functions. Panel (d) shows the time evolution of the rms roughness for all the sputtering time intervals studied as detailed in the legend, while panel (d) displays the final roughness reached in each case, as a function of the sputtering time interval. All lines are guides to the eye and all units are arbitrary. Equation parameters are: during sputtering intervals, $\nu_x = -\nu_y = \mathcal{K} = 1$, $\Omega_x = 2$, $\Omega_y = 0$, $\lambda_x^{(1)} = 0.4$, $\lambda_y^{(1)} = 0$, $\mu_x = -0.25$, and $\mu_y = r = 0$; during relaxation intervals, $\nu'_x = -\nu'_y = \Omega'_x = \Omega'_y = \lambda_x'^{(1)} = \lambda_y'^{(1)} = 0$, $\mathcal{K}' = 0.1$, $\mu'_x = -0.025$, and $\mu'_y = r' = 0$. The lateral system size is $L = 512$. 70

3.15 Sample surface morphologies obtained from numerical simulations of Eq. (3.6) under intermittent sputtering conditions for increasing relaxation time intervals $t_R = 2$ (a), $t_R = 7$ (b), and $t_R = 15$ (c), for a fixed sputtering time $t_S = 5$. The height scale (in arbitrary units) appears to the right of each image. Insets provide the corresponding FFT functions. Panel (d) shows the time evolution of the rms roughness for all the sputtering time intervals studied, as detailed in the legend (recall $C_{20} = R_0$), while panel (e) displays the final roughness reached in each case, as a function of the relaxation time interval. All lines are guides to the eye and all units are arbitrary. Equation parameters and lateral system size L are as in Fig. 3.14. 71

4.1 Schematic view of the swing geometry in azimuth (ϕ) during IBI. θ ($= 67^\circ$) is the polar angle between the 500 eV Ar$^+$ beam (blue arrow) and the (stationary) surface normal. The sample azimuthally swings for an angle $\triangle\phi$ ($-\phi \rightarrow +\phi$) across the incidence ion beam direction. 80

4.2 3×3 μm^2 AFM micrographs of 500 eV Ar$^+$ irradiated Si at 67°. (a) Without rotation with fluence of 7.5×10^{19} ions cm^{-2}, and for continuous rotation at fluence values of (b) 2.5×10^{19} ions cm^{-2}, (c) 5×10^{19} ions cm^{-2}, (d) 10×10^{19} ions cm^{-2}, (e) 1.2×10^{20} ions cm^{-2}, and (f) 1.5×10^{20} ions cm^{-2}, respectively. Black arrow indicates the initial direction of the ion beam prior to rotation. Top right insets: 2D FFTs of corresponding AFM images. Bottom left insets: Corresponding 1×1 μm^2 AFM images. (g) Plot showing rms roughness as a variation of irradiation time. (h) 1D PSD obtained from the AFM images for the irradiated samples. 81

4.3 1×1 μm^2 AFM micrographs of 500 eV Ar$^+$ irradiated Si at 67°. (a) Without rotation with fluence of 7.5×10^{19} ions cm^{-2}, and for continuous rotation at fluence values of (b) 2.5×10^{19} cm^{-2}, (c) 5×10^{19} cm^{-2}, (d) 10×10^{19} cm^{-2}, (e) 1.2×10^{20} cm^{-2}, and (f) 1.5×10^{20} cm^{-2}, respectively. Black arrow indicates the initial direction of the ion beam prior to rotation. 82

4.4 3×3 μm^2 AFM micrographs of 500 eV Ar$^+$ irradiated Si at 67° for different values of swinging angle ($\triangle\phi$): (a) 0°, (b) 10°, (c) 20°, (d) 30°, (e) 60°, (f) 70°, (g) 80°, (h) 90°, (i) 100°, (j) 110°, (k) 120°, (l) 180°, (m) 280°, (n) 360°, and (o) continuous rotation, respectively. Black arrow indicates the initial direction of ion beam prior to rotation. Top right insets: 2D FFTs of corresponding AFM images. Bottom left insets: Corresponding 1×1 μm^2 AFM images. 85

4.5 1×1 μm^2 AFM micrographs of 500 eV Ar$^+$ irradiated Si at 67° for different values of swinging angle ($\Delta\phi$): (a) 0°, (b) 10°, (c) 20°, (d) 30°, (e) 60°, (f) 70°, (g) 80°, (h) 90°, (i) 100°, (j) 110°, (k) 120°, (l) 180°, (m) 280°, (n) 360°, and (o) continuous rotation, respectively. Black arrow indicates the initial direction of ion beam prior to rotation. 86

4.6 Plots showing evolution of (a) rms roughness, (b) wavelength, (c) 1D PSD and (d) ripple wave vector direction for different values of swinging angles such as: $\triangle\phi = 0°$, 10°, 20°, 30°, 60°, 70°, 80°, 90°, 100°, 110°, 120°, 180°, 280°, 360°, and continuous rotation. 88

4.7 Log-log plot of 1D PSD versus spatial frequency q (extracted from 1D cuts of AFM images) along the ion beam direction (x-axis). Here q has been taken equal to 1/l for simplicity 89

4.8 Log-log plot of 1D PSD versus spatial frequency q (extracted from 1D cuts of AFM images) along the ion beam direction (x-axis) for an ordered and a disordered surface. Inset shows the corresponding AFM images. 90

4.9 Plot showing evolution of rms roughness of 500 eV Ar^+ irradiated at $\theta = 67°$ for different sputtering times at $\Delta\phi = 20°$. The dashed red lines are guides to the eye showing the behaviour of increase of roughness with sputtering time. 91

4.10 3×3 $\mu\mathrm{m}^2$ AFM micrographs of 500 eV Ar^+ irradiated at $\theta = 67°$ for different rotational speeds (RPM). (a) 1 RPM, (b) 2 RPM, (c) 4 RPM, (d) 6 RPM, (e) 8 RPM, (f) 10 RPM, (g) 12 RPM, and (h) 16 RPM, respectively. Black arrow indicates the initial direction of ion beam prior to rotation. Top right insets: 2D FFTs of corresponding AFM images. . . . 92

4.11 1×1 $\mu\mathrm{m}^2$ AFM micrographs of 500 eV Ar^+ irradiated Si at 67° for different rotational speeds (RPM). (a) 1 RPM, (b) 2 RPM, (c) 4 RPM, (d) 6 RPM, (e) 8 RPM, (f) 10 RPM, (g) 12 RPM, and (h) 16 RPM, respectively. Black arrow indicates the initial direction of ion beam prior to rotation. 93

4.12 Plots showing evolution of (a) 1D PSD, (b) rms roughness, and (c) wavelength for different rotational speeds of 1, 2, 4, 6, 8, 10, 12, 14, and 16 RPMs. 93

4.13 3×3 $\mu\mathrm{m}^2$ AFM micrographs of 500 eV Ar^+ irradiated Si at $\theta = 67°$ for fractional rotational speeds of (a) 0.3 RPM and (b) 0.6 RPM. Black arrow indicates the initial direction of ion beam prior to rotation. Top right insets: 2D FFTs of corresponding AFM images. Bottom left insets: Corresponding 1×1 $\mu\mathrm{m}^2$ AFM images. (c) 1D PSD plots for 0.3, 0.6 and 1 RPM obtained from AFM. 94

4.14 2D slope distributions of irradiated surfaces for different azimuthal angles. The horizontal axis is along ion beam direction and vertical axis is perpendicular to the ion beam direction. The red arrow indicates the initial direction of the ion beam prior to swinging. 95

4.15 Schematic demonstrating 2d slope distribution for symmetric and asymmetric nanopatterns. *Left panel*: Representative AFM images showing symmetric and asymmetric ripple patterns. *Middle panel*: Line profiles obtained from AFM images in parallel and perpendicular directions. Red arrows indicate the incident ion beam. Front and rear faces are marked with the signs of their respective slopes. *Right panel*: 2D slope distributions of the corresponding AFM images. 1D line profiles across the major axis of the distributions are also shown. 96

4.16 2D slope distributions of irradiated surfaces for $\triangle\phi = 70°$ rotating at different rotational speeds. The horizontal axis is along the ion beam direction. The red arrow indicates the initial direction of the ion beam prior to swinging. 97

4.17 1D line profiles obtained along the major axes of the 2D slope distributions for 500 eV Ar^+ irradiated Si surfaces for (a) different swinging angles from 0° to 360° and (b) different rotational speeds from 1 RPM to 16 RPM at $\triangle\phi = 70°$. The red arrow indicates the initial direction of the ion beam prior to swinging. 98

5.1 Schematic showing the swing geometry adapted during IBS. Here, θ (= 67°) is the polar angle between the 500 eV Ar^+ ion beam (blue arrow) and the surface normal. The sample azimuthally swings in a span of 20° about the z-axis. 108

5.2 3×3 μm^2 AFM images of static Si surfaces irradiated with 500 eV Ar^+ ions at $\theta = 67°$ for different values of sputtering time (or fluence) in mins (fluence in units of ions cm^{-2}) such as: (a) 0.5 (2.5×10^{18}), (b) 1 (5×10^{18}), (c) 2 (10×10^{18}), (d) 3 (1.5×10^{19}), (e) 4 (2×10^{19}), (f) 5 (2.5×10^{19}), (g) 7 (3.5×10^{19}), (h) 10 (5×10^{19}), (i) 15 (7.5×10^{19}), (j) 20 (10×10^{19}), (k) 25 (1.2×10^{20}), and (l) 30 (1.5×10^{20}), respectively. Black arrow indicates the ion beam direction. *Top right insets*: FFTs of corresponding AFM images. 110

5.3 1×1 μm^2 AFM images of static Si surfaces irradiated with 500 eV Ar$^+$ ions at $\theta = 67^\circ$ for different values of sputtering time (fluence) in mins (in ions cm^{-2}) such as: (a) 0.5 (2.5×10^{18}), (b) 1 (5×10^{18}), (c) 2 (10×10^{18}), (d) 3 (1.5×10^{19}), (e) 4 (2×10^{19}), (f) 5 (2.5×10^{19}), (g) 7 (3.5×10^{19}), (h) 10 (5×10^{19}), (i) 15 (7.5×10^{19}), (j) 20 (10×10^{19}), (k) 25 (1.2×10^{20}), and (l) 30 (1.5×10^{20}), respectively. Black arrow indicates the ion beam direction. *Top right insets*: FFTs of corresponding AFM images. 111

5.4 (a) 3×3 μm^2 AFM micrograph of pristine Si surface. Top right inset: 2D FFT (square root of the 2D PSD) corresponding to the AFM images. Bottom left inset: 2D slope distribution corresponding AFM image. (b) Power spectral density of the pristine Si surface. 112

5.5 3×3 μm^2 AFM images of swinging Si surfaces irradiated with 500 eV Ar$^+$ ions at $\theta = 67^\circ$, a total swinging angle of $\triangle\phi = 20^\circ$ and with a variation of sputtering time (or fluence) in mins (fluence in units of ions cm^{-2}) such as: (a) 0.5 (2.5×10^{18}), (b) 1 (5×10^{18}), (c) 2 (10×10^{18}), (d) 3 (1.5×10^{19}), (e) 4 (2×10^{19}), (f) 5 (2.5×10^{19}), (g) 7 (3.5×10^{19}), (h) 10 (5×10^{19}), (i) 15 (7.5×10^{19}), (j) 20 (10×10^{19}), (k) 25 (1.2×10^{20}), and (l) 30 (1.5×10^{20}) min, respectively. Black arrow indicates the initial ion beam direction prior to swing. *Top right insets*: FFTs of corresponding AFM images. 113

5.6 1×1 μm^2 AFM images of swinging Si surfaces irradiated with 500 eV Ar$^+$ ions at $\theta = 67^\circ$ for different values of sputtering time (fluence) in mins (in ions cm^{-2}) such as: (a) 0.5 (2.5×10^{18}), (b) 1 (5×10^{18}), (c) 2 (10×10^{18}), (d) 3 (1.5×10^{19}), (e) 4 (2×10^{19}), (f) 5 (2.5×10^{19}), (g) 7 (3.5×10^{19}), (h) 10 (5×10^{19}), (i) 15 (7.5×10^{19}), (j) 20 (10×10^{19}), (k) 25 (1.2×10^{20}), and (l) 30 (1.5×10^{20}), respectively. Black arrow indicates the ion beam direction. *Top right insets*: FFTs of corresponding AFM images. 114

5.7 Log-log plot of 1D PSD with spatial frequencies calculated from AFM images along ripple wave vector with increasing sputtering time at $\theta = 67°$ for (a) static and (b) azimuthally swinging ($\Delta\phi = 20°$) substrates. 115

5.8 Evolution of pattern disorder FWHM/PSD peak position for 500 eV Ar^+ irradiated Si surface for static substrate and azimuthally swinging substrate at $\Delta\phi = 0$, respectively. 116

5.9 Normalized 1D line profiles obtained along the major axes of the 2D FFTs for 500 eV Ar^+ irradiated Si surfaces for (a) static and (b) azimuthally swinging ($\Delta\phi = 20°$) substrates, respectively. 116

5.10 (a) 3×3 μm^2 AFM micrograph of Si surface. (b) 2D FFT of the AFM image. (c) Line profile obtained from the 2D FFT along the horizontal direction. Red arrows indicate that (b) is obtained from (a) and (c) is obtained from (b). 117

5.11 Evolution of pattern disorder $\delta\lambda/\lambda$ for 500 eV Ar^+ irradiated Si surfaces for static substrate and azimuthally swinging substrate at $\Delta\phi = 20°$, respectively. 118

5.12 Autocorrelation length obtained for Ar^+ irradiated Si surfaces at $\theta = 67°$ for different sputtering times, corresponding to static (closed square) and swinging (closed circle) substrates. 118

5.13 The plot depicts the PSD spectra of 3×3 μm^2 AFM images, along with both short and long wavelength components. 119

5.14 (a) Variation of wavelength with irradiation time for the static and swinging samples. (b) Variation of rms roughness σ, the short wavelength rms roughness σ_s, and the long wavelength rms roughness σ_l with irradiation time for the static sample. (c) The same calculated for the swinging sample. All irradiations were performed with 500 eV Ar^+ beam at an incidence angle of 67°. For the swinging samples, the total azimuthal angle was 20°. 120

5.15 Evolution of wavelength for 500 eV Ar^+ irradiated Si surface for (a) static, and (b) azimuthally swinging substrate. $1/z$ represents surface roughness exponent. 121

5.16 (a) 3×3 μm^2 AFM micrographs of 500 eV Ar^+ irradiated Si at 67° for 5 min : (b) 2D FFT of (a). The white circle includes(excludes) the long(short)-wavelength components of the pattern. (c) Topographic image for the short-wavelength component of (b) obtained using inverse FFT (z scale = 7 nm). and (d) Topographic image for the long wavelength component of (b) obtained using inverse FFT (z scale = 3.7 nm). 122

5.17 Fractal dimensional analyses of samples with increasing sputtering time at $\theta = 67°$ for (a) static and (b) azimuthally swinging ($\Delta\phi = 20°$) substrates. 123

5.18 Schematic (not to scale) demonstrating 2D slope distribution estimations. *Top left panel*: Representative AFM image showing ripple patterns. *Top right panel*: Shaded line profiles obtained from AFM images in parallel and perpendicular directions. Blue arrows indicate the incident ion beam directions. Front and rear faces are marked with the signs of their respective slopes. *Bottom left panel*: 2D slope distribution obtained from the 3×3 μm^2 AFM image. *Bottom right panel*: 1D line profile across the major axis of the 2D distribution. Red arrows indicate the image/plot from which the subsequent image/plot has been derived. 124

5.19 2D slope distributions of 1×1 μm^2 AFM images of Ar^+ irradiated static Si surfaces at $\theta = 67°$ have showed for different sputtering times. The horizontal (vertical) axis is parallel (perpendicular) to the ion beam projection. The red arrow indicates the initial direction of the ion beam. 125

5.20 2D slope distributions of 1×1 μm^2 AFM images of Ar$^+$ irradiated azimuthally swinging Si surfaces at $\theta = 67°$ and $\triangle\phi = 20°$ have showed for different sputtering time. The horizontal (vertical) axis is parallel (perpendicular) to the ion beam projection. The red arrow indicates the initial direction of the ion beam. 126

5.21 1D line profiles obtained along the major axes of the 2D slope distributions for 500 eV Ar$^+$ irradiated Si surfaces for *Left panel*: (a) static substrate and *Right panel*: (b) azimuthally swinging substrate at $\Delta\phi = 20°$, respectively. The red arrow indicates the initial direction of the ion beam and slope angle $(\alpha) = \tan^{-1}(\partial h/\partial x)$. 127

5.22 The plot illustrates the 2D slope corresponding to 3×3 μm^2 AFM images, along with the short and long wavelength components. 128

5.23 Height profiles along the incidence ion beam direction of Ar$^+$ irradiated Si surfaces at $\theta = 67°$ shown for different sputtering times for (a) static and (b) azimuthally swinging substrates. 129

5.24 Height profiles along the incidence ion beam direction of Ar$^+$ irradiated Si surfaces at $\theta = 67°$ shown for different sputtering times for (a) static and (b) azimuthally swinging substrates. 130

5.25 Schematic (not to scale) showing global ion beam incidence angle θ and local incidence angle ψ. α denotes the local slope positioned between the local and global normal to the surface. The ripple line profile is a real profile measured from an AFM image. 131

6.1 Schematic view of the swing geometry in azimuth (ϕ) during IBI. θ ($= 67°$) is the polar angle between the 500 eV Ar$^+$ beam (blue arrow) and the (stationary) surface normal. The sample azimuthally swings for an angle $\triangle\phi$ ($0 \rightarrow +\phi$) across the incidence ion beam direction. 138

6.2 3×3 μm^2 AFM micrographs of 500 eV Ar$^+$ irradiated Si at 67° with fluence of 7.5×10^{19} ions$\times$cm^{-2}, and for different value of $\triangle\phi$ such as (a) stationary, (b) 15°, (c) 30°, (d) 45°, (e) 60°, (f) 75°, (g) 90°, (h) 105°, (i) 105°, (j) 135°, (k) 135°, (l) 165°, and (m) 180°, respectively. Black arrow indicates the initial direction of the ion beam prior to rotation. Top right insets: 2D FFTs of corresponding AFM images. Bottom left insets: corresponding 1×1 μm^2 AFM images. 139

6.3 3×3 μm^2 AFM micrographs of 500 eV Ar$^+$ irradiated Si at 67° with fluence of 7.5×10^{19} ions$\times$ cm^{-2}, and for different value of $\triangle\phi$ such as (a) stationary, (b) 15°, (c) 30°, (d) 45°, (e) 60°, (f) 75°, (g) 90°, (h) 105°, (i) 120°, (j) 135°, (k) 150°, (l) 165°, and (m) 180°, respectively. Black arrow indicates the initial direction of the ion beam prior to rotation. Top right insets: 2D FFTs of corresponding AFM images. Bottom left insets: corresponding 1×1 μm^2 AFM images. 142

6.4 The variation in rms roughness and ripple wavelength with an azimuthal swinging angle for a fixed $\theta = 67°$ and fluence 7.5×10^{19} ions/cm^2. Top Panels (a-b) Open circle and (c) PSD for SAS substrates. Bottom panels (a-b) Closed square and (d) PSD for AAS substrates. 145

6.5 Autocorrelation length obtained from autocorrelation function for SAS (open circle) and AAS (closed square) substrates at fluence 7.5×10^{19} ions/cm^2 with the variation of azimuthal swinging angle at $\theta = 67°$. 147

List of Tables

3.1 Sputtering and relaxation time durations of samples subjected to intermittent 500 eV Ar^+ ion bombardment. C_{20} sample is irradiated continuously for 20 min; in this case, total sputtering time (t_C) is equivalent to continuous sputtering time. (*) S_7 sample is irradiated intermittently for a total time of 20 min (the last sputtering period is 6 min long). 50

Chapter 1

Introduction

1.1 Ion-Solid Interaction

Ion bombardment of solid surfaces serves various purposes across multiple fields, including surface cleaning, surface modification, surface etching, ion implantation, sputter deposition and various types of surface analysis techniques. During such a procedure, atoms are dislodged and removed from the surface, a process known as sputtering. During ion-solid interactions, ions can penetrate the surface, displace atoms, create defects, induce chemical reactions thereby altering the surface morphology and properties of the material. Studies on ion-solid interactions in its various forms are therefore important for applications in materials science, nanotechnology, surface engineering, and other fields where controlling the behavior of ions at solid surfaces is crucial.

1.1.1 Fundamental Aspects of Ion-Solid Interaction

The physics behind any ion-solid interaction process concerns the potential energy of a two-particle system varying with the distance separating the two centers determining both the equilibrium properties of an assembly of atoms and the way the energetic particles interact with a lattice of stationary atoms. The scattering probability of an ion–atom collision is directly related to the interaction potential between atoms. The interatomic potential between the atoms is influenced by distances shorter than the equilibrium distance. During collisions, the interaction distance varies according to the collision energy. This leads to a degree of closed-shell interpenetration and overlap, causing significant alteration of the particle wave function at the moment of impact. Therefore, a knowledge of the interatomic potential at small separations is important for understanding processes involving ion–solid interactions and radiation damage in solids. In this context, low energy (from 100 eV to 1.2 keV) ion-induced surface modification is primarily focussed in the present thesis. The considering energy range lies in the intermediate distance, when $a_0 < r < r_0$, where a_0, r, and r_0 are the Bohr radius, separation between the colliding atoms, and the separation between neighboring atoms in the crystal, respectively. In this regime, the potential energy leads to repulsion between two atoms, as the nuclear charge is screened by the electrons, which reduces the Coulomb potential [1]. Thus, the interatomic potential between two atoms of atomic numbers Z_1 and Z_2 is given by $V(r) = \frac{Z_1.Z_2}{r}\chi(r)$, where $\chi(r)$ is the screening function and is defined as the ratio of the actual atomic potential at radius r to the Coulomb potential. For large values of r, $\chi(r)$ tends to 0, while for a small values of r, it tends to 1.

In the event of such an energetic collision at or near the surface, collisions within atoms occur inside the solid. The incident particles lose their energy at a rate $\frac{dE}{dx}$ by transferring their energy through momentum exchange in the solid, which depend on factors such as the energy and mass of the incident particle, as well as the atomic number of both the ion and the substrate atom. The incident ion penetrates the solid by gradually losing its energy and finally stops after undergoing random collisions within the target atoms. Along this path, the ion triggers creation of primary recoil atoms within the solid. These recoil atoms, in a cascade effect, induce further recoils, forming what is known as a collision cascade. The energy loss primarily occurs through two mechanisms – (1) nuclear collision, where the moving ion transfers translational motion to another atom, and (2) electronic collision, where the moving particle excites or ejects atomic electrons [1, 2]. Thus, the total rate of energy loss can be formulated as:

$$\frac{dE}{dx} = \left(\frac{dE}{dx}\right)_n + \left(\frac{dE}{dx}\right)_e, \tag{1.1}$$

where the subscripts n and e denote nuclear and electronic collisions, respectively. In the present thesis, the main mechanism for energy loss is primarily nuclear, which can be estimated using SRIM [3]. The actual integrated distance travelled by the ion is defined the range R and the distance up to which the ion penetrates from the surface is called the projected range R_p of the ion. Thus, primary ions with incident energy, angle, and target material, do not come to rest at the same place. The range distribution thus follows a Gaussian profile which can also be estimated from SRIM [3]. Winterbon, Sigmund, and Sanders (WSS) in 1970 computed the distribution utilizing Lindhard's power law approximation to the Thomas-Fermi potential [1] where the energy decrement was given by

$$dE = NS_n(E(x))dx = F_D(x)dx, \tag{1.2}$$

where $S_n(E(x))$ is the energy-dependent nuclear stopping cross-section and $F_D(x)$ is the energy distribution function with depth. Sigmund derived the expression of $F_D(x)$ considering the linear collision cascade theory [4] and had shown that the average deposited energy at a point $r(x, y, z)$ in the target surface by an ion moving along the z-axis is

$$F_D(r) = \frac{E_0}{(2\pi)^{3/2}\alpha\beta^2} \exp\left(-\frac{(Z - h_0 - a)^2}{2\alpha^2} - \frac{(x + y)^2}{2\beta^2}\right). \tag{1.3}$$

Here, E_0 represents the total deposited energy, a is the average penetration depth of the ion, α and β are the lateral and longitudinal stragglings, respectively. These parameters depend on the incident ion energy, ion mass, and the mass of the target atom. Continued bombardment leads to the conversion of the crystalline surface to an amorphous state. The extent of the amorphous layer can be increased by increasing ion flux, ion energy, etc.

1.2 Surface Patterning using Ion Beams

In 1974, Taniguchi proposed using ion-beam irradiation (IBI) to create patterns on different materials surfaces, which was considered a fantastic method for producing small structures [5]. Based on Sigmund's theory, various continuum models have been developed to explain formation of ion-induced surface nanopatterns. The theory provides a framework for understanding how incident ions transfer energy to target atoms and cause ejection of atoms from a solid surface due to ion bombardment, commonly called sputtering or erosion of the surface. Ion beam processing induces the formation of self-organized regular periodic nanostructures in in the form of nanodots and nanoripples on material surfaces. These nanostructures, with characteristic length scales ranging from a few to hundreds of nanometers, demonstrate potential for technological applications due to their electronic, magnetic, and optical properties. In fact, this procedure can be carried out on various materials like amorphous or crystalline in just a few minutes and across areas of several square centimeters [6, 7]. Removal and reorganization of the atoms from the surface are deciding factors for the formation of these nanostructures. The diversity of nanostructures can be influenced by different physical parameters such as ion energy, ion flux, fluence, incidence ion beam angle, and substrate temperature, etc. Additional parameters such as substrate rotation, azimuthal swinging, and substrate rocking (ion incidence geometry) can give rise to diverse formations of nanostructures. In this way, it can yield functional surfaces and confined structures. The influence of these parameters adds complexity to the process, giving it non-equilibrium behaviour and ultimately playing a role in the development of well-organized nanopatterns. Therefore, the understanding of ion beam nanopatterning has become more challenging within this broad parameter space. In-depth examination of self-organization through ion beam erosion has been underway since its inception. The first periodic nanostructures induced by ion bombardment were observed by Navez et al. in 1962. Understanding the mechanisms behind this structuring is important for control. The first theoretical model to understand these pattern formations was proposed by Bradley and Harper (BH) in 1988. Through extensive theoretical and experimental research, a certain understanding of the involved processes and the regulation of topography has been achieved. Subsequent experimental observations were not fully explained by the BH model, leading to the development of advanced continuum models.

In general, numerous techniques and methods are carried out for the fabrication of nanostructured surfaces [8]. These methods for fabrication of nanostructured materials can be divided into two parts, which include the "top-down" approach [9] and the "bottom-up" approach [8], as shown in Fig. 1.1.

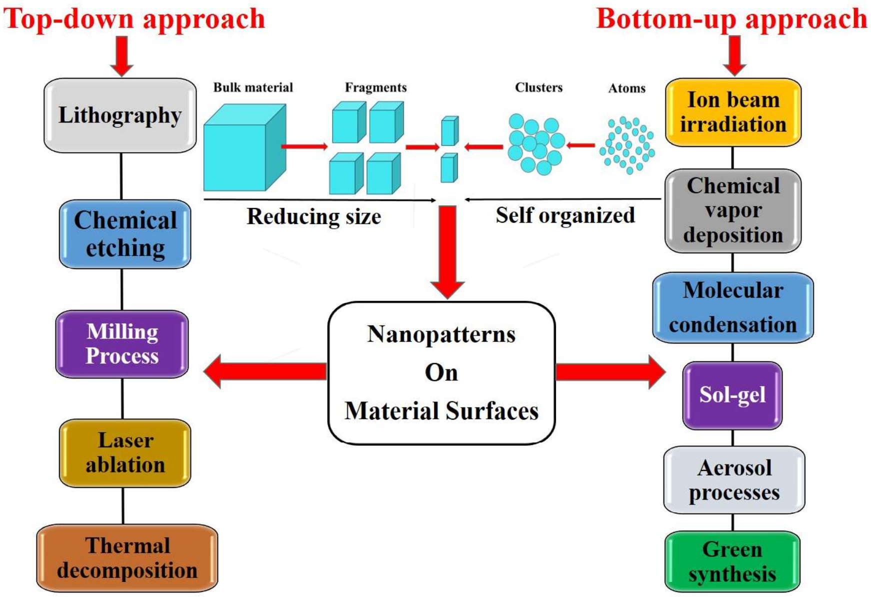
Top-down approach
Bottom-up approach
Lithography
Chemical etching
Milling Process
Laser ablation
Thermal decomposition
Bulk material
Fragments
Clusters
Atoms
Reducing size
Self organized
Nanopatterns On Material Surfaces
Ion beam irradiation
Chemical vapor deposition
Molecular condensation
Sol-gel
Aerosol processes
Green synthesis

Figure 1.1: Schematic representation of fabrication techniques.

In the top-down approach, a larger unit is scaled down to form a finished structure, whereas in the bottom-up approach, a structure is constructed by assembling small units [8], as illustrated in Fig. 1.1. Both top-down and bottom-up approaches have their advantages and limitations depending on specific requirements. Top-down methods face challenges such as the proximity effect, scattering effects, and costly fabrication. Conversely, the bottom-up approach offers advantage over top-down methods due to its capability for large-area patterning and lower cost of formation. Within the domain of bottom-up structuring approach, ion beam irradiation (IBI) method, was utilized for nanopatterning. In this methodology, the interaction of low-energy ion beam leads to self-organized fabrication of nanostructures (nanoripples, nanodots, nanocones, and nanoholes etc.) with high spatial resolution and accuracy on the surface of solid materials by precise control and manipulation of the surface morphology. This interaction induces defects at the surface, eliminates atoms from the outermost layers and forms significant topographical changes, potentially also altering the composition in certain cases. It is a cost-effective, single-step, fast process that can nanopattern areas even up to a few square centimeters with high resolution. Beyond the mentioned benefits, ion bombardment offers significant advantages in material science and industrial applications, particularly in precise control over ion concentration and topographical modifications, not achievable through other methods. Utilizing reactive ions can also induce changes not only in surface topography but also in material chemistry and physical properties. Additionally, ion beam patterning can be applied to a wide range of materials, including metals, semiconductors, insulators, and polymers making it versatile for various applications in nanotechnology, surface engineering, and device fabrication. Moreover, it also offers the flexibility to tailor the properties of the fabricated nanostructures by adjusting parameters such as ion energy, dose, and incident angle, allowing for customization based on specific requirements. However, several unresolved issues remain, prompting the need for further investigation of this technique. Energetic ions, as they sputter and penetrate the surface during ion bombardment, bring about modifications not only to the surface but also to the material interface. Overall, the precise control, versatility, and tunability of ion beam patterning make it a valuable technique for creating functional nanostructured surfaces with tailored properties. However, it is essential to note that ion bombardment can introduce structural defects during irradiation, which may have varying implications depending on the context. While some defects are beneficial, others may require control or minimization. This thesis focuses on studying methods to regulate and reduce such defects and structures induced by ion bombardment.

1.3 Theoretical Understanding of Ion Beam Patterning

1.3.1 Bradley and Harper (BH) model

In order to explain the several experimental findings by the ion beam community following the seminal work of Navez at al., Bradley and Harper (BH) introduced the first model in 1988 that explained the periodic pattern formation on amorphous materials based on Sigmund theory [4,10]. This model is based on the pattern formation in IBI as a result of interplay between relaxation through thermally activated surface diffusion and morphological instability. Sigmund noted that this instability is associated with the dependence of the sputtering yield on surface curvature [4]. The BH model successfully explained the periodic pattern formation up to some extent and orientation of nanopatterns observed in experiments by several groups. The linear continuum equation describing the evolution of surface topography combines curvature-dependent sputtering with surface smoothening due to thermally activated surface diffusion and is given by

$$\frac{\partial h}{\partial t} = -v_o + v_o^{'}\partial_x h + \nu_x \partial_x^2 h - \nu_y \partial_y^2 h - K\nabla^4 h. \tag{1.4}$$

Here, h is the surface height as a function of x, y and time (t), the first term v_o represents the erosion velocity or irradiation rate of flat surface at normal incidence, while the second term $v_o^{'}$ indicates the in-plane motion of the surface structure [10]. These two terms do not influence pattern. The terms, $\nu_{x,y}$, referred to as the curvature-dependent coefficients or surface tension parameters, primarily control the surface pattern and depend on beam parameters such as incident ion beam energy E, incidence ion beam angle θ, flux, etc. The last term, $K > 0$, is associated with thermally activated surface diffusion. The above surface height evolution equation is valid only when the radii of curvature are much larger than the ion range (a). A pattern will be formed in the direction parallel (x) and perpendicular (y) to the ion beam projection if $\nu_x < \nu_y < 0$ and $\nu_y < \nu_x < 0$, respectively. It is observed that ν_x can have either a negative or positive value depending on the incidence angle, while ν_y is always negative. At normal incidence, $\nu_x = \nu_y$, indicating no preferential orientation. At off-normal incidences and up to the critical angle (θ_c), $\nu_x \leq \nu_y$, resulting in ripples along the parallel (x-axis) to the ion beam projection on the surface. For larger incidence angles, where $\nu_x \geq \nu_y$, the ripples align along the y-axis (perpendicular) to the ion beam direction. To explain the periodic pattern, one needs to understand the surface height evolution (Eq. 1.4) which can be analyzed using Fourier transform. If $h(k_x, k_y, t)$ represent the Fourier transform of surface height $h(x, y, t)$, one can write Eq. 1.4 as

$$\frac{\partial h(k_x, k_y, t)}{\partial t} = [-\nu_x k_x^2 - \nu_y k_y^2 - K(k_x^4 + k_y^4)] h(k_x, k_y, t), \tag{1.5}$$

thus obtaining a solution given by

$$h(k_x, k_y, t) = h(k_x, k_y, 0) \exp[R(k)t]. \tag{1.6}$$

Here $h(x, y, 0)$ denote the initial amplitude of the Fourier component and $R(k) = R(k_x, k_y)$ represents the growth rate controlling the evolution of the pattern in a particular direction given by

$$R(k_x, k_y) = -\left(\nu_x k_x^2 + \nu_y k_y^2 + K(k_x^4 + k_y^4)\right). \tag{1.7}$$

Thus, when $R > 0$, the Fourier amplitude will grow exponentially. Moreover, the value of thermally activated diffusion term K is always positive. Thus, the amplitude growth depends on the curvature coefficients ν_x and ν_y. If both values are negative, then R must be positive. Additionally, R will also be positive if one of the coefficients is more negative than the other. The height will grow periodically in a direction for which the corresponding value is more negative. The value of R will be maximum at $k^* = (\max|\nu_{x,y}|/2K)^2$. Therefore, the wavelength of the periodic pattern will be given by

$$\lambda = 2\pi\sqrt{\frac{K}{max|\nu_{x,y}|}}. \tag{1.8}$$

The alignment of ripple wavelength is determined by the larger absolute value of ν_x and ν_y. Linear BH theory successfully explains several experimental observations, such as ripple pattern formation at oblique incidence, the rotation of ripple pattern at grazing angles and the exponential growth of ripple amplitude at an early time. However, it failed to explain numerous other observations such as ripple amplitude and ripple coarsening at long irradiation times, linear increase of ripple wavelength with ion energy, non-zero critical angle for ripple pattern formation, etc. These shortcomings were overcome after several theoretical attempts by adding non-linear terms in the BH equation (discussed in subsection 1.3.2).

1.3.2 Nonlinear Extension of BH Model

As discussed in subsection 1.3.1, attempts were made by theoretical groups to explain the experimental findings which could not be understood using BH theory. These included pattern formation for long irradiation times, sputtering at low temperatures where thermally activated diffusion does not appear to be the primary relaxation mechanism, etc. Cuerno et al., modified the BH equation by incorporating nonlinear terms, thereby arriving at what is known as anisotropic Kuramoto-Sivashinsky (KS) equation given by [11,12]

$$\partial_t h = -v_o + v_o^{'}\partial_x h + \nu_x \partial_x^2 h + \nu_y \partial_y^2 h + \frac{\lambda_x}{2}(\partial_x h)^2 + \frac{\lambda_y}{2}(\partial_y h)^2 - K\nabla^4 h + \eta. \tag{1.9}$$

Here, all the terms except fifth and sixth on the right-hand side of Eq. 1.9 are same as BH Eq. 1.4. The fifth variable λ_x, and sixth variable λ_y, signify the nonlinear effects resulting from lateral growth. These two terms λ_x and λ_y arrest the growth of the ripple amplitude [13]. The seventh term represents ion-induced effective surface diffusion (ESD) as relaxation mechanism. ESD is similar to surface diffusion does not imply mass transport along the surface. The last term is Gaussian white noise. $\lambda_{x,y}$ are the nonconserved Kardar-Parisi-Zhang (KPZ) nonlinearities [14,15]. Park et al. [16] showed that during the initial period, ripple formation aligns with linear theory, but beyond a characteristic time $t_c \left(\propto \frac{k}{(\nu_{x,y})^2} ln\left(\frac{\nu_{x,y}}{\lambda_{x,y}}\right)\right)$, nonlinear effects govern the evolution of morphology. This is when the surface roughness goes towards saturation. After the crossover time (t_c), depending on the sign of the product of non-linear terms λ_x and λ_y, two different scaling regimes are predicted, one algebraic and the other logarithmic. $\lambda_x\lambda_y > 0$ indicates an algebraic scaling behaviour similar to the KPZ equation [15] while $\lambda_x\lambda_y < 0$ might correspond to isotropic logarithmic scaling [12,17]. $\lambda_x\lambda_y < 0$ also predicts ripple rotation by an angle $\theta_c = tan^{-1}\left(\frac{\lambda_{x,y}}{\lambda_{y,x}}\right)$ [16]. Such a rotation was only observed for high temperature and at very high fluence (10^{19}) [18]. So far, logarithmic scaling behavior has not been observed experimentally. Nevertheless, it is expected that as the angle of ion incidence increases, a shift from KPZ scaling to logarithmic scaling will occur [11].

1.3.3 Damped Kuramoto-Sivashinsky Equation

The KS equation failed to explain some experimental phenomena such as the stabilization of ripples or dot formation after long time bombardment, as well as the emergence of hexagonal ordering of dot structure. Facsko et al. [19] turned to the isotropic damped

Kuramoto-Sivashinsky (dKS) equation to explain these under normal ion incidence or off-normal incidence with simultaneous sample rotation on III-V semiconductors and Si surfaces. Paniconi and Elder were the first to apply this equation to explain stationary pattern formation [20]. The dKS equation is same as the KS Eq. 1.9 with an additional damping term introduced by Chate et al. [21]. The presence of this additional damping term decreases the exponential surface height, essentially acting as a smoothing term thereby decreasing the kinetic roughening effects.

1.3.4 General Continuum Equation

The most general form of the BH equation can be obtained by adding higher order linear and nonlinear terms in Eq. 1.4 and can be expresses as [17]

$$\partial_t h = -v_o + v_o^{'}\partial_x h + \sum_{i=x,y}\left\{\nu_i\partial_i^2 h + \Omega_i\partial_i^2\partial_x h + \frac{\lambda_i}{2}\left(\partial_i h\right)^2 + \xi_i(\partial_x h\partial_i^2 h)\right\} - \sum_{i,j=x,y} D_{i,j}\partial_i^2\partial_j^2 h - K\nabla^4 h + \eta. \tag{1.10}$$

All the coefficients mentioned above are explained in detail in ref. [11], while the explanations for Ω and ξ are given in [17]. The terms with coefficients $D_{i,j}$ is diffusion like terms proportional to the fourth derivative of the surface height and thus leads to an additional anisotropic surface diffusion. Usually, this relaxation mechanism is known as ion-induced surface diffusion (ISD) [22]. ISD does not depend on the temperature, this smoothing mechanism is able to explain the temperature independence of the wavelength at low temperature where thermal diffusion can be neglected. In this case, the ripple wavelength is given by

$$\lambda = 2\pi\sqrt{\frac{2D_{xx/yy}}{max|\nu_{x,y}|}}. \tag{1.11}$$

The general continuum equation consists of linear and non-linear terms, the effect of these on surface morphology is difficult to predict. The complete understanding of the non-linear behavior described by Eqn. 1.11 is, thus still under investigation. Moreover, researchers working in this domain have developed other theoretical models which are discussed in detail in the literature [15, 16, 22–26].

1.4 Applications of Ion Beam Irradiation

Material surface properties are inherently related to the structure and morphology of the overlayers. Nanostructured surfaces, with characteristic length scales ranging from a few to hundreds of nanometers, exhibit potential interest for technological applications, primarily due to their electronic, magnetic, and optical properties. There are various kinds of applications of ion-induced nanoscale patterns in the field of plasmonics [27–29], electronics devices [30,31], magnetic storage devices [32–34], optical devices [35–37], functional/template surfaces [38–40] and more. **Plasmonics**: In recent times, there has been a focus on utilizing nanorippled surfaces for the fabrication of self-aligned noble metal nanoparticles or nanowires exhibiting anisotropic plasmonic properties [27–29]. These properties can be finely adjusted by altering the ripple wavelength using different physical parameters such as substrate temperature, angle of incidence, the orientation of metal atoms in relation to the ripples, as well as the deposition rate and duration. Oates et al. have reported that an array of aligned metal nanoparticles and nanorods with anisotropic plasmonic properties can be fabricated by metal deposition on self-organized rippled templates [27, 41]. Ranjan et al. have reported a similar local surface plasmonic response of self-organized Ag nanoparticles on nanorippled Si surfaces with varying ripple periodicity [42]. Strong plasmonic coupling has also been reported on nanorippled alumina surfaces by Camelio et al., where they had grown Ag over the surface [43]. **Magnetic**: The magnetic properties of ultrathin films are inherently influenced by their structural and morphological features. Depending on the specific application, such as in permanent magnets, information storage media, or magnetic cores for transformers and recording heads, materials with high, medium, or low magnetic anisotropy are essential for their respective purposes. The contribution of magnetic anisotropy from the surface, which is associated with the under-coordination of atoms at the interface, becomes increasingly significant in low-dimensional magnetic systems [34, 44]. Structuring magnetic materials on the nanometre scale leads to magnetic nanodots which used for a wide variety of technological applications. Many of these applications require the nanodots to be in the single domain state, to have well-controlled aniosotropy and low hysteresis. It is obtained by controlling the size and shape which makes them suitable for such a diverse range of applications from ultra-sensitive zero hysteresis magnetic sensors through to magnetic memory and logic devices [45]. Rippled silicon substrates have also been utilized to induce uniaxial anisotropy in a deposited thin permalloy film. These nanopatterns have also been used to control the interlayer exchange coupling in Fe/Cr/Fe trilayers [33] and exchange biased multilayers [46]. **Functional template**: The morphology of an anisotropic nanoripple surface can significantly affect the growth of the deposited thin films. Nanostructured surfaces are used as templates for material deposition [47–52]. Films can be grown on a nanopatterned template that perfectly resemble the morphology of the substrate. By tuning the periodicity of the template pattern, it is possible to tailor the step edge and the dipolar contributions to the uniaxial anisotropy of a magnetic thin film [32, 33, 53]. It has been shown that the conformal growth of magnetic thin films on rippled surfaces may result in substantial modifications of in-plane uniaxial anisotropy [54, 55]. **Wetting**: The wetting behavior of material surfaces depends highly on the surface structure of the materials. It is generally measured in terms of hydrophobicity i.e., water contact angle. The tailoring of hydrophobicity is controlled by surface texturing. However, the energetic ion bombardment has used for tuning hydrophobicity of a surface due to its precise control on surface texturing and chemical alteration [38–40, 56]. **Electronics**: Manipulating the nanoscale surface morphology of a metal electrode through self-organized ion beam sputtering allows precise adjustment of electrical resistivity anisotropy. Particularly, electrons traveling orthogonally to the nanoripples are affected by a strong increase in resistivity, while when electrons travel parallel to the undulations of the rippled film, the resistivity is almost unaffected and even shows a slight reduction [57]. **Optical applications**: Toma et al. reported a tunable optical anisotropy in the visible range on silver nanowire arrays grown on IBI nanopatterned amorphous glass surfaces [58, 59]. Gkogkou et. al. suggest that Ag metal deposition on rippled Si surface enhance the plasmonic response by utilizing the localized surface plasmon resonance of nanostructured metal surfaces [29, 60, 61]. **Photovoltaics/Solar cells**: In this field, Martella et al. have shown the light-trapping nature of silicon solar cells due to the ion beam irradiation-patterned surface with a high aspect ratio structure, thereby enhancing the solar cell efficiency [62]. Vivian et al. repoted that subwavelength scatterers can couple sunlight into guided modes in thin film Si and GaAs plasmonic solar cells whoseback interface is coated with a corrugated metal film [63]. A similar study by Mennucci et al. mentions that ion beam nanostructured gold thin film on borosilicate glass can also trap photons [64]. Nanocones by IBI can be used as broadband light-trapping surfaces as reported in [65]. **Biomaterials applications**: Recently, important aspects of ion beam irradiation have been identified and integrated into biomaterials applications, examining the effect of nanopatterned surfaces on the biomolecule adsorption and the response of adhering cells. [66–69]. The alignment of Schwann cells along nanorippled line has also been reported [66]. Neural stem cells have shown better adhesion on nanorippled glass surfaces [67].

1.5 Ion Beam Patterning: A brief experimental literature survey

In 1962, Navez et al., reported the first observation of relatively uniform structures (ripples) with a wavelength of less than 100 nm on silica surfaces through Ar^+ ion bombardment at oblique incidence. Since then, researchers have extensively investigated this phenomenon to understand the involved processes and gain control over the evolution of surface topography. Self-organizing nanostructures have been reported on a wide variety of materials, including semiconductors, metals, compound materials, insulators, and polymers, etc. [6,7,24,70–93]. The resulting morphologies are highly influenced by several experimental parameters, such as the incidence of ion beam angle, incidence ion beam energy, fluence, substrate temperature, ion type, simultaneous sample rotation, and co-deposition of metal impurity during the irradiation of substrate, etc.

Studies have demonstrated that the incidence ion beam angle plays an important role on the evolution of surface topography [94, 95]. In 1977, Carter et al. reported the formation of perpendicular mode ripples at $\theta = 45°$ and parallel columnar features at 75° on Si by bombardment with 45 keV Ar^+ [96]. The importance of this finding was the promise of an efficient approach for the fabrication of quantum dot arrays [94]. An important step forward from both experimental, and applied perspectives was the patterning of silicon surfaces with nanodots, first reported in 2001 by Gago et al. using 1.2 keV Ar^+ ions [95]. Ziberi et al. demonstrated the creation of perpendicular mode ripples at near-normal angles of incidence, consistent with BH theory [97–100]. These ripples, generated through erosion with noble gases at near-normal angles, have been observed solely on Si and Ge by Ziberi et al. [97], and on Ge by Carbone et al. [101]. They also observed the formation of nanodots at an incidence angle near 30° and smooth surfaces were obtained at incidence angles between $30° - 60°$ for an ion energy up to 2000 eV. Madi et al. reported the smoothening of the Si surface during ion bombardment with 1 keV Ar^+ at $\theta = 10°$ [102]. Zhang et al. observed no pattern formation on Si surface during the irradiation with Xe^+ at 75° with ion energy from 1000 eV to 50 keV [103]. Ziberi et al. observed the formation of holes without regular distribution on Si surface during irradiation with 500 eV Ar^+ at normal incidence [104]. Madi et al. reported the same observation with $E \leq 600$ eV [102]. However, while Ozaydin et al. [105] observed no pattern evolution with 1000 eV Ar^+ ion bombardment of Si, Gago et al. [106] reported the formation of nanodots under the same experimental conditions. Several reports describe the presence of ripples and columnar structures on Si surfaces obtained at incidence angles between 60° and 80° [106–110].

The surface topography is also influenced by incident ion beam energy along with the substrate temperature. It was demonstrated that at room temperature and using low energies, the amplitude and periodicity of ripples formed at near-normal incidence increased with the ion beam energy. Ziberi et al. showed that the periodicity of ripples could be adjusted from 35 to 65 nm by varying the ion beam energy from 500 eV to 2000 eV [97]. At room temperature, the lateral size of the nanodots formed using Kr^+ at 75° with simultaneous sample rotation was reported to vary from 25 to 50 nm with incidence ion energy from 300 to 2000 eV [75]. It was reported that the wavelength of the ripples formed at an angle between 60° and 65° also increased by 50 nm (2000 eV) and 1000 nm (100 keV) with variation of ion energy [111,112]. On the other hand, at high temperature, Brown and Erlebacher reported that ripple amplitude and wavelength on Si(111) at 60° with Ar^+ decreased with increasing ion beam energy from 250 eV to 1200 eV [113]. Hazra et al. reported that on Si(001) with an increase in ion energy (60-100 keV) at 60°, the ripple amplitude decreased while the wavelength increased [112].

It was reported that variations in fluence (irradiation time) influence the surface dynamics of self-organized structures. According to most experimental studies on Si surfaces, the amplitude of nanopatterns increases with fluence up to saturation [97, 99, 107, 114]. The amplitude saturation was also reported on different types of materials such as Ge, Cu and compound semiconductors. The saturation of amplitude is related to the nonlinear effect arising from the lateral growth of surface features, which becomes significant after a certain sputtering time. At room temperature, the wavelength of the features on Si surface is not affected by the fluence [6, 97]. At high temperatures, ranging from 873 K to 1023 K, nanopattern coarsening was observed at 75° between 250 eV to 1200 eV [107]. At normal incidence, the coarsening behaviour was also observed at temperatures higher than 673 K on Si(001) with 1000 eV Ar^+ [105]. In addition, Ziberi et al. observed that the size distribution of the dots formed at 75° with sample rotation becomes narrower with fluence [99].

The influence of target temperature on pattern formation by ion beam irradiation has been investigated, revealing a significant effect [6]. Erlebacher et al. reported on Si(001) with 750 eV at 65° that ripple wavelength increases with variation of substrate temperature from 733 K to 873 K [113]. Gago et al. observed the influence of substrate temperature on dot formation on Si(001) by irradiation with 1000 eV with Ar^+ at normal incidence. They observed that the nanopattern is not affected by the substrate temperature up to 425 K; dot height increased between 425 K and 525 K and finally above 550 K no patterns evolved. At low temperature, the Si surface is amorphized by ion bombardment and shows no pattern influence when substrate temperature is low while at high temperature it remains crystalline. The transition from amorphous to crystalline surface depend on the irradiation conditions for Si(001) with 1000 eV Ar^+ observed at 673 K and 773 K [105].

The evolution of the surface topography on surfaces is further affected by the choice of ion species. Ziberi et al. showed that pattern formation on Si with Ne^+ ions at ion energies 300 eV $\leq E_{ion} \leq$ 1000 eV influence surface structure formation. The surface remained smooth with ion energies 1000 eV $\leq E_{ion} \leq$ 2000 eV [115]. Carter et al. observed a similar dependence of surface topography on Si with Ne^+ and Ar^+ ion species for intermediate ion energies (above 20 keV) [116]. No surface structures are found on Ge surface by using Ne^+ and Ar^+ ions, while for Kr^+ and Xe^+ dot-like structures were observed on the surface with 1200 eV at 75°. Dot-like structures can also be observed when employing Ar^+ ions within the energy range of 300-2000 eV and incident angles between $0 - 20°$, but with no ordering and exhibit an amplitude below 1 nm [115]. It is known that the orientation of nanopatterns is determined by the direction of the ion beam. Under appropriate conditions, rotating the sample around the surface normal during ion bombardment eliminates the anisotropy caused by the ion beam direction. Rotating sample about its surface normal keeping the incidence angle fixed leads to additional effects not envisaged for fixed sample configurations. Zalar et al. demonstrated that adopting such a procedure enhances resolution, particularly in depth profile studies. [117]. Theoretical work by Bradley et al. indicated that the rate of surface roughening or smoothing during sample rotation, as well as the characteristic length scale of the resulting nanopatterns, depend upon the rotation period. [118]. Som et al. showed that the surface roughness decreases for large rotation speeds when Si is bombarded with Ar^+ ions [119]. This rotation during ion bombardment suppresses pattern formation, thereby enhancing the smoothing of surfaces [120]. At 75°, hexagonally ordered nanodots formed on Si during irradiation with simultaneous sample rotation [97–99]. Nanodots can also form without sample rotation at normal and near-normal incidence. However, those formed without simultaneous rotation exhibit a larger size distribution even after prolonged erosion times. In general, they have low amplitude and dots are not ordered in domains.

Investigation of self-organized nanopatterns on III/V compound semiconductors have been demonstrated as a fall-out of preferential sputtering due to the different sputtering yield of the components, which leads to the enrichment of the surface with one component. At normal incidence, Facsko et al. observed the formation of nanodots with 420 eV with Ar^+ hexagonal ordering on InP and GaAs [94]. The formation of nanodots organized in hexagonally ordered domain on InP and GaSb after Ar^+ irradiation but under oblique incidence with simulteneous sample rotation were reported by Frost et al. [121]. In 2009, Q. Wei et al. showed a hexagonal array of nanoholes produced by normal-incidence bombardment of Ge surface. T. Saito et al. showed that the nanorods of aluminum (Al) are embedded within a silicon thin film fabricated through magnetron sputtering in 2009 [122]. Ziberi et al. reported the formation of dots (0°) and ripples (5°) on Ge (001) with 2000 eV Xe^+ at room temperature [75, 99]. Nanodots were found to form along ripples at (10°) and at (30°) while the surface remained smooth with increasing ion incidence beam angle. Also, Carbone et al. reported simultaneous presence of ripples and nanodots on Ge (001) with 1000 eV Ar^+ at 10° [101].

Ion induced nanopatterns can also occur on insulators. Flamm et al. studied the irradiation with 800 eV Ar^+ on fused silica at different angles [81]. Similar results are observed on SiO_2 with 1000 eV Xe^+ by Mayer et al. [123]. Tomma et al. [83] studied the pattern formation on glass with 800 eV Ar^+ and observed parallel mode ripples at 35° and perpendicular ripples at 75°, respectively. The wavelength and amplitude of ripples on SiO_2 increased with fluence [83, 123]. Wavelength and amplitude was also observed to increase with increasing ion energy [81, 123] as well.

The impact of metal impurity under ion bombardment has been examined on several substrates [124]. Ozaydin et al. reported the formation of dots and ripple like structures using Mo impurity on Si during irradiation at normal incidence with 300 eV Ar^+ [105, 125–127]. Sanchez-Garcia at el. showed the formation nanoholes and nanodots through simultaneous incorporation of metal (Fe and Mo) impurity on Si surfaces [128, 129]. They observed that the topography could change from nanoholes to nanodots by increasing the ion current density or increasing the fluence at low ion current density. Hofsass and Zhang studied ion erosion with simultaneous co-sputtering, which they called surfactant sputtering [130]. Macko et al. observed both nanodots and ripples on Si with co-sputtering of a stainless steel target with 2000 eV Kr^+ at $\theta < 45°$ [131].

Ion induced pattern formation can also be affected by the sample crystallinity.In 2000, R. Reiche and W. Hauffe reported a forest of cones on copper surfaces [132]. The response of crystalline metals to ion bombardment differs from that of semiconductors and amorphous materials. This contrast arises from the higher diffusivity within metals and the non-directional nature of metallic bonds. Studies on metallic surfaces was developed substantially by Valbusa et al. [77]. Typically, a metal surface does not become amorphized by the impinging ions. Types of nanopatterns formed on metal surfaces and a complete description thereof can be found in ref [133–136].

Interestingly, one common factor between all the reported literature is that ion beam patterning was conducted traditionally at fixed angles of oblique or normal incidence, thereby creating nanopatterns of ripples and dots, respectively [6,124]. One major drawback of this method is the emergence of spatial defects in the patterns during bombardment, which limits its applicability. To mitigate these defects, researchers have explored alternative ion beam geometries. These geometries can be categorized into two groups: the conventional method, where the ion beam remains fixed as discussed earlier, and the unconventional method, where the ion beam is not fixed. Unconventional methods including multiple ion beam sputtering, sequential ion beam irradiation, rocking and azimuthally swinging substrates during ion bombardment. Moreover, researchers have noted the presence of salient structures with different symmetries using this geometry, which do not manifest when fixed ion beam geometries are employed. Kim et al. conducted experiments on gold (Au) using two Ar^+ ion beams placed perpendicular to each other at the azimuth. Their findings demonstrats that square-symmetric patterns of nanodots can be achieved in the erosive regime [137]. In another experiment conducted by the same group, based on sequential ion sputtering, it was demonstrated that nanobeads can be formed using this technique [138]. Studies by the same group also prove that patterning a prepatterned surface at azimuthally orthogonal directions leads to enhanced nonlinear effect (e.g., redeposition) as compared to an initially flat surface [139]. Keller and Frost conducted an experiment on silicon (Si) utilizing Ar^+ ions, which further demonstrated that defect densities can be reduced by up to 40% through a suitable selection of sequential ion beam sputtering [140]. In a recent study, Kim et al. investigated nanopattern formation on graphite substrates by azimuthally swinging the substrates during ion beam sputtering. Their findings revealed that swinging the substrate led to the formation of composite patterns, specifically wall-like structures, on graphite [141]. Thus, from the above discussion, it may be concluded that several research studies demonstrate that several research groups are turning to unconventional methods for ion patterning of surfaces. These approaches invoke new phenomena that cannot be achieved using a single fixed beam configuration.

1.6 Motivation and Objectives

From the previous section, it may be inferred that there are still numerous unresolved challenges associated with ion bombardment-induced self-organizing nanopatterns, primarily due to the emergence of disordered nanopatterns during irradiation with conventional methods. To address these challenges, researchers have employed unconventional strategies, including multiple ion beam sputtering [137], crossed ion beam sputtering [138], sequential sputtering [80,140,142], irradiation of the prepatterned surface [143], rocking the substrate [144], azimuthally rotating [145], and azimuthally swinging the substrate [141]. Cuenat et al. reported that the long-range order of the features on Si(001) using 1 KeV Ar^+ can be greatly enhanced by using the lateral-templating approach [143]. For the first time, the concept of dual-ion beam sputtering to induce interference patterns was proposed by Carter et al. [146,147]. Vogel et al. demonstrated the possibility of nanopatterning using multiple-ion beam sputtering [148]. Joe et al. showed the formation of highly ordered nanopatterns using dual-ion beam sputtering (DIBS) on Au(001). In addition, they have also examined the possibility of nanopatterns on Au(001) via squential ion beam sputtering (SIBS). Keller and Stefan Facsko have demonstrated that the quality of nanoscale ripple patterns on silicon surfaces can be substantially improved by applying sequential ion-beam sputtering (SIBS) and the defect density of the initial ripple pattern can be reduced by at least 40% [140]. Kim et al. [80] introduced a two-step process (sequential-ion beam sputtering) that combines a suitable pre-patterned target with subsequent irradiation at normal incidence. They were able to fabricate by IBS a novel nanobead pattern on Au(001). Although, Carter demonstrated theoretically that sample rocking inhibits ripple formation, Harrison et al. showed that ion bombardment can produce nearly defect-free ripples on the surface of an elemental solid if the sample is concurrently and periodically rocked about an axis orthogonal to the surface normal and the incident ion beam direction [149]. In their experimental work, Jeo et al. showed that applying low-energy Kr^+ irradiation to Si and amorphous carbon targets, along with rocking the substrates, tends to enhance the order of the ripple patterns. Notably, this improvement in order occurs even when the conditions prescribed in the anisotropic Kuramoto-Sivashinsky (aKS) model may not be fully met [144]. Kim et al. have shown that IBS of HOPG(0001) swinging substrates produces salient patterns and reveals novel pattern-formation mechanisms under 2 keV Ar^+, such as a quasi-2D mass flow and shadowing effects that have rarely worked simultaneously for pattern formation.

Considering the above works on unconventional ion beam patterning methods, the main objective in the present thesis is to understand how nanopatterns evolve under a few unexplored non-conventional configurations. Furthermore, the possibility of formation of patterns with increased order was explored using such techniques. Formation and evolution of surface patterns usually absent for the case of conventional methods was also studied. A detailed summary of the work done is given in the following section. This work includes to:

- Investigate pattern formation under intermittent sputtering sequences to study the effect of surface relaxation
- Investigate evolution of pattern formation on Si surfaces under azimuthal substrate swinging geometry at variable speeds
- Investigate ripple coarsening under azimuthal swinging geometry
- Investigate evolution of hierarchical surfaces under the above geometry

1.7 Thesis Overview

The thesis is arranged into the following six chapters in order to accomplish the above-mentioned objectives:

- ✓ **Chapter 2**: This chapter introduces the details of various structuring techniques, characterization tools, and theoretical simulations employed for the different experimental studies of the thesis. Section 2.1 and 2.2 contains information about sample cleaning and film structuring using low energy ion beam nanopatterning methods. Section 2.3 consists of information about AFM, and SEM utilized to characterize the surface morphology and optical information of the deposited samples.

- ✓ **Chapter 3**: In view of the above facts, in the first objective of the thesis, we aim to investigate the evolution and dynamics of ripple formation on paradigmatic Si surfaces [6] by introducing an unconventional method of intermittent sputtering, in which the surface is irradiated and left to relax intermittently within intervals of various time durations, thereby influencing the pattern formation process and ordering properties. The present method employed generalizes earlier works on sequential sputtering by performing repeated alternated irradiation and relaxation steps. While in those earlier works, the time interval between the two stages of sputtering is principally governed by the time required to change the incident beam angle, here we have carried out intermittent sputtering in varying degrees of relaxation times and sputtering durations. All the experiments were carried out at oblique incidence using an Ar^+ ion beam.

- ✓ **Chapter 4**: As the second objective of this thesis, we aim to explore the evolution of nanostructures and their unconventional characteristics on an azimuthally swinging Si surface for different azimuthal angles and rotation speeds. We first looked at a surface under static conditions and then compared it with a rotating surface at varying fluences. The outcomes of this experiment enhance our understanding of pattern formation for swinging geometries and pave the way for additional applications involving these alluring patterns by effectively utilising the ion beam parameter space.

- ✓ **Chapter 5**: Our third objective is to conduct an investigation of the evolution of nanostructures on an azimuthally swinging Si surface for a particular azimuthal swinging angle with increasing ion fluences. This geometry offers variable shadowing encountered by the sample, which alters continuously as the beam sweeps in the azimuthal direction.

- ✓ **Chapter 6**: As the fourth objective, we aim to explore the evolution of self-organized nanostructures and their unconventional characteristics of Si surface is produced by oblique incidence ion beam irradiation at different asymmetric azimuthal swinging angles (AAS).

- ✓ **Chapter 7**: This chapter summarizes the complete work elucidated in all the above-mentioned chapters. A future outlook is also presented in light of the present findings.

Chapter 2

Materials and Methods

This chapter provides an overview of the methods for structuring and the characterization tools utilized throughout the entire thesis. Section 2.1 focuses on the specifics of the initial step, namely, sample cleaning. Section 2.2 examines the structuring technique, including low-energy ion beam irradiation, employed for the fabrication of various semiconductor and PDMS nanostructures. The tools used for characterizing samples to determine their surface morphology and composition are described in Section 2.3.

2.1 Ultrasonication (Sample Cleaning)

The initial and most important step that needs to be completed before irradiating a sample is substrate cleaning. In our study, we have used silicon wafer (*purchased from Sigma Aldrich*) as a substrate. Substrates were cleaned in an ultrasonic bath before nanopattering. Ultrasonic cleaning is a technique that uses ultrasonic waves to agitate an aqueous solution, usually water, in order to remove naturally adhering contaminants from substrate surfaces such as dust, dirt, oil, fingerprints, and so forth.

2.1.1 Principle

Typically, an ultrasonicator consists of an ultrasound wave generator that creates alternating waves of compression (high pressure) and expansion (low pressure) in the liquid or solution at extremely high frequencies, generally between 25 and 130 kHz as a non-audible range (*"known as ultrasonic vibrations"*) as shown in Fig. 2.1. This high frequency ultrasonic wave triggers the rapid formation and rupture of small bubbles in the liquid, which is known as cavitation [150]. The rupture and implosion of the large number of bubbles result in a large amount of energy being created in the form of a wave. This high energetic wave passes through the liquid and helps in cleaning the substrate [151].

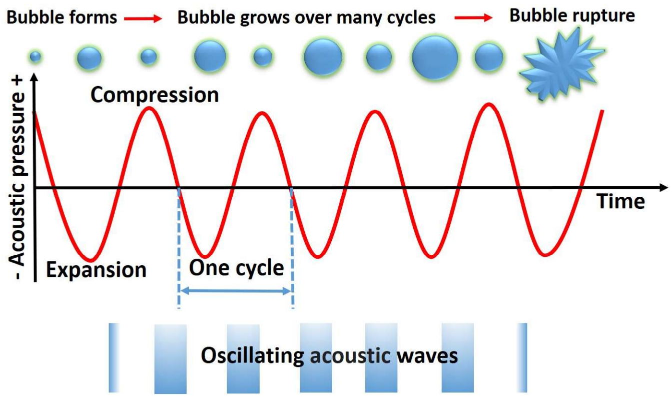

Figure 2.1: Schematic illustrating the cleaning mechanism during the sonication process.

2.1.2 Instrumentation

Our laboratory utilizes the commercially purchased *"QSonica"* ultrasonicator for the cleaning of all samples. This type of digital C-cleaner has a 1/2 gallon capacity. It has an operating frequency of 40 kHz and could heat up to a temperature of 70°C. It has four function indicators: the first shows the solution's current temperature (10–70°C, ±4°C); the second, the set tank temperature (01–69°C); the third, the ultrasonication time (01–99 minutes); and the fourth, the degassing time display (default, 5 minutes, with a range of 01 to 99 minutes). Degassing in this context refers to the process of eliminating dissolved gases, usually air from fresh solution. After degassing, the system is ready for ultrasonication. Finally, sonication can be performed with or without heating, depending on the requirements of the procedure.

2.2 Structuring Techniques

Several methods are available for producing nanostructures on diverse material surfaces. In our investigation, we applied a bottom-up approach to generate nanostructured arrays. Commonly employed bottom-up nanofabrication techniques encompass low-energy ion beam irradiation (IBI), chemical vapor deposition (CVD), sol-gel nanofabrication, laser pyrolysis synthesis, and green synthesis. Our study specifically incorporated a bottom-up strategy, low-energy **ion beam irradiation (IBI)** to prepare the samples.

Principle

When low-energy ions interact with a solid surface, they lose their kinetic energy through the transfer of momentum to atoms within the solid, and it penetrates a certain depth and then stops [152]. Through this procedure they induce different type of surface morphology which depends on incident ion beam parameters such as incident ion beam energy, target temperature, ion flux, ion fluence, and incident ion beam angle etc. The different types of ion beams parameters were extracted from Kaufman-type ion source, specifically the KDC 40 ion source in the Surface Modification and Application Laboratory (SMAL Lab) at Indian Institute of Technology (IIT) Ropar, Punjab, India. The whole experimental system was maintained at high vacuum (1.8×10^{-7} Torr). The Si(100) samples were bombarded by ion energies from 100 eV to 1.2 KeV. The power supply specifications for various functions of the ion source include the following: Cathode: 18 V, 20 mA, Discharge: 100 V, 2 mA; Beam: 1200 V, 200 mA; Accelerator: 600 V, 200 mA; Neutralizer: 30 V, 20 mA.

Instrumentation

Ion beam irradiation was carried out in a gridded ion source chamber fitted with a Kaufman-type ion source, specifically the KDC 40 ion source. The function of ion beam source chamber is to generate ions and accelerated these ions to high velocity, allowing their ejection downstream from the source. **Kaufman Ion Source:** The low-energy Ar^+ ion beam irradiation of all the samples was conducted using the Kaufman & Robinson Inc., KRI KDC 40 Ion Source facility available in our lab [153]. This ion source, which utilizes a direct-current (DC) discharge to generate ions, is a 3-gridded ion source. The fundamental components of the source are as follows:

- **Discharge Chamber** It is referred to as the main body of the ion source, where the operating gas is introduced into the chamber. Using the cathode, the source gas undergoes ionization within this chamber. Additionally, it includes a magnet designed to manipulate the trajectory of electrons through the generated magnetic field. The motion of electrons is carefully controlled, compelling them to undergo multiple collisions with the source gas before being collected on the anode. As a result, the ionization rate is heightened, leading to an increase in the number of generated ions.

- **Electron Source** The electron source is a heated filament commonly referred to as the *"cathode"*. In our system, cathodes made of tungsten wire with a thickness of 0.25 mm (0.010 in) and featuring three turns in the center were employed. These turns were wound around a 3 mm diameter rod. The primary function of the cathode is to generate ions of the source gas and form the plasma within the discharge chamber.

- **Grids** The performance of the source is significantly influenced by the 4-cm 3-grid focused molybdenum ion optics employed in the Kaufman ion source. This source is equipped with a 3-grid system. The role of grids is to accelerate the ions produced in discharge chamber. Grids are basically electrodes which are separated from each other by a distance of a few mm. A schematic of the grids used in source is as shown in Fig. 2.2. The grid nearest to the discharge chamber is known as *"screen" (S)* grid. The S grid is put with positive biased with respect to ground. Therefore, the formed plasma also gets positive biased. The next grid is called *"accelerating" (A)*, which is biased negative with respect to ground. Consequently, positive ions formed in the discharge chamber are accelerated due to this created electric field. The last *"decelerating grid" (D)* is employed to decelerate the beam after it passes through the A grid. The inclusion of the third grid is reason the profile shape does not change greatly as the accelerator voltage is increased at a given voltage.

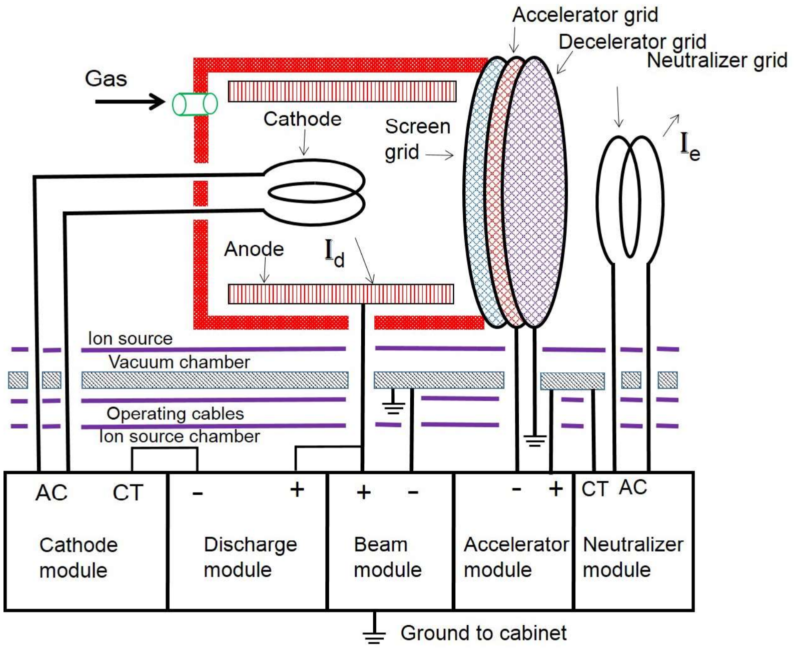
Accelerator grid
Decelerator grid
Neutralizer grid
Gas
Cathode
Screen grid
I_e
Anode
I_d
Ion source
Vacuum chamber
Operating cables
Ion source chamber
AC
CT
-
+
+
-
-
+
CT
AC
Cathode module
Discharge module
Beam module
Accelerator module
Neutralizer module
Ground to cabinet

Figure 2.2: A simple schematic representation of the Kaufman ion source.

- **Neutralizer** The neutralizer serves as an additional source of electrons in the form of a heated filament. In our configuration, it is constructed using tungsten wire with a thickness of 0.38 mm and features three turns in the center. These turns were wound around a 5 mm diameter rod. The primary goal of the neutralizer is to generate electrons and contribute to a net charge balance for the ions formed during the process, as they exit the source. Typically, the neutralizer emits more electrons than the source emits ions. Its role is crucial in minimizing surface charging and mitigating the divergence of the ion beam.

- **Vacuum pump** The ion source is equipped with a vacuum pump system, comprising both a rotary pump and a turbo molecular pump (TMP). The rotary pump is employed for maintaining the pressure in the range from atmospheric pressure down to 2×10^{-3} Torr. Further, the TMP pump is utilized to achieve lower pressures, reaching down to 1.5×10^{-7} Torr.

- **Mean free path** Mean free path is the average distance a particle travels between successive collisions with other particles. In a gas, the mean free path depends on factors such as pressure and temperature. It is larger than the separation between source and substrate in a high vacuum environment. It allows a simplified assumption that particles move relatively linearly from the source to the substrate without frequent collisions.

In summary, important parameters encompass the cathode filament current (which applies electrical current to heat the cathode filament for electron emission), discharge voltage (established between the filament cathode and anode, determining electron energy for ionizing collisions in the discharge chamber), discharge current (established between the filament cathode, controlling ion production), neutralizer filament current (applied to the neutralizer, heating the filament for electron emission), source gas flow, beam voltage (positive voltage applied to the discharge plasma), beam current (total ion current leaving the source), acceleration voltage (negative voltage applied to the accelerator grid), accelerator current (charge-exchange current collected by the accelerator grid), and neutralizer emission current (electron current emitted by the neutralizer). The sample holder

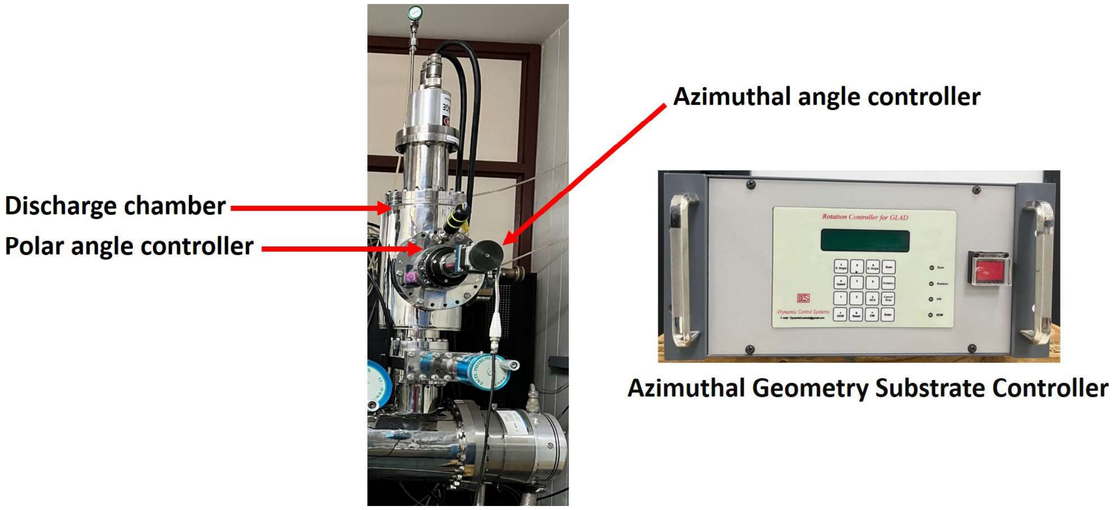
Azimuthal angle controller
Discharge chamber
Polar angle controller
Rotation Controller for GLAD
Azimuthal Geometry Substrate Controller

Figure 2.3: Kaufman ion source facility available in our lab.

is adjustable, allowing tilting within a range of 0° to 90° relative to the ion source axis. Additionally, it has the capability to rotate at a speed of 20 rotations per minute (RPM) around the axis of the ion source. The Kaufman ion source facility available in our lab as depicted in Fig. 2.3

Ion beam irradiation (IBI) of a solid surface is divided into two parts. The first is the conventional method, where the sample holder remains stationary during irradiation, as depicted in Fig. 2.4 (a). On the other hand, the unconventional method involves a sample holder that can continuously rotate, azimuthally swing about the surface normal, and rock (oscillation in polar direction) about the substrate normal, as illustrated in Fig. 2.4 (b).

2.3 Characterization tools

In this thesis, surface morphology analysis was conducted using Atomic Force Microscopy (AFM) after irradiation. Quantitative information of surface topography was determined by using imaging process tools such as Gwyddion [154], and ImageJ software [155]. The

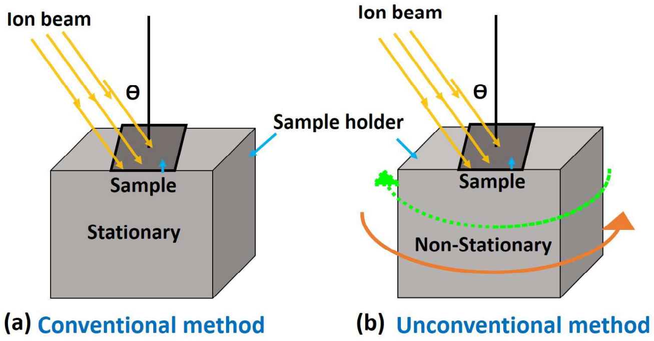
Ion beam
θ
Sample holder
Sample
Stationary
Ion beam
θ
Sample
Non-Stationary
(a) Conventional method
(b) Unconventional method

Figure 2.4: The schematic illustrates the sputtering geometry, with (a) representing the conventional setup where the sample remains stationary, and (b) depicting the unconventional setup where the sample can azimuthally rotate, swing, rock (polar angle oscillated), or be non-stationary.

nature of the composition was determined with the help of energy dispersive X-ray spectroscopy EDX [156].

2.3.1 Atomic Force Microscopy

The Atomic Force Microscopy (AFM) is a family of scanning probe microscopy (SPM) techniques, which came after the invention of scanning tunneling microscope (STM) in early 1980. In this technique, a sharp probe (tip) is used to scan over the sample surface and maps the height fluctuations from the surface. The tip is used as a cantilever, which is basically constructed from materials such as of silicon or silicon nitride having a radius of curvature nm. For the work carried out in this thesis, silicon tips with a 10 nm radius were used.

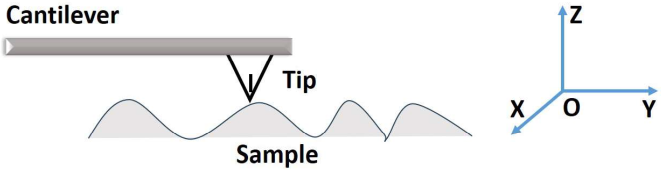
Cantilever
Tip
Sample
Z
X
O
Y

Figure 2.5: A simple schematic representation of the AFM sample tip geometry.

The tip height alters when it passes any bump or groove as illustrated in Fig 2.5, and the feedback reconstructs the surface as an image of the sample as shown in Fig 2.7. Hence, it gives three-dimensional information about the surface depending upon the force-distance measurement dynamics between the sample surface and AFM tip [157]. AFM offers several advantages, including high spatial resolution (down to atomic scales), the ability to work in various environments (air, liquid, or vacuum), and the potential to image nearly any kind of surface, including, conductors, semiconductors, biological samples, glass, ceramics, polymers, and composites.

Working Principle and Interatomic Forces

The principle behind **Atomic Force Microscopy** is based on the forces between the tip and sample. These forces are measured by bringing the tip close to the surface and measuring the resulting deflection following Hooke's law, which is expressed as $F = -kZ$. Where F is the force, k is the lever's stiffness, and Z is the cantilever deflection. The typical range of the force constant is from 0.01 to 1.0 N/m, which leads to the force in the range from nN to μN ~~μm~~. The force-distance curve shown in Fig. 2.6 explains the

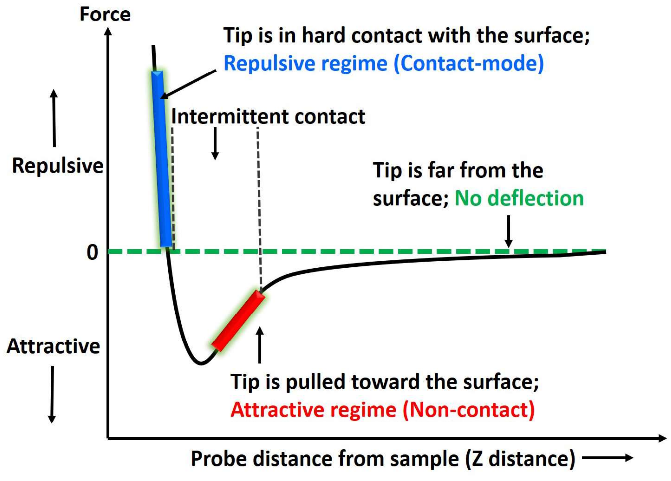

Figure 2.6: Schematic of force-distance curve.

several types of forces, which is based on the interaction with the cantilever and sample surface. As the tip scans over the surface, forces such as van der Waals force, mechanical contact forces, and repulsive forces between atoms influence the position of the tip as shown in Fig. 2.6. As the tip is kept at a distance from the sample surface, no interaction force works between them, when the tip and sample come closer but do not make contact, an attractive force (-1/z^6) generated by the van der Waals interaction develops as shown on the right side of the Fig. 2.6. At a particular distance, the tip makes contact with the sample when the repulsive force (1/z^{12}) is much larger then the attractive. Within this region, the repulsive force typically balances the cantilever in its position. This is known as electrostatic repulsion, and it causes the tip to move away from the sample. As a result, the cantilever oscillates in the regimes of attraction and repulsion forces. The force-detecting sharp tip at the forefront of the cantilever experiences oscillation. The Atomic Force Microscope (AFM) consists a cantilever, mirror, position sensitive photodetector (PSPD), piezoelectric scanner, and computer. The schematic diagram of the AFM setup is depicted in Fig. 2.7.

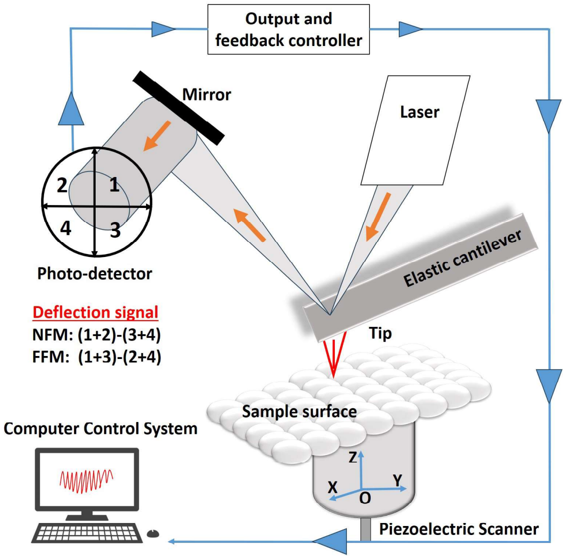
Output and feedback controller
Mirror
Laser
2
1
4
3
Photo-detector
Elastic cantilever
Deflection signal
NFM: (1+2)-(3+4)
FFM: (1+3)-(2+4)
Tip
Sample surface
Computer Control System
Z
X
Y
O
Piezoelectric Scanner

Figure 2.7: Schematic representation of the working of AFM.

A laser beam is incident on the shining surface of the cantilever, which is reflected from the surface and collected by a position sensitive photo detector (PSPD) and feedback loop as shown in Fig 2.7. The photodetector is utilized for measuring both normal forces (in normal force microscopy, NFM) and frictional forces (FFM) exerted on the moving tip. The combined response, derived from the oscillating beam on the PSPD and the scanning facilitated by the movement of the piezoelectric crystal, is then converted into an image. The combined response originating from the oscillating beam on the position sensitive photodetector (PSPD) is transmitted via controller to the piezoelectric crystal. Subsequently, the piezoelectric crystal converts the signal from electrical to mechanical to maintain constant the tip-sample distance, displaying both the surface topography and height profile on the computer screen. The piezoelectric crystal is attached beneath the sample surface which has a sub-A° movement in x, y, and z directions.

Based on the distance between the tip and sample, AFM operating modes are divided into three categories: contact mode, non-contact mode, and tapping mode as shown in Fig.2.8 [158]. **Contact operating mode** is the first and primary mode of operation. In this operating mode, the tip and sample make soft contact with each other while force

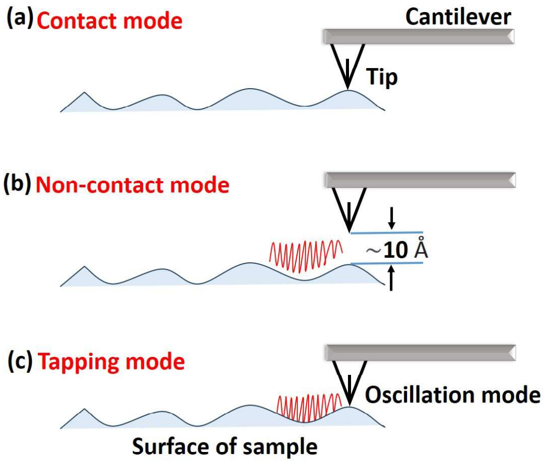

Figure 2.8: Different operating modes of AFM depending on distance between tip and sample.

remains within the repulsive range of van der Waals forces, typically occurring when the separation between the tip and surface is on the order of a few angstroms as shown in Fig.2.8 [158] (b). The cantilever shifts up or down relative to the surface topography corresponding to the presence of bumps or pits, respectively. In this mode, there are two methods of imaging: constant force or constant height. In **constant force mode**, the tip is continually adjusted to maintain a specified deflection so that the force between then remain constant during the scanning process. The amount of deflection of the cantilever is optimized by the response from the PSPD. It is this adjustment that is used to display an image [158]. When the tip scans in **constant height** mode, the sample must be relatively flat for the feedback loop to maintain control during scanning because otherwise the tip might crash. This is useful for small, high-speed atomic resolution scans. Due to the tip's hard contact with the surface, the lever's stiffness must be less than the effective spring constant holding atoms together, 1–10 nN/nm. Contact mode levers usually have spring constants below 1 N/m. This operational mode does not prevent contamination between the sample and tip. It is suitable for rough solid samples. The main disadvantage of this mode is that it may damage soft samples as the tip remains in very close proximity to the sample surface. Overcoming the problem mentioned above, the **non-contact mode** technique is used for scanning nanoscale surfaces without making direct physical contact with the material. The distance from the surface between the tip and sample is relatively larger compared to the contact mode in the attractive region of the force vs. distance curve as shown in Fig.2.8 (b). This is useful for fluid samples, soft materials and elastic samples as the tip does not touch the samples. The forces between the tip and sample are quite low, on the order of pN (10-12 N). The major drawback of this mode is that it yields low-resolution images. In **tapping mode**, the tip intermittently touches or taps the surface without inducing any frictional forces between tip and surface. The tip oscillates up and down the surface at or near its resonance frequency. As the tip approaches the surface, various forces such as van der Waals forces, dipole-dipole interactions, and electrostatic forces act on the cantilever, leading to a decrease in the amplitude of oscillation. A feedback loop maintains a constant separation between the tip and the sample, allowing for the generation of an image by scanning the surface. This method enables high-resolution and damage free imaging of soft and delicate biological samples. However, tapping mode encounters difficulties when used with liquid samples. The advantage of tapping the surface is improved lateral resolution on soft samples. In this mode, lateral forces such as drag, which are common in contact mode, are virtually eliminated.

Instrumentation

The surface morphology of the fabricated samples were determined by *MultiMode 8, Bruker, USA* Scanning Probe Microscope as shown in Fig. 2.9.

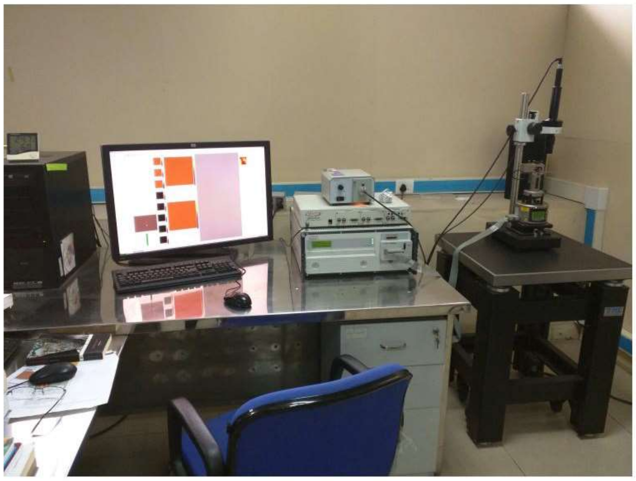

Figure 2.9: AFM instrument images in IIT Ropar.

The nanoscope MultiMode 8, Bruker has been used which consists of major components microscope, xyz scanner, controller, and computer as depicted in Fig. 2.9. All the images were acquired in tapping mode with resolution of 512×512 pixels. Various scanners with different maximum scan area E ($\times 10\mu m^2$) and J ($125 \times 125\mu m^2$) are used for imaging. The samples were scanned with the help of silicon cantilevers having a radius of curvature $\sim$ 10 nm with variable scan rate 0.5–1 Hz according to the requirement. The cantilever had a resonant frequency of the order of 300 kHz and a spring constant of 0.4 N/m. It was a 0.01-0.025 Ω cm Antimony (n) doped Si cantilever having rectangular geometry, with an average length, width and thickness of 125 m, 35 μm and 3.75 μm respectively. Post AFM image processing and analysis were performed by using various AFM softwares i.e, Nanoscope, Gwyydion, WSxM available.

Morphological Characteristics

The morphological characteristics of the samples such height fluctuations, power spectral density (PSD), periodicity, and fractal dimension etc., were determined using AFM topography analysis. The calculations were performed using Nanoscope and Gwyddion software. In the analysis of height fluctuations, the most commonly utilized statistical parameter for characterizing surface roughness is the interface width (w) or root mean square (RMS) roughness. It is calculated as the standard deviation (w) of surface heights derived from AFM pictures: $< w(t) >_N = \frac{1}{N}\left\{\sum_{i=1}^{N}[h_i - < h >_N]^2\right\}^{1/2}$, where $< h >$ is the average surface height, N is measured points. A larger value of the interface width indicate a rougher surface. In cases where surface topographies exhibit a predominant length scale, a correlation can be assumed between the root mean square (RMS) roughness and the amplitude of the topographical features. The root mean square (RMS) roughness is classified as a first-order statistical quantity, primarily employed for characterizing rough surfaces. First-order statistical quantities focus only on describing the statistical properties of individual points without considering the lateral dimensions of the features. Consequently, two surfaces with identical height distributions and RMS roughness values might appear distinctly different if there are variations in the length scales along the surfaces. In other words, differences in the frequencies of height fluctuations along different length scales can significantly influence the overall appearance and characteristics of the surfaces. To overcome this limitation, additional quantities are needed for proper characterization. The power spectral density (PSD), which belong to the second statistical quantities are used. PSD consider the relationship between two points on the surface. For the measurement of the PSD function, used frequency properties of surface topography, utilizing reciprocal space is more convenient than real space. To detect the dominant frequencies, performing the 2D Fast Fourier Transformation (FFT) of AFM image. Additionally, the FFT of an AFM image provides information about the periodic element and anisotropy present in the original image. The FFT of an AFM image displayed several spots or rings around central spots, revealing important details about the nanoscale surface topography and the arrangement of features. The central spot, known as the DC term, represent the average intensity or height of the entire image. Meanwhile the first spot corresponds to the dominant spatial frequency and provides information about the separation of features in the real space. Additional spots indicate higher lateral ordering or periodicity of structures on the surface. The width of a spot or ring is connected to the homogeneity and spatial correlation of features. Narrow spots or rings are indicative of a narrow size distribution. To facilitate the quantification of information within the FFT diagram, PSD functions are utilized. These functions, derived from the FFT spectra, provide quantitative insights into both the height and lateral distribution of features. Additionally, information about dominant relaxation mechanisms can be obtained from the decay of the PSD in the high frequency region. The PSD function were obtained from the 2D FFT diagram using the Gwyddion software [154]. It is known that RMS roughness can be obtained from the area under a band limit part of the PSD function [159]. In summary, while both FFT of an AFM image and PSD are tools for analyzing surface topography, the FFT focuses on revealing dominant spatial frequencies, whereas the PSD provides a statistical measure of the power distribution across different spatial frequencies, offering insights into the amplitude variations at different scales. They are complementary approaches and can be used together to comprehensively characterize surface features.

2.3.2 Scanning Electron Microscopy (SEM) and Energy Dispersive X-ray Spectroscopy (EDX)

Scanning Electron Microscopy (SEM) and Energy Dispersive X-ray Spectroscopy (EDX) are often used together to provide detailed information about the morphology and composition of materials [156].

Working Principle

Electron beam generation: SEM uses a focused beam of electrons instead of light to illuminate the specimen. An electron gun generates a beam of high-energy electrons. **Electron beam scanning:** The electron beam scans across the surface of the specimen in a raster pattern. As the beam interacts with the specimen, various signals are produced. **Signal Detection:** Secondary Electrons (SE) are emitted from the specimen's surface due to the interaction with the primary electron beam. These are commonly used for imaging the surface topography. Backscattered Electrons (BSE) are high-energy electrons that are scattered back from the specimen's atomic nucleus. The intensity of BSE is related to the atomic number of the elements, providing information about elemental composition. **Image Formation:** The signals are collected and used to create detailed, high-resolution images of the specimen's surface. The main component of SEM consists of the a electron source, a scanning system, electromagnetic lenses, vacuum system, display, detecor(s) and electronic controls as shown in Fig. 2.10

Working Principle of EDX

X-ray Emission: When the high-energy electrons from the SEM beam strike the specimen, they can displace inner shell electrons from atoms in the specimen. Electrons from outer shells then move to fill these vacancies, releasing energy in the form of X-rays. **X-ray Detection:** The EDX detector collects and analyzes these emitted X-rays. Each element emits characteristic X-rays with unique energies when excited, allowing identifi-

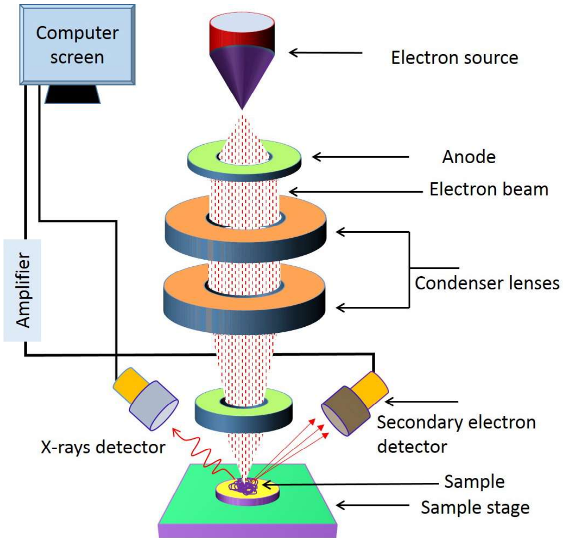
Computer screen
Electron source
Anode
Electron beam
Amplifier
Condenser lenses
Secondary electron detector
X-rays detector
Sample
Sample stage

Figure 2.10: A schematic diagram represents the basic components required for SEM.

cation of the elements present in the specimen. **Spectral Analysis:** The X-ray spectrum obtained provides information about the elemental composition of the sample. Peaks in the spectrum correspond to specific elements present in the specimen. **Mapping and Quantification:** EDX can be used for elemental mapping, providing spatial information about the distribution of elements on the specimen's surface. Quantitative analysis can be performed to determine the relative abundance of different elements.

Instrumentation

For characterizing the samples through SEM analysis, central research facilities of IIT Ropar has been used. The model of the SEM is JEOL JSM-6610/LV working under ultra-high vacumm. It is a high performance, high resolution tungsten SEM that could accommodate large samples up to 400 mm in diameter and 80 mm in height. It has the following resolutions in HV (High Vaccuum) mode: 3 nm (30 kV), 8 nm (3 kV) and 15 nm (1 kV). In LV (Low Vacuum) mode, it has a resolution of 4.0 nm at accelerating voltage of 30 kV. Accelerating voltage could be varied from 300 V to 30 kV and magnification is of the order of ×5 to 300,000. Vacuum pressure in chamber (LV regime) is adjustable from 10 to 270 Pa. JEOL JFC-1600 Gold coating unit has been used for making the sample conducting by coating thin layer of gold on it.

Chapter 3

Towards ordered Si surface nanostructuring: Role of an intermittent ion beam irradiation approach

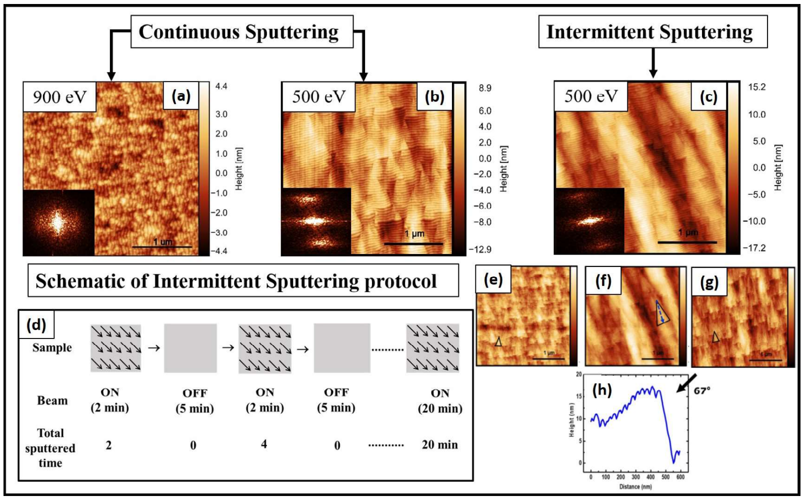

3.1 Introduction

Over the past few decades, engineering of materials at the nanoscale employing ion beam methods has been well established [160]. Of the various techniques considered, low energy ion beam irradiation induces self-organized nanopatterns on solid surfaces such as nanodots and nanoripples without the need of a mask or photoresist. Such self-organized nanopatterns often take the form of either one-dimensional (1D) ripples or 2D arrays of dots, depending on the direction of incidence of ion beam on the solid surface [7, 77, 161–163]. The generation of self-organized nanostructures with spatial and temporal periodicity on a wide range of solid surfaces has thus gained considerable attention using Ion Beam Irradiation (IBI) as a bottom-up, single-step, and cost effective approach in comparison to lithography [164]. IBI generates a diversity of self-organized nanostructures on a wide variety of crystalline or amorphous materials such as semiconductors [6], metals [77], insulators [83], and polymers [87] by varying irradiation conditions such as incidence ion energy, incident ion angle, ion flux, fluence, etc. The theoretical foundation for the current understanding of surface nanostructuring by IBI was seminally laid down by Bradley and Harper (BH) [10] by incorporating Sigmund's theory of sputtering [4] into a continuum evolution equation for the surface height $h(\mathbf{r}, t)$ of the irradiated target at time t at position $\mathbf{r} = (x, y)$ on a reference plane. The BH equation for the local velocity of the surface reads

$$\frac{\partial h}{\partial t} = -\nu_x \partial_x^2 h - \nu_y \partial_y^2 h - \mathcal{K} \nabla^4 h, \tag{3.1}$$

where $\nu_{x,y}$ (termed as the surface tension parameters) depend on beam parameters like incident ion energy E, incidence angle θ, flux, etc., while in the original BH model $\mathcal{K} > 0$ is related with thermally activated surface diffusion. The fact that at least $\nu_x > 0$ [10] implements Sigmund's unstable dependence of the sputtering yield with the local surface curvatures, which implies that a surface trough is sputtered away by irradiation faster than a surface peak [165] leading to a dynamical instability, counteracted upon by diffusive transport, which tends to smooth out surface height differences [10]. This model successfully explained experimental findings like the ripple alignment with respect to the ion beam [7], but failed to explain others, like the coarsening of the ripple wavelength at intermediate times or the stabilization of the ripple amplitude at long sputtering times [163]. Even more importantly, for the paradigmatic case of materials that become amorphous under IBI, like semiconductors, the main physical mechanisms behind $\nu_{x,y}$ and $\mathcal{K}$ are nowadays known not to be an unstable sputtering yield and thermal surface diffusion but, rather, material rearrangement and surface confined viscous flow, respectively [6]. Nevertheless, under such a reinterpretation of the physical significance of its parameters, Eq. (3.1) remains an accurate description of the short time evolution of many IBI experimental systems [164]. Equation (3.1) being linear in the surface height and its derivatives implies exponential growth of the height amplitude and the surface roughness under pattern-forming conditions [6, 7, 163]. Many efforts have been devoted to generalize it into a nonlinear model which, beyond describing saturation of the height to a finite steady-state profile, features suitable predictive power [6, 163]. Although the issue remains open, the following nonlinear model [166, 167] contains the main qualitative aspects of relevance for the present work:

$$\partial_t h = \sum_{i=x,y} \left[-\nu_i \, \partial_i^2 h + \Omega_i \partial_i^2 \partial_x h + \lambda_i^{(1)} \left(\partial_i h \right)^2 \right] + \sum_{i,j=x,y} \left[-\mathcal{K}_{ij} \partial_i^2 \partial_j^2 h - \lambda_{ij}^{(2)} \, \partial_i^2 (\partial_j h)^2 \right] . \quad (3.2)$$

Indeed, for standard ion fluxes $J \approx 1 - 10$ ions nm^{-2} s^{-1}, Eq. (3.2) follows from a more complete dynamical description in which the evolution of the surface height is explicitly coupled to that of the density of material transported along the surface, and all the parameters depend on physical conditions like E, θ, temperature, etc. [166, 167]. Equation (3.2), some of whose instances have been experimentally assessed [13, 168], generalizes the BH model (that corresponds to the terms with coefficients ν_i and $\mathcal{K}_{ij}$) via the occurrence of additional linear terms with parameters Ω_x and Ω_y, which are to be expected under

$\theta \neq 0$ oblique incidence conditions, as the ion beam breaks the $x \leftrightarrow -x$, but not the $y \leftrightarrow -y$ symmetry on the target plane (where we take x along the projected ion beam direction) [11]. Equation (3.2) further features nonlinear terms with coefficients $\lambda_i^{(1)}$ and $\lambda_{ij}^{(2)}$. The former are associated with nonlinear effects that, like sputtering, do not conserve the total amount of material on the surface, and efficiently arrest growth of the ripple amplitude while disordering the in-plane ripple arrangement [13]. The latter implements, e.g., surface-transport-related nonlinearities that preserve the total amount of material, and are known to induce e.g. coarsening of the ripple wavelength [13, 166, 167]. Although the parameter space of Eq. (3.2) is huge, the generic evolution it predicts under pattern forming conditions (e.g., $\nu_x > 0$, $\nu_y < 0$) agrees largely with experimental observations [166, 167]. Actually, this precise continuum model has been very recently shown [169] to correctly describe many linear and non-linear features of experimental systems like those we address in our present work. Over the years, IBI has gained potential to generate varied patterns having characteristic length scales of about tens of nanometers over large sample surfaces. To this effect, several unconventional methods of sputtering like dual-ion-beam sputtering, crossed-ion beam sputtering, etc. have been employed by several groups [137–139]. However, a major factor that hinders the applicability of this technique is the occurrence of spatial defects in the patterns which emerge [164]. Several attempts have been made to circumvent these defect formations and obtain near-perfect periodic structures. One of the early works by Aziz *et al.* demonstrated [143] that long range order is achievable by altering the spacing and orientation of pre-patterned lateral templates made on a substrate. Studies by Frost and co-workers on Si irradiated with noble gas ions (incident ion energy $E \simeq 2$ keV) indicated that defects on ion irradiated surfaces can be minimized at large fluences around 10^{19} ions cm^{-2} [100, 170]. The lateral ordering usually associated with a narrow size distribution of the surface nanostructures increases with the bombardment time. A separate study done by the same group also showed that excellent ripple ordering can be achieved by Xe$^+$ ions at low ion incidence angles even at moderate ion fluences and also for a diverging incident ion beam [75, 171]. However, these results may be affected by inadvertent, uncontrolled co-deposition of metallic impurities during the irradiation process [6, 172]. Further, ripple ordering properties at particular incidence energies have been observed to depend on the bombarding ion species [76], while non-standard irradiation setups like sequential and/or dual IBI [138, 139, 173] have been also employed with the goal to reduce pattern defects. In this context, a work by Keller and Facsko demonstrated that defect minimization in ripple morphology can be achieved by rotating a pre-sputtered sample by an azimuthal angle of 90° [174]. Kim *et al.* demonstrated that a defectless array of Au nanodots can be fabricated using sequential ion beam sputtering of an Au layer. The experiment essentially consisted of two separate sequences of ion sputtering after changing the ion beam angle [80]. Recently, Harrison and Bradley [149] have suggested on a theoretical basis that, if a sample surface is periodically rocked about a suitably chosen normal axis during ion bombardment, defect-free ripples might be obtained. The predictive power of this proposal has been assessed experimentally to a varying degree of success by Jo *et al.* [144]. All these works suggest the wide range of approaches that different groups have taken to realize defect-free nanostructured surfaces via IBI. In spite of these efforts, it still remains a challenge to obtain systematic conditions that lead to defect-free rippled surfaces considering the linear and non-linear regimes which are specific to a given ion-target combination. In view of the above facts, in the present work we have investigated the evolution and dynamics of ripple formation on the paradigmatic Si surfaces [6] by introducing an unconventional method of intermittent sputtering, in which the surface is irradiated and left to relax intermittently within intervals of various time durations, thereby influencing the pattern formation process and ordering properties. The present method employed generalizes earlier works on sequential sputtering by performing repeated alternated irradiation and relaxation steps. While in those earlier works, the time interval between the two stages of sputtering is principally governed by the time required to change the incident beam angle, here we have carried out intermittent sputtering in varying degrees of relaxation times and sputtering durations. All the experiments were carried out at oblique incidence using an Ar^+ ion beam. Initially, they were carried out at higher energy conditions where the evolved surface consisted of ripples only and hence was relatively a simple one. Next, the experiments were performed at lower energy, where individual ripples are known to be better formed. Intermittent sputtering was achieved by varying the sputtering time (beam-on condition) of each of the irradiation intervals separated by relaxation periods of a fixed duration, or else the relaxation time (beam-off condition) in between two consecutive irradiation intervals of a fixed dose. For the low energy conditions studied, the surface morphology exhibits ripple formation simultaneous with the development of hierarchical triangular morphologies that have focused theoretical [175] and experimental [176, 177] interest very recently. The intermittently sputtered samples are compared with those which have been sputtered continuously using Ar^+. The ripples are found to feature improved ordering for short durations of continuous or intermittent sputtering conditions. Our findings can be rationalized in terms of the physical principles underlying Eq. (3.2), as borne out from the numerical simulations that we report for this continuum model.

3.2 Materials and methods

Commercially available undoped Si (100) substrates were cut into pieces of 1×1 cm^2 area and cleaned ultrasonically in ethanol for 20 min. They were rinsed with de-ionised water subsequently. These were then mounted on a sample holder inside a vacuum chamber that houses a Kaufman ion source. The ion source is a three-gridded ion source with an in-built neutralizer. This configuration ensures minimum divergence of the beam up to a distance of 20 cm beyond which the beam diameter grows rapidly [153]. A Si(100) wafer of 2" diameter was placed in between the sample and the metal sample holder to avoid any metal impurity sputtering. The sample holder was at a distance of 15 cm from the source in a high vacuum chamber whose base pressure and working pressure were kept at 2.17×10^{-7} Torr and 3.14×10^{-3} Torr, respectively. The sample surfaces were irradiated at room temperature with 900 eV Ar^{+} ions at an incidence angle $\theta = 67^{\circ}$ with respect to the surface normal. The beam current was maintained at 13.3 mA. The Si substrates were sputtered continuously for 2, 5, 10, 15, and 20 min (referred to as N_2, N_5, N_{10}, N_{15}, and N_{20}, respectively) corresponding to 10×10^{18}, 2.5×10^{19}, 5×10^{19}, 7.5×10^{19}, and 10×10^{19} ions cm^{-2} fluences, respectively. Further, a separate set of Si samples were also irradiated at room temperature but at 500 eV incident energy, while all other conditions remained the same. This second set of experiments was divided into two categories. In the first category, the sputtering time intervals were altered (from 2 to 15 min) while keeping the relaxation time ($t_R = 5$ min) constant between two successive sputtering events (samples S_2 to S_{20} in Table 3.1). In the second category of experiments, the relaxation time between two consecutive sputtering events was altered (from 0 to 15 min) while keeping the sputtering time fixed ($t_S = 5$ min) (samples R_0 to R_{15} in Table 3.1). For all the above samples, the total fluence delivered was 10×10^{19} ions cm^{-2}. Correspondingly, the total time of sputtering i.e., 20 min, kept fixed for both categories, was divided as per the details given in Table 3.1. The relaxation times in the experiment have been chosen considering the time for linear regimes found from earlier studies [144, 178]. Estimates from the data in the above studies suggest that the time scale for linear regime (which corresponds to the growth rate of the most unstable Fourier mode of the surface height) is about 5 mins or less. Considering the beam conditions in our experiment, the corresponding values for the present case would be less than 5 mins. Therefore, the relaxation times were chosen from 2 mins to 20 mins since, the investigation had to be performed in the non-linear regime. It is to be noted that in comparison to the above, the time scale of a collision cascade and surface diffusion processes are of the order of 10^{-12} secs. In addition to the above, Si substrates were also sputtered continuously for $E = 500$ eV at room temperature for 2, 5, 7, 10, and 20 min (referred to as C_2,

Sample label	Sputtering time interval (t_S) (min)	Relaxation time interval (t_R) (min)	Total sputtering time (t_C) (min)
S_2	2	5	20
S_5	5		
S_7 (*)	7		
S_{10}	10		
S_{20} (= C_{20}= R_0)	20	0	
R_2	5	2	
R_5		5	
R_7		7	
R_{10}		10	
R_{15}		15	

Table 3.1: Sputtering and relaxation time durations of samples subjected to intermittent 500 eV Ar^+ ion bombardment. C_{20} sample is irradiated continuously for 20 min; in this case, total sputtering time (t_C) is equivalent to continuous sputtering time. (*) S_7 sample is irradiated intermittently for a total time of 20 min (the last sputtering period is 6 min long).

C_5, C_7, C_{10} and C_{20}, respectively) corresponding to ion fluences of 10×10^{18}, 2.5×10^{19}, 3.5×10^{19}, 5×10^{19}, and 10×10^{19} ions cm^2, respectively. Figure 3.1 gives a typical schematic view (corresponding to sample S_2) for intermittent sputtering with the beam on for 2 min windows and off for 5 min windows (in between two consecutive sputtering events). The total sputtering time is kept as 20 min, at which a total ion fluence of 10×10^{19} ions cm^{-2} is achieved. Surface morphologies of the Si surfaces were imaged *ex-situ* after intermittent irradiation by atomic force microscope (AFM) (MultiMode 8, Bruker, USA) in tapping mode, using a silicon cantilever with a tip of 10 nm radius under ambient conditions, with an image resolution of 512 × 512 pixels. After obtaining the topographical images of irradiated surface by AFM, quantitative information about

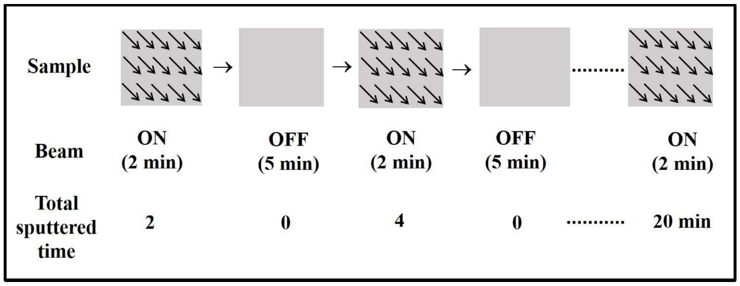

Figure 3.1: Schematic showing beam-on (sputtering time) and beam-off (relaxation time) steps for irradiation of samples with 500 eV Ar^+ ions at 67°. The schematic corresponds to S_2 of Table 3.1 as an example.

statistical surface parameters such as wavelength, periodicity, root mean square (rms) roughness (standard deviation of the height values), amplitude, correlation length, etc. were extracted using Gwyddion software (version 8.1) [154]. The results presented are an average of about 4 AFM scans for each sample. The images were further analyzed using ImageJ software [155] to obtain the average area of small features on irradiated surfaces. In the event of sputtering, starting out from a flat initial condition (in practice, a small-amplitude random perturbation thereof), a sinusoidal profile forms along the x direction (so-called parallel ripples [164]), whose wavelength remains time-independent, while the root mean square (rms) roughness of the surface increases exponentially. This behavior is shared by Eq. (3.1) and corresponds to the early time, linear regime of the process [7, 178]. Once the surface profile departs sufficiently far from a flat shape, height derivatives become non-negligible and dynamics are controlled by the nonlinear terms. In this nonlinear regime, the increase of the root mean square (rms) roughness slows down, while the ripple wavelength frequently becomes fluence dependent; eventually, a steady state can be reached, at which the rms roughness and the wavelength both stabilize [6, 163]. Additional morphological behaviors described below can be identified in the linear and nonlinear regimes described by Eq. (3.2). Fast Fourier Transform (FFT) has been used to check the periodicity and alignment of nanopatterns on the irradiated surfaces. In particular, the height power spectral density (PSD) was used to characterize the irradiated surfaces further. Specifically, the PSD of the surface height field is defined as [14, 179]

$$\mathrm{PSD}(\mathbf{q}, t) = \langle |h(\mathbf{q}, t)|^2 \rangle, \tag{3.3}$$

where $h(\mathbf{q}, t)$ is the space FFT of the surface height field $h(\mathbf{r}, t)$, brackets denote an average over scans or experiments, and $\mathbf{q} = (q_x, q_y)$ is two-dimensional wave vector. We have also evaluated the 1D PSD of 1D surface profiles along, e.g., the x-direction, namely,

$$\mathrm{PSD}(q_x, t) = \langle |h_{y_0}(q_x, t)|^2 \rangle, \tag{3.4}$$

where $h_{y_0}(q_x)$ is the FFT of the one-dimensional profile $h(x, y_0)$ for a fixed y_0 value. These two functions are related as [180, 181]

$$\mathrm{PSD}(q_x, t) = \frac{1}{\pi} \int_0^\infty dq_y \, \mathrm{PSD}(\mathbf{q}, t). \tag{3.5}$$

If a ripple structure exists which is periodic along the x direction, this reflects into the occurrence of a characteristic peak (local maximum) in the plot of $\mathrm{PSD}(q_x)$ vs q_x, say at $q_x = q_*$. In such a case, the ripple wavelength is $\lambda = 2\pi/q_*$ while the width of the peak is inversely correlated with the degree of space order in the morphology [144, 182]. On the other hand, for a finite time before the steady state has been reached, a finite value of $q = q_c$ separates the qualitative behavior of, e.g., $\mathrm{PSD}(q_x, t)$. Thus, for $q_x > q_c$ the PSD shows non-trivial behavior with q_x, while it is q_x-independent for $q < q_c$. In such a case we identify $\xi = 2\pi/q_c$ with a correlation length, in the sense that surface features separated by a smaller (longer) distance than ξ are statistically correlated (uncorrelated) [182].

3.3 Results and discussions

3.3.1 Surface evolution for continuous sputtering conditions at 900 eV

We first consider standard continuous sputtering experiments for an ion energy value which leads to a relatively simple pattern morphology. This will illustrate our method of analysis; most importantly, it will also provide us with an important reference case for comparison with the intermittent sputtering experiments. The morphology and PSD spectra of the pristine Si surface are shown in Fig. 3.2. Figure 3.3 shows 3×3 μm^2 AFM images of a Si surface under continuous sputtering condition as described in Section 3.2, with the black arrow indicating the projection of the incident ion beam direction on the Si surface (x-axis). The surface morphology of these Si surfaces undergoing IBI indeed exhibits an unambiguous parallel ripple pattern along the x-direction, as predicted by Eqs. (4.1) and (3.2) for $\nu_x > 0$ such that $\nu_x > \nu_y$. The orientation of the ripples is confirmed from the structure of the 2D FFT (square root of the 2D PSD) plots obtained from the AFM images. Indeed, note the preferential alignment of the 2D FFT function around the

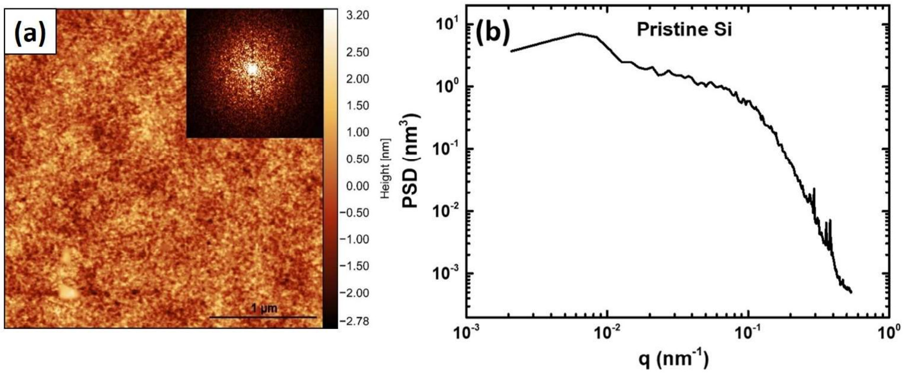

Figure 3.2: (a) 3×3 μm^2 AFM micrograph of pristine Si surface. Top right inset: 2D FFT (square root of the 2D PSD) corresponding to the AFM images. (b) Power spectral density of the pristine Si surface.

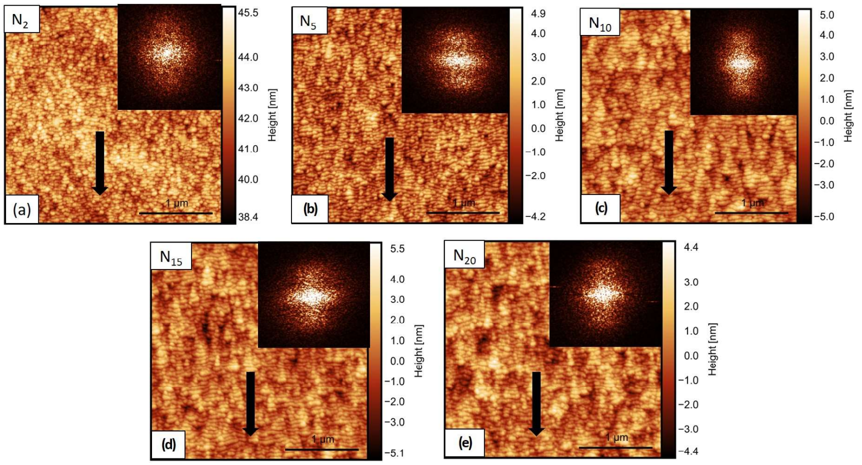
N2
(a)
1 µm
45.5
44.0
43.0
42.0
41.0
40.0
38.4
Height [nm]
N5
(b)
1 µm
4.9
4.0
3.0
2.0
1.0
0.0
−1.0
−2.0
−4.2
Height [nm]
N10
(c)
1 µm
5.0
4.0
3.0
2.0
1.0
0.0
−1.0
−2.0
−3.0
−5.0
Height [nm]
N15
(d)
1 µm
5.5
4.0
3.0
2.0
1.0
0.0
−1.0
−2.0
−3.0
−5.1
Height [nm]
N20
(e)
1 µm
4.4
3.0
2.0
1.0
0.0
−1.0
−2.0
−3.0
−4.4
Height [nm]

Figure 3.3: 3×3 μm^2 AFM micrographs of 900 eV Ar$^+$ irradiated Si at 67° for continuous sputtering times t$_N$ of (a) 2 min, (b) 5 min, (c) 10 min, (d) 15 min, and (e) 20 min. Black arrows indicate the ion beam direction. Top right insets: 2D FFT (square root of the 2D PSD) of the corresponding AFM images.

k_x direction [182]. In addition, both the real and reciprocal space images suggest an overall morphology which does not change much with increasing time. The ripples are frequently interrupted along the y-direction, leading to a relatively disordered 2D arrangement, while their wavelength (e.g., peak-to-peak distance) along the x-direction coarsens somewhat with increasing time, as seen in Fig. 3.4. Note, wavelength coarsening is a nonlinear property [13, 166, 167] that can be described by Eq. (3.2), but not by the linear Eq. (3.1). These observations can be substantiated more quantitatively from the analysis of Fig. 3.4(a), which plots the topographic parameters extracted from AFM micrographs for the 900 eV sputtered surface as functions of sputtering time (ion fluence). For the range of fluences shown, the overall change in amplitude and roughness is small; yet, the wavelength of the ripples does unambiguously increase up to 61 nm from the earlier value of 50 nm at the smallest fluence. It increases rapidly within the first 5 mins of irradiation and slows down thereafter. The behavior seen in Fig. 3.4(a) for the wavelength, rms, and amplitude is fully consistent with a nonlinear regime of evolution [178], implying that the total duration of the linear regime is shorter than 2 min under the present

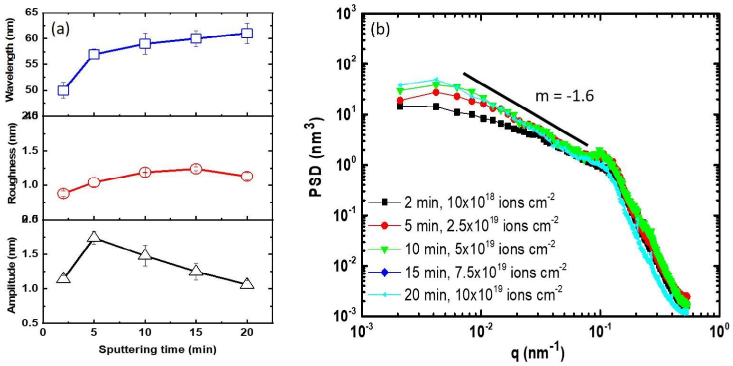

Figure 3.4: (a) Amplitude, rms roughness, and wavelength (bottom to top) vs sputtering time for continuously sputtered Si surfaces using 900 eV Ar$^+$, for ion fluences from 10×10^{18} to 10×10^{19} ions cm^{-2}. (b) Log-log plot of 1D PSD versus spatial frequency q (extracted from 1D cuts of AFM images) along the ion beam direction (x-axis). The straight solid line shown as a reference corresponds to power-law behavior as PSD(q) $\sim q^m$, for m as given. All other lines are guides to the eye.

irradiation conditions. The wavelength in Fig. 3.4(a) has been obtained from the fluence-dependent peak positions in the 1D PSD spectra as shown in Fig. 3.4(b). No change in the sharpness of the peak in PSD spectra is observed with increase of ion fluence from 10×10^{18} to 10×10^{19} ions cm^{-2}, implying that the quality of ordering of the ripples does not change appreciably during the process. Note that, on the other hand, the local peak associated with the ripple structure is not very pronounced, which is indicative of a high degree of space disorder, as assessed in other models and experiments of IBI, see e.g. Refs. [11,144] and works quoted therein. Furthermore, with increasing fluence the 1D PSD develops power-law behavior at small q that seems to converge to PSD(q) $\sim 1/q^{1.6}$. This speaks of strong height fluctuations and kinetic roughening at large scales [14,182,183]. Comparing with the theoretical behavior of the 1D PSD for kinetically rough 2D surfaces, PSD(q) $\sim 1/q^{2\alpha+1}$ [14,180,181], we obtain $\alpha = 0.3$ for the roughness exponent α, a value which is similar to those previously obtained for IBI of e.g. highly oriented pyrolytic graphite at 5 keV [184] or Si at 500 eV [185]. For comparison, a purely Brownian surface would lead to a 2D PSD [Eq. (3.3)] which behaves as $\mathrm{PSD}(\mathbf{q}) \sim 1/q^2$, hence a 1D PSD [Eq. (3.4)] behaving as $\mathrm{PSD}(q_x) \sim 1/q_x$, so that $\alpha_{\mathrm{Brownian}} = 0$ (implying that the increase of the (squared) surface roughness w with the lateral size ℓ of the observation window is logarithmic as $w^2 \sim \ln \ell$, rather than power-law as $w^2 \sim \ell^{2\alpha}$ [1] [14, 182]). From this point of view, $\alpha > 0$ as obtained in our experiments implies that the surface heights show persistent behavior if considered as random variables, due to strong positive correlations among them [14, 182]. Again, the time behavior of the PSD curves shown in Fig. 3.4(b) is consistent with fully nonlinear behavior [11, 186] akin to that found for particular instances of Eq. (3.2) [167], and a linear regime that is shorter than 2 min under the present irradiation conditions.

3.3.2 Surface evolution for continuous sputtering conditions at 500 eV

In order to make contact with the results of our novel intermittent method, reported in Sec. 3.3.3 below, we next proceed with continuous IBI experiments at the same ion energy, $E = 500$ eV, as will be employed later. Figure 3.5 thus shows 3×3 $\mu\mathrm{m}^2$ AFM images of Si surfaces sputtered continuously at 500 eV for 2, 5, 7, 10, 15, and 20 min. The black arrow indicates the direction of the incident ion beam on the Si surface. The surface morphology exhibits a parallel-mode nanoripple pattern which is generally more ordered than that obtained at $E = 900$ eV. The orientation of the pattern can be again confirmed by the 2D FFT of the 1×1 $\mu\mathrm{m}^2$ AFM images shown in Fig. 3.5. It is evident that the quality of individual ripples is far better than those on Si sputtered at 900 eV. The overall 2D order has also improved, as reflected by the sharper 2D FFT. However, at this energy the morphology structure is richer, as all the AFM images show triangular structures superposed on the parallel ripple pattern, which are oriented along the same direction. Formation of such hierarchical structures has been previously reported in the

---

[1] Recall the exact relation $w^2 = \int \mathrm{d}\mathbf{q}\, \mathrm{PSD}(\mathbf{q})$ [14, 182].

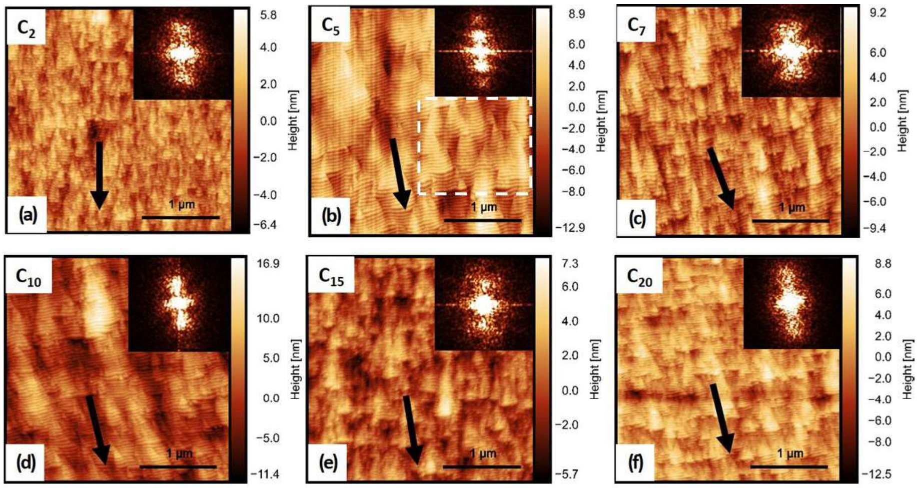
C$_2$
(a)
1 µm
5.8
4.0
2.0
0.0
−2.0
−4.0
−6.4
Height [nm]
C$_5$
(b)
1 µm
8.9
6.0
4.0
2.0
0.0
−2.0
−4.0
−6.0
−8.0
−12.9
Height [nm]
C$_7$
(c)
1 µm
9.2
6.0
4.0
2.0
0.0
−2.0
−4.0
−6.0
−9.4
Height [nm]
C$_{10}$
(d)
1 µm
16.9
10.0
5.0
0.0
−5.0
−11.4
Height [nm]
C$_{15}$
(e)
1 µm
7.3
6.0
4.0
2.0
0.0
−2.0
−5.7
Height [nm]
C$_{20}$
(f)
1 µm
8.8
6.0
4.0
2.0
0.0
−2.0
−4.0
−6.0
−8.0
−12.5
Height [nm]

Figure 3.5: 3×3 μm^2 AFM micrographs of 500 eV Ar$^+$ irradiated Si at 67° for continuous sputtering times t$_C$ of (a) 2 min, (b) 5 min, (c) 7 min, (d) 10 min, (e) 15 min, and (f) 20 min. Black arrow indicates the ion beam direction. Top right insets: 2D FFT of corresponding AFM images. The white dashed line in (b) selects a portion of the surface to be compared to a numerically simulated surface in Fig. 3.13.

literature, see e.g. Refs. [109, 175–177] and references therein. We will later confirm that all these experiments are also in a nonlinear regime of evolution, following an analysis similar to that made on the basis of Fig. 3.4. For now, let us stress that, from the point of view of the nonlinear continuum model discussed above, Eq. (3.2), the main qualitative feature to be noted is that, as realized in Ref. [175], the coefficients Ω_x and Ω_y need to be substantially larger for $E = 500$ eV than they are at $E = 900$ eV, thus implementing the enhanced morphological role observed for the triangular structures.

3.3.3 Surface evolution with intermittent sputtering conditions

We finally report on our intermittent sputtering experiments, which have been carried out as discussed in Section 3.2. Figure 3.6 shows 3×3 μm^2 AFM topographic images of Si(100) surfaces for intermittent sputtering of samples S$_2$ to S$_{20}$ as described in Table 3.1. The total sputtering time (t$_C$) was chosen to be 20 mins since the ripple ordering is best

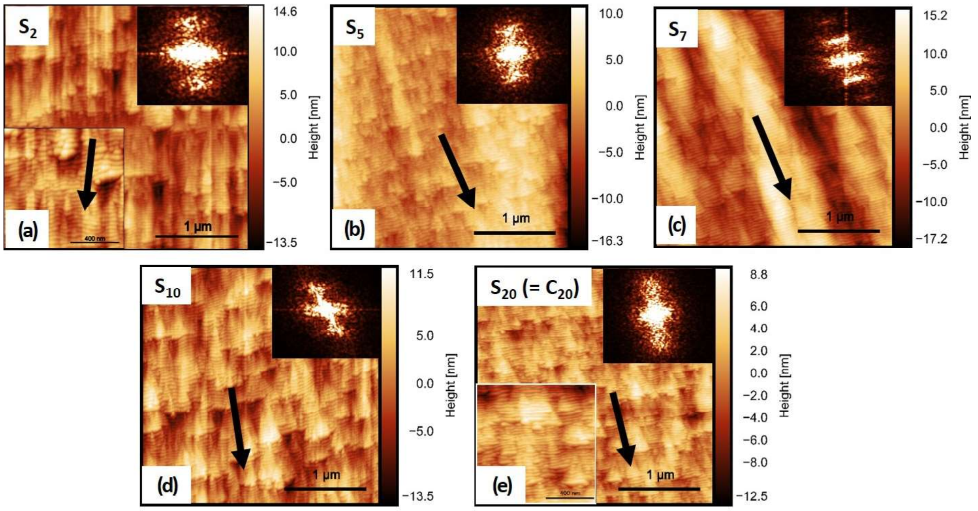
S_2
14.6
10.0
5.0
0.0
−5.0
−13.5
Height [nm]
(a)
400 nm
1 µm
S_5
10.0
5.0
0.0
−5.0
−10.0
−16.3
Height [nm]
(b)
1 µm
S_7
15.2
10.0
5.0
0.0
−5.0
−10.0
−17.2
Height [nm]
(c)
1 µm
S_{10}
11.5
5.0
0.0
−5.0
−13.5
Height [nm]
(d)
1 µm
S_{20} (= C_{20})
8.8
6.0
4.0
2.0
0.0
−2.0
−4.0
−6.0
−8.0
−12.5
Height [nm]
(e)
400 nm
1 µm

Figure 3.6: 3×3 μm^2 AFM micrographs of 500 eV Ar$^+$ irradiated Si at 67° for a relaxation time interval (t_R) of 5 min and sputtering time intervals t_S (a) 2 min, (b) 5 min, (c) 7 min, (d) 10 min, and (e) 20 min. The total sputtering time (t_C) is 20 min and the total ion fluence is 10×10^{19} cm^{-2}. Black arrows indicate the ion beam direction. As noted in Table 3.1, panel (e) for S_{20} is identical to C_{20} from Fig. 3.5 and is reproduced here for the reader's convenience. Top right insets: 2D FFT of corresponding AFM images. Bottom left insets in panels (a) and (e): 1×1 μm^2 AFM micrographs of corresponding AFM images.

observed at that time as exhibited by the 2D FFT images as shown in Fig. 3.7 (j). Here, the sputtering time interval is varied while the relaxation time interval is kept constant ($t_R = 5$ min). The black arrow indicates the direction of the incident ion beam on the Si surface. The surface morphology of Si exhibits well ordered parallel-mode nanoripples. It is observed that the nanoripples carry again triangular-shaped morphologies superposed, the sizes of which vary with the sputtering time intervals. Figure 3.6(c) corresponding to the sample S_7 ($t_S = 7$ min and $t_R = 5$ min) shows additional patch-like structures parallel to the ion beam direction, similar to the large-scale structures previously reported in Ref. [187]. The insets of Fig. 3.6 show the FFTs of the observed morphologies. It is evident from the FFT that the ripple periodicity as well as the ordering change with the intermittent sputtering time. The distinct spots in the FFT of S_7 suggest that the ripples

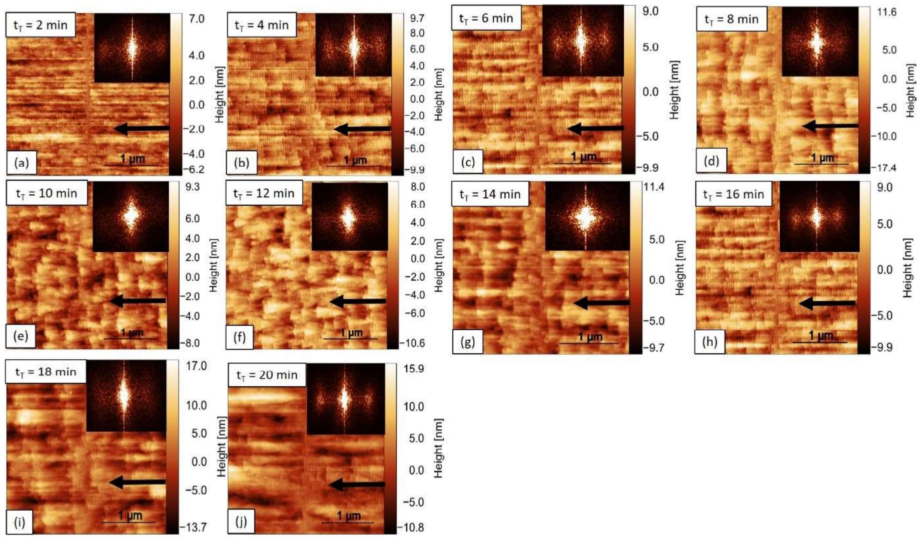

Figure 3.7: 3×3 μm^2 AFM micrographs of 500 eV Ar$^+$ irradiated Si at 67° for a relaxation time interval (t$_R$) of 5 min and sputtering time intervals (t$_S$) of 2 min with increasing total time of sputtering for each Si sample from (a) to (j) t$_T$ = (a) 2 min, (b) 4 min, (c) 6 min, (d) 8 min, (e) 10 min, (f) 12 min, (g) 14 min, (h) 16 min, (i) 18 min, and (j) 20 min. Black arrow indicates the direction of incidence of the ion beam. Top right insets: 2D FFT of corresponding AFM images.

are best ordered for this condition. Figure 3.8 sequentially shows the effect of variation of the relaxation time interval (t$_R$) for a constant sputtering time interval (t$_S$ = 5 min) using 3×3 μm^2 AFM images of Si surfaces. The results are for samples R$_0$ to R$_{15}$ as described in Table 3.1. The black arrow indicates the direction of incident ion beam on the Si surface. Similar morphologies as obtained for samples S$_2$ to S$_{20}$ are observed to form on the Si surfaces. The FFT images, however, indicate that now the ripples have a lesser degree of order as compared to the earlier case, since the FFT spots are not as distinct. Within the samples R$_2$ to R$_{15}$, the sample R$_7$ (t$_R$ = 7 min and t$_S$ = 5 min) seems to exhibit the best degree of order as compared to others. Beyond the 2D AFM topographs and their FFTs, we can further characterize all the experiments performed at $E = 500$ eV in a similar way as we did in Fig. 3.4 for the experiments done at $E = 900$ eV. Results are displayed in Fig. 3.9, which compares the rms roughness, ripple amplitude,

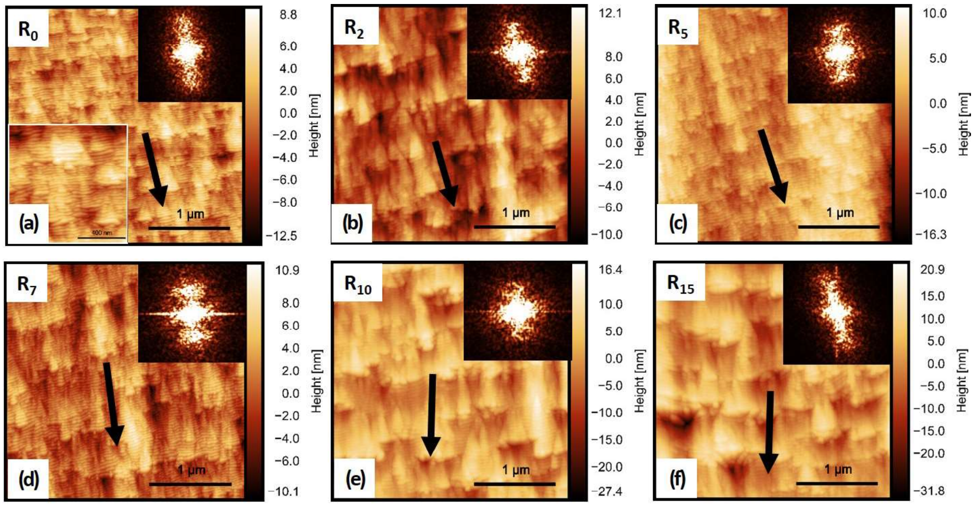
R₀
(a)
100 nm
1 µm
8.8
6.0
4.0
2.0
0.0
−2.0
−4.0
−6.0
−8.0
−12.5
Height [nm]
R₂
(b)
1 µm
12.1
8.0
6.0
4.0
2.0
0.0
−2.0
−4.0
−6.0
−10.0
Height [nm]
R₅
(c)
1 µm
10.0
5.0
0.0
−5.0
−10.0
−16.3
Height [nm]
R₇
(d)
1 µm
10.9
8.0
6.0
4.0
2.0
0.0
−2.0
−4.0
−6.0
−10.1
Height [nm]
R₁₀
(e)
1 µm
16.4
10.0
5.0
0.0
−5.0
−10.0
−15.0
−20.0
−27.4
Height [nm]
R₁₅
(f)
1 µm
20.9
15.0
10.0
5.0
0.0
−5.0
−10.0
−15.0
−20.0
−31.8
Height [nm]

Figure 3.8: 3×3 μm^2 AFM micrographs of 500 eV Ar$^+$ irradiated Si at 67° for a sputtering time interval (t$_S$) of 5 min and for relaxation time intervals t$_R$ (a) 0 min, (b) 2 min, (c) 5 min, (d) 7 min, (e) 10 min, and (f) 15 min. The total sputtering time (t$_C$) is 20 min and the total ion fluence is 10×10^{19} cm^{-2}. Black arrows indicate the ion beam direction. As noted in Table 3.1, panel (a) for R$_0$ is identical to C$_{20}$ from Fig. 3.5(f) and to S$_{20}$ from Fig. 3.6(e), and is reproduced here for the reader's convenience. Top right insets: FFT of the corresponding AFM images. Bottom left inset in panel (a): 1×1 μm^2 AFM micrograph of the corresponding AFM image.

and ripple wavelength for the three modes of sputtering implemented at $E = 500$ eV. The rms roughness for all the three modes of sputtering is seen to range between 1.5 to 6 nm in the time interval investigated. The ripple amplitude increases first, reaches a maximum and finally decreases slightly for the continuous mode. On the other hand, it tends to saturate at similar level for the variable sputtering time case while it shows an overall decrease for the variable relaxation time experiments. Comparison of Figs. 3.4(a) (for $E = 900$ eV) and 3.9(a) (for $E = 500$ eV) suggests a very similar time evolution for the roughness, ripple wavelength, and ripple amplitude when performing continuous IBI at both energy conditions. The main difference is the occurrence of larger fluctuations in the values of these variables for the lower ion energy case, possibly due to the increased complexity of the surface morphology introduced by the triangular structures, whose

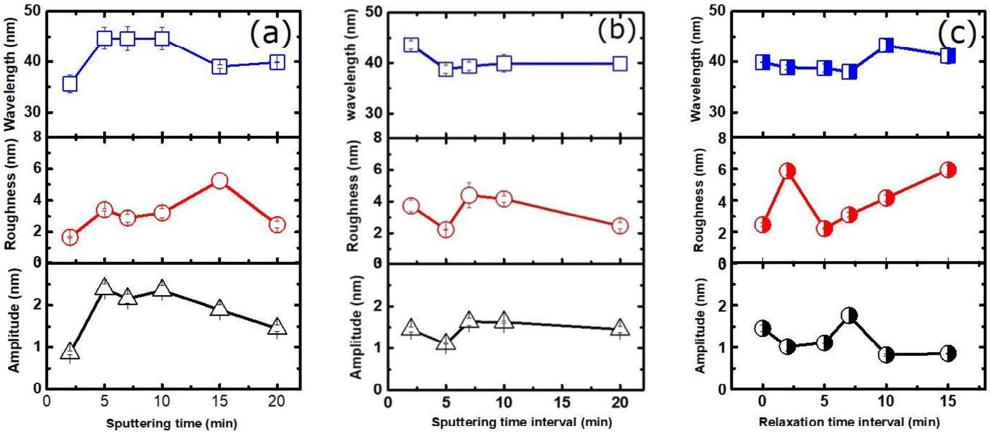

Figure 3.9: Plots showing amplitude, rms roughness, and wavelength dependence with time (bottom to top) for: (a) Continuous sputtering (varying t_C), (b) varying sputtering time interval (t_S), and (c) varying relaxation time interval (t_R). Lines are guides to the eye.

space distribution seems to be quite random as in other reports [175–177, 187]. From the point of view of Eq. (3.2), the most relevant change in the parameters with ion energy is an increase of $\Omega_{x,y}$ when reducing E, thereby enhancing triangular structures. The main conclusion we extract from these results for our intermittent IBI approach is that all the sputtering time intervals to be employed in our intermittent experiments at $E = 500$ eV are in the nonlinear regime of evolution. This is also confirmed by the time behavior of the 1D PSD function for continuous sputtering at this ion energy, shown in Fig. 3.10(a). By comparing this plot with Fig. 3.4(b), we again notice the larger amplitude of fluctuations that holds at low energy, together with a sharper main peak, which speaks of better defined individual ripples. The sizeable power-law behavior that takes place for $q < q_*$ irrespective of time is indicative of nonlinear behavior for all t_C values considered in this figure, as discussed above. The PSD curves in Fig. 3.10(a) show a decrease in the sharpness of the peak distribution for increasing sputtering time thereby indicating an increase in the number of space defects. The sharpest peak is observed

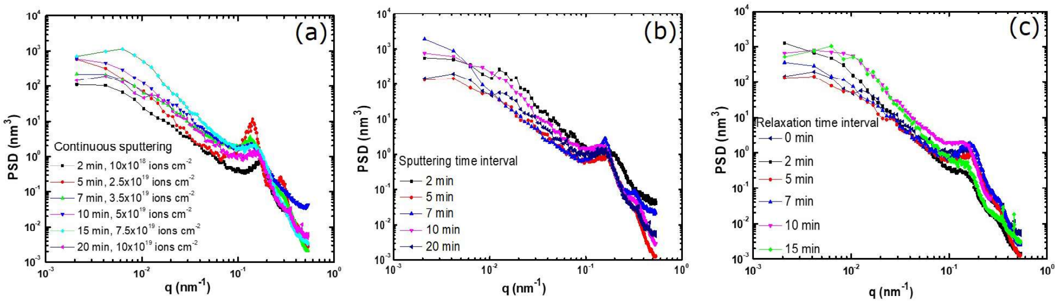

Figure 3.10: Log-log plot of 1D PSD versus spatial frequency q (as extracted from AFM images) along the projection of the ion beam direction. (a) Continuous sputtering, (b) variable t_S for $t_R = 5$ min and $t_C = 20$ min, and (c) variable t_R for $t_S = 5$ min and $t_C = 20$ min. Lines are guides to the eye.

for $t_C = 5$ min, thus corroborating its prominence as found by AFM in Fig. 3.5(b). In contrast, for $E = 900$ eV, Fig. 3.4(b) shows broad peaks thereby indicating ill-formed ripple structures as evident from the respective AFM images in Fig. 3.3. Figure 3.9(b) shows the variation of rms, ripple amplitude and wavelength with the sputtering time interval t_S. The wavelength first decreases linearly till about 5 min and then slowly saturates. The minimum wavelength is estimated to be 39 nm at $t_S = 5$ min and $t_R = 5$ min while the maximum wavelength equals 43 nm at $t_S = 2$ min and $t_R = 5$ min. As the temperature of the target does not increase substantially under our IBI treatments, we hypothesize that the surface morphology remains almost frozen during the relaxation periods of the intermittent sputtering method, possibly with some local rearrangement and defect elimination via surface diffusion. In such a case, for example 10 windows of 2 min sputtering each, separated by 5 min relaxation periods (as for S_2) will not be able to bring the surface into a state which fully reproduces C_{20} that is obtained via 20 min of uninterrupted sputtering. For this reason, the values of the rms, ripple wavelength and amplitude for S_2 will compare better with those of C_n for $n < 20$. By increasing the sputtering time interval t_S into S_5, S_7, etc. the corresponding final surfaces will more efficiently compare with C_{20} and for this reason the rms, ripple wavelength and amplitude values tend to become t_S-independent, as seen in Fig. 3.9(b). However, too high values of t_S imply that the surface is well into the nonlinear regime during each sputtering window, which largely increases the total number of defects. Therefore, there is an optimum value of $t_S \simeq 7$ min at which the space ordering of the pattern reaches its optimal quality within this intermittent IBI experiment, see panel (c) for S_7 in Fig. 3.6. The corresponding 1D PSD curves [Fig. 3.10(b)] also show a relatively sharper peak distribution indicating higher ordering of ripples for $t_S = 7$ min and $t_R = 5$ min. Finally, Fig. 3.9(c) shows the variation of the rms and the ripple amplitude and wavelength with the relaxation time interval t_R. Now e.g. for $t_R = 2$ min we have a total of four 5 min sputtering periods separated by short 2 min relaxation intervals, during which moderate surface rearrangement can take place. Thus, the rms and ripple wavelength and amplitude for R_2 are similar to those of e.g. C_{15}. At $t_R = 5$ min, the duration of the sputtering and relaxation periods is the same making the two intermittent IBI experiments indistinguishable so that $R_5 = S_5$, which was close to optimal space ordering among the S_n samples. For still longer t_R, the four 5 min sputtering windows are less and less efficient to bring the surface into a state like C_{15}, due to larger rearrangement during the increasingly long relaxation windows. This results into departure from optimal ordering. For example, R_{10} and R_{15} resemble quite closely long-time evolutions of triangular structures on rippled morphologies, obtained experimentally by continuous low-energy IBI of fused silica targets [188]. The 1D PSD curves in Figure 3.10(c) show a relatively less sharp peak distribution indicating a lower ripple ordering in general. A sharper peak is observed for $t_S = 5$ min and $t_R = 7$ min, denoting a better pattern.

3.3.4 Additional issues

All the AFM images corresponding to samples bombarded at 500 eV show hierarchical triangular structures on an underlying ripple morphology. Comparison was done between sample C_{20} and the intermittently sputtered samples. Amongst the latter, samples S_7

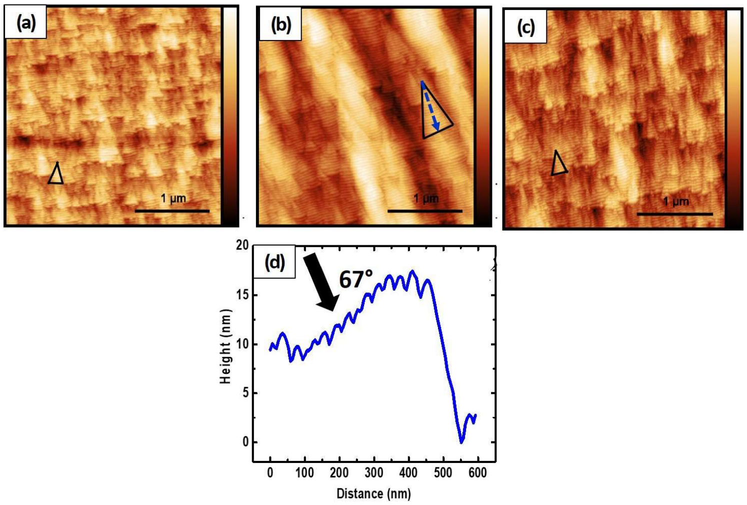

Figure 3.11: AFM images showing typical triangular structures highlighted as black triangles for (a) C_{20}, (b) S_7, and (c) R_7. (d) Typical line profile corresponding to the dashed line on the selected triangular structure shown in panel (b). Black arrow indicates the ion beam direction.

(i.e., $t_S = 7$ min, $t_R = 5$ min) and R_7 (i.e., $t_S = 5$ min, $t_R = 7$ min) were chosen since they exhibited the largest feature sizes, see Fig. 3.11. Figure 3.11(d) displays a typical line profile across a single triangular feature for S_7. The direction of the ion beam with respect to the triangle is indicated in the figure. The sharp leading edge of the structure is observed to have a height of around 17 nm. The opposite slow trailing edge consists of the nanoripples, evidenced by the oscillatory behavior of the line profile. The areas of these triangular structures were measured using ImageJ [155]. The average area for the triangular structures for continuous sputtering is approximately 0.067 μm^2, while for the sputtering time interval it is 0.13 μm^2 and for the case of relaxation time interval it is 0.07 μm^2. The change in the area of the triangular features with varying conditions shows the potential of intermittent sputtering as a tool for changing the hierarchical feature sizes during surface nanopatterning. As introduced above, the origin of the triangular structures is the increased relevance of dispersive effects [described in Eq. (3.2) by the linear terms with coefficients Ω_x and Ω_y during ion bombardment at oblique incidence under suitable conditions [175], in our case a relatively low ion energy, $E = 500$ eV as opposed to $E = 900$ eV. The most recent predictive modeling of IBI [26, 164] identifies their physical origin in the ion-induced plastic flow that occurs in the top-most surface layer of the target, whereby residual stress accumulates due to collision cascades, leading to amorphization and eventual relaxation via viscous flow. The variation of the triangular areas in this study suggest a variation of the stress conditions as the time durations (t_S and t_R) of intermittent sputtering are changed.

Although the 1D PSD data shown in Fig. 3.10 for the intermittent sputtering conditions are affected by strong fluctuations, as already noted, further additional information can be extracted from them. Thus, the small-q power-law behavior, characteristic of each nonlinear regime, changes with the intermittent IBI approach. We perform a similar analysis to that employed for continuous sputtering at $E = 900$ eV, see the discussion of Fig. 3.4(b) above. Thus, for continuous sputtering at 500 eV we estimate a roughness exponent value $\alpha = 0.54 \pm 0.1$. This increases to $\alpha = 0.65 \pm 0.1$ for intermittent sputtering conditions. Finally, for conditions where the relaxation time is varied, it further increases to $\alpha = 0.77 \pm 0.1$. It is important to mention here, that the roughness exponents for the variable relaxation time case shows a monotonic increase when t_R changes from 5 to 15 mins. Hence, the behaviour exhibited by the roughness exponent also demonstrates a dependence on the conditions for intermittent sputtering. When the irradiation is continuous, the roughness exponent takes on a minimum value, thereby suggesting a surface which is rougher at the corresponding length scales. Indeed, the fractal dimension of the surface is given by $D_f = 3 - \alpha$ [14, 189], so that reducing the roughness exponent brings D_f closer to 3, which implies strong fluctuations in the height values of the 2D surface. Recall our discussion in Sec. 3.3.1 where we noted that $\alpha = 0$ corresponds to a purely Brownian surface. The use of intermittent sputtering increases the value of α, making D_f closer to 2, implying a smoother 2D surface [14, 189]. More specifically, upon varying the relaxation time interval α increases, thereby suggesting smoothening of the surface at the corresponding length scales without largely affecting the interface rms roughness.

3.3.5 Numerical simulations

The interpretations of the experimental results discussed in Secs. 3.3.1 through 3.3.4 above are based on well-known published experimental results for continuous sputtering experiments, as well as on their description *via* continuum models like Eq. (3.2). Actually, this precise evolution equation has been very recently shown to satisfactorily account for many of the properties observed experimentally for Si targets (continuously) irradiated with Ar^+ ions at energies in the same range that we are presently addressing, both in the linear and in the nonlinear stages of evolution. Hence, it is only natural to consider the predictions of this model for the intermittent sputtering conditions just addressed in Secs. 3.3.3, 3.3.4 above. This is what we proceed to do next.

Specifically, for computational feasibility the evolution equation addressed in Ref. [169] is a particular case of Eq. (3.2) with a still very large parameter space, which reads

$$\begin{aligned}\partial_t h = {} & -\nu_x\, \partial_x^2 h - \nu_y\, \partial_y^2 h + \Omega_x \partial_x^3 h + \Omega_y \partial_y^2 \partial_x h - \mathcal{K} \nabla^4 h \\ & + \lambda_x^{(1)}\, (\partial_x h)^2 + \lambda_y^{(1)}\, (\partial_y h)^2 + (\partial_x^2 + r\partial_y^2)[\mu_x (\partial_x h)^2 + \mu_y (\partial_y h)^2]. \end{aligned} \tag{3.6}$$

As demonstrated in Ref. [169], Eq. (3.6) under continuous sputtering conditions features a very rich morphological dynamics that includes ripple formation and evolution, triangular shapes, and defects in the surface morphology, as seen in our own continuous sputtering experiments at $E = 500$ eV, see Sec. 3.3.2. Hence, under continuous sputtering conditions we consider virtually the same parameter values as in that reference, specifically, $\nu_x = -\nu_y = \mathcal{K} = 1$, $\Omega_x = 2$, $\Omega_y = 0$, $\lambda_x^{(1)} = 0.3$, $\lambda_y^{(1)} = 0$, $\mu_x = -0.25$, and $\mu_y = r = 0$. Note, these parameter values are in arbitrary units and have been calibrated in such a way that in our case one unit of simulation time corresponds to approximately 0.1 min of continuous irradiation. Given this, the simulation times employed for the numerical results shown below have been finally divided by a factor of ten to ease comparison with the experimental results. At the present stage of the theoretical development, no quantitative estimates seem to be available in dimensional units for the equation parameters for the case in which triangular structures appear. Indeed, fully quantitative simulation of continuous equations like Eq. (3.6) is in general not possible for the present class of experiments and remains an open challenge in the field [6,164]. With respect to our numerical integration scheme for Eq. (3.6), similar to e.g. Ref. [26], we combine a fourth-order Runge-Kutta scheme for time with finite differences in space, using periodic boundary conditions on a two-dimensional substrate of $L \times L$ size with $L = 512$ (unless otherwise indicated), a lattice (time) step $\Delta x = 1$ ($\Delta t = 10^{-4}$), and a flat initial condition for $h(x, y)$, perturbed by zero-mean, Gaussian white noise with standard deviation equal to 0.5.

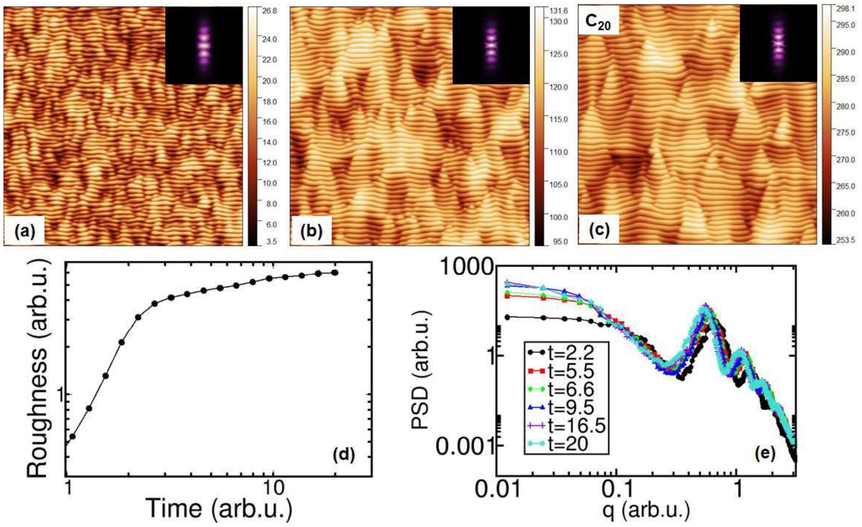

Figure 3.12: Surface morphologies obtained from numerical simulations of Eq. (3.6) under continuous sputtering conditions for increasing simulation times $t = 2.66$ (a), $t = 9.54$ (b), and $t = 20$ (c). The height scale (in arbitrary units) appears to the right of each image. Insets provide the corresponding FFT functions. Panel (d) shows the time evolution of the rms roughness while panel (e) displays the 1D PSD for times as given in the legend. All lines are guides to the eye and all units are arbitrary. Equation parameters are $\nu_x = -\nu_y = \mathcal{K} = 1$, $\Omega_x = 2$, $\Omega_y = 0$, $\lambda_x^{(1)} = 0.4$, $\lambda_y^{(1)} = 0$, $\mu_x = -0.25$, and $\mu_y = r = 0$ and the lateral system size is $L = 512$.

We follow a similar approach to that taken in the experiments and begin our numerical study by considering the continuous sputtering setup. Figure 3.12 shows results from numerical simulations of Eq. (3.6) under such conditions. Ripple formation is generally seen to be accompanied by the emergence of triangular structures, akin to the experiments discussed in Sec. 3.3.2. At small to intermediate scales, visual comparison between the simulated and experimental morphologies can actually be quite good, see an example in Fig. 3.13, in which the boxed portion of the experimental AFM top view of sample C_5 [panel (b) in Fig. 3.5 is compared to a portion of a surface obtained at time $t = 6.6$ from a numerical simulation of Eq. (3.6) using parameters as in Fig. 3.12.

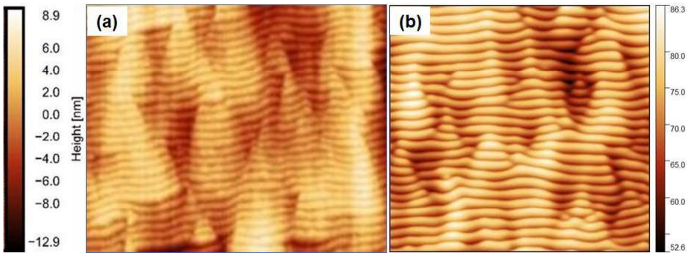

Figure 3.13: Comparison between the detail (a) that appears boxed in the AFM top view of the experimental C_5 sample displayed in Fig. 3.5(b) (see that figure for a scale bar) and a portion of a simulated surface morphology (b) obtained from a numerical simulation of Eq. (3.6) under continuous sputtering conditions for simulation time $t = 6.6$. The height scale for panel (b) is in arbitrary units. Equation parameters are as in Fig. 3.12, the lateral system size [approximately twice the side of (b)] is $L = 512$, and the initial condition is a random perturbation of a flat surface, see the text for more details.

Beyond visual comparison, Fig. 3.12 provides additional details on the surfaces simulated under continuous sputtering conditions. As expected, the rms roughness displays an exponential increase with time (linear regime) for $t \lesssim 2$, which is followed by a much slower increase for longer times, saturation being reached close to $t = 20$. Along this time evolution the ripple wavelength coarsens somewhat, as is clear from inspection of Figs. 3.12(a) through 3.12(c). By comparing the results of Figs. 3.12 with those of Figs. 3.5 and 3.9(a), the simulated topographies seem nevertheless somewhat more ordered than the experimental ones. This is probably unavoidable since: (i) stochastic height fluctuations are known to be experimentally relevant [11,24,164], while Eq. (3.6) is purely deterministic, and (ii) large-scale disorder is also quantitatively substantial for the experimental morphologies, but the numerical simulations are restricted to much smaller window sizes, which hinders agreement on the large-scale behavior. Indeed, both the 2D FFT and the 1D PSD functions are much more ordered (e.g. more satellite and sharper peaks occur) for the numerical images than for the experimental ones. Still, some degree of qualitative agreement is reached, specifically with respect to the fact that the PSD develops power-law behavior at small q with increasing irradiation time. However, the numerical value of the corresponding roughness exponent is strongly affected by our current computational limitations, in particular with respect to the value of L.

Next, we turn our attention to the intermittent sputtering experiments. To reproduce these numerically, we will consider the same equation parameters as in Fig. 3.12 for times during which the ion beam is on. For times during which the beam is off we simulate the same Eq. (3.6), but using the following (primed to ease visual identification) parameter values: $\nu'_x = -\nu'_y = \Omega'_x = \Omega'_y = \lambda'^{(1)}_x = \lambda'^{(1)}_y = 0$, $\mathcal{K}' = 0.1$, $\mu'_x = -0.025$, and $\mu'_y = r' = 0$. This choice is motivated by similar considerations to those that led to the analytical derivations [166, 167] of Eqs. (3.2) and (3.6), namely, the dominant contribution of sputtering for the terms with parameters ν'_i, Ω'_i, and $\lambda'^{(1)}_i$, and its non-negligible contribution to those with parameters $\mathcal{K}'$ and μ'_i, which remain non-zero in absence of the ion beam and implement linear and nonlinear (conserved) mechanisms [166,167].

Figure 3.14 displays results from numerical simulations of Eq. (3.6) under intermittent sputtering conditions for increasing sputtering time intervals t_S, for a fixed relaxation time $\mathrm{t}_R = 5$. Note, as in the experiments, $S_{20} = C_{20}$ which is shown in Fig. 3.12. Panels 3.14(a)-3.14(c) display sample surface morphologies for several values of t_S, which resemble (but for substantially smaller system sizes) the experimental ones shown in Fig. 3.6. An advantage of the simulations is the insight into the detailed dynamics of each S_n

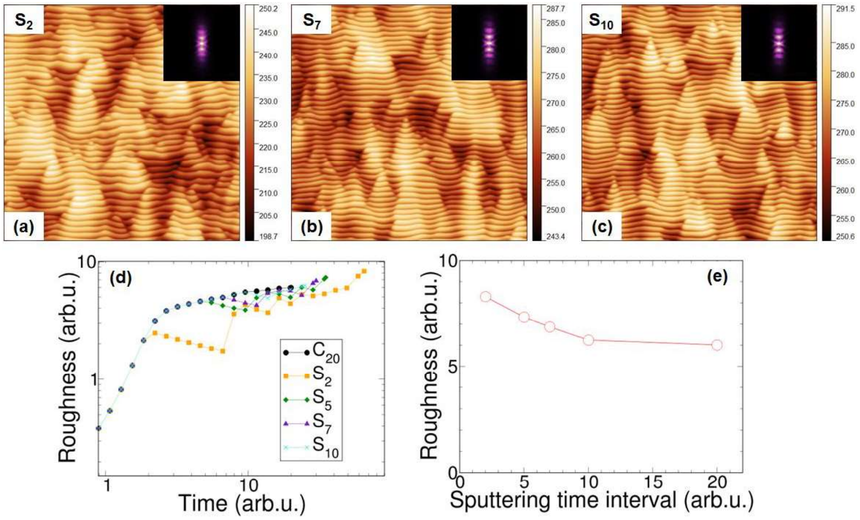

Figure 3.14: Sample surface morphologies obtained from numerical simulations of Eq. (3.6) under intermittent sputtering conditions for increasing sputtering time intervals $t_S = 2$ (a), $t_S = 7$ (b), and $t_S = 10$ (c) for a fixed relaxation time $t_R = 5$. The height scale (in arbitrary units) appears to the right of each image. Insets provide the corresponding FFT functions. Panel (d) shows the time evolution of the rms roughness for all the sputtering time intervals studied as detailed in the legend, while panel (d) displays the final roughness reached in each case, as a function of the sputtering time interval. All lines are guides to the eye and all units are arbitrary. Equation parameters are: during sputtering intervals, $\nu_x = -\nu_y = \mathcal{K} = 1$, $\Omega_x = 2$, $\Omega_y = 0$, $\lambda_x^{(1)} = 0.4$, $\lambda_y^{(1)} = 0$, $\mu_x = -0.25$, and $\mu_y = r = 0$; during relaxation intervals, $\nu'_x = -\nu'_y = \Omega'_x = \Omega'_y = \lambda_x'^{(1)} = \lambda_y'^{(1)} = 0$, $\mathcal{K}' = 0.1$, $\mu'_x = -0.025$, and $\mu'_y = r' = 0$. The lateral system size is $L = 512$.

system, provided by Fig. 3.14(d). This panel shows the full time evolution of each case, an information which would be exceedingly costly to retrieve experimentally. From this panel [2] it is clear that, for each value of the sputtering time interval, the roughness tries to follow the behavior obtained for continuous sputtering (C_{20} data, black bullets and line). The relaxation periods interrupt such a behavior leading to an expected decrease in the roughness, after which the roughness tries to catch up, and a similar alternation takes place a different number of times depending on the value of t_S. The system ends up with a final roughness that depends on t_S as shown in Fig. 3.14(e), which is to be compared with Fig. 3.9(b). The overall decreasing trend of the roughness with increasing t_S seems to be well reproduced by the simulations, although admittedly this is not the case with the the local minimum of the experimental roughness at $t_S = 7$ min.

---

[2] Note that Fig. 3.14(d) is a doubly logarithmic plot.

In the case of intermittent sputtering with a varying relaxation interval t_R for a fixed sputtering interval $t_S = 5$, numerically addressed in Fig. 3.15, the experimental behavior of the total rms roughness with t_R seen in Fig. 3.9(c) does seem to be better reproduced, see Fig. 3.15(e). Indeed, the numerical results show a local maximum before monotonically increasing for larger t_R, akin to the experimental results. Further, the surface morphologies in panels 3.15(a)-(c) again resemble their experimental counterparts from Fig. 3.8 at small to intermediate scales. And again 3.15(d) provides the dynamics of the

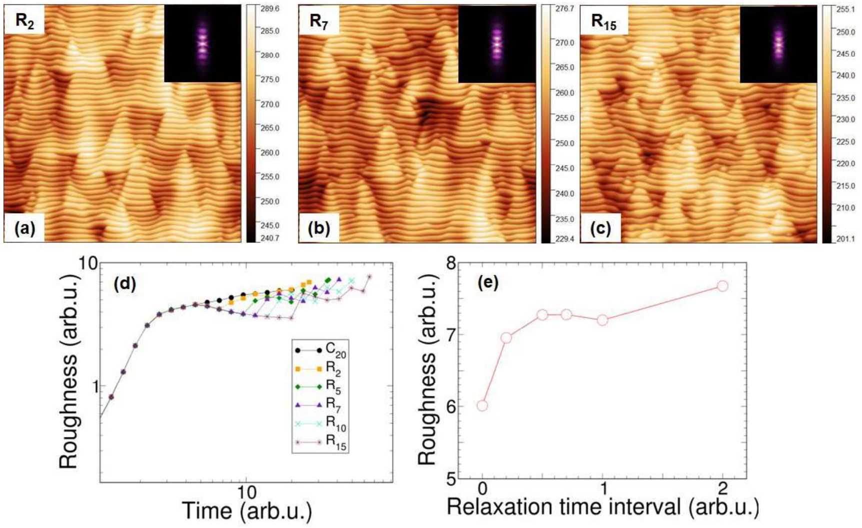

Figure 3.15: Sample surface morphologies obtained from numerical simulations of Eq. (3.6) under intermittent sputtering conditions for increasing relaxation time intervals $t_R = 2$ (a), $t_R = 7$ (b), and $t_R = 15$ (c), for a fixed sputtering time $t_S = 5$. The height scale (in arbitrary units) appears to the right of each image. Insets provide the corresponding FFT functions. Panel (d) shows the time evolution of the rms roughness for all the sputtering time intervals studied, as detailed in the legend (recall $C_{20} = R_0$), while panel (e) displays the final roughness reached in each case, as a function of the relaxation time interval. All lines are guides to the eye and all units are arbitrary. Equation parameters and lateral system size L are as in Fig. 3.14.

rms roughness in full detail for each fixed value of the relaxation time interval t_R. An analogous behavior to that discussed for Fig. 3.14(d) can be seen, with quantitative differences being due to the different combinations and values for the sputtering and relaxation time intervals.

Overall, we consider that the agreement between the simulations of Eq. (3.6) and the present experimental results for continuous and intermittent sputtering is fair and legitimates the use of the continuum model as a theoretical framework to understand the actual physical process that is taking place. Admittedly, the comparison leaves still room for widening and improvement, largely due to present computational limitations. These have required in our case to confine the simulations to relatively modest system sizes and to the neglect of time-dependent noise, conditioning the comparison with the large-scale properties of the experimental morphologies. Thus, the value of the roughness exponent or, e.g. large-scale rotated ripple structures as seen in the experiments, all remain to be systematically accounted for. Quantitatively, it would naturally be desirable to implement simulations that employ fully-dimensional parameter values, for which there is a dire scarcity of precise experimental estimates. This becomes particularly relevant for detailed comparison to intermittent sputtering experiments, where different physical processes like sputtering and relaxation contribute heterogeneously to a fixed number of (in some cases common) terms in the evolution equation for the surface height. In view of the huge parameter space that needs to be explored, this parameter estimation —together with the implementation of the correct space correlations in the initial condition— seems a worthy topic for future, perhaps machine-learning inspired [190], computational approaches.

3.4 Conclusions

In summary, we have shown that intermittent sputtering can influence ordering of ripples on hierarchical surface morphologies. Taking a reference case of Si surfaces sputtered at 900 eV, which feature the formation of relatively simple disordered ripple morphologies, we have addressed lower energy (500 eV) conditions for which individual ripples are more perfect, at the expense of formation of additional triangular structures. In order to further improve ripple ordering, an intermittent sputtering approach was followed. This had a crucial effect on the resulting surface morphology of Si substrates. The samples were subjected to low energy Ar^+ ions at oblique incidence for varied fluences. Intermittent sputtering was achieved by varying the time interval of sputtering or the time interval between two consecutive sputtering events. The wavelength of the ripples varies from 35 to 45 nm for the conditions studied. For the continuous sputtering case, the ripples have the best ordering after a sputter time as low as 5 min. For intermittent sputtering, well-ordered ripples are achieved for intermediate sputtering or relaxation time durations. Estimations from AFM images indicate that for an identical total sputtering duration of 20 min, medium intermittent sputtering intervals also give the largest and best ordered triangular structures. At larger length scales, all the surfaces produced show non-negligible height fluctuations that induce well-defined values for the roughness exponent. These values clearly indicate the occurrence of smoothening at correspondingly larger length scales when the ion beam remains off for longer durations, i.e., for higher relaxation time intervals. Moreover, under these conditions, the space correlations of the surface morphologies saturate at smaller scales than in the case of continuous sputtering. Our results can be rationalized in terms of known properties of the nonlinear regime of evolution for surfaces that become amorphous under IBI. Under continuous sputtering conditions, many of the observed properties (ripple orientation and amplitude saturation, wavelength coarsening, large-scale disorder, and triangular structures) agree qualitatively with predictions of the nonlinear Eq. (3.2) and, even more specifically, Eq. (3.6). In turn, the intermittent IBI experiments show how the system responds to periodic changes in irradiation conditions, which lend themselves (especially with respect to their morphological at short to intermediate distances) to fair modeling via numerical simulations of Eq. (3.6), while their more detailed defect and large-scale behavior remain challenling to simulations. Comparison with these theoretical models indicates that the observed effects are generally dominated by transport processes that originate in ion bombardment, with the induced defect structure seeming to still relax for short time scales even after the beam has been switched off. This study demonstrates the potential of intermittent sputtering for tuning the surface evolution of ion-beam nanostructured surfaces.

Chapter 4

Abrupt pattern transitions in argon ion bombarded swinging Si substrates

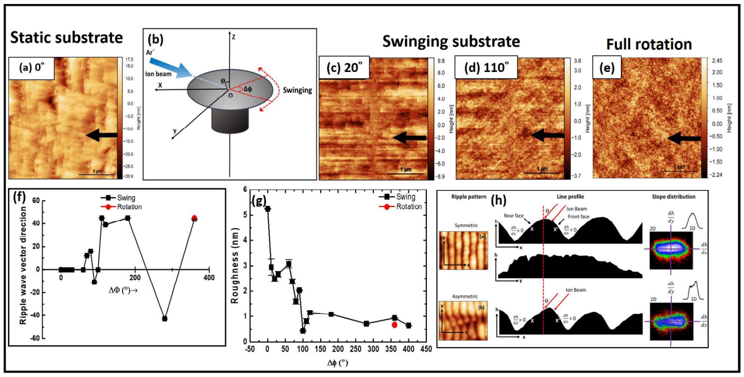

4.1 Introduction

Ion beam irradiation (IBI) has proven itself to be a versatile method to yield nanoscale patterns on solid surfaces by energetic ion collision [160]. The shape and size of these periodic height modulations (or nanopatterns) on solid surfaces can be controlled by suitable choice of physical parameters such as incidence ion energy, incident ion angle, ion flux, fluence (irradiation time), etc. [6, 77, 83, 87]. The underlying mechanism leading to pattern formation owes its origin to the basic model given by Bradley and Harper [10]. Essentially, it is an outcome of surface instability due to curvature dependent sputtering and a surface diffusive smoothening mechanism which reduces surface tension of the irradiated surface and is best represented by the equation

$$\partial_t h = -\nu_x \partial_x^2 h - \nu_y \partial_y^2 h - B\nabla^4 h \tag{4.1}$$

Here, ν_x and ν_y are incidence angle dependent effective surface tension coefficients. B quantifies the relaxation rate due to the surface diffusion. The model successfully predicted that for an ion incidence angle less (greater) than a critical angle θ_c with respect to the surface normal, the ripple wave vector is parallel (perpendicular) to the projection of the ion beam. However, this model cannot explain ripple orientations in directions different from the x and y axes. It also predicts an exponential increase in surface roughness that does not tally with experimental findings. The non-linear variant of the above equation used to explain ion-induced non-linear effects can qualitatively explain oblique ripple orientations [191] and is given by

$$\partial_t h = \sum_{i=x,y} \left[-\nu_i\, \partial_i^2 h + \Omega_i \partial_i^2 \partial_x h + \lambda_i^{(1)} \left(\partial_i h\right)^2 \right] + \sum_{i,j=x,y} \left[-\mathcal{K}_{ij} \partial_i^2 \partial_j^2 h - \lambda_{ij}^{(2)}\, \partial_i^2 (\partial_j h)^2 \right]. \tag{4.2}$$

Here, Ω_i denotes the x and y dependent coefficient of dispersive terms that contributes to the Fourier mode velocity in an anisotropic way, λ_i denotes non-linear effects owing to the non-conservative surface mass redistribution, $\mathcal{K}_{ij}$ signifies ion-induced diffusion and λ_{ij} denotes surface-transport-related nonlinearities that preserve the total amount of material.

Ion beam patterning has been traditionally done at fixed angles of oblique or normal incidence, thereby creating nanopatterns of ripples and dots, respectively [99, 124, 173, 178, 185, 192]. Rotating the sample about its surface normal keeping the incidence angle fixed leads to additional effects not envisaged for fixed sample configurations. Zalar et al. demonstrated that following such a procedure increases the resolution in the case of depth profile studies [117]. Bradley et al. showed theoretically that the rate at which the surface roughens or smoothens during sample rotation and the characteristic length scale of the nanopatterns formed are dependent on the period of rotation [193]. Som and co-workers suggested that the surface roughness decreases for large rotation speeds when Si is bombarded with Ar^+ ions. Moreover, the lateral size and height of the mounds scale progressively with fluence [119]. A study by Frost et al. on azimuthally rotating InP surfaces yielded hexagonally ordered nanodots at glancing incidence [121].

On the other hand, researchers have also attempted unconventional methods, mostly aimed towards defect minimization of the nanostructures or for creating nanopatterns having other symmetries. Experiments on Au with two perpendicularly placed Ar^+ ion beams at the azimuth done by Kim *et al.* showed that square-symmetric patterns of nanodots are achievable in the erosive regime [137]. Another experiment based on sequential ion sputtering by the same group demonstrated that nanobeads can be formed using the technique [138]. Studies by the same group also prove that patterning a pre-rippled surface at azimuthally orthogonal directions leads to enhanced non-linear effects (e.g., redeposition) as compared to an initially flat surface [139]. An experiment on Si using Ar^+ ions by Keller and Frost further demonstrated that defect densities can be reduced by as large as 40% by a suitable choice of sequential ion beam sputtering [173]. A recent work by Kim et al. explored nanopattern formation on graphite substrates by azimuthally swinging the substrates during ion beam sputtering [141]. Their study reported that with the swinging of substrate, composite patterns (wall-like structures) were formed on graphite. These patterns were believed to have formed due to quasi-2D mass flow and shadowing effect, two competing mechanisms which rarely work simultaneously during pattern formation. However, the universality of the effects observed have not been proven on other types of material substrates. The types of patterns formed were to a large extent disordered in terms of their surface topographies and orientations. Moreover, the amorphization process of the grain structures for graphite in the event of ion bombardment is less understood, thereby leading to an incomplete understanding of the phenomenon. It is thus evident from the above studies that several groups are resorting to unconventional methods of ion patterning of surfaces, which invokes new phenomena not achievable using a single fixed beam configuration. In spite of all these efforts, a comprehensive understanding of the physical origins leading to well-ordered patterns of varied geometries and orientations for a particular ion-target combination still remains elusive.

Keeping the above in mind, in this work we have investigated the evolution of nanostructures and their unconventional characteristics on an azimuthally swinging Si surface for different azimuthal angles and rotation speeds. We first looked at a surface under static conditions and then compared it with a rotating surface at varying fluences. The disordered morphology of the rotating samples showed drastic differences with the static one with respect to the ripple formation characteristics. Next, we studied an azimuthally swinging Si surface at identical ion beam parameters but for different values of azimuth. Results show transitions from hierarchical to ripple morphology via an intermediate smoothened (devoid of any nanostructure) surface. Abrupt changes of about 90° in ripple orientations are also observed for specific azimuthal angles above 100°. Four different regimes based on pattern transitions can be identified within the angular variations studied. The drastic shifts in ripple morphologies and their orientations are believed to be an outcome of the linear versus non-linear effects of sputtering. These effects define the different regimes that we observe in our experiments. Finally, we study the structure formation under similar conditions as above, but for varying rotational speeds. Results indicate better ordering of nanoripples specifically at lower rotation speeds. 2D slope distribution analyses of the sample surfaces exhibit formation of asymmetric structures owing to near-surface 2D mass distributions and curvature-dependent sputtering events for this unconventional mode of ion beam patterning. Shadowing is found to play an important role in the present context. These results enrich our understanding of pattern formation for swinging geometries and pave a way for further applications with these alluring patterns by suitably exploiting the ion beam parameter space.

4.2 Experimental Techniques

Commercially available undoped polished Si(100) substrates were cut into pieces of 1×1 cm^2 area and cleaned ultrasonically in ethanol for 20 min. Subsequently, they were rinsed with DI (de-ionised) water and dried in air. The choice of Si was done considering the fact that the structures formed on such surfaces are better ordered and have been well studied, both theoretically and experimentally, for conventional beam parameter conditions. Hence, results obtained for unconventional situations like the present one would be easy to compare with. Ion beam irradiation (IBI) experiments were carried out at room temperature in a vacuum chamber fitted with a 4 cm broad beam Kaufman ion source. The vacuum inside the chamber had a base pressure of 2×10^{-7} Torr. Irradiations were done with 500 eV Ar$^+$ ions at an incidence angle of 67° with respect to the surface normal. Each sample was marked at the back with an arrow indicating the ion incidence direction. This helped to ensure placing the samples identically aligned while doing AFM measurements. The current density used was 13.3 mA/cm^2. The ion fluence was kept constant at a value of 7.5×10^{19} ions/cm^2 (i.e., sputtering time of 15 mins) for the majority of the experiments, unless otherwise stated. The sample temperature was found to reach $42° \pm 1°$C during irradiation experiments. To carry out swinging experiments, the sample holder along with the sample was azimuthally swung by an angle $\triangle\phi$ (i.e., $-\phi \rightarrow +\phi$) as shown in Fig. 4.1. Here, the sample rotates to-and-fro in an oscillatory fashion, in contrast to a rotating sample where it always rotates in a particular direction (either clockwise or anti-clockwise). An alternating current (a.c) servo motor controlled the azimuthal swinging angle and rotational speed (in revolutions per minute (RPM)) of the sample holder.

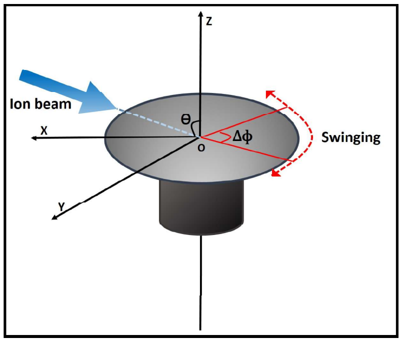

Figure 4.1: Schematic view of the swing geometry in azimuth (ϕ) during IBI. θ (= 67°) is the polar angle between the 500 eV Ar^+ beam (blue arrow) and the (stationary) surface normal. The sample azimuthally swings for an angle $\triangle\phi$ ($-\phi \rightarrow +\phi$) across the incidence ion beam direction.

Irradiation for a static sample was carried out using the conditions detailed above. For continuously rotating samples, irradiations were done for 5, 10, 20, 25 and 30 mins at the current density stated above with a constant rotating speed of 1 RPM (i.e., $6°/s$). For the swing experiments, samples were irradiated using identical conditions as stated above, but with varying angles of $\triangle\phi = 10°, 20°, 30°, 60°, 70°, 80°, 90°, 100°, 110°, 120°, 180°, 280°$and $360°$. A third set of experiments were performed at a fixed $\triangle\phi = 70°$ but with varying rotational speeds of 2, 4, 6, 8, 10, 12 and 16 RPMs. Experiments were repeated to check for reproducibility on several occasions. For all rotation/swing experiments, the rotation/swing and the ion beam were turned on simultaneously.

Post irradiation, the samples were characterized ex-situ using Atomic Force Microscopy (AFM) (MultiMode 8, Bruker, USA) in tapping mode. The radius of the cantilever used was 10 nm. AFM data was collected from multiple places from the central region of each sample. After obtaining the topographical images of the irradiated surfaces by AFM, quantitative information of the nanostructures were obtained from the acquired data using statistical surface parameters such as wavelength, root-mean-square (rms) roughness (standard deviation of the heights), 2D slope distribution, 2D FFT and power spectral density (PSD) etc. using Gwyddion (version 8.1) [154]. The 1D PSDs are estimated in the direction of the ripple wave vector as observed in the AFM images.

4.3 Results and discussions

4.3.1 Surface morphology evolution of Si surfaces rotating at 1 RPM

We first carried out experiments on rotating substrates and compared their morphology with a non-rotating one. This served as a reference for further swinging experiments.

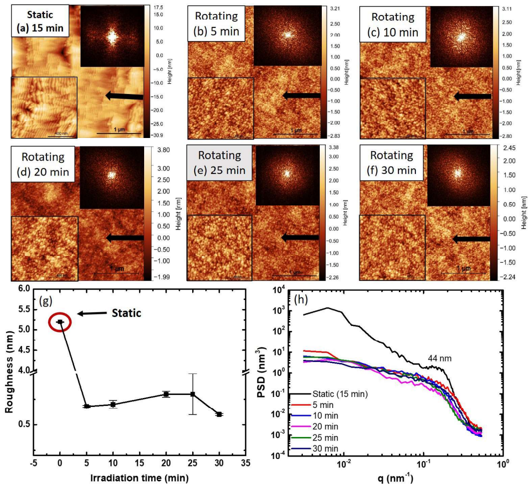
Static
(a) 15 min
Rotating
(b) 5 min
Rotating
(c) 10 min
Rotating
(d) 20 min
Rotating
(e) 25 min
Rotating
(f) 30 min
1 μm
Height (nm)
(g)
Static
Roughness (nm)
Irradiation time (min)
(h)
44 nm
PSD (nm^3)
q (nm^{-1})
Static (15 min)
5 min
10 min
20 min
25 min
30 min

Figure 4.2: 3×3 μm^2 AFM micrographs of 500 eV Ar$^+$ irradiated Si at 67°. (a) Without rotation with fluence of 7.5×10^{19} ions cm^{-2}, and for continuous rotation at fluence values of (b) 2.5×10^{19} ions cm^{-2}, (c) 5×10^{19} ions cm^{-2}, (d) 10×10^{19} ions cm^{-2}, (e) 1.2×10^{20} ions cm^{-2}, and (f) 1.5×10^{20} ions cm^{-2}, respectively. Black arrow indicates the initial direction of the ion beam prior to rotation. Top right insets: 2D FFTs of corresponding AFM images. Bottom left insets: Corresponding 1×1 μm^2 AFM images. (g) Plot showing rms roughness as a variation of irradiation time. (h) 1D PSD obtained from the AFM images for the irradiated samples.

Figure 4.2 shows 3×3 μm^2 AFM images of Si surfaces irradiated at 500 eV at an ion incident angle of 67° under static and continuously rotating conditions and corresponding

1×1 μm^2 AFM images provided in Fig. 4.3.

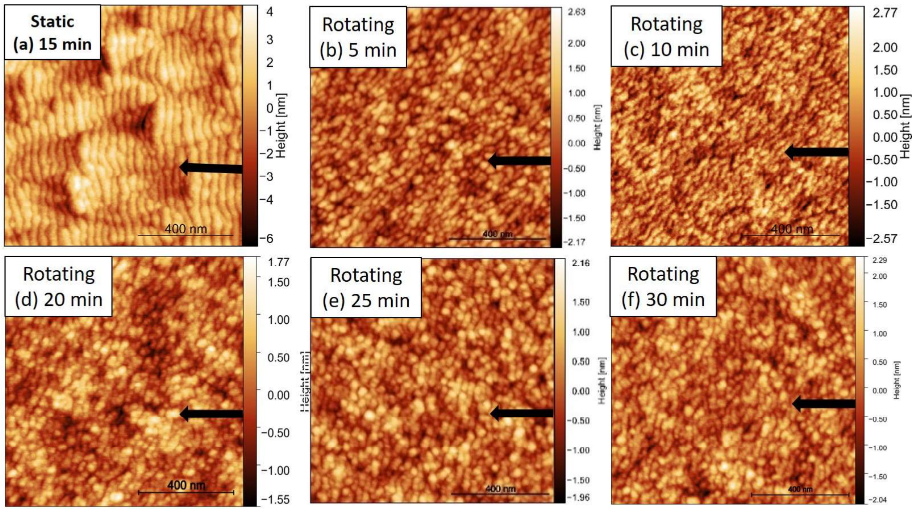

Figure 4.3: 1×1 μm^2 AFM micrographs of 500 eV Ar$^+$ irradiated Si at 67°. (a) Without rotation with fluence of 7.5×10^{19} ions cm^{-2}, and for continuous rotation at fluence values of (b) 2.5×10^{19} cm^{-2}, (c) 5×10^{19} cm^{-2}, (d) 10×10^{19} cm^{-2}, (e) 1.2×10^{20} cm^{-2}, and (f) 1.5×10^{20} cm^{-2}, respectively. Black arrow indicates the initial direction of the ion beam prior to rotation.

The static sample was irradiated for 15 mins while the rotating ones were irradiated for 5, 10, 20, 25 and 30 mins at a speed of 1 RPM as depicted in the figure. The black arrow indicates the initial direction of the incident ion beam on the Si surface. This is considered as the x-axis in all our subsequent discussions, unless stated otherwise. For a static sample, this is fixed for the entire period of sputtering. For a rotating or swinging sample, however, the beam is initially aligned in this direction (i.e., at $t = 0$). The top right corners in Fig. 4.2 show the 2D FFTs while the bottom left corners show 1×1 μm^2 scans corresponding to the AFM images. For the static sample, parallel-mode nanoripples are observed to form on the surface, which are fairly ordered as evident from the satellite peaks of the 2D FFT image (inset of Fig. 4.2(a)). The parallel-mode orientation of the ripples is also ascertained from this image. In addition to the ripples, the morphology shows superposed triangular structures which make the morphology a hierarchical one. This observation is commensurate with previous findings in the literature [144, 164, 169, 173, 175, 178, 194, 195]. It turns out that the sputtering yield is not only dependent on the second derivatives of surface heights h but also on their third derivatives $\partial_i^2 \partial_x h$ as discussed in Ref. [17]. Inclusion of this term in the equation of motion (EOM) makes the ripples asymmetric and the ripple propagation dispersive, meaning that the different surface propagating wave vectors (k) travel with different speeds. This dispersive effect can be induced by ion-induced plastic flow or viscous relaxation of ion-induced stresses in the near-surface region. The triangular structure formation at an oblique incidence of the ion beam, theoretically put forward by Bradley and co-workers [175], thus owes its origin to the dispersion terms leading to raised and depressed triangular regions traversed by parallel mode ripples. A highly ordered ripple is formed if both dispersion and transverse smoothening are sufficiently strong. The continuously rotating samples irradiated for different fluences (time durations) show marked distinctions from the static case. The morphology becomes extremely disordered with emergence of fragmented nanoscale structures which show a slight ordering exhibited by the elongated 2D FFT insets. Earlier studies [118, 119] have confirmed emergence of similar anisotropic topographies for substrates rotating at very low rotation speeds. This eventually gives way to mounded morphologies as the fluence increases. At higher rotation speeds of 1 RPM, mounded morphologies were obtained in contrast to the current observation. It is worth noting here that the current density in their case [119] was 21.4 μA/cm^{-2} which was more than 600 times lower than in the present case (13.3 mA/cm^{-2}). Thus, the two studies indicate that under continuous rotation at high enough fluences slightly anisotropic morphologies can be obtained. The surface roughness and 1D PSD of the irradiated samples are shown in the bottom panel of Fig. 4.2. For the static sample, the roughness and ripple wavelength are found to be about 5.25 nm and 44 nm, respectively. When the samples rotate, the roughness decreases and saturates to a value of around 0.6 nm. The absence of any characteristic peak in the PSD spectra for all the rotating samples corroborates to the fact that ripple-like structures are not present in the rotating samples.

An earlier study done by Frost and co-workers [121] on rotating InP surfaces using Ar^+ ions at 500 eV indicates the roughness to scale increasingly with fluence in accordance with early- or late-time regimes. They had observed mounded structures for these surfaces. Similar mounded morphology has also been observed for the case of Si at 0.08 and 1 RPMs [196]. This study also exhibited a saturation of surface roughness at higher fluences. It is to be noted that both these studies were performed at fluences of the order of $10^{15} - 10^{18}$ ions cm^{-2}. For the present case, the fluence lies between $2.5 \times 10^{19} - 15 \times 10^{19}$ ions/cm^2 corresponding to sputtering durations of $5 - 30$ mins at 500 eV. A recent work by Kim *et al.* using Ar on Si at 2 keV at a speed of 1.12 RPM showed almost no increase of roughness with fluence (1.44×10^{16} ions/cm^2 for their case). The saturation of surface roughness for the present case suggests that the irradiation conditions are in the non-linear (late-time) regime of sputtering. Moreover, the formation of predominantly disordered structures for all subsequent fluences bear testimony to this fact. The rotating surfaces are also devoid of triangular morphologies, which strongly suggest that dispersive terms (as discussed above) play a non-dominant role in the morphology evolution.

4.3.2 Surface morphology of irradiated Si surfaces swinging by different azimuthal angles at a speed of 1 RPM

Figure 4.4 shows 3×3 $\mu\mathrm{m}^2$ AFM images of Si surfaces irradiated with increasing values of the azimuthal angle interval ($\triangle\phi$) starting from $\triangle\phi = 0°$ to $\triangle\phi = 360°$. For easy reference and subsequent comparison, the Si surface irradiated under static conditions with beam parameters as described in Sec. 4.2 is shown. The black arrow in each image signifies the direction of incident ion beam on the Si surface about which the substrate symmetrically swings as shown in Fig.4.1. The top right corners in Fig. 4.4 show the 2D FFTs while the bottom left corners show 1×1 $\mu\mathrm{m}^2$ scans corresponding to the AFM images as shown in Fig. 4.5. The orientation of the ripples can be confirmed from the 2D FFT images for the

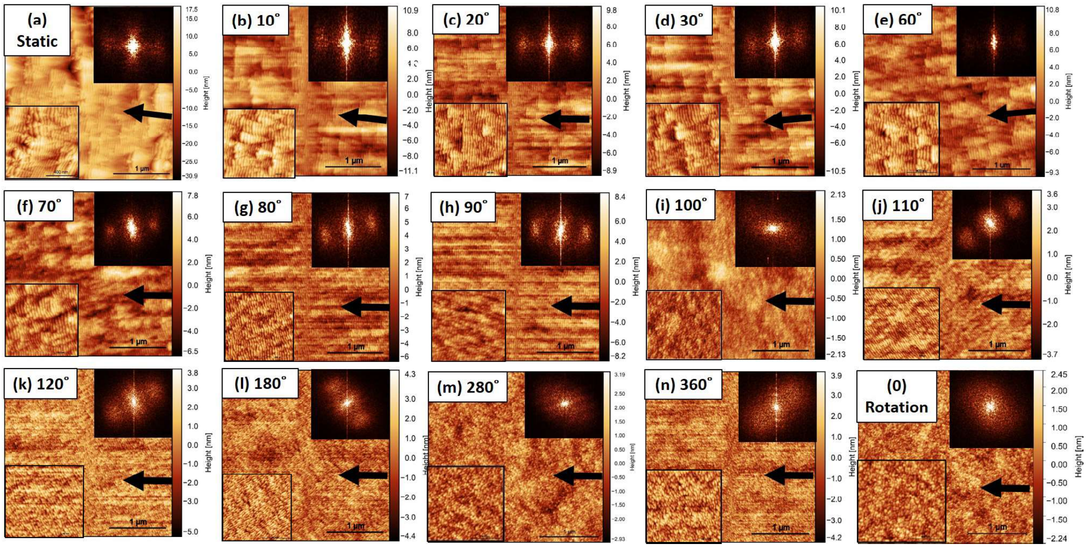

Figure 4.4: 3×3 μm^2 AFM micrographs of 500 eV Ar$^+$ irradiated Si at 67° for different values of swinging angle ($\triangle\phi$): (a) 0°, (b) 10°, (c) 20°, (d) 30°, (e) 60°, (f) 70°, (g) 80°, (h) 90°, (i) 100°, (j) 110°, (k) 120°, (l) 180°, (m) 280°, (n) 360°, and (o) continuous rotation, respectively. Black arrow indicates the initial direction of ion beam prior to rotation. Top right insets: 2D FFTs of corresponding AFM images. Bottom left insets: Corresponding 1×1 μm^2 AFM images.

respective irradiated surfaces. The hierarchical morphology obtained for the static sample case ($\triangle\phi = 0°$) has already been described above. Similar hierarchical morphologies are also observed for $\triangle\phi$ angles of $10°, 20°, 30°, 60°$ and $70°$ although with a diminishing indication of well-formed triangular structures. For the azimuthal swing angle of $\triangle\phi =$ 80°, the triangular morphology is completely absent. The 2D FFT images further suggest that the ripple wavevector is aligned with the starting direction of incident ion beam (x-axis as described above) on the Si surface about which the substrate symmetrically swings. Higher swings of azimuthal angles greater than 80° do not show any triangular morphology. Within the experimental conditions, the ripples almost disappear for $\triangle\phi =$ 90°. At an angle of 100°, a smooth surface is obtained, devoid of any ripples or triangular morphologies. Furthermore, with increasing swing angle of 110° and 120°, the ripples start to form, but these are oriented at 45° with respect to the x-axis. A drastic flip in

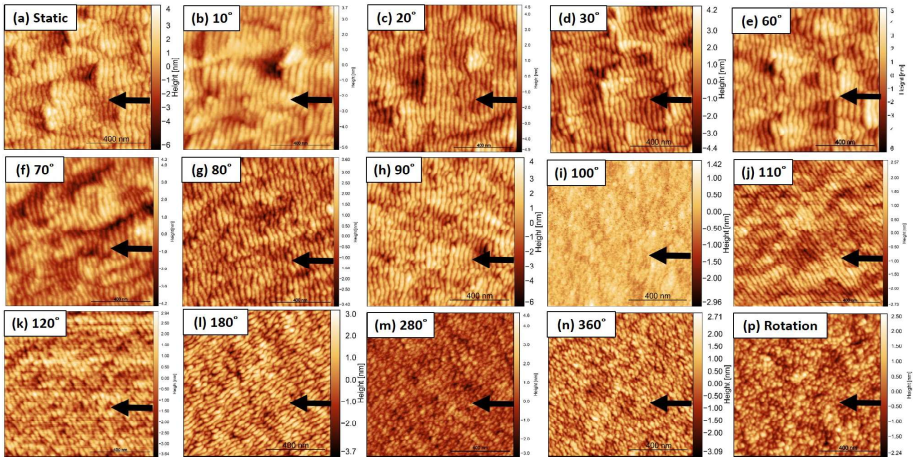

Figure 4.5: 1×1 μm^2 AFM micrographs of 500 eV Ar^+ irradiated Si at 67° for different values of swinging angle ($\Delta\phi$): (a) 0°, (b) 10°, (c) 20°, (d) 30°, (e) 60°, (f) 70°, (g) 80°, (h) 90°, (i) 100°, (j) 110°, (k) 120°, (l) 180°, (m) 280°, (n) 360°, and (o) continuous rotation, respectively. Black arrow indicates the initial direction of ion beam prior to rotation.

the ripple orientation by an angle of about $\pi/2$ is observed for a swing angle of 180°. The ripple orientation again flips by $\pi/2$ for a swing angle of 360°. Thus, at higher azimuthally swinging angles, small-scale patterns are observed which are not oriented in either x- or y-direction. These patterns are oriented approximately at 45° with reference to $+x$ and $-x$ axis. It is to be noted that the ripples formed beyond a swing angle of 100°, in general, shows less ordering as compared to the ripples formed at lower angles of swing (i.e. less than 100°). Thus, within the range of the azimuthal angles studied, a minimum of four regimes can be identified based on the morphological transitions observed. The first regime which shows a hierarchical morphology spans up to $\triangle\phi = 70°$. Beyond this, the second regime exists where only ripples are observed in the absence of triangular structures. The third regime is identified by a flat morphology at $\triangle\phi = 100°$. Beyond this azimuthal angle, there is an onset of the fourth regime which continues till $\triangle\phi = 360°$. During this regime, the irradiated surface is marked by disordered ripple structures. It is to be noted here that the transitions in the ripple orientations have not been taken into consideration during the demarcation of the above regimes.

The evolution of these surface topographies are quantified by evaluating the root-mean-square (rms) roughness, wavelength, and 1D power spectral density (PSD) from the corresponding AFM images (Figure 4.6). The rms roughness for the static irradiated sample is about 3.0 nm as evident from Fig. 4.6(a). It is observed that the roughness decreases drastically as the swing angle increases. The surface has a minimum roughness of about 0.4 nm at a swing angle of 100° where neither ripples nor triangles are observed. As the swing angle is further increased, the roughness increases slightly, essentially saturating to a value of about 0.8 nm. In contrast, the rotating sample has a lower roughness (about 0.7 nm) in comparison to the swinging ones as evident from Fig. 4.6(a).

The ripple wavelengths were estimated from the peaks of the 1D PSD spectra obtained along the ripple wave vectors from the respective AFM images. The variation of the wavelengths with respect to the swing angle is shown in Fig. 4.6(b). It is observed that the wavelength is the highest for the static case having a value of about 42.6 nm. With increase in swing angle, this gradually decreases (with some fluctuations) to about 35 nm for $\triangle\phi = 90°$. The wavelength finally saturates to around 28 nm for higher angles of swing. Thus, a sharp drop in ripple wavelength is observed beyond $\triangle\phi = 100°$ at which we observe neither ripples nor triangles (indicated by vertical strips in the figure). The ripple wavelength obtained for continuous rotations of the sample yields a value of 26 nm.

Figure 4.6(c) shows the 1D PSD spectra obtained along the direction of the ripple wave vector for the AFM images shown in Fig. 4.4. A sharp peak in the PSD spectra usually corresponds to better ripple ordering with fewer defects. The structure factor calculated in the PSD defined as $S(q,t)$ scales as $S(q,t) \sim q^{-m} \sim q^{-(2\alpha+1)}$ under the Family-Vicsek formalism where α is the roughness exponent [185] and $q = 2\pi/l$. For simplicity, Fig. 4.7 shows a similar graph with x-axis as $q = 1/l$. The PSD spectra is divided into two regimes such as low-q and large-q regime as shown in Fig. 4.6(c). At a low-q value, a flat plateau extends out to a critical wave number $\mathrm{q}_c = \frac{2\pi}{\lambda_c}$, after which the PSD spectra decreases linearly with a negative slope at a large-q value. The slope m of the curves for low-q

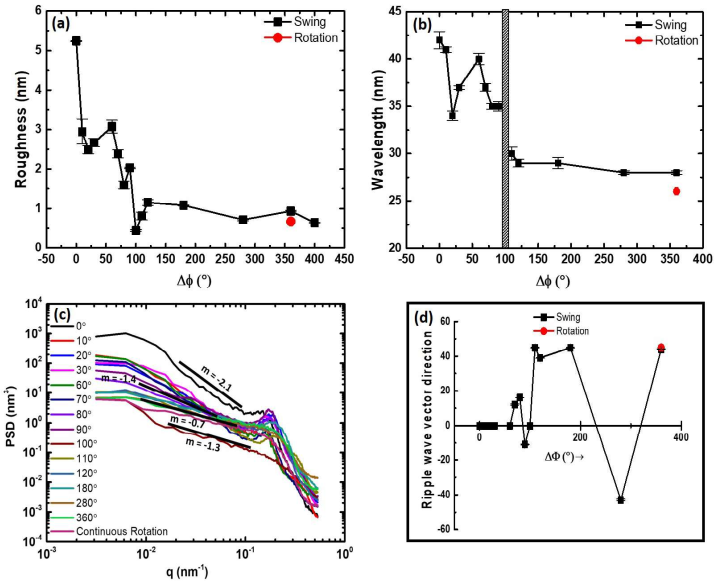

Figure 4.6: Plots showing evolution of (a) rms roughness, (b) wavelength, (c) 1D PSD and (d) ripple wave vector direction for different values of swinging angles such as: $\triangle\phi =$ 0°, 10°, 20°, 30°, 60°, 70°, 80°, 90°, 100°, 110°, 120°, 180°, 280°, 360°, and continuous rotation.

values has been calculated from the log-log plots of

Fig. 4.6(c). The corresponding roughness exponents have been subsequently calculated using the values of m. It is observed that the PSD spectra fall into four different categories in terms of their m values. For 0° to 70°, $m = 2.1$ and $\alpha = 0.55$; for 80° to 90°, $m = 1.4$ and $\alpha = 0.2$; for 100°, $m = 1.3$ and $\alpha = 0.15$ for 110° to 360°, $m = 0.7$ and $\alpha = -0.15$. Thus, the surface is rougher at large length scales for lower azimuthal angles below 70°. Beyond this azimuth, the surface displays a smoother morphology at these length scales.

Fig. 4.8 depicts a comparison of 1D PSD plots for an ordered and disordered surface. The ion beam tends to hit the ripple walls more obliquely or even the other side of the ripple walls as we go to higher azimuthal angles. Finally, Fig. 4.6(d) shows the variation of the ripple wave vector direction with the azimuthal swing angle.

The different regimes observed as discussed above are surmised to have originated

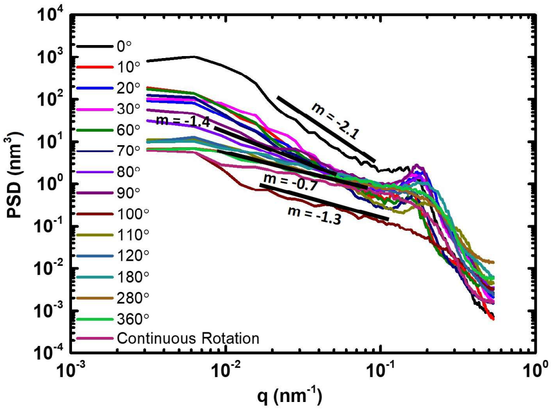

Figure 4.7: Log-log plot of 1D PSD versus spatial frequency q (extracted from 1D cuts of AFM images) along the ion beam direction (x-axis). Here q has been taken equal to 1/l for simplicity

from a chain of events owing to different ion-induced effects. A sharp morphological transition is observed at 100° beyond which hierarchical surfaces and ripples are observed on either sides. As discussed above, the emergence of triangular morphology is necessitated by the dispersion terms in the surface evolution. Non-existence of the hierarchical morphology thus indicates weakness of these dispersion terms as compared to the transverse smoothening ones. Results imply that as the azimuthal swinging angle is increased, the effect of incidence ion beam angle on dispersion becomes weak and the smoothening effect becomes stronger as compared to the dispersion effect. At a critical swinging angle of $\triangle\phi$=100°, the smoothening effect overcomes the dispersion effect, thereby rendering the surface a flat featureless morphology. This morphological character bears testimony to the fact that all coefficients of the growth equation have attained stability under such conditions. In a couple of earlier works reported by Madi et al. [70, 102], they identified stable flat regions between two differently oriented nanostructured regions in the control parameter space of E and θ which was considered to take place via a bifurcation between the pattern forming and non-pattern forming regions. In the present context, the

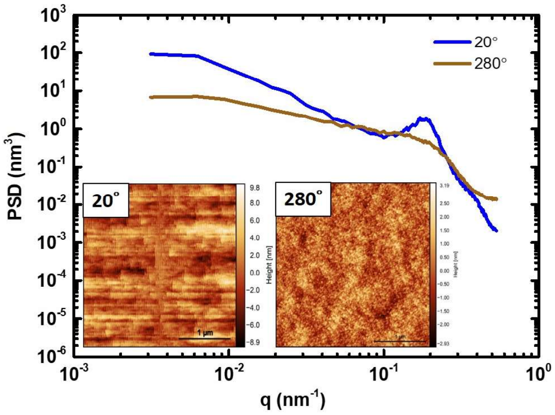

Figure 4.8: Log-log plot of 1D PSD versus spatial frequency q (extracted from 1D cuts of AFM images) along the ion beam direction (x-axis) for an ordered and a disordered surface. Inset shows the corresponding AFM images.

control parameter happens to be the azimuthal swing angle (ϕ). The above studies are indicative of the fact that such a bifurcation point may exist in the ϕ parameter space as well. However, establishing this fact necessarily requires an extensive study as done by the previous ones. Above this critical azimuthal angle, the dispersion term diminishes even further, making the surface devoid of any triangular structures. The surface eventually enters the non-linear regime, as confirmed by the saturation of the rms roughness. The change in orientation of the ripples at 110°, 180° and 360° is brought about by the phase difference between the ripple wave vector and the direction of the ion beam owing to the swinging of the substrate about the initial position of the substrate, which can leave the system in an unstable mode. In order to incorporate swinging effects the surface evolution equation should depend temporally in a triangular ramp fashion. According to a study [191], Eqn. 4.1 predicts existence of cancellation modes that are height Fourier modes with wave vector in the unstable band for which the non-linear terms cancel each other. Such a cancellation can leave the system non-linearly unstable and induce ripple formation. The orientation of ripples, however, would be in an oblique direction, i.e., not

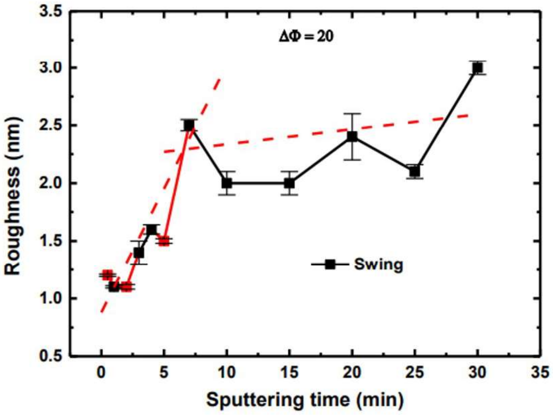

Figure 4.9: Plot showing evolution of rms roughness of 500 eV Ar^+ irradiated at $\theta = 67°$ for different sputtering times at $\Delta\phi = 20°$. The dashed red lines are guides to the eye showing the behaviour of increase of roughness with sputtering time.

parallel to both $x-$ or $y-$ directions. Further, the surface roughness does not saturate in such a case. For the present situation, however, the surface roughness almost goes towards saturation although not completely as indicated by Fig. 4.9. Therefore, there is a very weak possibility that cancellation mode plays a role in this context. Eventually, with more elapsed time, this effect may die out. Hence, the role of swinging is considered to be of primary importance for the observed effects.

4.3.3 Effect of swing speed on surface morphology of irradiated Si surfaces

Consequent to investigating the effect of azimuthal angle on the surface topography of the irradiated Si surfaces, the effect of swing speed was also studied for the same. Figure 4.10 shows 3×3 μm^2 AFM images of Si surfaces irradiated with 500 eV at a fixed azimuthal angle interval of $\triangle\phi = 70°$ for varying swing speeds. The black arrow indicates the initial direction of the incident ion beam, as stated above. The top right corners in Fig. 4.10 show the 2D FFTs and corresponding 1×1 μm^2 scans shows in Fig. 4.11. The orientation

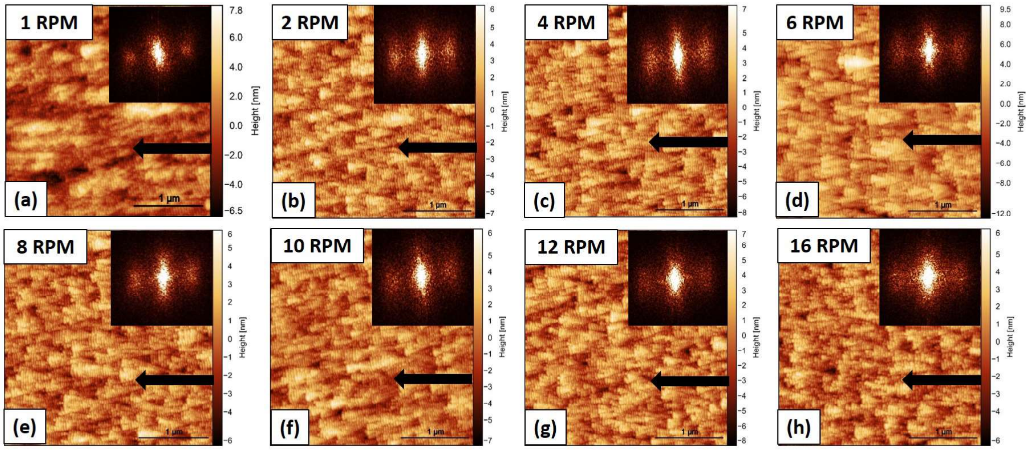

Figure 4.10: 3×3 μm^2 AFM micrographs of 500 eV Ar$^+$ irradiated at $\theta = 67°$ for different rotational speeds (RPM). (a) 1 RPM, (b) 2 RPM, (c) 4 RPM, (d) 6 RPM, (e) 8 RPM, (f) 10 RPM, (g) 12 RPM, and (h) 16 RPM, respectively. Black arrow indicates the initial direction of ion beam prior to rotation. Top right insets: 2D FFTs of corresponding AFM images.

of the ripples can be confirmed from the 2D FFT images for the respective irradiated surfaces. Hierarchical morphologies consisting of nanoripples and triangles are found for all swing speeds on the irradiated surfaces. The triangular structures are more apparent for speeds of 2 RPM and above. At 1 RPM, they are less ordered and are difficult to notice from AFM images. The 2D FFT images indicate that the ripple wave vectors for all the swing speeds are aligned in similar direction. The satellite peaks of the 2D FFTs also indicate the order of the ripples formed. It is seen that the ripples are best formed at the lowest speed of 1 RPM as confirmed from its narrow satellite peak. As the speed increases, the ripples gradually lose their order and eventually shows the least order for 16 RPM within the present experimental domain. The blurriness of the satellite peaks of the 2D FFT (Fig. 4.10) confirm this fact. The surface morphologies were better compared and quantified using surface topographical parameters of 1D PSD, surface roughness and ripple wavelength (Figure 4.12). The PSD spectra in Fig. 4.12(a) shows that the peak shifts towards smaller q-values as the swing speed increases. The PSD corresponding to

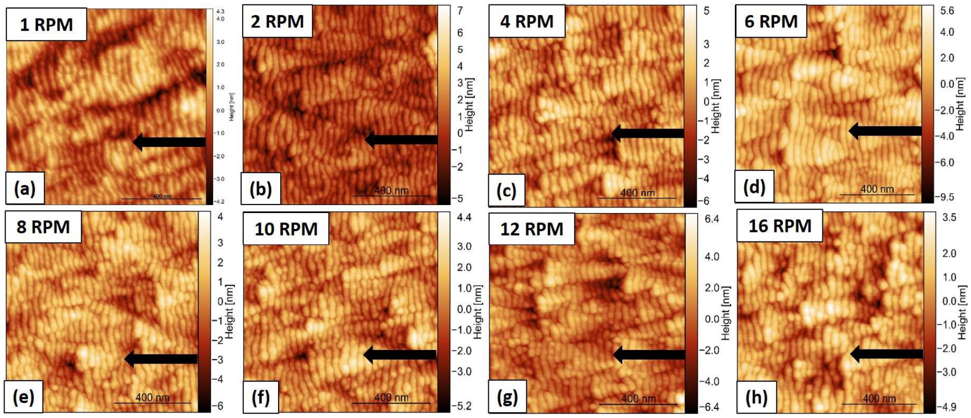

Figure 4.11: 1×1 μm^2 AFM micrographs of 500 eV Ar$^+$ irradiated Si at 67° for different rotational speeds (RPM). (a) 1 RPM, (b) 2 RPM, (c) 4 RPM, (d) 6 RPM, (e) 8 RPM, (f) 10 RPM, (g) 12 RPM, and (h) 16 RPM, respectively. Black arrow indicates the initial direction of ion beam prior to rotation.

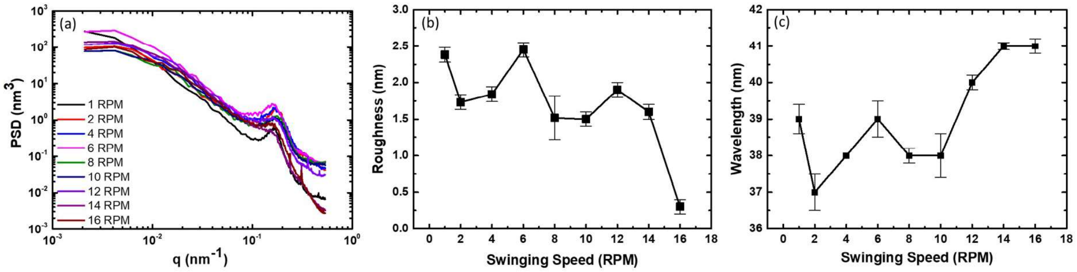

Figure 4.12: Plots showing evolution of (a) 1D PSD, (b) rms roughness, and (c) wavelength for different rotational speeds of 1, 2, 4, 6, 8, 10, 12, 14, and 16 RPMs.

a speed of 1 RPM has the sharpest peak thereby asserting that ripples formed under this condition has the best ordering. The rms roughness plot shows that the roughness of the irradiated surface remains within 1.5 to 2.4 nm up to a speed of 14 RPM (AFM image not shown for brevity). This finally drops to 0.3 nm at 16 RPM. Upon increasing the swing speed, the wavelength of the ripples increases from 37 nm at 2 RPM to a value of 41 nm at 16 RPM. The fluctuations observed in the rms roughness and wavelength values can be attributed to the highly disordered ripples obtained with increase in swinging speeds. It is important to comment here that in contrast to complete rotation at higher speeds where the odd derivatives in the surface evolution equation (Eqn. 4.1) cancel out [197], all the terms would survive under a swing configuration, thereby making the scenario a non-trivial one. In order to investigate pattern formation at fractional speeds, experiments were carried out at 0.3 and 0.6 RPMs. Figure 4.13 shows 3 × 3 μm^2 AFM images and the corresponding PSDs of the resulting surfaces. The black arrow indicates direction as discussed above. It is clearly observed from the AFM images that ordered nanoripples are formed even at fractional speeds. Ripples are seen to be formed better at 0.6 RPM compared to 0.3 RPM as evident from the less spread of satellite peaks of the 2D FFT inset images. This is further corroborated from the broad PSD peak of 0.3 RPM in comparison to that at 0.6 RPM as found from the 1D PSD plots (Fig. 4.13) comparing 0.3, 0.6 and 1 RPMs. Out of the above, ripples are probably better formed at 1 RPM as evident from its sharp 1D PSD peak. However, the rms roughness increases as one goes to higher speeds.

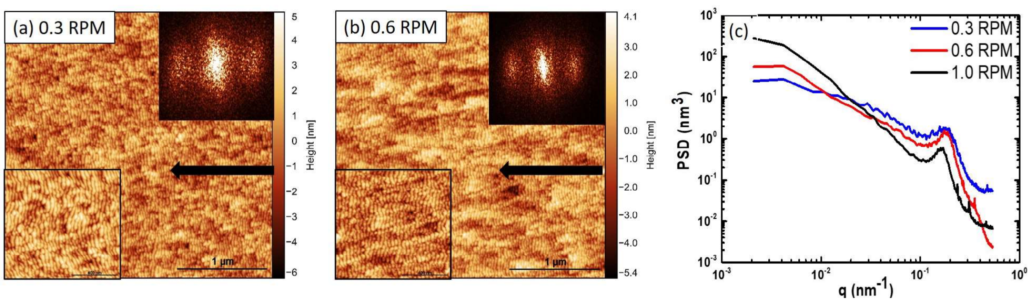

Figure 4.13: 3 × 3 μm^2 AFM micrographs of 500 eV Ar^+ irradiated Si at $\theta = 67°$ for fractional rotational speeds of (a) 0.3 RPM and (b) 0.6 RPM. Black arrow indicates the initial direction of ion beam prior to rotation. Top right insets: 2D FFTs of corresponding AFM images. Bottom left insets: Corresponding 1 × 1 μm^2 AFM images. (c) 1D PSD plots for 0.3, 0.6 and 1 RPM obtained from AFM.

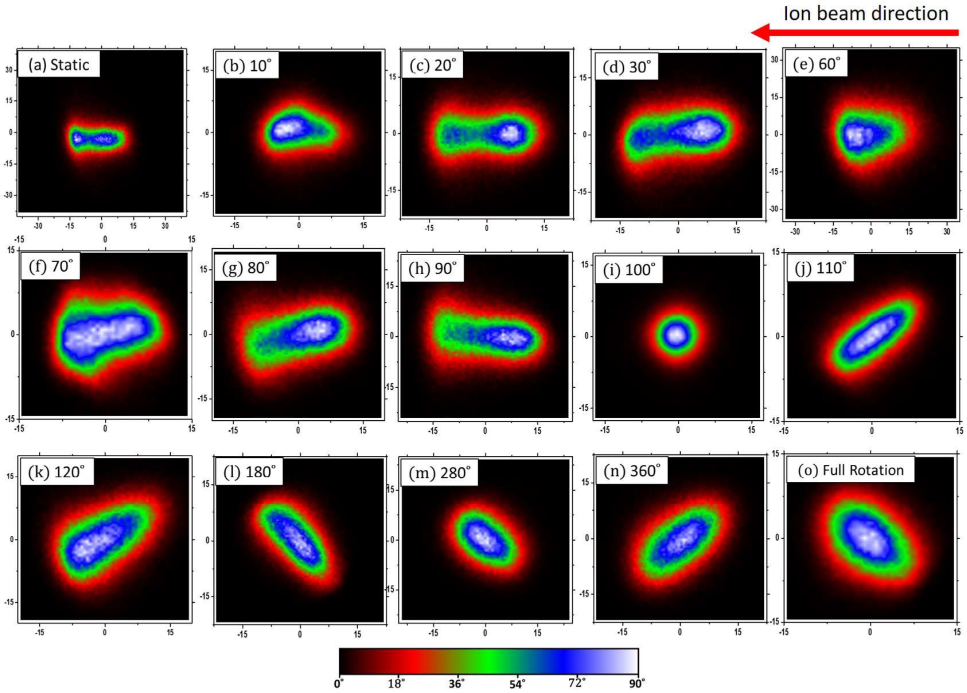

Figure 4.14: 2D slope distributions of irradiated surfaces for different azimuthal angles. The horizontal axis is along ion beam direction and vertical axis is perpendicular to the ion beam direction. The red arrow indicates the initial direction of the ion beam prior to swinging.

4.3.4 Effect on local slope distribution

Figure 4.14 shows the 2D slope distributions obtained from the AFM images (Fig. 4.4). The shapes of the slope distributions indicate the symmetry or asymmetry of the evolved structures on the irradiated surfaces. It is observed that until a swing angle of about 90°, the distribution predominantly shows a bimodal behaviour indicating an asymmetry in the structures. For 100°, a circular distribution is obtained denoting an isotropic surface that corroborates with the flat topography observed in the corresponding AFM image (Fig. 4.4(i)). Beyond this azimuth, the distributions indicate an elliptical symmetry arising out of symmetrical nanoripples formed at these angles. The inclinations of the major axes of the 2D slope distributions (about 45°) conform to those of the corresponding FFTs or the ripple wave vector. Finally, for a complete rotation (Fig. 4.14(o)) the orientation of the distribution flips by an angle of 90°. In contrast to the geometry of complete rotation where each azimuth is bombarded only once per cycle, in the case of swinging it is bombarded twice, thus influencing the curvature-dependent sputtering and other mass redistribution effects in a much more complicated manner.

The above are elucidated through a schematic given in Fig. 4.15. In this figure, the left panel shows both symmetric and asymmetric AFM images. The middle panel shows line profiles parallel and perpendicular to the ripple wave vector. The right panel shows the corresponding 2D slope distributions and the 1D line profile along the major axis of the slope distribution. For the sake of discussion, the positive x and y directions are

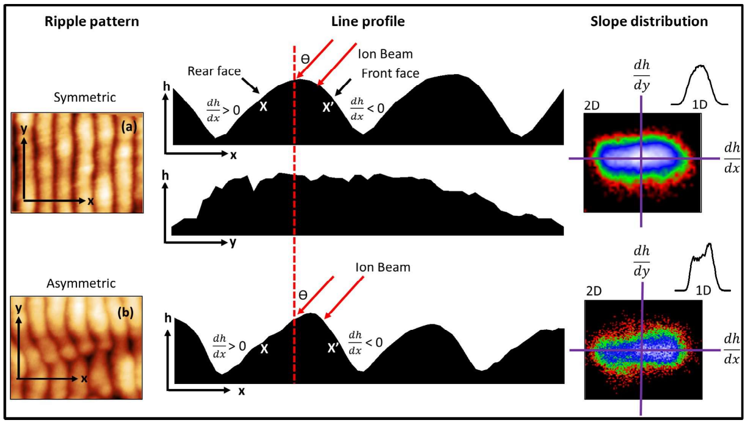
Ripple pattern
Line profile
Slope distribution
Symmetric
(a)
y
x
Rear face
θ
Ion Beam
Front face
h
$\frac{dh}{dx} > 0$
X
X'
$\frac{dh}{dx} < 0$
x
h
y
$\frac{dh}{dy}$
2D
1D
$\frac{dh}{dx}$
Asymmetric
(b)
y
x
Ion Beam
θ
h
$\frac{dh}{dx} > 0$
X
X'
$\frac{dh}{dx} < 0$
x
$\frac{dh}{dy}$
2D
1D
$\frac{dh}{dx}$

Figure 4.15: Schematic demonstrating 2d slope distribution for symmetric and asymmetric nanopatterns. *Left panel*: Representative AFM images showing symmetric and asymmetric ripple patterns. *Middle panel*: Line profiles obtained from AFM images in parallel and perpendicular directions. Red arrows indicate the incident ion beam. Front and rear faces are marked with the signs of their respective slopes. *Right panel*: 2D slope distributions of the corresponding AFM images. 1D line profiles across the major axis of the distributions are also shown.

considered as depicted in the diagram (left panel). The red arrows indicate direction of the incident ion beam with respect to the polar (incident) angle. The slope of the surface facing the beam is called the front face while the other is termed as the rear face as marked in the image. The slopes are thus positive for the rear face and negative for the front face of ripple patterns. For a symmetric ripple, the slopes on either sides of the peak (i.e., direction parallel to the ripple wave vector) will have similar values except for the opposite (+ve or -ve) signs of $\partial h/\partial x$ ($h(x, y)$ being the surface height). This can easily be understood from the corresponding 2D slope distribution in the right panel. The 1D line profile along the major axis of the distribution having a single peak reinforces this fact. An asymmetric ripple, on the other hand, exhibits slopes as represented in the bottom row of the middle panel of the diagram. This is well represented in the 2D slope distribution and 1D line profile in the left panel. Existence of more than one peak in the 1D line profile indicates unequal weightages of slope distributions for a surface. Slopes in the y direction (i.e., $\partial h/\partial y$) are evenly distributed for both the types of ripples and will thus have a narrow and symmetric distribution as shown in the middle row of the middle panel.

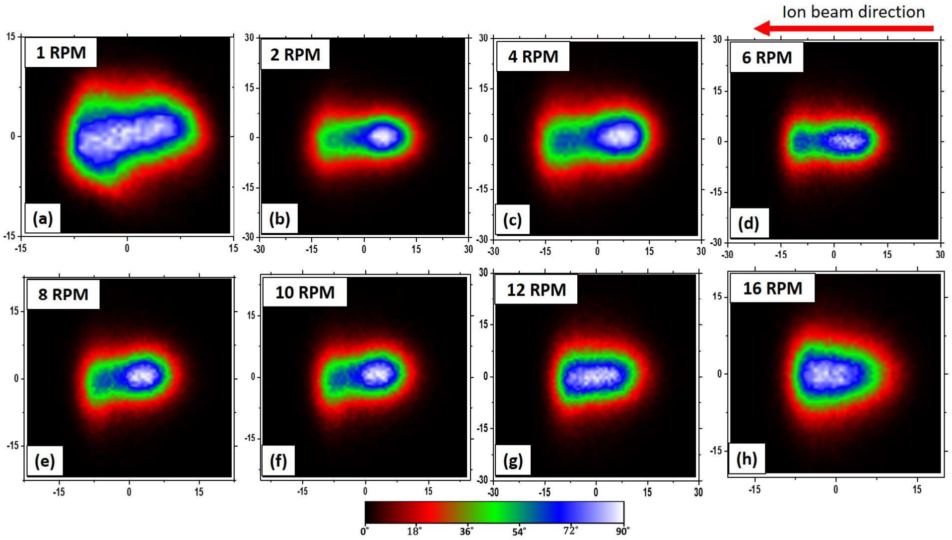

Figure 4.16: 2D slope distributions of irradiated surfaces for $\triangle\phi = 70°$ rotating at different rotational speeds. The horizontal axis is along the ion beam direction. The red arrow indicates the initial direction of the ion beam prior to swinging.

Figure 4.16 shows the 2D slope distributions obtained from the AFM images (Fig. 4.10) for different rotational speeds (1 to 16 RPM) for a fixed azimuth of 70°. Based on the

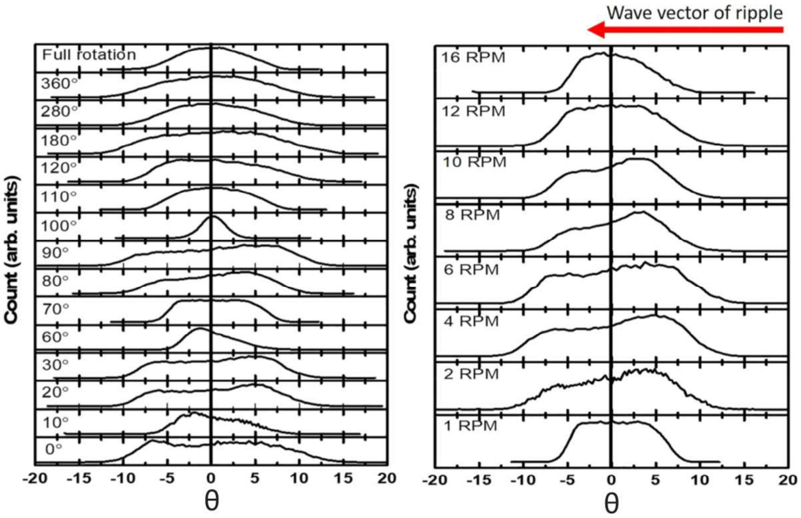

Figure 4.17: 1D line profiles obtained along the major axes of the 2D slope distributions for 500 eV Ar^+ irradiated Si surfaces for (a) different swinging angles from 0° to 360° and (b) different rotational speeds from 1 RPM to 16 RPM at $\triangle\phi = 70°$. The red arrow indicates the initial direction of the ion beam prior to swinging.

above discussion, it is evident from the images that the distribution is asymmetric till 10 RPM, beyond which the asymmetricity reduces to a large extent.

For a better insight, line profiles along the ripple wave vectors are extracted from Fig. 4.14 and 4.16 and plotted in Fig. 4.17. It is evident from Fig. 4.17(a) that up to an azimuthal angle of 90°, the ripples are asymmetric. At 70°, however, the distribution depicts a flat symmetric nature, indicating ripples formed with almost identical slopes on both the front and rear faces. The single narrow symmetric peak at 100° signifies a flat surface as confirmed from its corresponding AFM image. At higher azimuthal angles, the ripples grow in a more symmetric fashion. The asymmetry at lower angles is due to the fact that the beam is initially encountered by the front side of the ripple structures. As the azimuthal angle increases, the ripple slopes are bombarded from oblique (azimuthal) incidences with respect to the normal on the ripple slopes (side walls). This amounts to a large deposition of energy much closer to the surface than for the case of lower or zero azimuthal angles. As a consequence, phenomena like curvature-dependent sputtering and ion-induced surface mass-redistribution effects start playing dominant roles at these conditions. For low azimuthal angles in-depth (bulk) collision cascade events would dominate for a fixed incident (polar) angle. Thus, at higher azimuths, this essentially helps in smoothening of the surface as $\triangle\phi$ increases till at 100° when a flat morphology is obtained. The contribution of the linear dispersion terms towards surface instability becomes weak as evidenced from the loss of triangular structures. Beyond this point, the distribution becomes isotropic as noticed from the figure. Now, keeping $\triangle\phi$ fixed at 70° and increasing the swing speeds does not visibly show a change in the AFM images (Fig. 4.10) but changes the local slopes altogether (as shown in fig. 4.17(b)). For larger speeds, the ripples become asymmetric with the rear faces yielding predominantly smaller slopes as the speed increases. This is clear from the shift of the right hand peak towards lower values. At large speeds of 12 and 16 RPM, the slopes become more symmetric as seen from the figure. In general, large positive slopes refer to shadowed regions on the surface. However, in the present context, the situation becomes more complicated due to the swinging process. At certain angles, these positive slopes do not produce shadowing whereas other negative sloped regions could induce it. Thus, due to the configuration of the process, the full understanding of these shadowing processes is not obvious. Most of the earlier studies have reported variations in slope distributions with increase of ion fluence or incident angle [196, 198–203]. Bimodal distributions are generally observed at high fluences and incident angles indicating a strong shadowing phenomenon. They also signify transitions between linear and non-linear regimes of pattern formation. In contrast, the present study shows that asymmetric slope distributions can be achieved in an unconventional sputtering scenario even in the absence of a shadowing phenomenon. This is primarily driven by near-surface effects rather than the bulk owing to a higher frequency of bombardment at each azimuth.

4.4 Conclusions

In this study, we performed experiments on Ar^+ irradiated Si surfaces by swinging them through different azimuthal angles at a fixed ion incidence angle of 67°. In addition, surface morphologies were also studied for different swing speeds from 1 RPM up to a maximum of 16 RPM. Based on the nanostructure morphology, four different regimes were observed for different azimuthal angles which included ripples along with triangular structures, ripples devoid of triangles, smooth surfaces and disordered rippled topographies. In addition, in the last regime of disordered ripple morphology, the orientations of the ripple wave vector exhibited abrupt changes of as large as 45° with respect to the incident ion direction. The PSD spectra clearly corroborated the presence of the above four different regimes stated above. Slope calculations reveal that the surface is rougher at large length scales for lower swing angles. Beyond this, the surface tends to be smoother at these length scales. The ripple wavelength decreased from 42.6 nm for the static surface to 28 nm for the swinging surface while the rms roughness was found to decrease from 3.0 nm to 0.4 nm respectively.

For a particular azimuth, the most ordered ripples were formed for the swing speed of 1 RPM as compared with fractional or higher rotational speeds. On comparing static and rotating surfaces, we have illustrated that hierarchical structures are obtained from the former configuration whereas isotropically rough surfaces are obtained for the latter ones. The roughness however decreases with fluence or higher rotation speeds. The rms roughness varied from 5.25 to 0.6 nm over this range.

2D and 1D slope distribution calculations were also carried out from the AFM images. They demonstrated presence of asymmetric ripple patterns on Si surface for smaller swing angles primarily owing to the ion-induced near-surface 2D mass distribution. Further, shadowing is found to play a definitive role in deciding the surface topography in this unconventional format of ion irradiation. Our results were explained in the light of dispersive effects of the propagating wave vectors owing to ion-induced surface phenomena.

We find that as long as the triangular structures appear owing to the role of dispersive effects, the ripple direction does not change. Once the dispersive effects disappear, the ripples change their orientation. Further, the existence of cancellation modes are believed to have a minimal effect on the ripple characteristics.

We believe, our study sheds light on the evolution of pattern formation in unconventional formats of ion sputtering within the present azimuthal regime and swinging speeds. The observed results also indicate lacunae within the current surface evolution models which fail to predict the findings which demonstrate the existence of a plethora of interplaying ion-induced effects capable of driving the system into instabilities, hence giving rise to abrupt transitions. Given that the amorphization process for semiconductors under ion bombardment is better understood than that for graphite (as in reference [141]) in addition to the presence of grain boundaries in the latter, the present results can encourage advancement of existing theoretical models for these unconventional geometries. Thus, apart from the possible applications emanating from the intriguing patterns, these results augment a better understanding of this unique IBS format.

Chapter 5

Prolonged pattern coarsening in ion irradiated swinging Si substrates

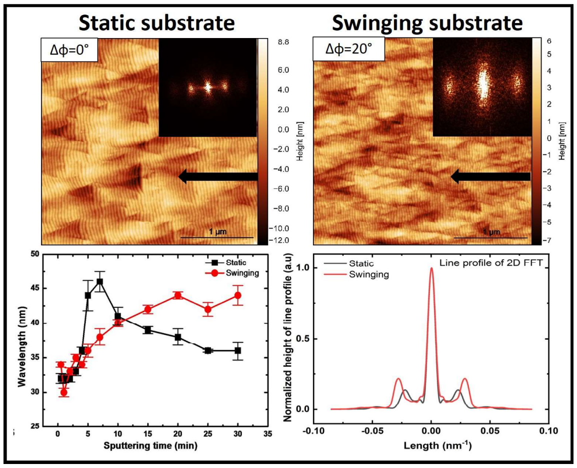

5.1 Introduction

Periodic pattern formation on material surfaces, more specifically on solid ones, have been an active area of research during the past few decades [204]. The spatio-temporal patterns formed in systems away from equilibrium can usually be simulated using a set of linear and nonlinear terms in a partial differential equation with stochastic perturbations. Earlier studies by Carter et al. showed the effects of sample rotation upon surface roughening during oblique incidence ion irradiation [205]. He also demonstrated through considerations of pertinent equations that such formation can be described by the competition between surface curvature enhanced sputtering erosion and surface atomic diffusion [206]. Morphological transitions on Si irradiated surfaces have also been observed experimentally [119, 207]. The resulting pattern, however, is a consequence of instabilities that dominate the system at short and long time scales. Such instabilities, in addition to several factors can also be triggered in the presence of impurity gases like C, O, H, etc. as found in a recent work [208]. The situation can be different at higher energies where porous or sponge-like surfaces can be obtained owing to the presence of thermal-spikes at these energies [209]. For the particular case of nanopattern formation on solid surfaces using low-energy ion beams, continuum approaches are employed to understand micron-scale pattern formations [6]. Over the years and with subsequent modifications of these partial differential equations-of-motion (EOM) nanoripple and nanodot formations arising out of instabilities driven by curvature-dependent sputtering [10], surface diffusion, ion-induced diffusion [22], viscous flow [6], redeposition effects, etc. could be successfully explained. A modified form (omitting zeroth, first-order and other terms not contributing to pattern formation) of the EOM looks like

$$\partial_t h = \sum_{i=x,y} \left[-\nu_{x,y}\, \partial_i^2 h + \Omega_i \partial_i^2 \partial_x h + \lambda_i^{(1)} \left(\partial_i h\right)^2 \right] + \sum_{i,j=x,y} \left[-\mathcal{K} \partial_i^2 \partial_j^2 h - \lambda_{ij}^{(2)}\, \partial_i^2 (\partial_j h)^2 \right], \quad (5.1)$$

where $\nu_{x,y}$ are incidence angle dependent effective surface tension coefficients, Ω_i denotes coefficients of dispersive terms that affect the pattern anisotropically, λ_i denotes coefficients for lateral growth and $\mathcal{K}$ signifies surface diffusion effects.

In this context, one can define two regimes of pattern formation, one for shorter time scales referred to as a linear regime and the other for longer time scales known as the nonlinear regime [6, 17]. In the earlier one, roughness increases exponentially while the wavelength remains constant. In the non-linear regime, however, the surface roughness saturates while the wavelength increases with irradiation time due to the lateral growth of surface features, generally referred to as ripple coarsening in the literature [188]. Usually, these two regimes are separated by a crossover time (t_c) [17, 210]. Beyond t_c, the nonlinear effects responsible for the in-plane ordering of the structures start dominating the surface morphology, which arise not only due to prolonged sputtering giving rise to geometrical shadowing but also due to redeposition effects [211]. The latter, based on a "hydrodynamic" model built on continuum theory shows that redeposition effects lead to wavelength coarsening while the subsequent saturation of the wavelength and amplitude are caused by shadowing [212]. Nonlinearities appear beyond the small slope approximation ($| \partial h/\partial x | \ll 1$) when $\lambda_i^{(1)}$ increases the pattern disorder while $\lambda_{ij}^{(2)}$ induces ripple coarsening in terms of amplitude and wavelength [113, 211]. The continuum approaches employed are responsive to higher order derivatives of the surface height fluctuations h (e.g., $\partial_x^2 h$) in addition to the lower order ones that are exploited to understand micron-scale pattern formations [6]. Consequently, surface defect densities increase in the nonlinear regime of pattern formation. Thus, in spite of the simplicity of this method to create surface nanostructures on static or continuously rotating substrates at oblique or near normal incidences [6], the technique suffers from a drawback of creating undesirable structural defect densities during the pattern formation process [187], thereby limiting their applicability in interdisciplinary application areas. Hence, several groups, both theoretical and experimental, have endeavoured to minimize these defects using specific ion beam conditions or by adopting unconventional techniques of ion beam sputtering (IBS). Ziberi et. al. demonstrated the formation of ordered nanodots at normal and oblique ion incidence angles with respect to the surface normal by rotating the Si substrate using Ar^+ ions. The degree of ordering and size homogeneity of these nanostructures increases with erosion time eventually leading to self-organized dots on Si surfaces [99]. A theoretical work done by Harrison et al. [193] demonstrated that sample rotation can increase the characteristic length scale of the patterns and hence minimize surface defects. Frost et al. [121] showed that rotating InP surfaces when bombarded with Ar^+ ions yields regular nanodots with hexagonal symmetry. Grazing incidence Ar^+ ion erosion on Pt surfaces have shown athermal coarsening via mobile defect annihilation [213]. Defect minimization can also be substantially achieved by rocking the substrate in the polar direction with an optimal frequency as demonstrated by Jo et al. [144, 149]. On the other hand, Kim et al. [80] in their work proved that sequential ion beam sputtering (SIBS) using oblique and normal incidences respectively, can produce ordered nanobead patterns on Au using an Ar^+ beam. Such SIBS when done azimuthally can also result in minimizing topological imperfections by preferential erosion of pattern defects as observed in a study by Keller et al. [174]. A recent work by Kim et al. [141] on HOPG substrates explored the role of azimuthal swinging on pattern formation where quasi-2D mass transport along with other angle-dependent sputtering effects come into play which is not the case for conventional sputtering conditions. A recent work by the present authors [214] employing an identical irradiation geometry demonstrated abrupt pattern transitions and hierarchical ordering on Si surfaces influenced by dispersive effects for varying degrees of azimuthal rotation.

In the light of the linear and nonlinear regimes of sputtering, the above works indicate that the ordering of the evolved nanostructures will depend on the magnitude of t_c i.e., how short or long is the linear regime. Thus, an effort to modify the linear regime by altering bombarding conditions/geometries could be an elegant way to achieve nanostructures with a better ordering. Keeping this in mind, in this work, we investigated the evolution of nanostructures on an azimuthally swinging Si surface for a particular azimuthal swinging angle with increasing ion fluences. This geometry, at suitable incidence angles, offers a variable shadowing encountered by the sample, which alters continuously as the beam sweeps in the azimuthal direction. This alters the symmetry/asymmetry of the surface structures as compared to that for a fixed angle of azimuth, keeping all other conditions identical. The azimuthal angle preferred in the current set of experiments were based on our earlier study [214] and has been elucidated in Sec. 5.2. Results were compared with those irradiated under static conditions. The nanometer scale ripples thus obtained showed a better ordering, as confirmed from atomic force microscopy and power spectral density analyses. Results showed a slow increase in ripple wavelength in comparison to those obtained using static geometry. 2D slope distribution analyses confirmed that the surface structures evolved under swinging were more symmetric in nature. Differential exposure and mass redistribution effects seem to play a key role in the present geometry. The current results undoubtedly enhance our understanding of pattern formation under this unconventional configuration, thereby unraveling a new pathway to control and modify surface nanostructures and their formation regimes for potential applications [29, 64, 215–217].

5.2 Materials and Methods

Commercially available undoped polished Si(100) substrates were cut into pieces of 1 × 1 cm^2 area and cleaned ultrasonically in ethanol for 20 min. They were rinsed with DI (de-ionized) water and dried in air subsequently prior to loading them in the vacuum chamber. Ion beam irradiation (IBI) was performed inside a chamber fitted with a 4 cm broad beam Kaufman ion source. The ion source is a three-gridded system with an in-built neutralizer. This configuration ensures minimum divergence of the beam up to a distance of 20 cm beyond which the beam diameter grows progressively [153]. A Si(100) wafer of 2" diameter was placed in between the sample and the metal sample holder to avoid any metal impurity sputtering. The sample holder was at a distance of 15 cm from the source in a high vacuum chamber whose base pressure of 2×10^{-7} Torr using an azimuthally swung substrate holder as shown in Fig. 5.1. Each sample was marked at the back with an arrow indicating the ion incidence direction. This helped to ensure placing the samples identically aligned while doing AFM measurements. The current density used was 13.3 mA/cm^2. Two sets of experiments were carried out using the cleaned samples. In the

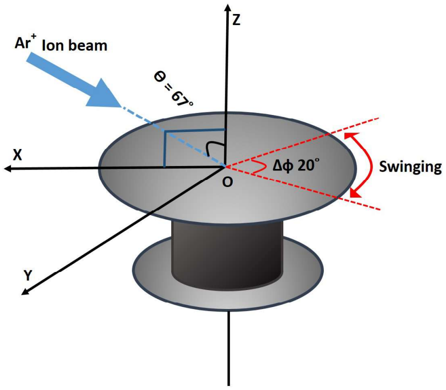

Figure 5.1: Schematic showing the swing geometry adapted during IBS. Here, θ (= 67°) is the polar angle between the 500 eV Ar^+ ion beam (blue arrow) and the surface normal. The sample azimuthally swings in a span of 20° about the z-axis.

first set, the samples were irradiated by 500 eV Ar^+ at an incidence polar angle of 67° with a variation of irradiation time (fluence) from 0.5 min (2.5×10^{18} ions cm^{-2}) to 30 min (1.5×10^{20} ions cm^{-2}). For the second set of experiments, the sample was swung in the azimuthal direction by keeping it fixed at a value of $\triangle\phi = 20°$ ($-10°$ to $+10°$) with a fixed rotational speed of 1 rpm. This particular azimuth was chosen based upon our previous study [214] where reasonably ordered ripples were obtained under the above conditions. An alternating current (a.c.) servo motor was used to control the azimuthal swinging angle and speed (revolution per second) of the sample holder. During ion irradiation, the partial pressure of argon (purity$\sim$ 99.999%) inside the chamber and ion current were 2.5×10^{-4} Torr and 1.3 mA, respectively. The substrate temperature during all irradiations was found to be around 40°C., thereby nullifying recrystallization of the amorphous layer.

The surface morphology of samples were analyzed ex-situ using Atomic Force Microscopy (AFM) (MultiMode 8, Bruker, USA) in tapping mode. The radius of curvature of the cantilever tip used was 10 nm. The vertical height variations of the surface features were evaluated using root-mean-square (RMS) roughness. 2D Fast Fourier transforms (FFT) and 1D power spectral densities (PSD) were extracted from the AFM images using Gwyddion (Ver. 8.1) [154] to further quantify the topographical nature of the self-assembled nanostructures. The height power spectral density (PSD) was used to characterize the irradiated surfaces further. Specifically, the PSD of the surface height field is defined as [14, 179]

$$\mathrm{PSD}(\mathbf{q}, t) = \langle |h(\mathbf{q}, t)|^2 \rangle, \tag{5.2}$$

where $h(\mathbf{q}, t)$ is the space FFT of the surface height field $h(\mathbf{r}, t)$, brackets denote an average over scans or experiments, and $\mathbf{q} = (q_x, q_y)$ is two-dimensional wave vector. We have also evaluated the 1D PSD of 1D surface profiles along, e.g., the x-direction, namely,

$$\mathrm{PSD}(q_x, t) = \langle |h_{y_0}(q_x, t)|^2 \rangle, \tag{5.3}$$

where $h_{y_0}(q_x)$ is the FFT of the one-dimensional profile $h(x, y_0)$ for a fixed y_0 value. These two functions are related as [180, 218]

$$\mathrm{PSD}(q_x, t) = \frac{1}{\pi} \int_0^\infty dq_y \, \mathrm{PSD}(\mathbf{q}, t). \tag{5.4}$$

If a ripple structure exists which is periodic along the x direction, this reflects into the occurrence of a characteristic peak (local maximum) in the plot of $\mathrm{PSD}(q_x)$ vs q_x, say at $q_x = q^*$. In such a case, the ripple wavelength is $\lambda = 2\pi/q^*$ while the width of the peak is inversely correlated with the degree of space order in the morphology [144, 182]. 2D slope distributions were estimated in order to understand the symmetry/asymmetry of the formed nanostructures.

5.3 Results and discussions

5.3.1 Morphology evolution on static Si surfaces

Experiments were first carried out on static substrates and the results compared with those of an azimuthally swinging one.

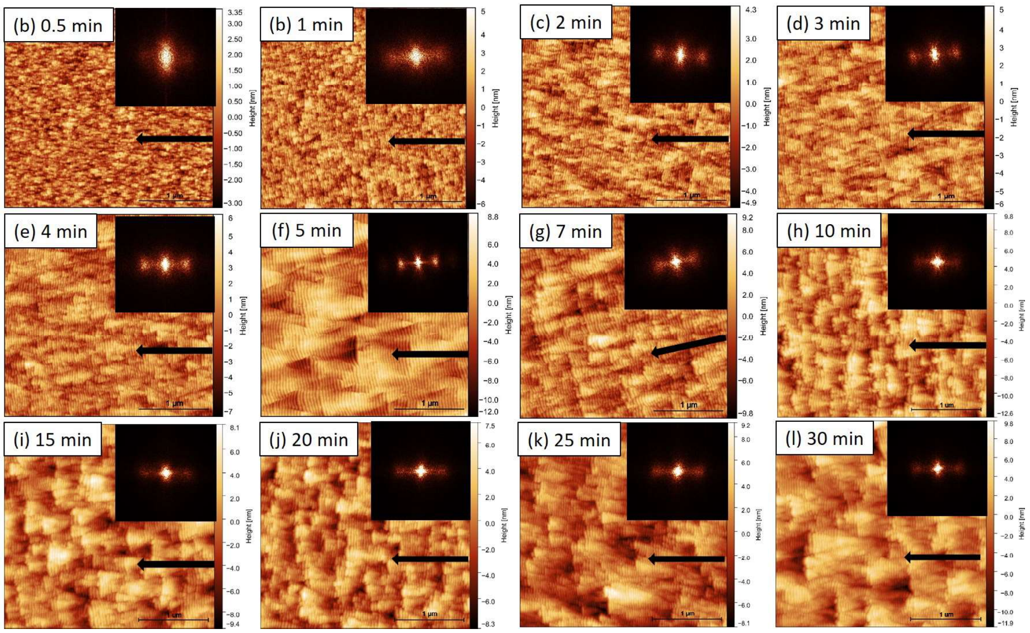
(b) 0.5 min
3.35 3.00 2.50 2.00 1.50 1.00 0.50 0.00 −0.50 −1.00 −1.50 −2.00 −3.00
(b) 1 min
5 4 3 2 1 0 −1 −2 −3 −4 −6
(c) 2 min
4.3 3.0 2.0 1.0 0.0 −1.0 −2.0 −3.0 −4.0 −4.9
(d) 3 min
5 4 3 2 1 0 −1 −2 −3 −4 −5 −6
(e) 4 min
6 5 4 3 2 1 0 −1 −2 −3 −4 −5 −7
(f) 5 min
8.8 6.0 4.0 2.0 0.0 −2.0 −4.0 −6.0 −8.0 −10.0 −12.0
(g) 7 min
9.2 8.0 6.0 4.0 2.0 0.0 −2.0 −4.0 −6.0 −9.8
(h) 10 min
9.8 8.0 6.0 4.0 2.0 0.0 −2.0 −4.0 −6.0 −8.0 −10.0 −12.6
(i) 15 min
8.1 6.0 4.0 2.0 0.0 −2.0 −4.0 −6.0 −8.0 −9.4
(j) 20 min
7.5 6.0 4.0 2.0 0.0 −2.0 −4.0 −6.0 −8.3
(k) 25 min
9.2 8.0 6.0 4.0 2.0 0.0 −2.0 −4.0 −6.0 −8.1
(l) 30 min
9.8 8.0 6.0 4.0 2.0 0.0 −2.0 −4.0 −6.0 −8.0 −10.0 −11.9
Height [nm]
1 μm

Figure 5.2: 3×3 μm^2 AFM images of static Si surfaces irradiated with 500 eV Ar$^+$ ions at $\theta = 67°$ for different values of sputtering time (or fluence) in mins (fluence in units of ions cm^{-2}) such as: (a) 0.5 (2.5×10^{18}), (b) 1 (5×10^{18}), (c) 2 (10×10^{18}), (d) 3 (1.5×10^{19}), (e) 4 (2×10^{19}), (f) 5 (2.5×10^{19}), (g) 7 (3.5×10^{19}), (h) 10 (5×10^{19}), (i) 15 (7.5×10^{19}), (j) 20 (10×10^{19}), (k) 25 (1.2×10^{20}), and (l) 30 (1.5×10^{20}), respectively. Black arrow indicates the ion beam direction. *Top right insets*: FFTs of corresponding AFM images.

Fig. 5.2 depicts 3×3 μm^2, while Fig. 5.3 shows the corresponding 1×1 μm^2 scans AFM topographies of the static Si surfaces bombarded at 500 eV Ar$^+$ ions at an ion incident angle of 67° corresponding to the irradiation time from 0.5 to 30 mins.

AFM image for the pristine Si surface has been provided in Fig. 5.4 (a) for comparison. The black arrow in each image indicates the direction of the incident ion beam on the Si surface. This is considered as the x-axis in all our subsequent discussions. The top right insets in Fig. 5.2 show the 2D FFTs of the respective AFM images. Each FFT image comprises a central bright spot accompanied by at least two side lobes with varying intensities. The central spot represents the origin (0,0) of the frequency space. The finite size of the central region indicates low frequency information or large length scale

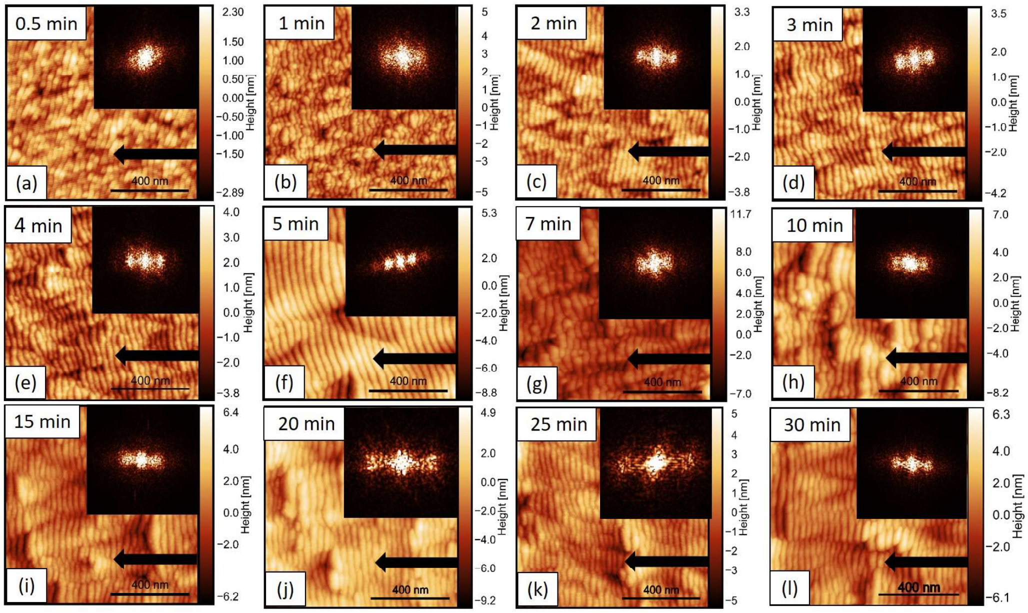
0.5 min
(a)
400 nm
2.30
1.50
1.00
0.50
0.00
−0.50
−1.00
−1.50
−2.89
Height [nm]
1 min
(b)
400 nm
5
4
3
2
1
0
−1
−2
−3
−5
Height [nm]
2 min
(c)
400 nm
3.3
2.0
1.0
0.0
−1.0
−2.0
−3.8
Height [nm]
3 min
(d)
400 nm
3.5
2.0
1.0
0.0
−1.0
−2.0
−4.2
Height [nm]
4 min
(e)
400 nm
4.0
3.0
2.0
1.0
0.0
−1.0
−2.0
−3.8
Height [nm]
5 min
(f)
400 nm
5.3
2.0
0.0
−2.0
−4.0
−6.0
−8.8
Height [nm]
7 min
(g)
400 nm
11.7
8.0
6.0
4.0
2.0
0.0
−2.0
−7.0
Height [nm]
10 min
(h)
400 nm
7.0
4.0
2.0
0.0
−2.0
−4.0
−8.2
Height [nm]
15 min
(i)
400 nm
6.4
4.0
2.0
0.0
−2.0
−6.2
Height [nm]
20 min
(j)
400 nm
4.9
2.0
0.0
−2.0
−4.0
−6.0
−9.2
Height [nm]
25 min
(k)
400 nm
5
4
3
2
1
0
−1
−2
−3
−5
Height [nm]
30 min
(l)
400 nm
6.3
4.0
2.0
0.0
−2.0
−6.1
Height [nm]

Figure 5.3: 1×1 μm^2 AFM images of static Si surfaces irradiated with 500 eV Ar^+ ions at $\theta = 67°$ for different values of sputtering time (fluence) in mins (in ions cm^{-2}) such as: (a) 0.5 (2.5×10^{18}), (b) 1 (5×10^{18}), (c) 2 (10×10^{18}), (d) 3 (1.5×10^{19}), (e) 4 (2×10^{19}), (f) 5 (2.5×10^{19}), (g) 7 (3.5×10^{19}), (h) 10 (5×10^{19}), (i) 15 (7.5×10^{19}), (j) 20 (10×10^{19}), (k) 25 (1.2×10^{20}), and (l) 30 (1.5×10^{20}), respectively. Black arrow indicates the ion beam direction. *Top right insets*: FFTs of corresponding AFM images.

periodicities in the AFM image. The orientation and size of the side lobes or satellite peaks imply the ripple direction and their corresponding wavelengths. 2D FFT for the pristine Si surface has been provided in Fig. 5.4 (a).

For all the samples, nanoripples are observed to form after irradiation which are oriented along the ion beam direction (known as parallel-mode ripples) as fairly evident from the satellite peaks of the 2D FFT images. This is in complete agreement with that found in literature [10]. It is further observed that the sizes and periodicities of ripples change with ion fluence which can be corroborated from the FFT insets. The brightness and sharpness of spots in the FFT images give an idea about the ordering of the periodic structures, a sharper spot usually indicating higher order [219]. It is observed from the AFM images, that nanoripples form as early as 0.5 min, although they are quite ill-

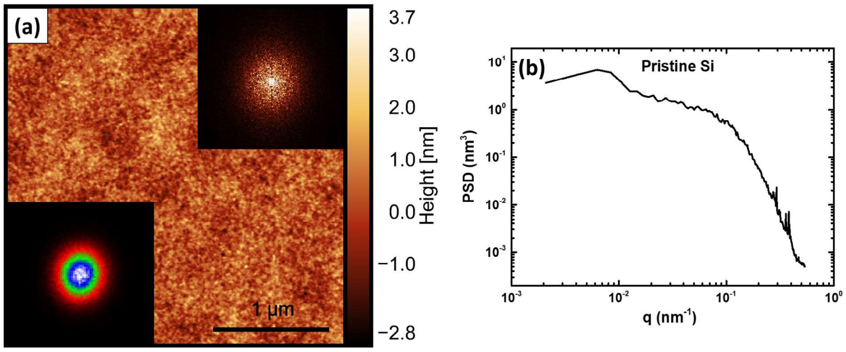

Figure 5.4: (a) 3×3 μm^2 AFM micrograph of pristine Si surface. Top right inset: 2D FFT (square root of the 2D PSD) corresponding to the AFM images. Bottom left inset: 2D slope distribution corresponding AFM image. (b) Power spectral density of the pristine Si surface.

formed at this fluence. Ordering of the ripples improve for 1 min although the FFT shows faintly formed spots. Upon increasing fluence, well-formed sinusoidal ripple patterns are observed, as supported by sharp and well-separated first order spots in the FFT images (Fig. 5.2(c) through (e)). At 1 min, in addition to the ripples, the surface morphology starts showing triangular structures underneath the ripple morphology also observed from Fig. 5.3, thereby rendering a hierarchical surface [6,187,210]. These triangular structures gain prominence with increasing fluence. The nanoripples are best formed at 5 min, as evident from the extremely sharp spots in the FFT image. Beyond 5 mins, the ripples progressively show disorder with increasing ion fluence as demonstrated clearly in Fig. 5.2(g) through (l). This is further confirmed by the blurring and eventual near disappearance of spots in the 2D FFT spectra. Moreover, the triangular type features start to superimpose on each other. Thus, the overall surface morphology degrades for higher bombarding times (fluences).

5.3.2 Morphology evolution on azimuthally swinging Si surfaces

Fig. 5.5 shows 3×3 μm^2, while Fig. 5.6 shows the corresponding 1×1 μm^2 scans of the AFM topographies of Si surfaces bombarded at beam parameters identical with those

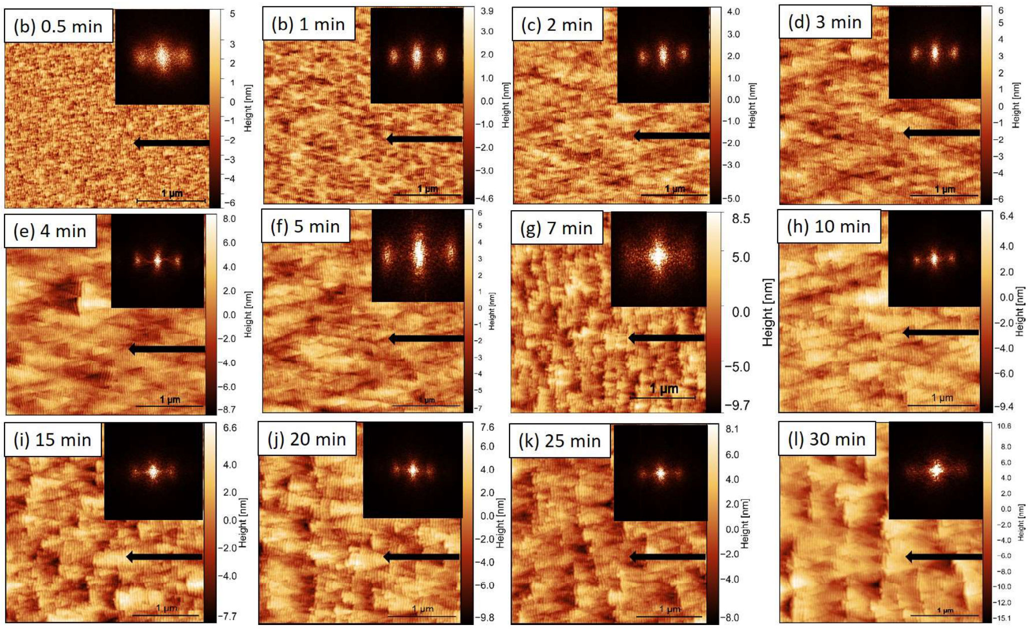

Figure 5.5: 3×3 μm^2 AFM images of swinging Si surfaces irradiated with 500 eV Ar$^+$ ions at $\theta = 67°$, a total swinging angle of $\triangle\phi = 20°$ and with a variation of sputtering time (or fluence) in mins (fluence in units of ions cm^{-2}) such as: (a) 0.5 (2.5×10^{18}), (b) 1 (5×10^{18}), (c) 2 (10×10^{18}), (d) 3 (1.5×10^{19}), (e) 4 (2×10^{19}), (f) 5 (2.5×10^{19}), (g) 7 (3.5×10^{19}), (h) 10 (5×10^{19}), (i) 15 (7.5×10^{19}), (j) 20 (10×10^{19}), (k) 25 (1.2×10^{20}), and (l) 30 (1.5×10^{20}) min, respectively. Black arrow indicates the initial ion beam direction prior to swing. *Top right insets*: FFTs of corresponding AFM images.

for the static case, but for an oscillating azimuthal angle of $\triangle\phi = 20°$. The black arrow indicates the initial (prior to swinging) direction of the incident ion beam on the Si surface about which the substrate symmetrically swings, as depicted in Fig. 5.1. The AFM images reveal that, similar to the static case, parallel-mode nanoripples are formed for all fluences upon irradiation. The inset FFT images substantiate the ripple directionality through the existence of first order spots in the horizontal direction. Upon comparing the FFTs with those of the static case, it is evident that ripples are better formed at earlier times for the azimuthally swinging case, as proven by the distinct spots obtained for 0.5 min. The ordering of the ripples increases with increasing fluence up to 4 mins of irradiation, where the sharpest and brightest spots are observed in the FFT spectra. As observed for the case

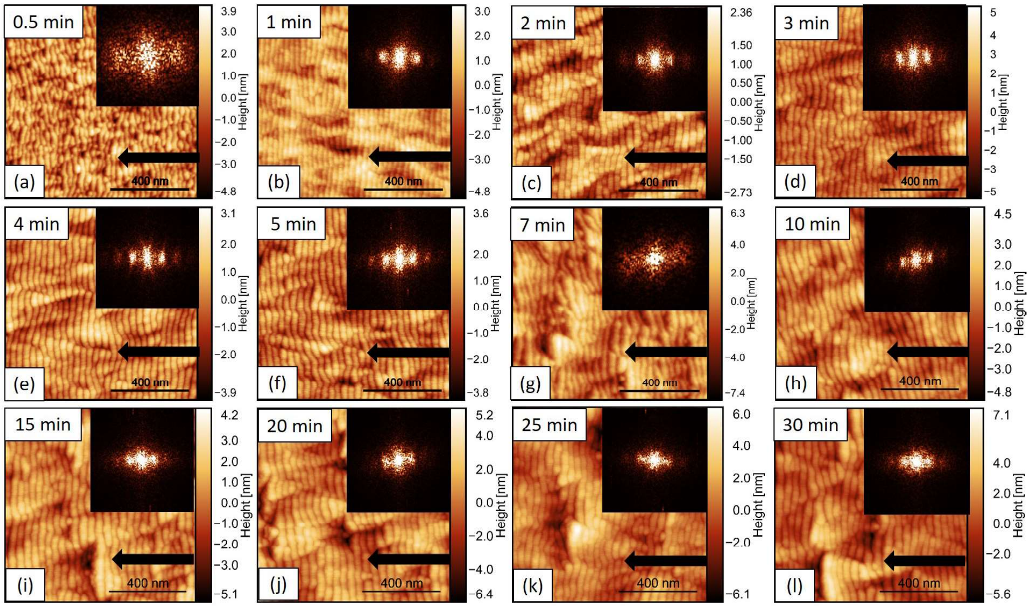
0.5 min
(a)
400 nm
3.9
3.0
2.0
1.0
0.0
−1.0
−2.0
−3.0
−4.8
Height [nm]
1 min
(b)
400 nm
3.0
2.0
1.0
0.0
−1.0
−2.0
−3.0
−4.8
Height [nm]
2 min
(c)
400 nm
2.36
1.50
1.00
0.50
0.00
−0.50
−1.00
−1.50
−2.73
Height [nm]
3 min
(d)
400 nm
5
4
3
2
1
0
−1
−2
−3
−5
Height [nm]
4 min
(e)
400 nm
3.1
2.0
1.0
0.0
−1.0
−2.0
−3.9
Height [nm]
5 min
(f)
400 nm
3.6
2.0
1.0
0.0
−1.0
−2.0
−3.8
Height [nm]
7 min
(g)
400 nm
6.3
4.0
2.0
0.0
−2.0
−4.0
−7.4
Height [nm]
10 min
(h)
400 nm
4.5
3.0
2.0
1.0
0.0
−1.0
−2.0
−3.0
−4.8
Height [nm]
15 min
(i)
400 nm
4.2
3.0
2.0
1.0
0.0
−1.0
−2.0
−3.0
−5.1
Height [nm]
20 min
(j)
400 nm
5.2
4.0
2.0
0.0
−2.0
−4.0
−6.4
Height [nm]
25 min
(k)
400 nm
6.0
4.0
2.0
0.0
−2.0
−6.1
Height [nm]
30 min
(l)
400 nm
7.1
4.0
2.0
0.0
−2.0
−5.6
Height [nm]

Figure 5.6: 1×1 μm^2 AFM images of swinging Si surfaces irradiated with 500 eV Ar$^+$ ions at $\theta = 67°$ for different values of sputtering time (fluence) in mins (in ions cm^{-2}) such as: (a) 0.5 (2.5×10^{18}), (b) 1 (5×10^{18}), (c) 2 (10×10^{18}), (d) 3 (1.5×10^{19}), (e) 4 (2×10^{19}), (f) 5 (2.5×10^{19}), (g) 7 (3.5×10^{19}), (h) 10 (5×10^{19}), (i) 15 (7.5×10^{19}), (j) 20 (10×10^{19}), (k) 25 (1.2×10^{20}), and (l) 30 (1.5×10^{20}), respectively. Black arrow indicates the ion beam direction. *Top right insets*: FFTs of corresponding AFM images.

of static substrates, hierarchical morphologies are also found to evolve from 1 min. The triangular structures gain prominence in size as sputtering proceeds. For 5 and 7 mins, the FFT shows elongated central and side spots, thereby indicating a larger dispersion of triangle sizes (in the direction perpendicular to the ion beam) as compared to the rest. As the irradiation continues, ripples are found to sustain on the eroded surfaces for a considerable amount of fluence. Thus, it is evident from the above findings that ripples are formed at an early stage upon varying the azimuthal angle during ion irradiation. For comparison, the surface topography and description of a Si surface after irradiation for a full azimuthal rotation can be found in a recent study [214].

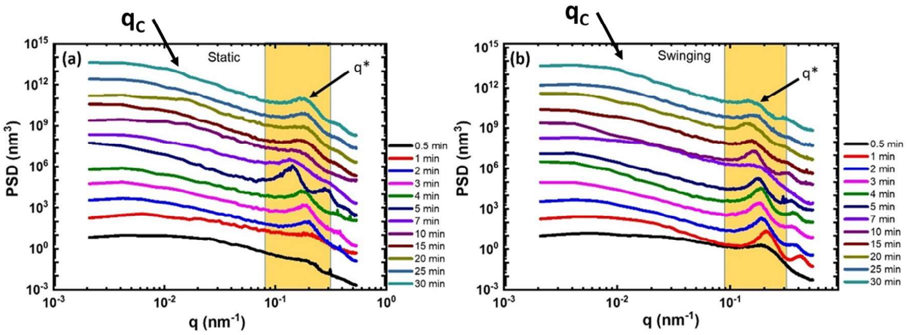

Figure 5.7: Log-log plot of 1D PSD with spatial frequencies calculated from AFM images along ripple wave vector with increasing sputtering time at $\theta = 67°$ for (a) static and (b) azimuthally swinging ($\Delta\phi = 20°$) substrates.

5.3.3 Spatio-temporal dynamics of statistical topography indicators

Power spectral densities (PSDs) obtained from the AFM topographical images were further used to characterize the samples. For 1D (e.g., x-direction), these are defined as [179]

$$\mathrm{PSD}(q_x, t) = \langle |h_{y_0}(q_x, t)|^2 \rangle \sim q_x^{-(2\alpha+1)} \sim q_x^{-m}, \tag{5.5}$$

where q_x is the wave vector in the x-direction, $h_{y_0}(q_x)$ is the FFT of the one-dimensional profile $h(x, y_0)$ for a fixed y_0 value, α is the roughness scaling exponent used to characterize the roughness of the saturated interface [14]. If the ripples are periodic in the x-direction, the PSD spectrum shows a characteristic peak (local maximum) at $q_x = q^*$ (say) in the plot of PSD(q_x) vs q_x. The ripple wavelength is then given by $\lambda = 2\pi/q^*$ while the inverse of the width of the peak gives a measure of order of the surface features [144]. A sharp peak in the PSD spectra signifies better ordering of ripple patterns. Further, a PSD spectrum is divided into low-q and high-q regions, as observed in Fig. 5.7.

The PSD for the pristine Si surface has been provided in Fig. 5.4 (b) for comparison.

The full width at half maxima (FWHM) of the peaks indicate a measure of order of the ripple structures as shown in Fig. 5.8, as discussed above. The sharpest PSD peak

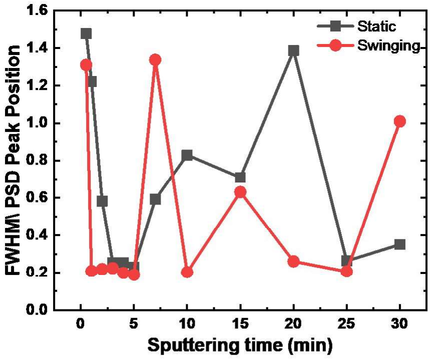

Figure 5.8: Evolution of pattern disorder FWHM/PSD peak position for 500 eV Ar^+ irradiated Si surface for static substrate and azimuthally swinging substrate at $\Delta\phi = 0$, respectively.

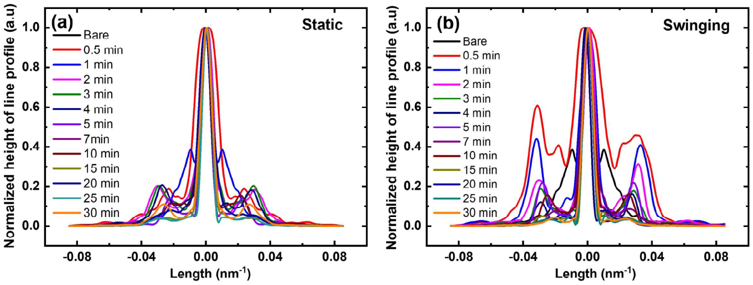

.

Figure 5.9: Normalized 1D line profiles obtained along the major axes of the 2D FFTs for 500 eV Ar^+ irradiated Si surfaces for (a) static and (b) azimuthally swinging ($\Delta\phi = 20°$) substrates, respectively.

is observed for the 5 min static sample. However, in general, the PSD peaks are broader for the static samples than the swinging ones. Moreover, the sharpness of the peaks of PSD spectra for the swinging samples approximately remain the same with increasing ion fluence.

In order to get a better idea of the ripple ordering, line profiles were drawn along the horizontal axis of the FFT insets and the normalized profiles with respect to the central maxima as shown in Fig. 5.10 are shown in Fig. 5.9. It is observed that the side peaks of the FFT spectra pertaining to the swinging case are stronger than the static ones, thereby

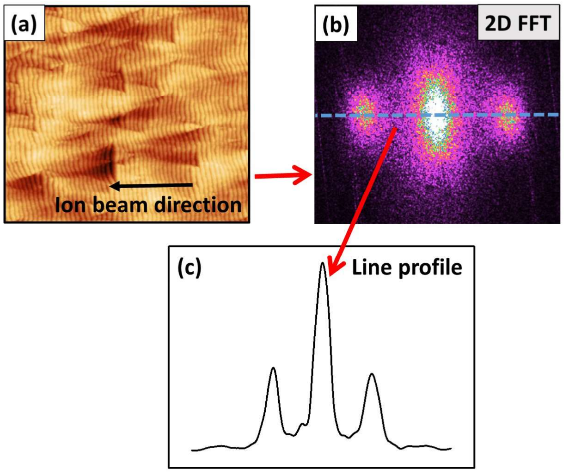

Figure 5.10: (a) $3 \times 3\ \mu\text{m}^2$ AFM micrograph of Si surface. (b) 2D FFT of the AFM image. (c) Line profile obtained from the 2D FFT along the horizontal direction. Red arrows indicate that (b) is obtained from (a) and (c) is obtained from (b).

indicating a change in ripple morphology associated with swing. Further, a quantitative estimate of ripple order can be obtained by plotting $\delta\lambda/\lambda$ with the sputtering time as shown in Fig. 5.11. Here, λ is the average wavelength obtained from four measurements of a particular sample and $\delta\lambda$ is the corresponding standard deviation. Consequently, one can define a correlation length such that surface features separated by a smaller (longer) distance than ξ are statistically correlated (uncorrelated) [182]. It is a measure of the distance over which the surface heights and properties remain correlated. In a surface characterized by a large correlation length, adjacent points on the surface exhibit similar height fluctuations. Conversely, in a surface with a small correlation length, neighboring points may show different height variations. The correlation length, denoted as ξ, can be obtained from the relation $\xi = 1/q_c$, where q_c is derived from the PSD spectra.

The in-plane correlation length of the ripples shows an overall increase for both static and swinging cases as the fluence increases as dipicted in Fig. 5.12.

The correlation length arises from triangular structures, as evidenced by the PSD of the short and long wavelength components as shown in Fig. 5.13. The short-wavelength

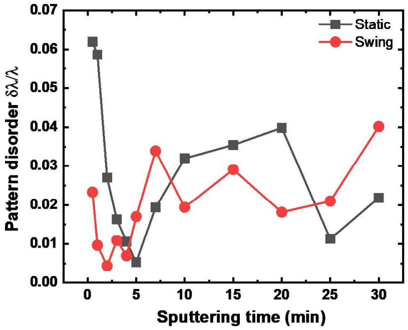

Figure 5.11: Evolution of pattern disorder $\delta\lambda/\lambda$ for 500 eV Ar^+ irradiated Si surfaces for static substrate and azimuthally swinging substrate at $\Delta\phi = 20°$, respectively.

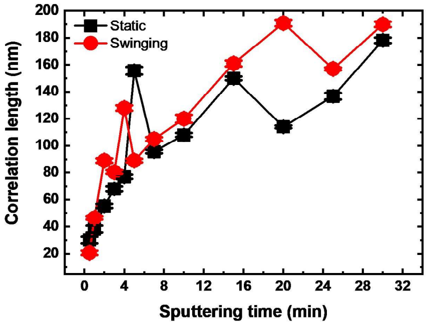

Figure 5.12: Autocorrelation length obtained for Ar^+ irradiated Si surfaces at $\theta = 67°$ for different sputtering times, corresponding to static (closed square) and swinging (closed circle) substrates.

parallel ripples were filtered from the long-wavelength triangular structure components using an FFT filter method, as illustrated in Fig. 5.16, following the methodology outlined in a previous study by Engler et al. [220].

The ripple wavelengths ($\lambda = 2\pi/q^*$) were evaluated from the PSD peaks as elucidated above. The wavelength variations for the static and the swinging Si substrates are shown in Fig. 5.14(a) For the static case, an initial coarsening in wavelength was observed from 33 to 46 nm within 7 mins of irradiation. Thereafter, the wavelength decreases and finally saturates to a value of 36 nm at 30 minutes. For the swinging sample, on the other hand, the ripple wavelength steadily increases towards saturation from 32 nm (for 0.5 min) to

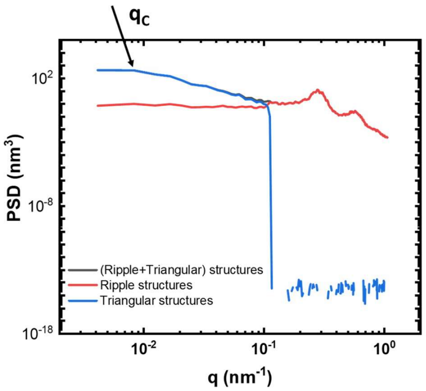

Figure 5.13: The plot depicts the PSD spectra of 3×3 μm^2 AFM images, along with both short and long wavelength components.

44 nm within 30 mins of bombardment. Thus, the wavelength variations reveal different trends for the static and swinging cases. It appears that for both the cases, the linear regimes are very short. For the static case, the wavelength remains almost the same until 4 mins which is a clear indication of existence of a linear regime. Furthermore, a rare occurrence of anti-coarsening is observed for the static case at high fluences (beyond 7 mins).

During the static case, the ripple coarsening exponent 1/z was found to be 0.4 ± 0.06 as demonstrated in Fig. 5.15 (a) . For the swinging case however, the wavelength increases steadily right from the beginning and continues to coarsen until the highest fluence studied with a coarsening exponent $1/z = 0.13 \pm 0.01$ as shown in Fig. 5.15(b) . Thus, a noteworthy difference between the two is that the coarsening rate is considerably slower for the swinging case. Ripple coarsening has been theoretically demonstrated to be a fallout of re-depositing atoms on the evolving surface that can be described using an anisotropic model following a “hydrodynamical” approach and has been observed in other experimental studies [6, 221]. In contrast, anticoarsening has hardly been reported in IBS literature. A study by Garg et al. [222] done with medium energy 60 keV Ar^+ ions on Si showed ripple anticoarsening in the linear regime. While the present study

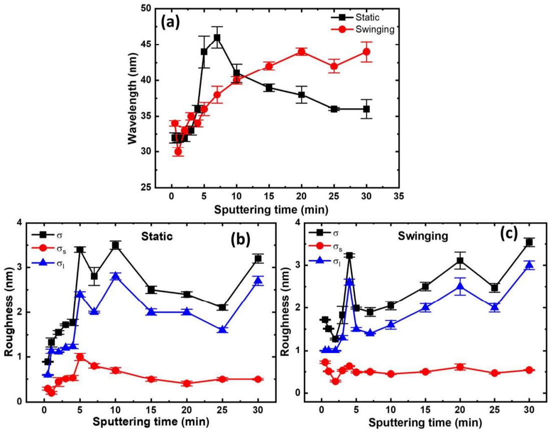

Figure 5.14: (a) Variation of wavelength with irradiation time for the static and swinging samples. (b) Variation of rms roughness σ, the short wavelength rms roughness σ_s, and the long wavelength rms roughness σ_l with irradiation time for the static sample. (c) The same calculated for the swinging sample. All irradiations were performed with 500 eV Ar^+ beam at an incidence angle of 67°. For the swinging samples, the total azimuthal angle was 20°.

has been done at a much lower energy (500 eV), the observed anticoarsening noticed here occurs in the nonlinear regime, as substantiated by 2D slope distribution analyses discussed in detail below. Anticoarsening has also been reported recently in a different context of wavelength selection [223]. Upon careful observation of the AFM images, it can be seen that the triangular domain sizes drop drastically beyond 7 mins. It is envisaged that this domain size degradation and the observed anticoarsening can be interconnected through a complex phenomenon which is not quite evident at present. Coarsening has been observed by other groups on Si surfaces [185, 224]. However, in the work done by Keller et al., the temperature was less than 180°C while in the present case it is around 40°C. On the other hand, our current density is more than 13 times than what was used by Chowdhury and co-workers in their study. Hence, temperature and current density can also have significant influences on ripple coarsening.

The root-mean-square (rms) roughness variation for the static and swinging substrates are shown in Fig. 5.14(b) and (c). As observed from the AFM images, the morphology

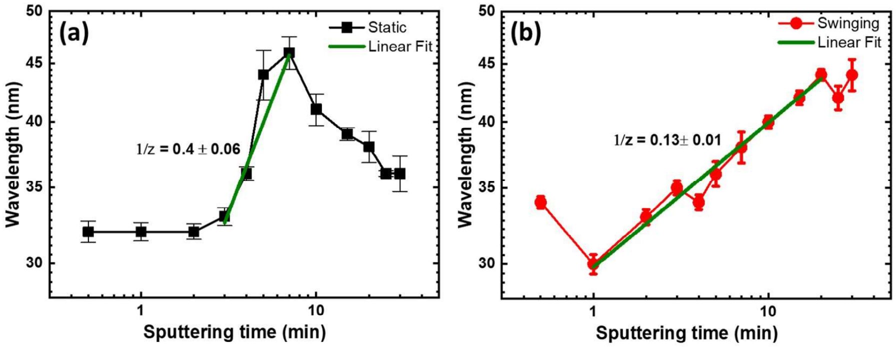

Figure 5.15: Evolution of wavelength for 500 eV Ar^+ irradiated Si surface for (a) static, and (b) azimuthally swinging substrate. $1/z$ represents surface roughness exponent.

exhibits hierarchical structures for the majority of the irradiated samples. These triangular structures were theoretically explained by Bradley and co-workers [175] by considering dispersive effects during ion irradiation. It turns out that the sputtering yield is not only dependent on the second derivatives of surface heights h but also on their third derivatives ($\partial_i^2 \partial_x h$) as reported earlier [175]. The inclusion of the additional linear terms in the equation of motion (EOM) makes the ripples asymmetric and the ripple propagation dispersive, meaning that the different surface propagating wave vectors (k) travel at different speeds [11]. Such a dispersive effect can be induced by ion-induced plastic flow or viscous relaxation of ion-induced stresses in the near-surface region where collision-induced stress originates resulting in amorphization and relaxation via viscous flow [225]. Studies suggest that highly ordered ripples can be formed if both dispersion and transverse smoothening are sufficiently strong [175]. In the context of the hierarchical topology obtained, one can define small- and large-scale roughnesses.

In order to quantify this, the short-wavelength parallel ripple contribution were separated from the long-wavelength disordered components using an FFT filter method, as elucidated in Fig. 5.16 following a scheme as laid out in an earlier study [220]. Fig 5.14(b) and (c) display rms roughness σ, short-wavelength (along ion beam direction) rms roughness σ_s, and long-wavelength rms roughness σ_l for the static and swinging sample, re-

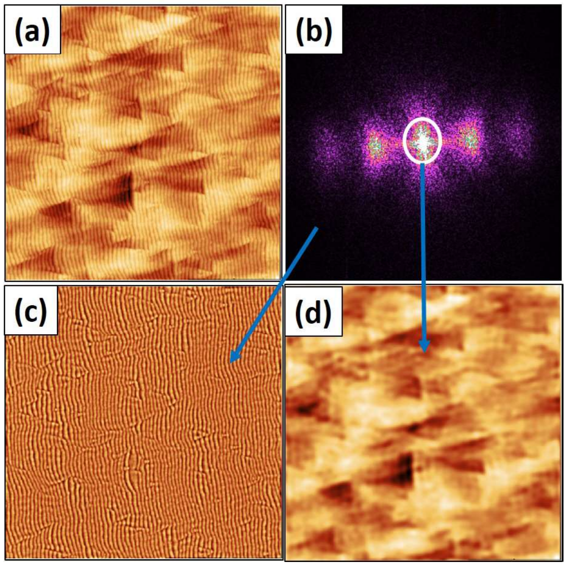

Figure 5.16: (a) 3×3 μm^2 AFM micrographs of 500 eV Ar$^+$ irradiated Si at 67° for 5 min : (b) 2D FFT of (a). The white circle includes(excludes) the long(short)-wavelength components of the pattern. (c) Topographic image for the short-wavelength component of (b) obtained using inverse FFT (z scale = 7 nm). and (d) Topographic image for the long wavelength component of (b) obtained using inverse FFT (z scale = 3.7 nm).

spectively. It is observed that for both the cases, σ_s is less. Notably, σ_l grows faster than σ_s with increasing ion fluence. The main contribution to the RMS roughness primarily arises from the triangular structures rather than the nanoripples.

Further, results obtained from fractal analyses [226, 227] performed on the AFM images are plotted in Fig. 5.17. The fractal dimensions were obtained by cube counting method using Gwyddion [154]. For early sputtering times, the fractal dimensions of the swinging samples are higher than those of the static ones, indicating greater surface height fluctuations for the former. After about 5 mins, it reduces below that of the static case. Finally, for the highest fluences studied, the surfaces almost become identical from a fractal dimensional aspect. 2D local slope distributions which reveal the symmetry or asymmetry of the evolving surface were obtained from the AFM images [214]. Earlier studies have indicated that the ripple patterns are symmetric in the linear regime and

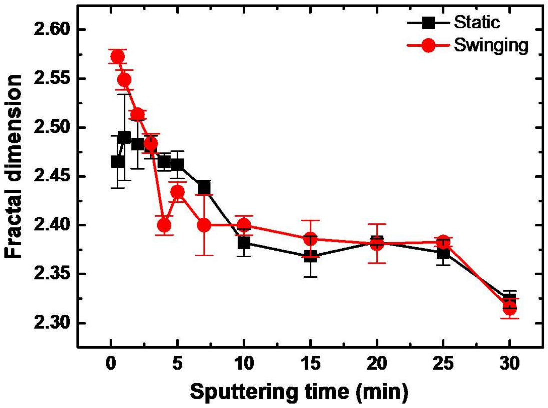

Figure 5.17: Fractal dimensional analyses of samples with increasing sputtering time at $\theta = 67°$ for (a) static and (b) azimuthally swinging ($\Delta\phi = 20°$) substrates.

become asymmetric in the nonlinear one [196, 198, 200, 201, 203, 228]. The ensuing evaluations were done as shown using a schematic (not to scale) in Fig. 5.18. The topleft panel shows a typical AFM image. The shaded line profiles in the x (horizontal) and y (vertical) directions are shown in the top right panel. The arrow indicates the direction of the incoming ion beam. The front and rear faces and their corresponding slopes are also indicated in the schematic. The bottom left panel gives the 2D slope distribution obtained from the 3×3 μm^2 AFM image. The bottom right panel provides the corresponding 1D line profile drawn along the major axis of the 2D slope distribution. For a symmetric structure, the slopes on either sides of the 1D profile would look the same. For example, a circular distribution indicates a flat isotropic surface as in the case of pristine Si as shown in Fig. 5.4. A symmetric elliptical 2D profile usually indicates structures which have similar slopes on both sides and hence also considered symmetric. Any asymmetry in the surface structure will result in an asymmetric dumb-bell shaped 2D distribution, as shown. This eventually would give rise to an asymmetric 1D profile with unequal bimodal peaks, as depicted in the schematic. The 2D slope distributions for the static and the azimuthally swinging samples are shown in Figs. 5.19 and 5.20. 1D line profiles extracted from these distributions have been plotted separately for the static and swinging

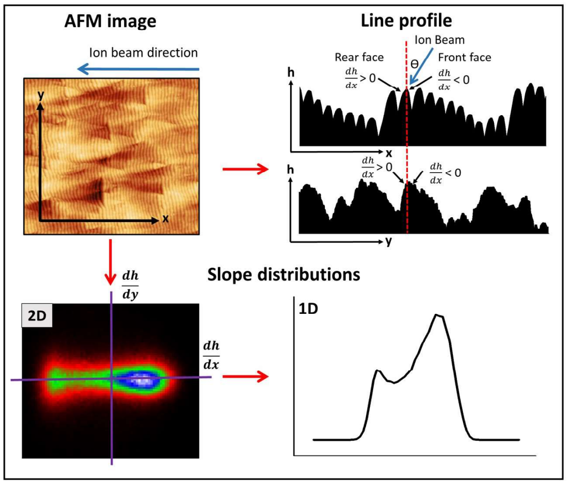

Figure 5.18: Schematic (not to scale) demonstrating 2D slope distribution estimations. *Top left panel*: Representative AFM image showing ripple patterns. *Top right panel*: Shaded line profiles obtained from AFM images in parallel and perpendicular directions. Blue arrows indicate the incident ion beam directions. Front and rear faces are marked with the signs of their respective slopes. *Bottom left panel*: 2D slope distribution obtained from the 3×3 μm^2 AFM image. *Bottom right panel*: 1D line profile across the major axis of the 2D distribution. Red arrows indicate the image/plot from which the subsequent image/plot has been derived.

substrate in Fig. 5.21. The contribution of asymmetry in nanopatterns arises from the dominance of triangular structures rather than ripples, as depicted in Fig. 5.22. For static samples, with increasing fluence, the amplitude of the structures increases as evident from Fig. 5.14 (b). In Fig 5.23, line profiles drawn across the AFM images for different fluences depict an increasing saw-tooth-like morphology with increasing fluence. The nature of the sawtooth pattern indicates that the slope is primarily influenced by triangular structures rather than ripples. This is further proven by the fact that similar line profiles plotted in a scale of 200 nm as shown in Fig. 5.24 demonstrate a symmetric morphology across various fluences, where shadowing does not seem to occur. Fig. 5.25 shows a schematic (not to scale) of local and global incidence angles to the sample surface. It is evident from Figs. 5.21 and Fig 5.23 that asymmetry sets in progressively as sputtering proceeds. The sputtering yield is a function of the incident ion beam angle. However, the actual local

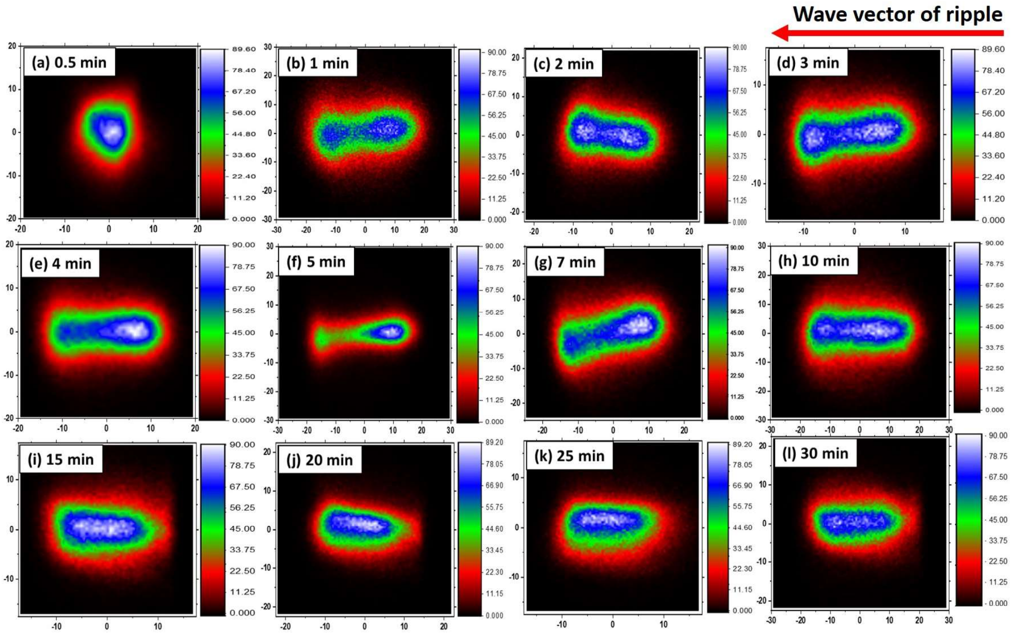

Figure 5.19: 2D slope distributions of 1×1 μm^2 AFM images of Ar$^+$ irradiated static Si surfaces at $\theta = 67°$ have showed for different sputtering times. The horizontal (vertical) axis is parallel (perpendicular) to the ion beam projection. The red arrow indicates the initial direction of the ion beam.

sputtering yield varies across the surface due to the modified surface slopes caused due to a change in the local incidence ion beam angle, which is different from the incident polar angle [228,229]. Such a scenario gives rise to nonlinear effects which includes shadowing in extreme cases and redeposition effects as mentioned earlier. The situation changes when the substrate is swung in the azimuthal direction. Here, the exposure direction changes continuously and oscillates between two extremities ($\Delta\phi = 20°$) and therefore is not in a fixed direction as for the static case. Thus, in effect, the growth of the nanostructures will be slowed down in comparison to the static case. For a swinging sample, each azimuth is bombarded twice, which influences the curvature-dependent sputtering and other mass redistribution effects in a complex manner. Of particular consideration could be the redepositing atoms, which have a preferential direction owing to the sputtered flux when

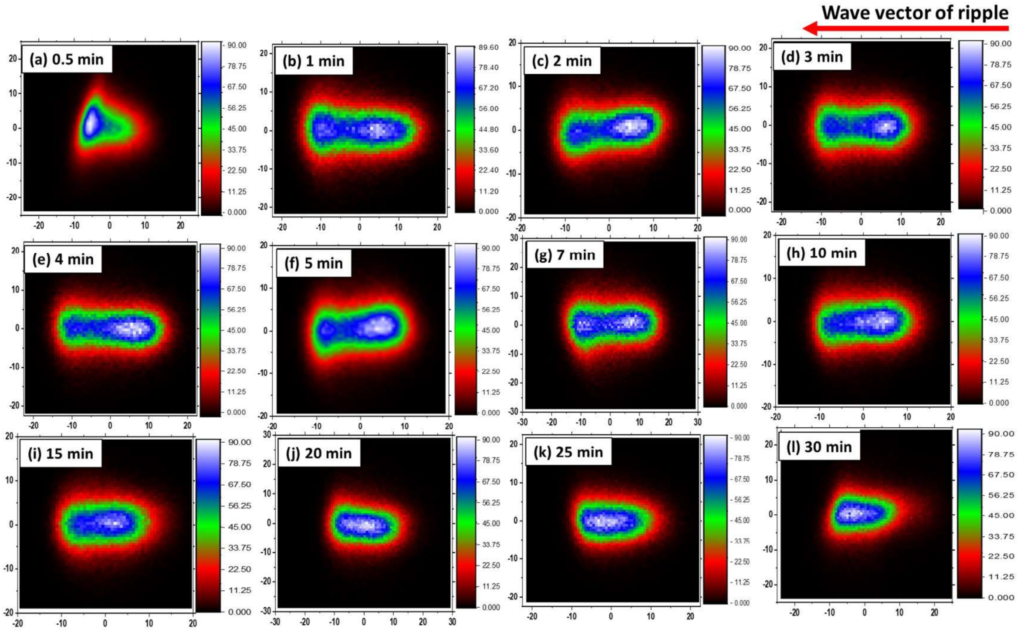

Figure 5.20: 2D slope distributions of 1×1 μm^2 AFM images of Ar$^+$ irradiated azimuthally swinging Si surfaces at $\theta = 67°$ and $\triangle\phi = 20°$ have showed for different sputtering time. The horizontal (vertical) axis is parallel (perpendicular) to the ion beam projection. The red arrow indicates the initial direction of the ion beam.

an impinging ion beam hits a surface. For the static case, the sputtered flux and hence the redepositing atoms will have a preferred directionality in the direction of the fixed incoming beam. For the swinging sample, however, this too oscillates with the azimuth (direction of ϕ) of the beam. A theoretical model describing the observed findings would probably need the azimuthal angle to appear in the EOM along with its coefficients in some form of $\phi(t)$ thereby accounting for its oscillating nature. Upon observing the line profiles in Fig. 5.21, it is seen that for the static case, the slope distribution is symmetric for the initial 30 secs. Asymmetry sets in as early as 1 min of sputtering and continues until about 7 mins, as evident from the asymmetric nature of the 1D profiles. Beyond this time, the distribution indicates symmetry owing to symmetrical structures formed at larger times. This is even more evident from the symmetrical ellipses in the 2D slope distribution as shown in Fig. 5.19. For the swinging sample, the asymmetry, although

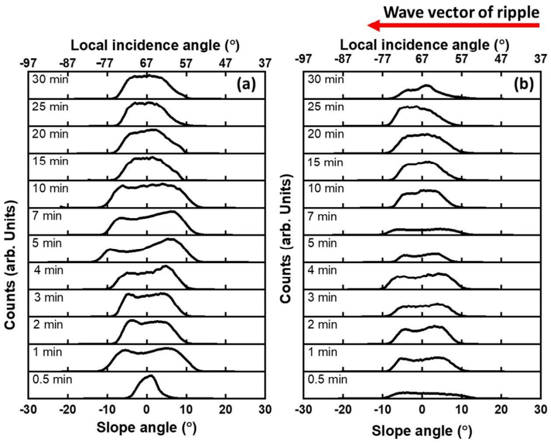

Figure 5.21: 1D line profiles obtained along the major axes of the 2D slope distributions for 500 eV Ar^+ irradiated Si surfaces for *Left panel*: (a) static substrate and *Right panel*: (b) azimuthally swinging substrate at $\Delta\phi = 20°$, respectively. The red arrow indicates the initial direction of the ion beam and slope angle $(\alpha) = \tan^{-1}(\partial h/\partial x)$.

present, is of far less intensity than the static one. For example, the large asymmetries observed for the 5 and 7 mins cases are not observed for any of the swinging samples. The bimodal distribution of almost equal intensity peaks for the swinging samples corroborate to a far lesser asymmetry within an azimuthal interval ($\Delta\phi = 20°$ for this case). Fig. 5.21 (plotted with identical y-axes scales) suggest a reduction in overall asymmetry for the swinging substrates. The overall asymmetricity is also observed in the 2D slope distributions as illustrated in Fig. 5.20. Finally, it is worth noting that the 2D distributions almost take similar forms at around 30 mins, but with a weaker distribution for the swinging case. This indicates that the angular slope dispersion is lower for this case, which is certainly an outcome of the differential exposure effect. A constantly changing azimuth erodes each point on a surface from all possible directions ranging over $\Delta\phi$. This can eventually reduce the local surface slope. As an extreme case, it is observed that for complete rotation a surface normally exhibits a smooth morphology. Thus, it is evident that the swinging geometry brings in an additional factor of a changing directional exposure and redeposition effects that is inconceivable in the static configuration. In effect,

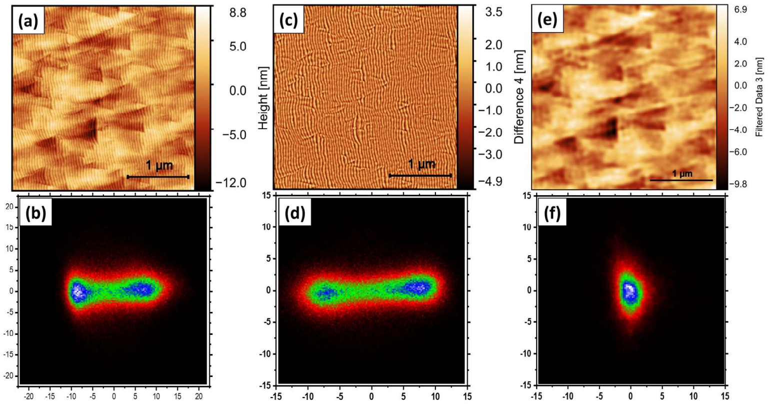

Figure 5.22: The plot illustrates the 2D slope corresponding to 3×3 μm^2 AFM images, along with the short and long wavelength components.

this potentially alters the associated regimes during the nanopattern formation process.

5.4 Conclusions

In summary, we performed experiments using 500 eV Ar$^+$ species incident at a polar angle of 67° on Si(100) surfaces which were swinging around the azimuth within an angle of 20° ($= \Delta\phi$) with a speed of 1 rpm. In contrast to alternative configurations explored by various groups, we believe this offbeat geometry offers better control to alter the nonlinear effects that decide pattern formation regimes. In this study, samples obtained from this unconventional approach were compared with those for which the azimuthal angle was kept fixed. Experiments were carried out for a range of fluences of the ion beam. For both the static and swinging geometries, the morphology exhibited hierarchical architecture comprising parallel-mode nanoripples and triangular structures. Power spectral density (PSD) spectra indicate that the width of the peak is narrower for a swinging substrate compared to a static one. Estimation of the order parameter ($\delta\lambda/\lambda$) shows that ripple ordering is almost similar for the two geometries. Line profiles derived from FFTs of the AFM images show that the side peaks of the FFT spectra related to the swinging

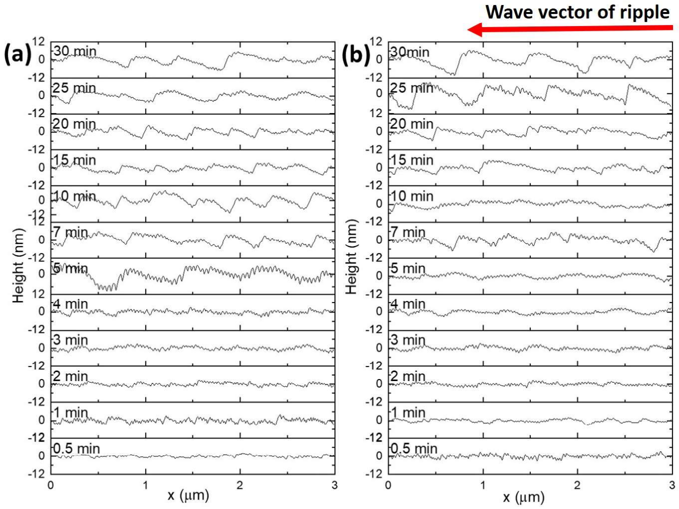

Figure 5.23: Height profiles along the incidence ion beam direction of Ar^+ irradiated Si surfaces at $\theta = 67°$ shown for different sputtering times for (a) static and (b) azimuthally swinging substrates.

case are considerably stronger compared to the static ones. This suggests that the swinging motion plays a substantial role in altering the resulting surface morphology. In the swinging case the coarsening is slowed down but, at the same time, prolonged. Anticoarsening was exhibited for the static samples in the nonlinear regime, in contrast to what has been observed earlier at a much higher energy in the linear regime. The dominance of coarsening behavior occurs through the redeposition of surface atoms during irradiation. The anticoarsening observed could be due to the reduction of triangular domain sizes. The exact mechanisms, however, still remain an open question. The measurements of short and long wavelength components of the surface structures demonstrate that the contribution to rms roughness and correlation length originates predominantly from the triangular structures. The 2D slope distributions and subsequent 1D line profiles derived therefrom reveal that samples bombarded under static configuration develop more asymmetric surface features in comparison to the swinging samples. This is primarily dominated by the presence of asymmetric triangular structures on the surface revealed

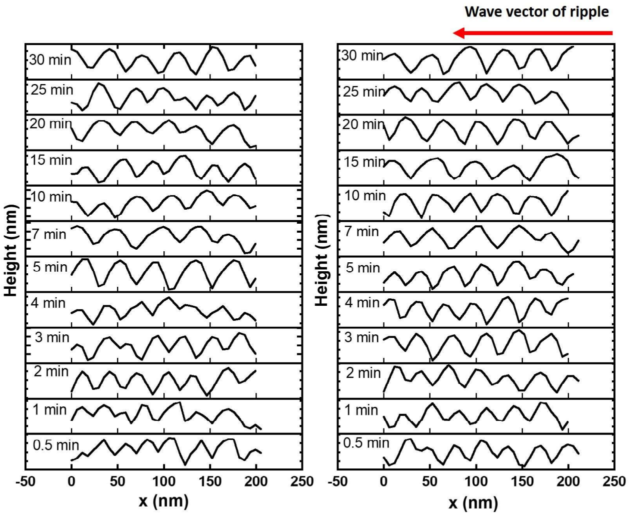

Figure 5.24: Height profiles along the incidence ion beam direction of Ar^+ irradiated Si surfaces at $\theta = 67°$ shown for different sputtering times for (a) static and (b) azimuthally swinging substrates.

from their sawtooth-like line profiles. The ripples on the other hand demonstrate a symmetric morphology as evident from their line profiles. Our results are explained in the light of near-surface mass redistribution events, sputtered atom re-deposition effects and differential exposure conditions that come into play when the sample swings between two extremities ($\phi = -10°$ to $10°$ in the present study). In contrast, for the static samples, the former two play a more significant role as established in earlier studies. We believe this study illumines the spatio-temporal pattern formation benefits of atypical azimuthally swinging geometry in the domain of IBS by augmenting a better understanding of this unique IBS format.

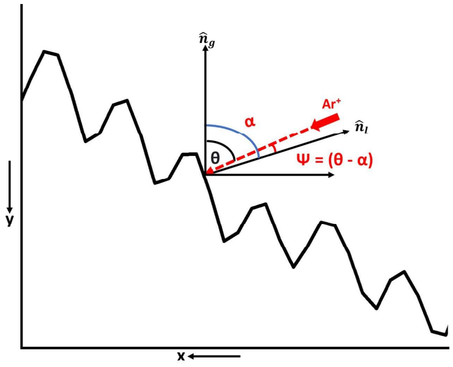

Figure 5.25: Schematic (not to scale) showing global ion beam incidence angle θ and local incidence angle ψ. α denotes the local slope positioned between the local and global normal to the surface. The ripple line profile is a real profile measured from an AFM image.

Chapter 6

Rotation of hierarchical surface structures under ion bombarded asymmetric swinging geometries

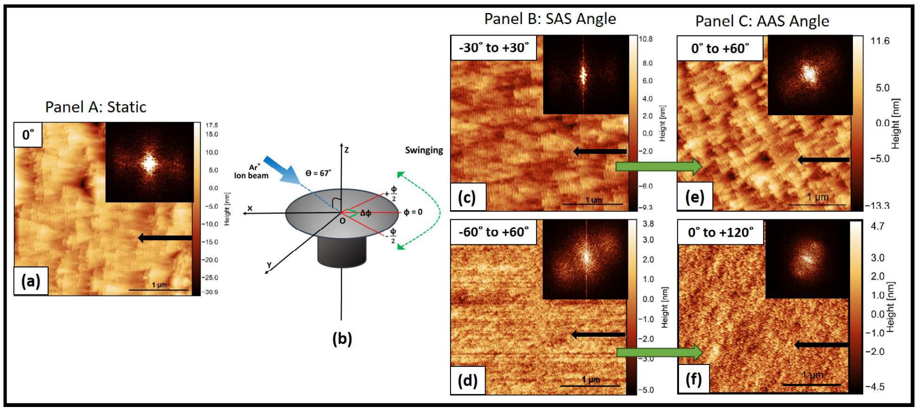

6.1 Introduction

Research on self-organizing nanoscale patterns formed by ions on solid surfaces has become increasingly popular in recent years. Low-energy ion beam irradiation significantly changes surface morphology depending on physical parameters such as ion flux, ion species, and angle of incidence ion beam [6, 7]. The driving mechanism leading to pattern formation originates from the basic linear model by Bradley and Harper [10]. In this model, oblique incident ion bombardment often leads to the formation of periodic height modulation on the surface of an amorphous solid. The model successfully predicted that for an ion incidence angle smaller (greater) than a critical angle θ_c with respect to the surface normal, the ripple wave vector is parallel (perpendicular) to the ion beam projection. Despite this, it is unable to explain the oblique orientation of nanopatterns under any particular physical conditions. In addition, this model cannot also describe ripple wavelength coarsening and roughness saturation after a long irradiation time. To explain this later effect, Makeev, Barbasi, and Cuerno added a nonlinear term in the BH equation. This nonlinear effect is induced due to the lateral growth of surface features and other nonlinear effects [17].

From an experimental perspective, IBI has been conducted in two geometrical ways: static (conventional) and nonstatic (unconventional) [6, 7]. Ion bombardment of static surfaces with ions at oblique (off-normal) incidence is a well studied phenomena which results in patterns that consist of nanodots or nanoripples [99,124,173,178,185,192]. Afterwards, to sculpt intricate surface features, unconventional methods have also been used through the application of IBI [117,119,121,193]. For example, rotating the sample about its surface normal by keeping the incidence angle fixed leads to additional effects not envisaged for fixed sample configurations. Zalar et al. demonstrated that following such a procedure increases the resolution in the case of the depth profile studies [117]. Bradley et al. showed theoretically that the rate at which the surface roughens or smoothens during sample rotation and the characteristic length scale of the nanopatterns formed is dependent on the period of rotation [193]. Som and co-workers suggested that the surface roughness decreases for large rotation speeds. Moreover, the lateral size and height of the mounds scale progressively with fluence [119]. A study by Frost et al. on azimuthally rotating InP surfaces yielded hexagonally ordered nanodots at glancing incidence [121]. Kim *et al* showed that square-symmetric patterns of nanodots are achievable in the erosive regime using experiments with two perpendicularly placed ion beams at the azimuth [137]. Another experiment based on sequential ion sputtering by the same group demonstrated that nanobeads could be formed using such a technique [138]. Studies prove that patterning a pre-rippled surface at azimuthally orthogonal directions leads to enhanced non-linear effects (e.g., redeposition) as compared to an initially flat surface [139]. Researchers in recent studies have found that azimuthal swinging of the substrate about the incident angle of the ion beam leads to additional effects not predicted by following the above methods. Kim et al. explored nanopatterns formation on graphite substrates by azimuthally swinging the substrates during ion beam sputtering [141]. This study shows composite patterns (wall-like structures) exhibit re-entrant reorientation transitions when the substrate swings. These patterns were believed to have formed due to quasi-2D mass flow and shadowing effect. The types of patterns formed were to a large extent disordered in terms of their surface topographies and orientations. Rakhi et al. observed four different regimes upon azimuthally swinging Si surface by different angles at a speed of 1 RPM. These regimes demonstrated drastic changes in the orientation of the ripple wave vector at certain angles [214].

Therefore, the surface topography evolution during low energy ion beam irradiation by using conventional and unconventional is a complex matter. Generation of various nanostructured surfaces with respect to decreasing defect density is possible via self-organization along unconventional process for example, nanoripples, nanodots, nanobeads, and nanoholes. The triangular structures along with nanoscale ripple patterns spontaneously form during oblique incidence low energy ion beam [6, 176], low temperature ion sputtering [177] are observed. It has also been unknown until now what the appropriate physical parameter space of triangular structures would be using the above unconventional techniques. According to Bradley's theory and experimental evidence, nanoripples are perpendicularly rotated with respect to incident ion beam projections. Nevertheless, triangular surface features have not been found to be rotated using any physical parameters with conventional and unconventional methods so far. The parallel mode triangular structures on an amorphous surface are defined in accordance with the incidence angle of the ion beam by using conventional methods [10]. No focus has still been given on the orientation of rotated triangular structures riding with ripple patterns experimentally or theoretically. Solid surface structures are less studied using azimuthal swinging angles. Rakhi et al. demonstrate that these structures obliquely rotate with symmetrically azimuthal angles at constant angles of incidence of polar ions [214]. Asymmetrically azimuthal swinging angles have not been studied for their effect on the surface structure still.

Based on the aforementioned facts, we investigated the evolution of self-organized nanostructures and their unconventional characteristics of Si surface produced by oblique incidence ion beam irradiation at different asymmetric azimuthal swinging angles (AAS). Symmetric azimuthal swinging (SAS) angles resulted in four distinct regimes of morphology, as reported previously by Rakhi et al.. Initially, a hierarchical structure (regime 1) comprised of ripples and triangles oriented along ion beam direction were obtained which gave way to only obliquely oriented ripples (regime 2) at $\triangle\phi = 80°$. A narrow 3rd regime showed a completely flat surface at 100°. Above this angle, only disordered ripples devoid of any triangles were obtained up to 360° (regime 4). In addition, we observed the formation of obliquely rotated triangular structures at certain asymmetrical azimuthal swinging angles of $\triangle\phi$. First, we looked at a surface under static conditions and then compared it with symmetric and asymmetrical azimuth swinging surfaces for constant fluences. The surface morphology of symmetric and asymmetrical azimuth swinging samples showed drastic differences from the static one with respect to the nanopattern's oblique orientation. Results show transitions of ripple wave vector from incidence ion beam direction via an intermediate smoothened (devoid of any nanostructure) surface. The drastic shifts in ripple morphologies and their orientations are believed to be an outcome of the linear versus non-linear effects of sputtering. The dispersive effect is triggered by an azimuthally swinging substrate that is either asymmetric or symmetric. In both cases, dispersive effect disappears at large azimuth swinging angles. For the case of asymmetric azimuthal swinging geometry, rotation of hierarchical structures were observed in contrast to the symmetric swinging case. Shadowing effect is also found to play an essential role in the present context. These results enrich our understanding of pattern formation for swinging geometries and pave a way for further applications with these alluring patterns by suitably exploiting the ion beam parameter space.

6.2 Experimental Techniques

Commercially available undoped polished Si(100) substrates were cut into pieces of 1×1 cm^2 area and cleaned ultrasonically in ethanol for 20 min. Subsequently, they were rinsed with DI (de-ionised) water and dried in air. The choice of Si was done considering the fact that the structures formed on such surfaces are better ordered and have been well studied, both theoretically and experimentally, for conventional beam parameter conditions. Hence, results obtained for unconventional situations like the present one would be easy to compare. Ion beam irradiation (IBI) experiments were carried out at room temperature in a vacuum chamber fitted with a 4 cm broad beam Kaufman ion source. The vacuum inside the chamber had a base pressure of 2×10^{-7} Torr. Irradiations were done with 500 eV Ar$^+$ ions at an incidence angle of 67° with respect to the surface normal. Each sample was marked at the back with an arrow indicating the ion incidence direction. This helped to ensure placing the samples identically aligned while doing AFM measurements. The current density used was 13.3 mA/cm^2. The ion fluence was kept constant at a value of 7.5×10^{19} ions/cm^2 (i.e., sputtering time of 15 mins). To carry out swinging experiments, the sample holder along with the sample was azimuthally swung by an angle $\triangle\phi$ (i.e., $0 \rightarrow +\phi$) as shown in Fig. 6.1. Here, the sample rotates to-and-fro in an oscillatory fashion along one side of the incident ion beam direction, in contrast to an azimuthally swung sample to-and-fro in an oscillatory manner along ion beam projection. An alternating current (a.c) servo motor controlled the azimuthal swinging angle and rotational speed (in revolutions per minute (RPM)) of the sample holder.

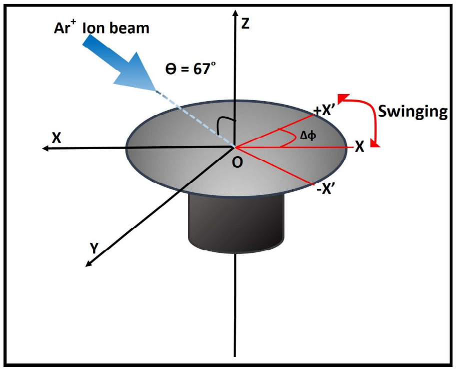

Figure 6.1: Schematic view of the swing geometry in azimuth (ϕ) during IBI. θ (= 67°) is the polar angle between the 500 eV Ar^+ beam (blue arrow) and the (stationary) surface normal. The sample azimuthally swings for an angle $\triangle\phi$ ($0 \rightarrow +\phi$) across the incidence ion beam direction.

In tapping mode, off-normal sputtering samples were characterized ex-situ using Atomic Force Microscopy (AFM) (MultiMode 8, Bruker, USA). The radius of the cantilever used was 10 nm. After obtaining the topographical images of the irradiated surfaces by AFM, quantitative information of the nanostructures were obtained from the acquired data using statistical surface parameters such as wavelength, root-mean-square (rms) roughness (standard deviation of the heights), 2D FFT and power spectral density (PSD), etc. using Gwyddion (version 8.1) [154]. The 1D PSDs are estimated in the direction of the ripple wave vector as observed in the AFM images.

6.3 Results and discussions

The aim of this work is to study the evolution of the surface morphology during low energy ion beam sputtering. Several parameters play a crucial role in the formation of nanopatterns on surfaces. In the beginning of the first experiment, we measured the topography on the SAS substrates and compared it with the stationary substrate. Further azimuthally swinging experiments were conducted using this as a reference. Figure 6.2 demonstrates 3×3 μm^2 AFM images of Si surfaces irradiated at 500 eV at an ion incident angle of 67° under static and symmetrically azimuth swinging conditions. A static sample was irradiated for 15 minutes, while SAS samples were also irradiated for 15 minutes for different azimuth values from 15° to 180°, respectively, at 1 rpm as depicted in the figure. The black arrow indicates the initial direction of the incident ion beam on the Si surface. In all cases, unless otherwise stated, this is considered as the x-axis in all

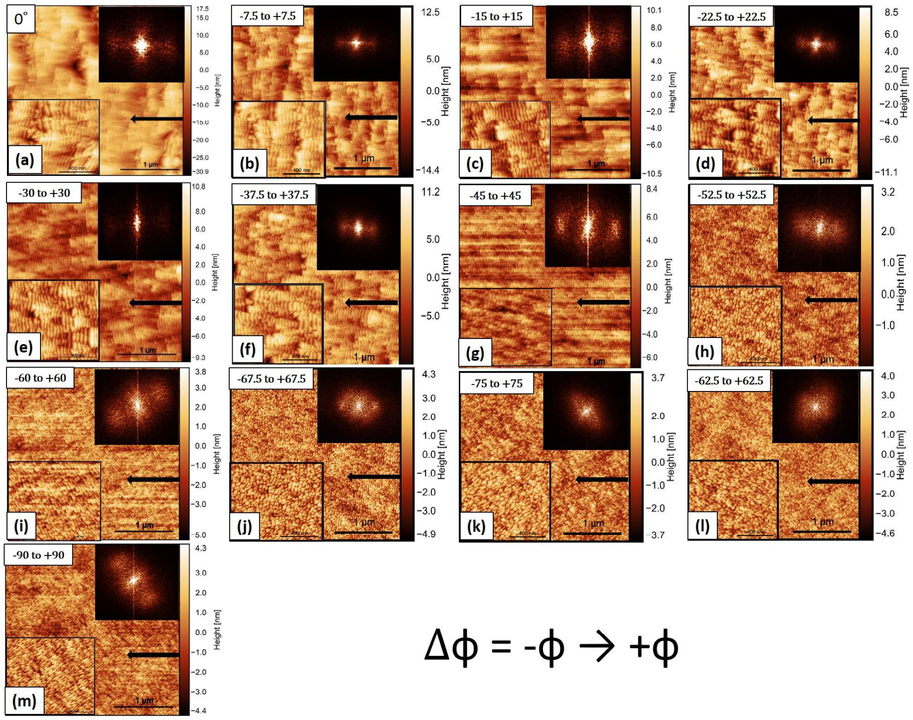

Figure 6.2: 3×3 μm^2 AFM micrographs of 500 eV Ar$^+$ irradiated Si at 67° with fluence of 7.5×10^{19} ions$\times$cm^{-2}, and for different value of $\triangle\phi$ such as (a) stationary, (b) 15°, (c) 30°, (d) 45°, (e) 60°, (f) 75°, (g) 90°, (h) 105°, (i) 105°, (j) 135°, (k) 135°, (l) 165°, and (m) 180°, respectively. Black arrow indicates the initial direction of the ion beam prior to rotation. Top right insets: 2D FFTs of corresponding AFM images. Bottom left insets: corresponding 1×1 μm^2 AFM images.

our subsequent discussions. In static samples, this is fixed throughout the sputtering period. For azimuthally swinging samples, the beam is initially aligned in the direction (i.e., at t = 0). The top right corners in Fig. 6.2 show the 2D FFTs while the bottom left corners show $1 \times 1\ \mu\text{m}^2$ scans corresponding to the AFM images. For the static sample, parallel-mode nanoripples are observed to form on the surface, which is fairly ordered, as evident from the satellite peaks of the 2D FFT image (inset of Fig. 6.2(a)). The orientation of these nanopatterns is also ascertained, as can see from the above images. In addition to the ripples, the morphology shows superposed triangular structures, making the morphology hierarchical. This observation is commensurate with previous findings in the literature [144, 164, 173, 175, 178, 195]. It turns out that the sputtering yield depends on the second derivatives of surface heights h and also their third derivatives such as $\partial_i^2 h$, and $\partial_i^3 h$ as discussed in Ref. [17]. Including these terms in the equation of motion (EOM) makes the ripples anisotropic asymmetric and the ripple propagation dispersive, meaning that the different surface propagating wave vectors (k) travel at different speeds. This dispersive effect can be induced by ion-induced plastic flow or viscous relaxation of ion-induced stresses in the near-surface region. The triangular structure formation at an oblique incidence of the ion beam, theoretically put forward by Bradley and co-workers [175], thus owes its origin to the dispersion terms leading to raised and depressed triangular regions traversed by parallel mode ripples. A highly ordered ripple is formed if dispersion and transverse smoothening mechanisms are sufficiently strong [175]. The SAS samples were irradiated for different values of $\triangle\phi$, showing marked distinctions from the static one. In the range from 15° to 75°, similar hierarchical morphologies are observed here. The triangular surface topography is oriented along the incident ion beam direction, which is fairly evident from the satellite peak of the 2D FFT image [inset of Fig.6.2]. It turns out that sputtering yield depends on second and third order derivatives of surface height h up to 75° as discussed in Ref. [17]. With further increase of azimuthal symmetrical swinging angles from 80° to 90°, triangular morphology entirely vanishes, and only nanoripples are formed on Si surface. It is indicated that the dispersive effect suppresses as the symmetric azimuthal angle increase. The nanoripple orientation is shown from the first satellite peak of 2D FFT image, which is aligned along the incident ion beam direction (x axis as described above) on Si surface. The orientation of structured surfaces is also determined by the anisotropy in the evolution of the surface morphology naturally determined by the projection of the ion beam incidence. For the symmetric azimuthal angle between 100° and 105°, the surfaces remain smooth, nearly independent of incidence ion beam angle and ion energy. At this symmetric azimuthal angle, energy, and incidence polar angle, the surface is stable against ion beam induced instability. Furthermore, by increasing the symmetric azimuthal swinging angle from 110° to 180°, new rotated nanoripple form with a ripple wave vector no longer oriented parallel to the projection of the ion beam. A drastic flip in the ripple orientation by an angle of about $\pm\pi/2$ is observed for a swing angle of from 120° - 180°. The small-scale patterns are observed at higher azimuthal symmetric swing angles, which are not oriented in either the x or y direction. These patterns are oriented approximately at 45° with reference to $+x$ to $-x$ axis. It is noted that the ripples formed beyond a symmetric azimuth swinging angle of 105°, in general, show less ordering as compared to the ripples formed at lower angles of swing (i.e., less than 100°). In full range of symmetric azimuthally swinging angles, four regimes can be identified based on the morphological transitions. The first regime, which shows a hierarchical morphology, spans up to $\triangle\phi = 70^\circ$. Beyond this, the second regime exists where ordered nanoripples are observed which are oriented at 45° from x-axis. The third regime shows smooth surface at $100 - 105^\circ$ [see in suppl material]. The four regimes is identified by less ordered ripple morphology which continues until $\triangle\phi = 180^\circ$. Here, it is shown that the transitions from triangular to ripple structures formation and changes in ripple orientations for a symmetrically azimuthally swinging Si substrate. It was also observed in this case that the ripples are only rotating but not the triangular surface features. Experimentally and theoretically, the change in orientation of triangular type surface topography is still not observed using any surface parameters space.

In addition to examining the effect of symmetric azimuthal swinging angles on the surface morphology of irradiated Si surfaces, asymmetric azimuth swung angles was also investigated, as shown in Fig.6.1. Figure 6.3 shows 3×3 μm^2 AFM images of Si surfaces irradiated at 500 eV at an ion incident angle of 67° under asymmetrically azimuth swinging conditions. An asymmetrical azimuthal swinging sample is irradiated with ion fluences (time durations) 7.5×10^{19} ions cm^{-2} for a different value of $\triangle\phi$ (0 to $+2\phi$) same as the

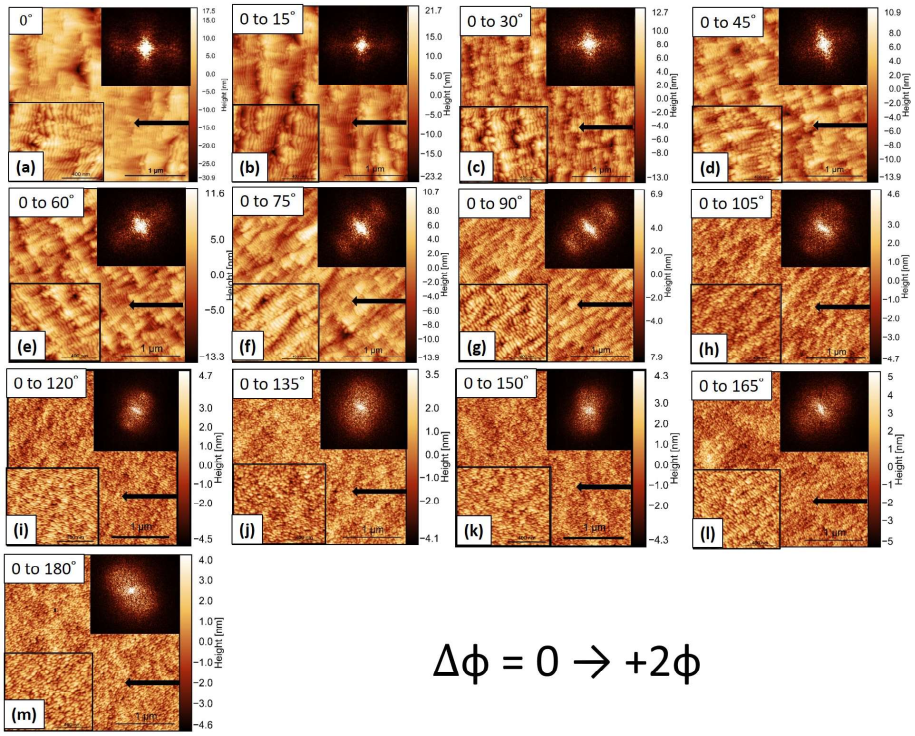

Figure 6.3: 3×3 μm^2 AFM micrographs of 500 eV Ar$^+$ irradiated Si at 67° with fluence of 7.5×10^{19} ions$\times$ cm^{-2}, and for different value of $\triangle\phi$ such as (a) stationary, (b) 15°, (c) 30°, (d) 45°, (e) 60°, (f) 75°, (g) 90°, (h) 105°, (i) 120°, (j) 135°, (k) 150°, (l) 165°, and (m) 180°, respectively. Black arrow indicates the initial direction of the ion beam prior to rotation. Top right insets: 2D FFTs of corresponding AFM images. Bottom left insets: corresponding 1×1 μm^2 AFM images.

previous one. A marked distinction is shown from the static and symmetric azimuthal swinging Si surface topography. The black arrow indicates the initial direction of the incident ion beam direction, as stated above. The top right corners in Fig.6.3 show the 2D FFTs while the bottom left corners show 1×1 μm^2 scans corresponding to the AFM images. The orientation of the ripples can be confirmed from the 2D FFT images for the respective irradiated surfaces. For static Si substrate, the hierarchical topography has already been described above. Similar hierarchical morphology consisting of nanoripples and triangles are also observed for asymmetrical azimuth swinging $\triangle\phi$ formed from 15° (0 - 15°) to 75° (0 - 75°). From 0° to 30°, the hierarchical features are oriented along incident ion beam direction. For a range from 45° to 75°, the triangular type surface features with a wave vector are no longer oriented along the projection of the ion beam These are oriented approximately at 45° with respect to the incident ion beam direction as shown in Fig. 6.3 (b-f). Further, hierarchical structures start to transform into ordered nanoripples along the previously existing triangular structures as depicted in Fig.6.3 (g). A representative example of this scenario can be seen from the top right insets: 2D FFTs of corresponding AFM image. With increasing asymmetric azimuth angle from 105° to 180° as shown in Fig. 6.3 (h-m), only surface anisotropy induced at 45° with respect to incidence ion beam direction instead of periodic patterns. Further, the 2D FFTs images suggest that the ripple wave vector is aligned at 45° with respect to the incidence ion beam projection (x-axis as described above). Within the experimental conditions, the ripples are higher ordered with increasing asymmetric swing angle at 90°, which is shown by the satellite peak of corresponding 2D FFT image. $105° - 180°$, order of ripples decreased, it can be seen from the absence of first staellike peak in FFT Images. The orientation of nanoripples is changed by 45° with respect to $-x$ axis at 180° shown in Fig.6.3 (m). At a higher azimuthally asymmetric swinging angle, the absence of periodic nanopatterns could be confirmed by the absence of peaks in 2D FFT images corresponding to AFM images.

For the role of AAS angles on evolving surfaces, generally, four regimes could be distinguished. In the first regime (extending from 0° to 30°) triangles develop on the Si surface with a wave vector parallel to the incidence ion beam direction. In second regime, the orientation of triangular types structures changes slowly with increasing $\triangle\phi$ up to 75°. In this range, the size of triangular structures is changed, the length of triangles increases and its width perpendicular to the pattern wave vector decreases. Beyond this, the third regime exists where higher ordered nanoripples are oriented at 45° from the x-axis. Finally, for AAS angle from 105° to 180°, a decrease in ripple order is observed. In this regime, some anisotropy is induced in neither x nor y-direction. Similar results for metal substrates (for conventional geometries) have also been reported, such as Ag(110) [230] and Cu(110) [134] for elevated temperature. In the case of metals, the wave vector dependence on the substrate crystallographic directions is also observed for off-normal ion incidence. The rotation of wave vector for amorphous surface depends on asymmetric azimuthal swinging angle no role of the crystallographic directions of the substrate, and at elevated temperature.

The evolution of these topographies is quantified in-depth in terms of root mean square (rms) roughness, wavelength, and 1D power spectral density (PSD) from the corresponding AFM images as shown in Fig. 6.4. The rms roughness for static substrate is about 5.25 nm as evident from Fig. 6.4 (a). For symmetric swinging Si substrate, the rms decreases and saturates, whereas, in case of asymmetric swinging Si substrate, first rms roughness increase then decrease to a saturated value. The variation of the rms roughness for both cases are approximately same. For increasing symmetrical/asymmetrical azimuthal swinging angle, the rms roughness of irradiated surfaces decreases and saturate at higher azimuth angles. For asymmetrically azimuthally swinging substrate, the roughness decreases and saturates to a value of around 0.6 nm. An earlier study done by Moon and co-workers [141] on azimuthlly swinging graphite surfaces using Ar^+ ions at 2 KeV indicate the roughness to scale increasingly for <180° and after that deceased to a

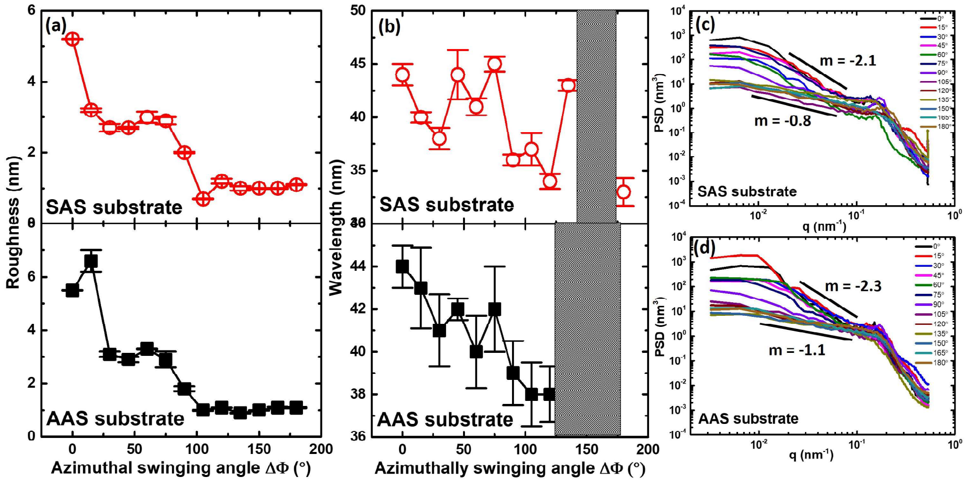

Figure 6.4: The variation in rms roughness and ripple wavelength with an azimuthal swinging angle for a fixed $\theta = 67°$ and fluence 7.5×10^{19} ions/cm^2. Top Panels (a-b) Open circle and (c) PSD for SAS substrates. Bottom panels (a-b) Closed square and (d) PSD for AAS substrates.

fixed value. They had observed wall like structures for these surfaces. Similar mounded morphology has also been observed for the case of Si at 0.08 and 1 RPMs [196]. The saturation of surface roughness for the present case suggests that the irradiation conditions are in the non-linear regime of sputtering. The wavelength or period of the structures is measured from the first position of peak of PSD spectra [214]. The wavelength changes non-monotonically with increasing of SAS angles (open circle) whereas for AAS angles case, it monotonically decreases (closed square) as shown in Fig. 6.4. The absence of any characteristic peak in the PSD spectra for all the AAS samples corroborate to the fact that periodic nanopatterns are not present on Si surfaces. For static substrate, ripple wavelength is 44 nm and it decreases with change in azimuthal angles. Typically, wavelength for SAS angles between 40 to 33 nm are measured. At 150° − 165°, periodic structures disappear with residue of directional features. In case of AAS angles, the wavelength is between 38 and 44 nm. In between 135° − 180°, anisotropic non periodic structures are observed.

The dynamic scaling behavior of ion irradiated surfaces have been analyzed by evaluating its one dimensional structure factor. According to the dynamic scaling hypothesis of Family-Viscek [231], the one dimensional structure factor $S(q,t)$ is given by the relation $S(q,t) \sim q^{-m} \sim q^{-(2\alpha+1)}$ where α is the roughness exponent, it provides a quantitative measure of the imperfection of the surface morphology [173] and $q = 2\pi/l$. Figure 6.4(c)-(d) shows the 1D PSD spectra obtained along the direction of the ripple wave vector for the AFM images shown in Fig. 6.2-6.3. A sharp peak in the PSD spectra usually corresponds to better ripple ordering with fewer defects. The PSD spectra is divided into two regimes such as low-q (small length scale) and large-q (large length scale) regime as shown in Fig. 6.4(c). At a low-q value, a flat plateau extends out to a critical wave number q$_c = \frac{2\pi}{\lambda_c}$, after which the PSD spectra decreases linearly with a negative slope at a large-q value. The slope m of the curves for low-q values has been calculated from the log-log plots of Fig. 6.4(c) and (d). The corresponding roughness exponents have been subsequently calculated using the values of m. In Fig.6.4 (c) for $q<q_c$, the slope m of the spectra in this regimes is about -2.1 and 0.8 corresponding roughness exponent $\alpha = 0.55 \pm 0.01$ and $\alpha = 0.1 \pm 0.02$. with increasing SAS angle the ripples coarsen and the position of the peak is shifting to smaller q values. In Fig.6.4 (d), the slope is - 2.3 and - 1.1, and roughness exponent $\alpha = 0.65 \pm 0.03$ and $\alpha = 0.05 \pm 0.01$. The nanopatterns coarsen and the position of the peak shifting to larger q values. The observed peak in the PSD spectra in the direction of incident ion beam with the -2.3 slope at small q values indicates the presence of a KS like instability. The lateral correlation length is also measured from the autocorrelation function at fluence 7.5×10^{19} ions/cm^2 for SAS and AAS samples as shown in Fig. 6.5. The correlation length is defined as the value of the distance at which it is decreased the $1/e$ of its original value. It shows that two surface heights are significantly are correlated on average if their lateral separation is less than the lateral correlation length [179]. In Fig.6.5, we observed lateral correlation on the AAS surface is larger than on the SAS surface.

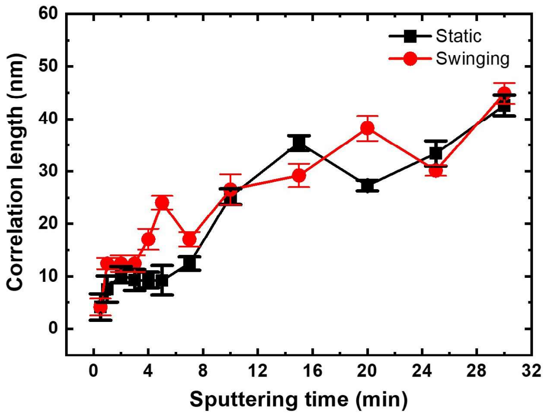

Figure 6.5: Autocorrelation length obtained from autocorrelation function for SAS (open circle) and AAS (closed square) substrates at fluence 7.5×10^{19} ions/cm^2 with the variation of azimuthal swinging angle at $\theta = 67°$.

6.4 Conclusions

We have reported a parameter space where induced triangular features on Si surface are rotated using low energy Ar^+ ion bombardment with concurrent azimuthally swinging substrate. According to earlier published work, only ripples whose wavevector is rotated at oblique incidence $\theta = 67°$ on SAS Si surfaces with low angular velocity [119, 214]. Bradley predicted this type of azimuthal rotation of ripples at low angular speeds [118]. On AAS Si surface, at a fixed angle of incidence $\theta = 67°$, we have observed rotated triangular structures at 45° to the projection beam within the range from 0° to 180°. At room temperature, the orientation of surface features on amorphous Si surfaces is independent of crystallographic directions as opposed to metals as previously mentioned [214]. In simple words, this orientation of triangular type surface structures is the result of the balance between the erosion rate and phase lag of the ion beam vector. Here, we want to emphasize that the oriented triangular surface morphology is observed on amorphous AAS Si(100) surface at fixed off-normal incidence ion bombardment, while in other cases [134, 230] at the recrystallization temperature, it has been observed only by a balance between erosion rates and anisotropic surface diffusion. Our experiment confirms the generality of the proposed model [12]. Thus, when fixing the incidence angle and ion fluence, the roughness effect shows a strong dependence on the symmetric/asymmetric azimuthal swinging angles. The effect of azimuthal swinging sample on the roughness evolution was explored, yielding exciting results. We observed interrupted coarsening of nanostructures with concurrent azimuthal swinging samples. Another novelty of the present work is to provide experimental evidence of the existence of rotating triangular structures on Si surfaces under asymmetric swinging conditions. The experiment reported here will be important for application in the field of ion-beam shaping of surface nanostructures and roughness engineering. In addition, the theoretical model for completely explaining such surface transitions still needs to be explored.

Chapter 7

Summary and Future Outlook

7.1 Summary

The central theme of this thesis is the exploration of the dynamic evolution of self-organized pattern formation on Si(001) by Ar^+ erosion at low energy (from 100 eV to 1200 eV) using broad-beam ion source. The studies in this thesis focus on exploring surface morphological transitions and reduction in morphological surface defects in terms of enhancing periodicity of surface structure using unconventional methods during bombardment. The low energy ion beam technique provides large-scale modification on a surface, which has made this technique unique. In addition to its primary role in surface modification, this technique also impacts the compositional, optical, electrical, magnetic, and mechanical properties of surfaces. Overall, the studies, presented in this thesis, demonstrate the ion beam induced periodic pattern formation under unconventional geometries for the fundamental understanding of ion-solid interaction and for potential applications.

We have studied the formation of periodic nanostructures on Si(100) surface using low energy ion bombardment. In this approach, we explored a novel strategy to reduce defects by employing intermittent ion beam irradiation at varying and constant intermittent ion fluences. Prior to implementing these conditions, the Si surface was sputtered at 900 eV, resulting in the formation of relatively simple disordered ripple morphologies. Subsequently, we investigated lower energy conditions (500 eV), which yielded more perfect individual ripples at the expense of formation of additional triangular structures. In order to further improve ripple ordering, an intermittent sputtering approach was followed. This method significantly impacts the surface morphology of Si substrates. The samples were subjected to low energy Ar^+ ions at oblique incidence with varying ion fluences. Intermittent sputtering was achieved by varying the time interval of sputtering or the time interval between two consecutive sputtering events. The wavelength of the ripples is well tuned for the conditions studied. For the continuous sputtering case, the ripples have the best ordering after a sputter time as low as 5 min. For intermittent sputtering, well-ordered ripples are achieved for intermediate sputtering or relaxation time durations. Analysis of AFM images suggests that with an identical total sputtering duration of 20 min, medium intermittent sputtering intervals result in the largest and most orderly triangular structures. In continuous sputtering conditions, numerous observed properties, including ripple orientation, amplitude saturation, wavelength coarsening, large-scale disorder, and triangular structures, qualitatively agree with the predictions of the nonlinear model. More specifically, they correspond closely with simulated results. The intermittent IBI experiments show how the system responds to periodic changes in irradiation conditions. This research shows how intermittent sputtering can shape the surface development of ion-beam nanostructured surfaces, indicating its potential to control their evolution over time.

Next, we conducted experiments on Si surfaces bombarded by Ar^+ ions, rotating them through various azimuthal angles while maintaining a fixed ion incidence angle of 67°. Furthermore, we examined surface morphologies under different rotation speeds ranging from 1 RPM up to a maximum of 16 RPM. Based on the nanostructure morphology, four different regimes were observed for different azimuthal angles which included ripples along with triangular structures, ripples devoid of triangles, smooth surfaces and disordered rippled topographies. In addition, in the last regime of disordered ripple morphology, the orientations of the ripple wave vector exhibited abrupt changes of as large as 45° with respect to the incident ion direction. Slope calculations reveal that the surface is rougher at large length scales for lower swing angles. Beyond this, the surface tends to be smoother at these length scales. The ripple wavelength and roughness can tuned along with swinging surface. For a particular azimuth, the most ordered ripples were formed for the swing speed of 1 RPM as compared with fractional or higher rotational speeds. On comparing static and rotating surfaces, we found that the former configuration produces hierarchical structures, while the latter configuration results in isotropically rough surfaces. The roughness can adjusted with fluence or higher rotation speeds. Analysis of the AFM images also included calculations of slope distributions in both two dimensions (2D) and one dimension (1D). These calculations revealed the existence of asymmetric ripple patterns on the silicon surface, particularly noticeable for smaller swing angles. This asymmetry mainly arises from the ion-induced near-surface two-dimensional mass distribution. We interpret our findings in light of the dispersive effects of the propagating wave vectors influenced by ion-induced surface phenomena. Our observations suggest that as long as dispersive effects appear owing to the role of dispersive effects, the ripple direction does not change. However, when these effects diminish, ripple orientation shifts. Further, the existence of cancellation modes are believed to have a minimal effect on the ripple characteristics. These findings could motivate the advancement of current theoretical frameworks for these unconventional geometries.

Continuing our investigation, we explored variations in fluence while maintaining a constant incidence ion beam angle of $\theta = 67°$ and a fixed azimuthal angle of $\Delta\phi = 20°$. Our study introduces an unconventional geometric setup for ion beam patterning, revealing a prolonged coarsening of wavelength selection compared to conventional configurations. Furthermore, we observed a rarely documented phenomenon of ripple anticoarsening in hierarchical morphologies at low energies, a novel discovery in this field. The precise control of surface patterning demonstrated in our study holds significant importance for various applications in functional materials design, such as anisotropic magnetism, plasmonics, thermal conductivity, and renewable energy. Moreover, our results highlight gaps in existing spatio-temporal patterning models, underscoring the need for more robust models in both conventional and unconventional geometries. The insights provided by our findings offer valuable information for refining or developing new models. Our study reveals novel facets in this domain, explaining our findings through a fresh mechanism that encompasses dynamic shadowing and redeposition events. Additionally, by examining both linear (including dispersive) and nonlinear aspects of surface growth within the unconventional geometry, we enhance our understanding of the nanostructuring process.

Lastly, we have identified a parameter space where triangular features induced on a Si surface can be rotated using low-energy Ar^+ ion bombardment along with concurrent azimuthal swinging of the substrate. Previous studies have primarily focused on ripples whose wavevectors are rotated under fixed oblique incidence ($\theta = 67°$) on symmetric azimuthal swinging (SAS) Si surfaces, with predictions made by Bradley (1996) regarding such azimuthal rotation at low angular speeds. Our experiments on asymmetric azimuthal swinging (AAS) Si surfaces, under fixed angle of incidence ($\theta = 67°$), revealed rotated triangular structures at 45° with respect to the projection beam within the range from from 0° to 180°. This unique orientation of triangular surface structures on amorphous AAS Si(100) surfaces, observed under fixed off-normal incidence ion bombardment, contrasts with observations in metals where similar features are observed only at recrystallization temperatures, indicating a balance between erosion rates and anisotropic surface diffusion. Our findings underscore the importance of symmetric/asymmetric azimuthal swinging angles in influencing roughness effects when incidence angle and ion fluence are fixed. Specifically, we observed interrupted coarsening of nanostructures with concurrent azimuthal swinging samples, highlighting the significance of this dynamic substrate motion. Additionally, our work provides experimental evidence for the existence of rotating triangular structures on AAS substrates, although theoretical and experimental verification of this phenomenon remains unexplored. This experiment holds promise for applications in ion-beam shaping of surface nanostructures and roughness engineering. However, further refinement of comprehensive models is needed to fully explain sputter ripple formation on surfaces.

7.2 Future Outlook

Our research indicates a study utilizing a variety of physical factors and unconventional methodologies with ion bombardment of solid surfaces. At the present time, several aspects of the self-organization induced by ion bombardment are not fully answered. Experimentally, our group is working closely to provide answers to several of the open questions in this field for future development. We believe our work has been able to address to a large extent some of the challenges associated with the issue of scale-up fabrication of unconventional methods using Si (100) substrates using a simple and cost-effective bottom-up approach. The interaction of Ar^+ ions and Si (100) surfaces proves itself to be a promising candidate for surface analysis.

Nonetheless, the following studies can be conducted for further insights and to gain more understanding. Despite the experimental confirmation of a solid substrate undergoing azimuthal swinging during ion bombardment [214], there remains a gap in theoretical exploration regarding the structural implications of this phenomenon across various physical parameters. In our work, we have investigated how the dispersive effect causes the formation of triangle structures. Further, investigation is required to explore the influence of metal impurities on the formation of triangular structures using unconventional techniques. After irradiation, the conductivity of the solid surface has been determined ex-situ. However, in the future, it would provide more insight to measure the conductivity of a solid surface in-situ during irradiation. In our work, we have conducted all of our research without adding any metal impurities. Subsequent investigations may determine the lowest amount of metal impurities needed to generate nanopatterns or nanodots on the Si surface in response to low-energy argon ion beam radiation. It is essential to determine the wettability of any irradiated solid or soft surface at both normal and oblique ion incidence after metal deposition.

List of Publications

Peer-reviewed Journals:

1. **Rakhi** and Subhendu Sarkar, “Abrupt pattern transitions in argon ion bombarded swinging Si substrates”, **Physical Review B**, 106, 245420 (2022). https://doi.org/10.1103/PhysRevB.106.245420
2. Damanpreet Kaur, **Rakhi**, Subhendu Sarkar, and Mukesh Kumar, “Surface Nanopatterning of Amorphous Gallium Oxide Thin Film for Enhanced Solar-blind Photodetection”, **Nanotechnology** 33, 375302 (2022). https://doi.org/10.1088/1361-6528/ac76d3
3. **Rakhi**, Javier Muñoz-García, Rodolfo Cuerno, and Subhendu Sarkar, “Towards ordered Si surface nanostructuring: Role of an intermittent ion beam irradiation approach”, **Physica Scripta** 98, 055902 (2023). https://doi.org/10.1007/s11468-022-01618-7
4. **Rakhi** and Subhendu Sarkar, “Prolonged pattern coarsening in ion irradiated swinging Si substrates” **Vacuum**, (2024). https://doi.org/10.1016/j.vacuum.2024.113210
5. Damanpreet Kaur, **Rakhi**, Raghvendra Posti, Jaspreet Singh, Subhendu Sarkar, Debangsu Roy, and Mukesh Kumar, “Nanopatterning Induced Si Doping in Amorphous Ga2O3 for Enhanced Electrical Properties and Ultra-Fast Photodetection”, **Small**, (2024). https://doi.org/10.1002/smll.202309277
6. **Rakhi**, and Subhendu Sarkar, “Transient surface wavevectors for asymmetric azimuthally geometries”, **In preparation**

7. **Rakhi**, and Subhendu Sarkar, "Tailored spatial correlation length of Si nanostructured surface using intermittent irradiation", **In preparation**

Conference proceedings:

1. **Rakhi**, and Subhendu Sarkar, "Impact of Intermittent Sputtering on the Ordering of Triangular Surface Topography", **Nuclear Inst. and Methods in Physics Research, B Conference Proceeding**, (2024). https://doi.org/10.1016/j.nimb.2024.165356

Bibliography

[1] Michael Nastasi, James W Mayer, and James K Hirvonen. *Ion-solid interactions: fundamentals and applications*. Cambridge University Press, 1996.

[2] Rainer Behrisch and K Wittmaack. *Sputtering by particle bombardment*, volume 1. Springer-Verlag New York, 1981.

[3] James F Ziegler and Jochen P Biersack. The stopping and range of ions in matter. In *Treatise on heavy-ion science: volume 6: astrophysics, chemistry, and condensed matter*, pages 93–129. Springer, 1985.

[4] P. Sigmund. Sputtering by ion bombardment. theoretical concepts. In R. Behrisch, editor, *Sputtering by Particle Bombardment I*. Springer, Heidelberg, 1981.

[5] Norio Taniguchi. On the basic concept of'nano-technology'. In *Proc. Intl. Conf. Prod. Eng. Tokyo, Part II, 1974*. Japan Society of Precision Engineering, 1974.

[6] Javier Muñoz-García, Luis Vazquez, Mario Castro, Raúl Gago, Andrés Redondo-Cubero, Ana Moreno-Barrado, Rodolfo Cuerno, Javier Muñoz-García, Luis Vázquez, Mario Castro, Raúl Gago, Andrés Redondo-Cubero, Ana Moreno-Barrado, and Rodolfo Cuerno. Self-organized nanopatterning of silicon surfaces by ion beam sputtering. *Materials Science and Engineering R: Reports*, 86:1–44, 2014.

[7] Wai Lun Chan and Eric Chason. Making waves: Kinetic processes controlling surface evolution during low energy ion sputtering. *Journal of Applied Physics*, 101:1–46, 2007.

[8] Naumih M Noah. Design and synthesis of nanostructured materials for sensor applications. *Journal of Nanomaterials*, 2020:1–20, 2020.

[9] Mamoun Muhammed. Engineering of nanostructured materials. In *Nanostructures: synthesis, functional properties and applications*, pages 37–79. Springer, 2003.

[10] R. Mark Bradley and James M. E. Harper. Theory of ripple topography induced by ion bombardment. *Journal of Vacuum Science and Technology A: Vacuum, Surfaces, and Films*, 6:2390–2395, 1988.

[11] Rodolfo Cuerno and Albert-László Barabási. Dynamic scaling of ion-sputtered surfaces. *Physical Review Letters*, 74(23):4746, 1995.

[12] Rodolfo Cuerno, Hernán A Makse, Silvina Tomassone, Stephen T Harrington, and H Eugene Stanley. Stochastic model for surface erosion via ion sputtering: Dynamical evolution from ripple morphology to rough morphology. *Physical Review Letters*, 75(24):4464, 1995.

[13] Javier Muñoz-García, Raúl Gago, Luis Vázquez, José Angel Sánchez-García, and Rodolfo Cuerno. Observation and modeling of interrupted pattern coarsening: Surface nanostructuring by ion erosion. *Physical Review Letters*, 104(2):026101, 2010.

[14] A.-L. Barabási and H. E. Stanley. *Fractal Concepts in Surface Growth*. Cambridge University Press, Cambridge, UK, 1995.

[15] Mehran Kardar, Giorgio Parisi, and Yi-Cheng Zhang. Dynamic scaling of growing interfaces. *Physical Review Letters*, 56(9):889, 1986.

[16] S Park, B Kahng, Hawoong Jeong, and A-L Barabási. Dynamics of ripple formation in sputter erosion: nonlinear phenomena. *Physical Review Letters*, 83(17):3486, 1999.

[17] Maxim A Makeev, Rodolfo Cuerno, and Albert-Laszlo Barabasi. Morphology of ion-sputtered surfaces. *Nuclear Instruments and Methods in Physics Research Section B*, 197:185–227, 2002.

[18] Debasree Chowdhury, Biswarup Satpati, and Debabrata Ghose. Temperature and high fluence induced ripple rotation on si (100) surface. *Materials Research Express*, 3(12):125003, 2016.

[19] Stefan Facsko, Thomas Bobek, Arne Stahl, Heinrich Kurz, and Thomas Dekorsy. Dissipative continuum model for self-organized pattern formation during ion-beam erosion. *Physical Review B*, 69(15):153412, 2004.

[20] Marco Paniconi and KR Elder. Stationary, dynamical, and chaotic states of the two-dimensional damped kuramoto-sivashinsky equation. *Physical Review E*, 56(3):2713, 1997.

[21] Hugues Chaté and Paul Manneville. Transition to turbulence via spatio-temporal intermittency. *Physical review letters*, 58(2):112, 1987.

[22] Maxim A. Makeev and Albert-László László Barabási. Ion-induced effective surface diffusion in ion sputtering. *Applied Physics Letters*, 71:2800–2802, 1997.

[23] Rodolfo Cuerno, Mario Castro, Javier Muñoz-García, Raúl Gago, and Luis Vázquez. Nanoscale pattern formation at surfaces under ion-beam sputtering: A perspective from continuum models. *Nuclear Instruments and Methods in Physics Research Section B: Beam Interactions with Materials and Atoms*, 269(9):894–900, 2011.

[24] Charbel S. Madi, Eitan Anzenberg, Karl F. Ludwig, and Michael J. Aziz. Mass redistribution causes the structural richness of ion-irradiated surfaces. *Physical Review Letters*, 106:1–4, 2011.

[25] R. Mark Bradley and Hans Hofsäss. Nanoscale patterns produced by self-sputtering of solid surfaces: The effect of ion implantation. *Journal of Applied Physics*, 120, 2016.

[26] J. Muñoz-García, R. Cuerno, and Mario Castro. Stress-driven nonlinear dynamics of ion-induced surface nanopatterns. *Physical Review B*, 100(20):205421, 2019.

[27] Thomas WH Oates, Adrian Keller, Stefan Facsko, and Arndt Mücklich. Aligned silver nanoparticles on rippled silicon templates exhibiting anisotropic plasmon absorption. *Plasmonics*, 2:47–50, 2007.

[28] A Toma, D Chiappe, and D Massabo. , c. boragno, f. buatier de mongeot."self-organized metal nanowire arrays with tunable optical anisotropy". *Applied Physics Letters*, 93(16):163104, 2008.

[29] Shinki and Subhendu Sarkar. Au0.5ag0.5alloy nanolayer deposited on pyramidal si arrays as substrates for surface-enhanced raman spectroscopy. *ACS Applied Nano Materials*, 3:7088–7095, 7 2020.

[30] VK Smirnov, DS Kibalov, OM Orlov, and VV Graboshnikov. Technology for nanoperiodic doping of a metal–oxide–semiconductor field-effect transistor channel using a self-forming wave-ordered structure. *Nanotechnology*, 14(7):709, 2003.

[31] Mahesh Saini, Ranveer Singh, KP Sooraj, Tanmoy Basu, Abhijit Roy, Biswarup Satpati, Sanjeev Kumar Srivastava, Mukesh Ranjan, and Tapobrata Som. Cold cathode electron emission with ultralow turn-on fields from au-nanoparticle-decorated self-organized si nanofacets. *Journal of Materials Chemistry C*, 8(47):16880–16895, 2020.

[32] J Fassbender, T Strache, MO Liedke, D Markó, S Wintz, K Lenz, A Keller, S Facsko, I Mönch, and J McCord. Introducing artificial length scales to tailor magnetic properties. *New Journal of Physics*, 11(12):125002, 2009.

[33] M Körner, K Lenz, MO Liedke, T Strache, A Mücklich, A Keller, S Facsko, and J Fassbender. Interlayer exchange coupling of fe/cr/fe thin films on rippled substrates. *Physical Review B*, 80(21):214401, 2009.

[34] MO Liedke, M Körner, K Lenz, M Fritzsche, M Ranjan, A Keller, E Čižmár, SA Zvyagin, S Facsko, K Potzger, et al. Crossover in the surface anisotropy contributions of ferromagnetic films on rippled si surfaces. *Physical Review B*, 87(2):024424, 2013.

[35] François Flory, Ludovic Escoubas, and Gérard Berginc. Optical properties of nanostructured materials: a review. *Journal of Nanophotonics*, 5(1):052502–052502, 2011.

[36] PN Bartlett, JJ Baumberg, S Coyle, and ME Abdelsalam. Optical properties of nanostructured metal films. *Faraday Discussions*, 125:117–132, 2004.

[37] Aleksandra B Djurišić and Yu Hang Leung. Optical properties of zno nanostructures. *small*, 2(8-9):944–961, 2006.

[38] Robert N Wenzel. Resistance of solid surfaces to wetting by water. *Industrial and engineering chemistry*, 28(8):988–994, 1936.

[39] Christian Haase and Helmut Stiebig. Thin-film silicon solar cells with efficient periodic light trapping texture. *Applied physics letters*, 91(6), 2007.

[40] JS Yoo, IO Parm, U Gangopadhyay, Kyunghae Kim, SK Dhungel, D Mangalaraj, and Junsin Yi. Black silicon layer formation for application in solar cells. *Solar energy materials and solar cells*, 90(18-19):3085–3093, 2006.

[41] TWH Oates, A Keller, S Noda, and S Facsko. Self-organized metallic nanoparticle and nanowire arrays from ion-sputtered silicon templates. *Applied physics letters*, 93(6), 2008.

[42] Mukesh Ranjan, Mukul Bhatnagar, and Subroto Mukherjee. Localized surface plasmon resonance anisotropy in template aligned silver nanoparticles: A case of biaxial metal optics. *Journal of Applied Physics*, 117(10), 2015.

[43] S. Camelio, E. Vandenhecke, S. Rousselet, and D. Babonneau. Optimization of growth and ordering of ag nanoparticle arrays on ripple patterned alumina surfaces for strong plasmonic coupling. *Nanotechnology*, 25, 2014.

[44] DA Garanin and H Kachkachi. Surface contribution to the anisotropy of magnetic nanoparticles. *Physical review letters*, 90(6):065504, 2003.

[45] RP Cowburn. Magnetic nanodots for device applications. *Journal of magnetism and magnetic materials*, 242:505–511, 2002.

[46] MO Liedke, B Liedke, A Keller, B Hillebrands, A Mücklich, S Facsko, and J Fassbender. Induced anisotropies in exchange-coupled systems on rippled substrates. *Physical Review B*, 75(22):220407, 2007.

[47] Qiangmin Wei, Jie Lian, Sha Zhu, Weixing Li, Kai Sun, and Lumin Wang. Ordered nanocrystals on argon ion sputtered polymer film. *Chemical Physics Letters*, 452(1-3):124–128, 2008.

[48] Alessandro Molle, F Buatier de Mongeot, C Boragno, R Moroni, F Granone, D Sekiba, R Buzio, U Valbusa, R Felici, and C Quirós. Dense arrays of co nanocrystals epitaxially grown on ion-patterned cu (110) substrates. *Applied Physics Letters*, 86(14), 2005.

[49] J Petersen and Stefan G Mayr. Dewetting of ni and niag solid thin films and formation of nanowires on ripple patterned substrates. *Journal of Applied Physics*, 103(2), 2008.

[50] M Buljan, J Grenzer, A Keller, N Radić, V Valeš, S Bernstorff, T Cornelius, HT Metzger, and V Holỳ. Growth of spatially ordered ge nanoclusters in an amorphous matrix on rippled substrates. *Physical Review B*, 82(12):125316, 2010.

[51] Adrian Keller, Luca Peverini, Jörg Grenzer, György J Kovacs, Arndt Mücklich, and Stefan Facsko. Polycrystalline ni thin films on nanopatterned si substrates: From highly conformal to nonconformal anisotropic growth. *Physical Review B*, 84(3):035423, 2011.

[52] Satoshi Numazawa, Mukesh Ranjan, Karl-Heinz Heinig, Stefan Facsko, and Roger Smith. Ordered ag nanocluster structures by vapor deposition on pre-patterned sio2. *Journal of Physics: Condensed Matter*, 23(22):222203, 2011.

[53] F Bisio, R Moroni, F Buatier de Mongeot, M Canepa, and L Mattera. Isolating the step contribution to the uniaxial magnetic anisotropy in nanostructured fe/ag (001) films. *Physical Review Letters*, 96(5):057204, 2006.

[54] Sarathlal KV, Dileep Kumar, and Ajay Gupta. Growth study of co thin film on nanorippled si (100) substrate. *Applied Physics Letters*, 98(12), 2011.

[55] KV Sarathlal, Dileep Kumar, V Ganesan, and Ajay Gupta. In-situ study of magnetic thin films on nanorippled si (1 0 0) substrates. *Applied Surface Science*, 258(9):4116–4121, 2012.

[56] Adrian Keller, Monika Fritzsche, Ryosuke Ogaki, Ilko Bald, Stefan Facsko, Mingdong Dong, Peter Kingshott, and Flemming Besenbacher. Tuning the hydrophobicity of mica surfaces by hyperthermal ar ion irradiation. *The Journal of Chemical Physics*, 134(10), 2011.

[57] Daniele Chiappe, Andrea Toma, and Francesco Buatier de Mongeot. Tailoring resisitivity anisotropy of nanorippled metal films: Electrons surfing on gold waves. *Physical Review B*, 86(4):045414, 2012.

[58] Mukesh Ranjan, Thomas WH Oates, Stefan Facsko, and Wolfhard Mller. Optical properties of silver nanowire arrays with 35 nm periodicity. *Optics Letters*, 35(15):2576–2578, 2010.

[59] A Toma, D Chiappe, D Massabo, C Boragno, and F Buatier de Mongeot. Self-organized metal nanowire arrays with tunable optical anisotropy. *Applied Physics Letters*, 93(16), 2008.

[60] Joseph B Jackson and Naomi J Halas. Surface-enhanced raman scattering on tunable plasmonic nanoparticle substrates. *Proceedings of the National Academy of Sciences*, 101(52):17930–17935, 2004.

[61] Dimitra Gkogkou, Benjamin Schreiber, Timur Shaykhutdinov, Hoang Khoa Ly, Uwe Kuhlmann, Ulrich Gernert, Stefan Facsko, Peter Hildebrandt, Norbert Esser, Karsten Hinrichs, Inez M. Weidinger, and Thomas W.H. Oates. Polarization- and wavelength-dependent surface-enhanced raman spectroscopy using optically anisotropic rippled substrates for sensing. *ACS Sensors*, 1:318–323, 2016.

[62] C. Martella, D. Chiappe, P. Delli Veneri, L. V. Mercaldo, I. Usatii, and F. Buatier De Mongeot. Self-organized broadband light trapping in thin film amorphous silicon solar cells. *Nanotechnology*, 24, 2013.

[63] VE Ferry. L. a. sweatlock, d. pacifici, and h. a. atwater. *Nano letters*, 8:4391, 2008.

[64] C Mennucci, Sorbo S Del, S Pirotta, M Galli, L C Andreani, C. Martella, M C Giordano, and F Buatier de Mongeot. Light scattering properties of self-organized nanostructured substrates for thin-film solar cells. *Nanotechnology*, 29:355301, 2018.

[65] Ying Qiu, Hong-Chen Hao, Jing Zhou, and Ming Lu. A close to unity and all-solar-spectrum absorption by ion-sputtering induced si nanocone arrays. *Optics Express*, 20(20):22087–22094, 2012.

[66] P Pedraz, S Casado, V Rodriguez, MC Giordano, F Buatier de Mongeot, A Ayuso-Sacido, and E Gnecco. Adhesion modification of neural stem cells induced by nanoscale ripple patterns. *Nanotechnology*, 27(12):125301, 2016.

[67] Cecilia Masciullo, Rossana Dell'Anna, Ilaria Tonazzini, Roman Böettger, Giancarlo Pepponi, and Marco Cecchini. Hierarchical thermoplastic rippled nanostructures regulate schwann cell adhesion, morphology and spatial organization. *Nanoscale*, 9(39):14861–14874, 2017.

[68] BD Ratner. In bd ratner, hoffman as, schoen fj and lemons je (eds.) biomaterials science, 2013.

[69] Yu Yang and Adrian Keller. Ion beam nanopatterning of biomaterial surfaces. *Applied Sciences*, 11(14):6575, 2021.

[70] Charbel S. Madi, Benny Davidovitch, H. Bola George, Scott A. Norris, Michael P. Brenner, and Michael J. Aziz. Multiple bifurcation types and the linear dynamics of ion sputtered surfaces. *Physical Review Letters*, 101:10–13, 2008.

[71] Charbel S. Madi and Michael J. Aziz. Multiple scattering causes the low energy-low angle constant wavelength topographical instability of argon ion bombarded silicon surfaces. *Applied Surface Science*, 258:4112–4115, 2012.

[72] Ana Moreno-Barrado, M Castro, Raúl Gago, Luis Vázquez, Javier Muñoz-García, Andrés Redondo-Cubero, B Galiana, C Ballesteros, and Rodolfo Cuerno. Nonuniversality due to inhomogeneous stress in semiconductor surface nanopatterning by low-energy ion-beam irradiation. *Physical Review B*, 91(15):155303, 2015.

[73] H Hofsäss, Omar Bobes, and K Zhang. Argon ion beam induced surface pattern formation on si. *Journal of Applied Physics*, 119(3), 2016.

[74] Scott A Norris and Michael J Aziz. Ion-induced nanopatterning of silicon: Toward a predictive model. *Applied Physics Reviews*, 6(1), 2019.

[75] B. Ziberi, M. Cornejo, F. Frost, and B. Rauschenbach. Highly ordered nanopatterns on ge and si surfaces by ion beam sputtering. *Journal of Physics Condensed Matter*, 21, 2009.

[76] Marc Teichmann, Jan Lorbeer, Bashkim Ziberi, Frank Frost, and Bernd Rauschenbach. Pattern formation on Ge by low energy ion beam erosion. *New journal of physics*, 15(10):103029, oct 2013.

[77] U Valbusa, C Boragno, and F de Mongeot. Nanostructuring surfaces by ion sputtering. *Journal of Condensed Matter Physics*, 14:8153, 2002.

[78] Sameena Shah Zaman, Petr Dvořák, Robert Ritter, Andreas Buchsbaum, Daniel Stickler, Hans Peter Oepen, Michael Schmid, and Peter Varga. In-situ magnetic nano-patterning of fe films grown on cu (100). *Journal of Applied Physics*, 110(2), 2011.

[79] Kai Chen, Robert Frömter, Stefan Rössler, Nikolai Mikuszeit, and Hans Peter Oepen. Uniaxial magnetic anisotropy of cobalt films deposited on sputtered mgo(001) substrates. *Physical Review B*, 86:1–7, 2012.

[80] JH Kim, NB Ha, JS Kim, M Joe, KR Lee, and R Cuerno. One-dimensional pattern of au nanodots by ion-beam sputtering: formation and mechanism. *Nanotechnology*, 22(28):285301, 2011.

[81] D Flamm, F Frost, and D Hirsch. Evolution of surface topography of fused silica by ion beam sputtering. *Applied Surface Science*, 179(1-4):95–101, 2001.

[82] Christopher C Umbach, Randall L Headrick, and Kee-Chul Chang. Spontaneous nanoscale corrugation of ion-eroded sio 2: the role of ion-irradiation-enhanced viscous flow. *Physical Review Letters*, 87(24):246104, 2001.

[83] A Toma, F Buatier de Mongeot, R Buzio, G Firpo, S R Bhattacharyya, C Boragno, and U Valbusa. Ion beam erosion of amorphous materials: evolution of surface morphology. *Nuclear Instruments and Methods in Physics Research Section B*, 230:551–554, 2005.

[84] Henning Fouckhardt, Ingo Steingoetter, Matthias Brinkmann, Malte Hagemann, Helmut Zarschizky, and Lin Zschiedrich. Nm- and μm-scale surface roughness on glass with specific optical scattering characteristics on demand. *Advances in Opto-Electronics*, 2007, 2007.

[85] Tim Luttrell and Matthias Batzill. Nanoripple formation on tio 2 (110) by low-energy grazing incidence ion sputtering. *Physical Review B*, 82(3):035408, 2010.

[86] Andrés Redondo-Cubero, Luis Vázquez, Denis Jalabert, Katharina Lorenz, and Nebiha Ben Sedrine. Modelling of optical damage in nanorippled zno produced by ion irradiation. *Crystals*, 9(9):453, 2019.

[87] Qiangmin Wei, Jie Lian, Sha Zhu, Weixing Li, Kai Sun, and Lumin Wang. Ordered nanocrystals on argon ion sputtered polymer film. *Chemical Physics Letters*, 452:124–128, 2008.

[88] Cecilia Masciullo, Rossana Dell'Anna, Ilaria Tonazzini, Roman Böettger, Giancarlo Pepponi, and Marco Cecchini. Hierarchical thermoplastic rippled nanostructures regulate schwann cell adhesion, morphology and spatial organization. *Nanoscale*, 9:14861–14874, 2017.

[89] Yu Yang and Adrian Keller. Ion beam nanopatterning of biomaterial surfaces. *Applied Sciences*, 11(14):6575, 2021.

[90] Myoung-Woon Moon, Jun Hyun Han, Ashkan Vaziri, Eun Kyu Her, Kyu Hwan Oh, Kwang-Ryeol Lee, and John W Hutchinson. Nanoscale ripples on polymers created by a focused ion beam. *Nanotechnology*, 20(11):115301, 2009.

[91] Meetika Goyal, Sanjeev Aggarwal, Annu Sharma, and Sunil Ojha. Surface structuring in polypropylene using ar$^+$ beam sputtering: Pattern transition from ripples to dot nanostructures. *Applied Surface Science*, 439:380–385, 2018.

[92] Sandra L Arias, Ming Kit Cheng, Ana Civantos, Joshua Devorkin, Camilo Jaramillo, and Jean Paul Allain. Ion-induced nanopatterning of bacterial cellulose hydrogels for biosensing and anti-biofouling interfaces. *ACS Applied Nano Materials*, 3(7):6719–6728, 2020.

[93] Jun-Yeong Yang, Sunghoon Jung, Eun-Yeon Byeon, Hyun Hwi Lee, Do-Geun Kim, Hyo Jung Kim, Ho Won Jang, and Seunghun Lee. Preliminary validation of a continuum model for dimple patterns on polyethylene naphthalate via ar ion beam sputtering. *Polymers*, 13(12):1932, 2021.

[94] Stefan Facsko, Thomas Dekorsy, Clemens Koerdt, Cyril Trappe, Heinrich Kurz, Alexander Vogt, and Hans L Hartnagel. Formation of ordered nanoscale semiconductor dots by ion sputtering. *Science*, 285(5433):1551–1553, 1999.

[95] Raúl Gago, Luis Vázquez, Rodolfo Cuerno, Marıa Varela, Carmen Ballesteros, and José Marıa Albella. Production of ordered silicon nanocrystals by low-energy ion sputtering. *Applied Physics Letters*, 78(21):3316–3318, 2001.

[96] G. Carter, M. J. Nobes, and F. Paton. Ion bombardment induced ripple topography on amorphous solids. *Radiation Effects*, 33:65–73, 1977.

[97] B. Ziberi, F. Frost, Th Höche, and B. Rauschenbach. Ripple pattern formation on silicon surfaces by low-energy ion-beam erosion: Experiment and theory. *Physical Review B*, 72:1–7, 2005.

[98] B. Ziberi, F. Frost, M. Tartz, H. Neumann, and B. Rauschenbach. Importance of ion beam parameters on self-organized pattern formation on semiconductor surfaces by ion beam erosion. *Thin Solid Films*, 459:106–110, 2004.

[99] Bashkim Ziberi, Frank Frost, Thomas Höche, and Bernd Rauschenbach. Ion-induced self-organized dot and ripple patterns on si surfaces. *Vacuum*, 81:155–159, 2006.

[100] B. Ziberi, F. Frost, B. Rauschenbach, and Th Höche. Highly ordered self-organized dot patterns on si surfaces by low-energy ion-beam erosion. *Applied Physics Letters*, 87, 2005.

[101] D Carbone, A Alija, Olivier Plantevin, R Gago, Stefan Facsko, and Till-Hartmut Metzger. Early stage of ripple formation on ge (001) surfaces under near-normal ion beam sputtering. *Nanotechnology*, 19(3):035304, 2007.

[102] Charbel S Madi, H Bola George, and Michael J Aziz. Linear stability and instability patterns in ion-sputtered silicon. *Journal of Condensed Matter Physics*, 21:224010, 2009.

[103] Shaojun Zhang, Yuanyuan Liu, Shasha Lv, and Jianping Cheng. Surface modification of polymers by ion irradiation: Reactivity principle and application. *Nuclear Instruments and Methods in Physics Research Section B: Beam Interactions with Materials and Atoms*, 543:165097, 2023.

[104] B Ziberi, F Frost, and B Rauschenbach. Self-organized dot patterns on si surfaces during noble gas ion beam erosion. *Surface science*, 600(18):3757–3761, 2006.

[105] Gozde Ozaydin, Karl F. Ludwig, Hua Zhou, Lan Zhou, and Randall L. Headrick. Transition behavior of surface morphology evolution of si(100) during low-energy normal-incidence ar+ ion bombardment. *Journal of Applied Physics*, 103, 2008.

[106] Raúl Gago, L Vázquez, Rodolfo Cuerno, María Varela, C Ballesteros, and José María Albella. Nanopatterning of silicon surfaces by low-energy ion-beam sputtering: dependence on the angle of ion incidence. *Nanotechnology*, 13:304, 2002.

[107] Ari-David David Brown and Jonah Erlebacher. Temperature and fluence effects on the evolution of regular surface morphologies on ion-sputtered si(111). *Physical Review B*, 72:17–20, 2005.

[108] K Zhang, F Rotter, Michael Uhrmacher, Carsten Ronning, H Hofsäss, and Johann Krauser. Pattern formation of si surfaces by low-energy sputter erosion. *Surface and Coatings Technology*, 201(19-20):8299–8302, 2007.

[109] Adrian Keller, Steven Rossbach, Stefan Facsko, and Wolfhard Möller. Simultaneous formation of two ripple modes on ion sputtered silicon. *Nanotechnology*, 19:135303, 2008.

[110] Tapas Kumar Chini, Debi Prasad Datta, and Satya Ranjan Bhattacharyya. Ripple formation on silicon by medium energy ion bombardment. *Journal of Physics Condensed Matter*, 21, 2009.

[111] Marina Inés Cornejo. *Pattern formation on Si surfaces by low-energy ion beam erosion*. PhD thesis, Saarland University, 2011.

[112] S Hazra, TK Chini, MK Sanyal, J Grenzer, and U Pietsch. Ripple structure of crystalline layers in ion-beam-induced si wafers. *Physical Review B*, 70(12):121307, 2004.

[113] Jonah Erlebacher and Ari David Brown. Nonlinear stabilization mechanisms in amplitude saturation during sputter ripple formation on silicon. *Materials Research Society*, 849:59–68, 2005.

[114] Jonah Erlebacher, Michael J Aziz, Eric Chason, Michael B Sinclair, and Jerrold A Floro. Nonclassical smoothening of nanoscale surface corrugations. *Physical Review Letters*, 84:5800, 2000.

[115] B Ziberi, F Frost, M Tartz, H Neumann, and B Rauschenbach. Importance of ion beam parameters on self-organized pattern formation on semiconductor surfaces by ion beam erosion. *Thin Solid Films*, 459(1-2):106–110, 2004.

[116] G. Carter and V. Vishnyakov. Ne+ and ar+ ion bombardment-induced topography on si. *Surface and Interface Analysis*, 23:514–520, 1995.

[117] Anton Zalar. Improved depth resolution by sample rotation during auger electron spectroscopy depth profiling. *Thin Solid Films*, 124:223–230, 1985.

[118] R Mark Bradley. Dynamic scaling of ion-sputtered rotating surfaces. *Physical Review E*, 54:6149, 1996.

[119] Tanmoy Basu, Daniel A. Pearson, R. Mark Bradley, and Tapobrata Som. Temporal evolution of a silicon surface subject to low energy ion irradiation and concurrent sample rotation. *Applied Surface Science*, 379:480–488, 2016.

[120] F. Frost, R. Fechner, B. Ziberi, J. Völlner, D. Flamm, and A. Schindler. Large area smoothing of surfaces by ion bombardment: fundamentals and applications. *Journal of Condensed Matter Physics*, 21:224026, 2009.

[121] F. Frost, A. Schindler, and F. Bigl. Roughness evolution of ion sputtered rotating inp surfaces: Pattern formation and scaling laws. *Physical Review Letters*, 85:4116–4119, 2000.

[122] T Saito, R Horie, T Den, A Bendavid, E Preston, and PJ Martin. Phase separated alsi thin films prepared by filtered cathodic arc deposition. *Thin Solid Films*, 517(5):1567–1571, 2009.

[123] T M Mayer, E Chason, and A J Howard. Roughening instability and ion-induced viscous relaxation of sio2 surfaces. *Journal of Applied Physics*, 76:1633–1643, 1994.

[124] Wai Lun Chan and Eric Chason. Temperature and flux dependence of ion induced ripple: A way to study defect and relaxation kinetics during ion bombardment. *Materials Research Society*, 849:97–102, 2005.

[125] Gozde Ozaydin, Ahmet S. Özcan, Yiyi Wang, Karl F. Ludwig, Hua Zhou, Randall L. Headrick, and D. Peter Siddons. Real-time x-ray studies of mo-seeded si nanodot formation during ion bombardment. *Applied Physics Letters*, 87:1–3, 2005.

[126] G. Ozaydin-Ince and K. F. Ludwig. In situ x-ray studies of native and mo-seeded surface nanostructuring during ion bombardment of si(100). *Journal of Physics Condensed Matter*, 21, 2009.

[127] Gozde Ozaydin, Ahmet S. Özcan, Yiyi Wang, Karl F. Ludwig, Hua Zhou, and Randall L. Headrick. Real-time x-ray studies of the growth of mo-seeded si nanodots by low-energy ion bombardment. *Nuclear Instruments and Methods in Physics Research B*, 264:47–54, 2007.

[128] J. A. Sánchez-García, L. Vázquez, R. Gago, A. Redondo-Cubero, J. M. Albella, and Zs Czigány. Tuning the surface morphology in self-organized ion beam nanopatterning of si(001) via metal incorporation: From holes to dots. *Nanotechnology*, 19, 2008.

[129] JA Sánchez-García, R Gago, R Caillard, A Redondo-Cubero, JA Martin-Gago, FJ Palomares, M Fernández, and L Vázquez. Production of nanohole/nanodot patterns on si (001) by ion beam sputtering with simultaneous metal incorporation. *Journal of Physics: Condensed Matter*, 21(22):224009, 2009.

[130] H. Hofsäss, H. Feldermann, R. Merk, M. Sebastian, and C. Ronning. Cylindrical spike model for the formation of diamondlike thin films by ion deposition. *Applied Physics A: Materials Science and Processing*, 66:153–181, 1998.

[131] Sven Macko, Frank Frost, Bashkim Ziberi, Daniel F Förster, and Thomas Michely. Is kev ion-induced pattern formation on si (001) caused by metal impurities? *Nanotechnology*, 21(8):085301, 2010.

[132] R Reiche and W Hauffe. Pyramid formation on a high index copper bicrystal during bombardment with 10 kev argon and krypton ions. *Applied surface science*, 165(4):279–287, 2000.

[133] P. Karmakar and D. Ghose. Low energy ar+ ion beam induced kinetic roughening of thin pt films on a si substrate. *Nuclear Instruments and Methods in Physics Research B*, 222:477–483, 2004.

[134] S Rusponi, G Costantini, C Boragno, and U Valbusa. Scaling laws of the ripple morphology on cu(110). *Physical Review Letters*, 81:4184–4187, 1998.

[135] K Zhang, Michael Uhrmacher, H Hofsäss, and Johann Krauser. Magnetic texturing of ferromagnetic thin films by sputtering induced ripple formation. *Journal of Applied Physics*, 103(8), 2008.

[136] A. Toma, D. Chiappe, D. Massab, C. Boragno, and F. Buatier De Mongeot. Self-organized metal nanowire arrays with tunable optical anisotropy. *Applied Physics Letters*, 93:1–4, 2008.

[137] M Joe, C Choi, B Kahng, and J-S Kim. Nanopatterning by dual-ion-beam sputtering. *Applied Physics Letters*, 91:233115, 2007.

[138] M Joe, J S H Kim, C Choi, B Kahng, and J S H Kim. Nanopatterning by multiple-ion-beam sputtering. *Journal of Condensed Matter Physics*, 21:224011, 2009.

[139] Keun Soo Kim, Yue Zhao, Houk Jang, Sang Yoon Lee, Jong Min Kim, Kwang S Kim, Jong-Hyun Ahn, Philip Kim, Jae-Young Choi, and Byung Hee Hong. Large-

scale pattern growth of graphene films for stretchable transparent electrodes. *Nature*, 457(7230):706–710, 2009.

[140] Adrian Keller and Stefan Facsko. Tuning the quality of nanoscale ripple patterns by sequential ion-beam sputtering. *Physical Review B*, 82:155444, 2010.

[141] Sun Mi Yoon and J-S S. Kim. Nanopatterning of swinging substrates by ion-beam sputtering. *Journal of Applied Physics*, 119:205301, 2016.

[142] J. H. Kim, S. M. Yoon, Sujin Jo, J. Seo, and J. S. Kim. Nanopatterning by ion beam sputtering in unconventional formats. *Journal of Physics Condensed Matter*, 30, 2018.

[143] Alexandre Cuenat, H. Bola George, Kee Chul Chang, Jack M. Blakely, and Michael J. Aziz. Lateral templating for guided self-organization of sputter morphologies. *Advanced Materials*, 17:2845–2849, 2005.

[144] Sujin Jo, Jihee Jun, Eunsu Lee, S M Yoon, J Seo, Javier Javier Mu noz García, Rodolfo Cuerno, and J-S Kim. Order improvement of surface nanopatterns via substrate rocking under ion bombardment: Experiments and nonlinear models. *Physical Review B*, 102:45421, 2020.

[145] Eunsu Lee, J Seo, Javier Muñoz-García, M Castro, R Cuerno, and J-S Kim. Nanopatterning of rotating highly oriented pyrolytic graphite (0001) surfaces by ion beam irradiation: Experiments and modeling. *Physical Review B*, 105(8):085413, 2022.

[146] G. Carter. Proposals for producing novel periodic structures by ion bombardment sputtering. *Vacuum*, 77:97–100, 2004.

[147] G. Carter. Surface ripple amplification and attenuation by sputtering with diametrically opposed ion fluxes. *Vacuum*, 79:106–109, 2005.

[148] Sebastian Vogel and Stefan J Linz. Surface structuring by multiple ion beams. *Physical Review B*, 75(8):085425, 2007.

[149] Matt P. Harrison and R. Mark Bradley. Producing virtually defect-free nanoscale ripples by ion bombardment of rocked solid surfaces. *Physical Review E*, 93:1–5, 2016.

[150] F.J. Fuchs. 19 - ultrasonic cleaning and washing of surfaces. In Juan A. Gallego-Juárez and Karl F. Graff, editors, *Power Ultrasonics*, pages 577–609. Woodhead Publishing, Oxford, 2015.

[151] D.G. Eskin. 20 - ultrasonic degassing of liquids. In Juan A. Gallego-Juárez and Karl F. Graff, editors, *Power Ultrasonics*, pages 611–631. Woodhead Publishing, Oxford, 2015.

[152] Hubert Gnaser, Alexander Brodyanski, and Bernhard Reuscher. Focused ion beam implantation of ga in si and ge: Fluence-dependent retention and surface morphology. *Surface and Interface Analysis*, 40:1415–1422, 2008.

[153] https://ionsources.com/products/kdc-40.

[154] http://gwyddion.net/.

[155] https://imagej.nih.gov/ij/.

[156] L Reimer. Scanning electron microscopy: Physics of image formation and microanalysis, second edition. *Measurement Science and Technology*, 11(12):1826, dec 2000.

[157] Helen G Hansma and Jan H Hoh. Biomolecular imaging with the atomic force microscope. *Annual review of biophysics and biomolecular structure*, 23(1):115–140, 1994.

[158] H. Kumar Wickramasinghe. Scanning probe microscopy: Current status and future trends. *Journal of Vacuum Science and Technology A*, 8(1):363–368, 1990.

[159] Tevis D B Jacobs, Till Junge, and Lars Pastewka. Quantitative characterization of surface topography using spectral analysis. *Surface Topography: Metrology and Properties*, 5(1):013001, jan 2017.

[160] Werner Wesch and Elke Wendler, editors. *Ion Beam Modification of Solids*, Cham, 2016. Springer.

[161] G Carter. The physics and applications of ion beam erosion. *Journal of Physics D: Applied Physics*, 34:R1, 2001.

[162] M. V. Ramana Murty. Sputtering: The material erosion tool. *Surface Science*, 500(1-3):523–544, 2002.

[163] Javier Muñoz-García, Luis Vázquez, Rodolfo Cuerno, José A Sánchez-García, Mario Castro, and Raúl Gago. Self-organized surface nanopatterning by ion beam sputtering. In Z. M. Wang, editor, *Toward Functional Nanomaterials*, pages 323–398. Springer, 2009.

[164] Rodolfo Cuerno and J-S Kim. A perspective on nanoscale pattern formation at surfaces by ion-beam irradiation. *Journal of Applied Physics*, 128:180902, 2020.

[165] Peter Sigmund. A mechanism of surface micro-roughening by ion bombardment. *Journal of Materials Science*, 8(11):1545–1553, 1973.

[166] Javier Muñoz-García, Mario Castro, and Rodolfo Cuerno. Nonlinear ripple dynamics on amorphous surfaces patterned by ion beam sputtering. *Physical Review Letters*, 96(8):086101, 2006.

[167] Javier Muñoz-García, Rodolfo Cuerno, and Mario Castro. Coupling of morphology to surface transport in ion-beam irradiated surfaces: Oblique incidence. *Physical Review B*, 78(20):205408, 2008.

[168] Hubert Gnaser, Bernhard Reuscher, and Anna Zeuner. Propagation of nanoscale ripples on ion-irradiated surfaces. *Nuclear Instruments and Methods in Physics Research Section B*, 285:142, 2012.

[169] J. Seo, D. A. Pearson, R. M. Bradley, and J. S. Kim. Nanoscale pattern formation on silicon surfaces bombarded with a krypton ion beam: Experiments and simulations. *Journal of Condensed Matter Physics*, 34(26):265001, 2022.

[170] B. Ziberi, F. Frost, T. Höche, and B. Rauschenbach. Dot pattern formation on silicon surfaces by low-energy ion beam erosion. *Materials Research Society*, 849:199–204, 2005.

[171] B. Ziberi, F. Frost, M. Tartz, H. Neumann, and B. Rauschenbach. Ripple rotation, pattern transitions, and long range ordered dots on silicon by ion beam erosion. *Applied Physics Letters*, 92:2006–2009, 2008.

[172] L Vázquez, A Redondo-Cubero, K Lorenz, F J Palomares, and R Cuerno. Surface nanopatterning by ion beam irradiation: compositional effects. *Journal of Condensed Matter Physics*, 34(33):333002, 2022.

[173] Adrian Keller and Stefan Facsko. Ion-induced nanoscale ripple patterns on si surfaces: Theory and experiment. *Materials*, 3:4811–4841, 2010.

[174] Adrian Keller and Stefan Facsko. Tuning the quality of nanoscale ripple patterns by sequential ion-beam sputtering. *Physical Review B*, 82(15):155444, 2010.

[175] Kevin M Loew and R Mark Bradley. Effect of dispersion on the nanoscale patterns produced by ion sputtering. *Physical Review E*, 100:12801, 2019.

[176] Sukriti Hans and Mukesh Ranjan. Emergence of triangular features on ion irradiated silicon (100) surface. *Surface Science*, 715:121951, 2022.

[177] Sukriti Hans, Basanta Kumar Parida, Vivek Pachchigar, Sebin Augustine, Mahesh Saini, K. P. Sooraj, and Mukesh Ranjan. Temperature influence on the formation of triangular features superimposed on nanoripples produced by low-energy ion beam. *Surfaces and Interfaces*, 28(November 2021):101619, 2022.

[178] Mario Castro and Rodolfo Cuerno. Hydrodynamic approach to surface pattern formation by ion beams. *Applied Surface Science*, 258:4171–4178, 2012.

[179] Matthew Pelliccione and Toh-Ming Lu. *Evolution of thin film morphology*, volume 108. Springer, 2008.

[180] Edoardo Vivo, Matteo Nicoli, and Rodolfo Cuerno. Strong anisotropy in two-dimensional surfaces with generic scale invariance: Gaussian and related models. *Physical Review E*, 86:51611, 2012.

[181] Edoardo Vivo, Matteo Nicoli, Martin Engler, Thomas Michely, Luis Vázquez, and Rodolfo Cuerno. Strong anisotropy in surface kinetic roughening: Analysis and experiments. *Physical Review B*, 86:245427, 2012.

[182] Y.-P. Zhao, G.-C. Wang, and T.-M. Lu. *Characterization of Amorphous and Crystalline Rough Surfaces: Principles and Applications*. Academic Press, San Diego, 2001.

[183] William M Tong and R Stanley Williams. Kinetics of surface growth: phenomenology, scaling, and mechanisms of smoothening and roughening. *Annual Review of Physical Chemistry*, 45:401–438, 1994.

[184] S. Habenicht, W. Bolse, K. P. Lieb, K. Reimann, and U. Geyer. Nanometer ripple formation and self-affine roughening of ion-beam-eroded graphite surfaces. *Physical Review B*, 60:R2200–R2203, 1999.

[185] Adrian Keller, Rodolfo Cuerno, Stefan Facsko, and Wolfhard Möller. Anisotropic scaling of ripple morphologies on high-fluence sputtered silicon. *Physical Review B*, 79:115437, 2009.

[186] Enrique Rodríguez-Fernández and Rodolfo Cuerno. Transition between chaotic and stochastic universality classes of kinetic roughening. *Physical Review Research*, 3(1):L012020, 2021.

[187] Adrian Keller, Stefan Facsko, and Wolfhard Möller. Minimization of topological defects in ion-induced ripple patterns on silicon. *New Journal of Physics*, 10:063004, 2008.

[188] Marc Teichmann, Jan Lorbeer, Frank Frost, and Bernd Rauschenbach. Ripple coarsening on ion beam-eroded surfaces. *Nanoscale Research Letters*, 9:1–8, 2014.

[189] Rodolfo Cuerno and Luis Vázquez. Universality issues in surface kinetic roughening of thin solid films. *arXiv preprint cond-mat/0402630*, 2004.

[190] D. Reiser. Model discovery for studies of surface morphological modifications based on Kuramoto-Sivashinsky dynamics. *Physical Review E*, 100(3):033312, 2019.

[191] Rodolfo Cuerno, Javier Javier Mu noz García, Mario Castro, Raúl Gago, and Luis Vázquez. Interplay between morphology and surface transport in nanopatterns produced by ion-beam sputtering. *Materials Research Society*, 1059, 2007.

[192] Rodolfo Cuerno, Luis Vázquez, Raúl Gago, and Mario Castro. Surface nanopatterns induced by ion-beam sputtering. *Journal of Physics Condensed Matter*, 21:1–2, 2009.

[193] Matt P Harrison and R Mark Bradley. Nanoscale patterns formed by ion bombardment of rotating binary materials. *Journal of Condensed Matter Physics*, 27:295301, 2015.

[194] A Lopez-Cazalilla, D Chowdhury, A Ilinov, S Mondal, P Barman, SR Bhattacharyya, D Ghose, F Djurabekova, K Nordlund, and S Norris. Pattern formation on ion-irradiated si surface at energies where sputtering is negligible. *Journal of Applied Physics*, 123(23):235108, 2018.

[195] B Fares, B Gautier, Ph Holliger, N Baboux, G Prudon, and J-Cl Dupuy. Surface roughening and erosion rate change at low energy sims depth profiling of silicon during oblique o_2^+ bombardment. *Applied Surface Science*, 253:2662–2670, 2006.

[196] D. P. Datta, S. K. Garg, T. Basu, B. Satpati, H. Hofsäss, D. Kanjilal, and T. Som. Temporal evolution of ge surface topography under kev ion irradiation: Combined effects of curvature-dependent sputter erosion and atomic redistribution. *Applied Surface Science*, 360:131–142, 2016.

[197] Eunsu Lee, J Seo, J Muñoz-García, M Castro, R Cuerno, and J-S Kim. Nanopatterning of rotating highly oriented pyrolytic graphite (0001) surfaces by ion beam irradiation: Experiments and modeling. *Physical Review B*, 105(8):085413, 2022.

[198] Xin Ou and Stefan Facsko. Crystalline nanostructures on ge surfaces induced by ion irradiation. *Nuclear Instruments and Methods in Physics Research B*, 341:13–16, 2014.

[199] Rossana Dell'Anna, Erica Iacob, Mario Barozzi, Lia Vanzetti, René Hübner, Roman Böttger, Damiano Giubertoni, and Giancarlo Pepponi. The role of incidence angle in the morphology evolution of ge surfaces irradiated by medium-energy au ions. *Journal of Physics: Condensed Matter*, 30(32):324001, 2018.

[200] Mohit Kumar, D P Datta, Tanmoy Basu, S K Garg, H Hofsäss, and Tapobrata Som. Temporal evolution on SiO2 surface under low energy Ar^+ ion bombardment: roles of sputtering, mass redistribution, and shadowing. *Journal of Condensed Matter Physics*, 30(33):334001, 2018.

[201] A Redondo-Cubero, R Gago, F J Palomares, A Mücklich, M Vinnichenko, and L Vázquez. Nanopatterning dynamics on si (100) during oblique 40-kev ar^+ erosion with metal codeposition: Morphological and compositional correlation. *Physical Review B*, 86:85436, 2012.

[202] Debasree Chowdhury and Debabrata Ghose. Ar+-sputtered ge (001) surface nanostructuring at target temperature above the recrystallization threshold. *Journal of Physics D: Applied Physics*, 53(33):335304, 2020.

[203] Prasanta Karmakar. Nano pyramid array on si by concurrent growth of parallel and perpendicular spatial wave and local angle-dependent sputtering. *Applied Surface Science*, 552:149517, 2021.

[204] M C Cross and P. C. Hohenberg. Pattern formation outside of equilibrium. *Reviews of Modern Physics*, 65(3):851–1112, 1993.

[205] G. Carter. Sample rotation and reduced surface roughening in oblique incidence ion sputtering erosion. *Vacuum*, 49:285–295, 1998.

[206] G. Carter. The transport of ion bombardment induced ripples. *Vacuum*, 85:349–351, 2010.

[207] Tanmoy Basu, Jyoti Ranjan Mohanty, and T. Som. Unusual pattern formation on si(1 0 0) due to low energy ion bombardment. *Applied Surface Science*, 258:9944–9948, 2012.

[208] Dipak Bhowmik, Manabendra Mukherjee, and Prasanta Karmakar. Presence of reactive impurities in ar+ ion beam plays a key role for si ripple formation. *Nuclear Instruments and Methods in Physics Research Section B: Beam Interactions with Materials and Atoms*, 444:54–61, 2019.

[209] Yu Kudriavtsev, A. Hernandez-Zanabria, C. Salinas, and R. Asomoza. The formation of porous silicon by irradiation with low-energy ions. *Vacuum*, 177:109393, 2020.

[210] Mario Castro, Raúl Gago, Luis Vázquez, J. Muñoz-García, Rodolfo Cuerno, Javier Muñoz-García, and Rodolfo Cuerno. Stress-induced solid flow drives surface nanopatterning of silicon by ion-beam irradiation. *Physical Review B*, 86:1–12, 2012.

[211] Mario Castro, Rodolfo Cuerno, Luis Vázquez, and Raúl Gago. Self-organized ordering of nanostructures produced by ion-beam sputtering. *Physical Review Letters*, 94:1–4, 2005.

[212] Debi Prasad Datta and Tapas Kumar Chini. Coarsening of ion-beam-induced surface ripple in si: Nonlinear effect vs. geometrical shadowing. *Physical Review B*, 76:1–8, 2007.

[213] Henri Hansen, Alex Redinger, Sebastian Messlinger, Georgiana Stoian, Joachim Krug, and Thomas Michely. Rapid coarsening of ion beam ripple patterns by defect annihilation. *Physical Review Letters*, 102:1–4, 2009.

[214] Rakhi and Subhendu Sarkar. Abrupt pattern transitions in argon ion bombarded swinging si substrates. *Physical Review B*, 106, 12 2022.

[215] Khushboo Bukharia, Prasanta Karmakar, Dileep Kumar, V. R. Reddy, and Ajay Gupta. Evolution of magnetic anisotropy in cobalt film on nanopatterned silicon

substrate studied in situ using MOKE. *Journal of Magnetism and Magnetic Materials*, 497, mar 2020.

[216] Taishan Zhu, Krishnan Swaminathan-Gopalan, Kelly Stephani, and Elif Ertekin. Thermoelectric phonon-glass electron-crystal via ion beam patterning of silicon. *Physical Review B*, 97(17), may 2018.

[217] Damanpreet Kaur, Rakhi, Pargam Vashishtha, Govind Gupta, Subhendu Sarkar, and Mukesh Kumar. Surface nanopatterning of amorphous gallium oxide thin film for enhanced solar-blind photodetection. *Nanotechnology*, 33(37):375302, 2022.

[218] Edoardo Vivo, Matteo Nicoli, and Rodolfo Cuerno. Strong anisotropy in two-dimensional surfaces with generic scale invariance: Gaussian and related models. *Physical Review E*, 86(5):051611, 2012.

[219] Debasree Chowdhury and Debabrata Ghose. Highly-ordered ripple structure induced by normal incidence sputtering on monocrystalline gaas (001): ion energy and flux dependence. *Vaccum*, 129:122–125, 2016.

[220] Martin Engler, Sven Macko, Frank Frost, and Thomas Michely. Evolution of ion beam induced patterns on si(001). *Physical Review B*, 89:1–14, 2014.

[221] Javier Muñoz-García, Mario Castro, and Rodolfo Cuerno. Nonlinear ripple dynamics on amorphous surfaces patterned by ion beam sputtering. *Physical Review Letters*, 96:86101, 2006.

[222] Sandeep Kumar Garg, Rodolfo Cuerno, Dinakar Kanjilal, and Tapobrata Som. Anomalous behavior in temporal evolution of ripple wavelength under medium energy Ar^+ ion bombardment on Si: A case of initial wavelength selection. *Journal of Applied Physics*, 119(22), 2016.

[223] Fridtjof Brauns, Henrik Weyer, Jacob Halatek, Junghoon Yoon, and Erwin Frey. Wavelength Selection by Interrupted Coarsening in Reaction-Diffusion Systems. *Physical Review Letters*, 126(10):104101, 2021.

[224] Debasree Chowdhury, Biswarup Satpati, and Debabrata Ghose. Temperature and high fluence induced ripple rotation on si(100) surface. *Materials Research Express*, 3:1–11, 2016.

[225] Javier Muñoz-García, Rodolfo Cuerno, Subhendu Sarkar, et al. Towards ordered si surface nanostructuring: role of an intermittent ion beam irradiation approach. *Physica Scripta*, 98(5):055902, 2023.

[226] G. Maity, Sunil Ojha, I. Sulania, K. Devrani, and Shiv P. Patel. Fractal characterizations of energetic si ions irradiated amorphized-si surfaces. *Surface and Interface Analysis*, 51:817–825, 8 2019.

[227] R P Yadav, Tanuj Kumar, Vandana Baranwal, Vandana, Manvendra Kumar, P K Priya, S N Pandey, and A K Mittal. Fractal characterization and wettability of ion treated silicon surfaces. *Journal of Applied Physics*, 121:55301, 2017.

[228] G. Carter. The effects of surface ripples on sputtering erosion rates and secondary ion emission yields. *Journal of Applied Physics*, 85:455–459, 1999.

[229] Prasanta Karmakar and Biswarup Satpati. Site specific isolated nanostructure array formation on a large area by broad ion beam without any mask and resist. *Applied Physics Letters*, 104, 6 2014.

[230] S Rusponi, C Boragno, and U Valbusa. Ripple structure on ag(110) surface induced by ion sputtering. *Physical Review Letters*, 78:2795–2798, 1997.

[231] Fereydoon Family and Tamas Vicsek. Scaling of the active zone in the eden process on percolation networks and the ballistic deposition model. *Journal of Physics A: Mathematical and General*, 18(2):L75, 1985.